



SILICON BASED MICROACTUATORS
FOR TELEROBOTIC TACTILE STIMULATION
THESIS

Britton C. Read III, BSEE
Second Lieutenant, USAF

AFIT/GE/ENG/94D-25

19941228 075

DEPARTMENT OF THE AIR FORCE
AIR UNIVERSITY
AIR FORCE INSTITUTE OF TECHNOLOGY

Wright-Patterson Air Force Base, Ohio

AFIT/GE/ENG/94D-25

Accession For	
NTIS CRA&I	<input checked="checked" type="checkbox"/>
DTIC TAB	<input type="checkbox"/>
Unannounced	<input type="checkbox"/>
Justification	
By	
Distribution/	
Availability Codes	
Dist	Avail and/or Special
A-1	

SILICON BASED MICROACTUATORS
FOR TELEROBOTIC TACTILE STIMULATION
THESIS

Britton C. Read III, BSEE
Second Lieutenant, USAF

AFIT/GE/ENG/94D-25

DRG QUALITY INSPECTED 2

Approved for public release; distribution unlimited

REPORT DOCUMENTATION PAGE			Form Approved OMB No. 0704-0188	
<small>Public reporting burden for this collection of information is estimated to average 1 hour per response, including the time for reviewing instructions, searching existing data sources, gathering and maintaining the data needed, and completing and reviewing the collection of information. Send comments regarding this burden estimate or any other aspect of this collection of information, including suggestions for reducing this burden, to Washington Headquarters Services, Directorate for Information Operations and Reports, 1215 Jefferson Davis Highway, Suite 1204, Arlington, VA 22202-4302, and to the Office of Management and Budget, Paperwork Reduction Project (0704-0188), Washington, DC 20503.</small>				
1. AGENCY USE ONLY (Leave blank)	2. REPORT DATE December 94	3. REPORT TYPE AND DATES COVERED Master's Thesis		
4. TITLE AND SUBTITLE Silicon Based Microactuators For Telerobotic Tactile Stimulation		5. FUNDING NUMBERS		
6. AUTHOR(S) Britton C Read III, Second Lieutenant, USAF				
7. PERFORMING ORGANIZATION NAME(S) AND ADDRESS(ES) Air Force Institute of Technology Wright-Patterson AFB, OH 45433		8. PERFORMING ORGANIZATION REPORT NUMBER AFIT/GE/ENG/94D-25		
9. SPONSORING / MONITORING AGENCY NAME(S) AND ADDRESS(ES) Armstrong Laboratory/CFBA Wright-Patterson AFB, OH 45433		10. SPONSORING / MONITORING AGENCY REPORT NUMBER		
11. SUPPLEMENTARY NOTES				
12a. DISTRIBUTION / AVAILABILITY STATEMENT Distribution Unlimited			12b. DISTRIBUTION CODE	
13. ABSTRACT (Maximum 200 words) <p>Silicon based microelectromechanical (MEM) devices using both surface and bulk micromachining have been realized to provide tactile stimulation. The bulk MEM devices utilize the bimorph principle and are fabricated in a complementary metal oxide semiconductor (CMOS) process through MOS implementation system (MOSIS). The surface MEM devices utilize the electrostatic principle and are fabricated in the multi-user MEM process (MUMPS) through MCNC. Eleven major designs are presented and tested to determine if they are suitable to provide tactile stimulation.</p> <p>The bimorph and electrostatic designs were tested using a probe station, a laser interferometer, and a force tester. Measurements were taken on the deflections, cutoff frequencies, and loaded operation of the devices.</p> <p>The bimorph designs fabricated in the CMOS process showed the most potential. The test results indicate that the cantilever beam designs deflect over 30 μm. They operate at frequencies below 130 Hz. The devices operate under a load of approximately 5 μN. An endurance test was performed by actuating a device over 2.5 million times.</p>				
14. SUBJECT TERMS MEM, tactile, stimulators, bimorph, actuator			15. NUMBER OF PAGES 191	
			16. PRICE CODE	
17. SECURITY CLASSIFICATION OF REPORT Unclassified	18. SECURITY CLASSIFICATION OF THIS PAGE Unclassified	19. SECURITY CLASSIFICATION OF ABSTRACT Unclassified	20. LIMITATION OF ABSTRACT UL	

GENERAL INSTRUCTIONS FOR COMPLETING SF 298

The Report Documentation Page (RDP) is used in announcing and cataloging reports. It is important that this information be consistent with the rest of the report, particularly the cover and title page. Instructions for filling in each block of the form follow. It is important to *stay within the lines* to meet optical scanning requirements.

Block 1. Agency Use Only (Leave blank).

Block 2. Report Date. Full publication date including day, month, and year, if available (e.g. 1 Jan 88). Must cite at least the year.

Block 3. Type of Report and Dates Covered. State whether report is interim, final, etc. If applicable, enter inclusive report dates (e.g. 10 Jun 87 - 30 Jun 88).

Block 4. Title and Subtitle. A title is taken from the part of the report that provides the most meaningful and complete information. When a report is prepared in more than one volume, repeat the primary title, add volume number, and include subtitle for the specific volume. On classified documents enter the title classification in parentheses.

Block 5. Funding Numbers. To include contract and grant numbers; may include program element number(s), project number(s), task number(s), and work unit number(s). Use the following labels:

C - Contract	PR - Project
G - Grant	TA - Task
PE - Program Element	WU - Work Unit Accession No.

Block 6. Author(s). Name(s) of person(s) responsible for writing the report, performing the research, or credited with the content of the report. If editor or compiler, this should follow the name(s).

Block 7. Performing Organization Name(s) and Address(es). Self-explanatory.

Block 8. Performing Organization Report Number. Enter the unique alphanumeric report number(s) assigned by the organization performing the report.

Block 9. Sponsoring/Monitoring Agency Name(s) and Address(es). Self-explanatory.

Block 10. Sponsoring/Monitoring Agency Report Number. (If known)

Block 11. Supplementary Notes. Enter information not included elsewhere such as: Prepared in cooperation with...; Trans. of...; To be published in.... When a report is revised, include a statement whether the new report supersedes or supplements the older report.

Block 12a. Distribution/Availability Statement. Denotes public availability or limitations. Cite any availability to the public. Enter additional limitations or special markings in all capitals (e.g. NOFORN, REL, ITAR).

DOD - See DoDD 5230.24, "Distribution Statements on Technical Documents."

DOE - See authorities.

NASA - See Handbook NHB 2200.2.

NTIS - Leave blank.

Block 12b. Distribution Code.

DOD - Leave blank.

DOE - Enter DOE distribution categories from the Standard Distribution for Unclassified Scientific and Technical Reports.

NASA - Leave blank.

NTIS - Leave blank.

Block 13. Abstract. Include a brief (*Maximum 200 words*) factual summary of the most significant information contained in the report.

Block 14. Subject Terms. Keywords or phrases identifying major subjects in the report.

Block 15. Number of Pages. Enter the total number of pages.

Block 16. Price Code. Enter appropriate price code (*NTIS only*).

Blocks 17. - 19. Security Classifications. Self-explanatory. Enter U.S. Security Classification in accordance with U.S. Security Regulations (i.e., UNCLASSIFIED). If form contains classified information, stamp classification on the top and bottom of the page.

Block 20. Limitation of Abstract. This block must be completed to assign a limitation to the abstract. Enter either UL (unlimited) or SAR (same as report). An entry in this block is necessary if the abstract is to be limited. If blank, the abstract is assumed to be unlimited.

AFIT/GE/ENG/94D-25

SILICON BASED MICROACTUATORS
FOR TELEROBOTIC TACTILE STIMULATION

THESIS

Presented to the Faculty of the Graduate School of Engineering
of the Air Force Institute of Technology

Air University

In Partial Fulfillment of the
Requirements for the Degree of
Master of Science in Electrical Engineering

Britton C. Read III, BSEE

Second Lieutenant, USAF

December 1994

Approved for public release; distribution unlimited

Acknowledgments

I would like to thank all the people who helped me with my thesis research and writing. First, I would like to thank my advisor, Dr. Victor M. Bright, for his continuous support and guidance. I would also like to thank Captain John Comtois for his ceaseless help in taking SEM pictures, setting up test equipment, building force testers, and offering design suggestions. I greatly appreciate the assistance of Mr. Chris O'Brien in the lab. I would like to thank my sponsor, Captain Paul Whalen, Human Sensory Feedback and Telepresence branch of the USAF Armstrong Laboratory, Lieutenant Chris Hasser and Ms. Jan Weisenberger for their research help. Finally, I would like to thank my wife, Mrs. Elizabeth Read, for her support and encouragement.

Table of Contents

	Page
Acknowledgment.....	ii
List of Figures	ix
List of Tables.....	xv
Abstract.....	xvi
1. Introduction.....	1-1
1.1. Background	1-1
1.2. Justification.....	1-2
1.3. Problem Statement.....	1-4
1.4. Approach.....	1-4
1.4.1. Silicon Micromachining	1-5
1.4.1.1. Bulk Micromachining.....	1-5
1.4.1.2. Surface Micromachining	1-7
1.4.2. Commercial Fabrication Facilities	1-9
1.4.2.1. CMOS Process	1-9
1.4.2.2. MUMPS Process	1-11
1.4.3. Actuation Methods.....	1-13
1.4.3.1. Bimorph	1-13
1.4.3.2. Electrostatic	1-14
1.4.3.3. Thermal.....	1-15
1.4.4. Designs	1-16
1.4.5. Summary of Approach.....	1-17

1.5. Thesis Overview	1-17
2. Literature Review	2-1
2.1. History of Tactile Stimulation.....	2-1
2.2. Current Tactile Stimulation Methods.....	2-2
2.2.1. Piezoelectric.....	2-2
2.2.1.1. Optacon.....	2-3
2.2.1.2. Other Piezoelectric Devices	2-4
2.2.1.3. Advantages and Disadvantages	2-4
2.2.2. Shape Memory Alloy.....	2-4
2.2.2.1. Current SMA Design	2-6
2.2.2.2. Other SMA Devices.....	2-7
2.2.2.3. Advantages and Disadvantages	2-8
2.2.3. Air Jets.....	2-8
2.2.4. Other Macro Actuation Methods	2-9
2.2.5. Summary of Current Actuation Methods	2-9
2.3. Human Factors.....	2-10
2.3.1. Cutaneous Sensory System.....	2-10
2.3.2. Fingertip Specifications	2-16
2.3.3. Information Presentation	2-19
2.4. Current Silicon MEM Actuators and Heaters	2-22
2.3.1. Piezoelectric.....	2-22
2.3.2. Shape Memory Alloy.....	2-24
2.3.2.1. Fabrication.....	2-25
2.3.2.2. Fabrication Example	2-26
2.3.2.3. Typical Results	2-28

2.3.2.4. Advantages and Disadvantages	2-28
2.3.3. Bimorph.....	2-30
2.3.3.1. Fabrication.....	2-30
2.3.3.2. Fabrication Example	2-31
2.3.3.3. Typical Results	2-32
2.3.3.4. Advantages and Disadvantages	2-33
2.3.4. Electrostatic	2-34
2.3.4.1. Fabrication.....	2-35
2.3.4.2. Typical Results	2-37
2.3.4.3. Advantages and Disadvantages	2-37
2.3.5. Electromagnetic	2-38
2.3.5.1. Fabrication.....	2-38
2.3.5.2. Results.....	2-40
2.3.5.3. Advantages and Disadvantages	2-40
2.4. Conclusions	2-40
3. Theory and Design.....	3-1
3.1. Bimorph Actuation.....	3-1
3.1.1. Bimorph Theory	3-1
3.1.2. Multi-morph Theory	3-8
3.1.3. Heat Transfer	3-11
3.1.4. Force.....	3-12
3.2. Electrostatic Actuation.....	3-13
3.3. Design	3-15
3.3.1. CMOS Designs	3-15
3.3.1.1. Layer Test	3-18

3.3.1.2. Size Test.....	3-19
3.3.1.3. Resistor Test	3-20
3.3.1.4. Support Test.....	3-20
3.3.1.5. Wall Test.....	3-22
3.3.1.6. Heater Test.....	3-22
3.3.2. MUMPS Designs	3-23
3.3.2.1. Electrostatic Attraction Test	3-24
3.3.2.2. Electrostatic Repelling Test	3-25
3.3.2.3. Comb Arch Test	3-26
3.3.2.4. Flexure Test.....	3-27
3.3.2.5. Heater Test.....	3-27
3.4. Conclusions	3-28
4. Experimental Procedure and Analysis of Results	4-1
4.1. Fabrication.....	4-1
4.1.1. Traychip 1 Fabrication.....	4-1
4.1.2. Traychip 1 Fabrication Results.....	4-1
4.1.3. MUMPS 4 Fabrication	4-4
4.1.4. MUMPS 4 Fabrication Results	4-5
4.1.5. Traychip 2 Fabrication.....	4-6
4.1.4. Traychip 2 Fabrication Results.....	4-6
4.2. Etching Procedure.....	4-7
4.2.1. CMOS Etch Procedure.....	4-8
4.2.2. CMOS Etch Results	4-11
4.2.3. MUMPS Etch Procedure.....	4-14
4.2.4. MUMPS Etch Results	4-14
4.3. Bonding Procedure	4-15
4.4. Probe Station	4-17

4.4.1. CMOS Tests and Observations	4-18
4.4.1.1. Wall Test.....	4-18
4.4.1.2. Heater Test.....	4-18
4.4.1.3. Support Test.....	4-19
4.4.1.4. Layer Test	4-20
4.4.1.5. Resistor Test	4-22
4.4.1.6. Displacement Test	4-31
4.4.1.7. Endurance Test.....	4-31
4.4.2. MUMPS Tests and Observations	4-32
4.4.2.1. Electrostatic Attraction Beam	4-32
4.4.2.2. Electrostatic Repelling Beam	4-33
4.4.2.3. Flexure Test.....	4-33
4.4.2.4. Arching Test and Heater Test	4-33
4.5. Force Testing	4-34
4.6. Laser Interferometer Testing	4-37
4.6.1. Sample Interferometer Data.....	4-38
4.6.2. Interferometer Comparison to Optical Microscope Measurements ...	4-38
4.6.3. Heating and Cooling Measurements.....	4-41
4.6.3.1. Typical Heating and Cooling Measurement	4-41
4.6.3.2. Average Heating and Cooling Time	4-41
4.6.3.3. Beam Deflection for Triangle Wave Input	4-48
4.6.4. Comparison of Input Signals.....	4-49
4.6.5. Contour Plot During Actuation.....	4-49
4.6.6. Layer Test Using Interferometer	4-62
4.7. Finger Test.....	4-62
4.8. Summary of Experimental Results	4-74
5. Conclusions and Recommendations.....	5-1

5.1. Conclusions	5-1
5.1.1. Requirements for a Tactile Stimulator.....	5-1
5.1.2. MEM Designs	5-2
5.1.2.1. MUMPS Designs.....	5-2
5.1.2.2. CMOS Designs.....	5-3
5.1.2.3. Bimorph Problems	5-3
5.2. Recommendations.....	5-4
Appendix A: List of Common Acronyms	A-1
Bibliography	BIB-1
Vita	VITA-1

List of Figures

Figure	Page
1.1. Cubic lattice structure showing primary crystal planes	1-5
1.2. Anisotropic etch of (100) and (110) oriented silicon.....	1-6
1.3. Example of released bulk micromachined cantilever beam on silicon.....	1-7
1.4. Surface micromachining of cantilever beam.....	1-8
1.5. OPEN and PSTOP layers in a bulk micromachining MOSIS's CMOS process used in fabricating a cantilever beam.	1-11
1.6. MUMPS layers	1-12
1.7. Bimorph cantilever beam.....	1-14
1.8. Electrostatic cantilever beam on a silicon wafer.....	1-15
2.1. The vibrotactile display unit from an Optacon (TeleSensory, Mountain View, CA)	2-3
2.2. Modes of shape memory alloy	2-5
2.3. SMA tactile stimulator element, dormant and actuated	2-7
2.4. Cross section of skin showing the four receptors	2-12
2.5. Action potentials of the four nerve endings scanned over Braille dots	2-15
2.6. Displacement required to stimulate the finger as a function of frequency.....	2-18
2.7. The letter 'S' in five different modes of presentation.....	2-21
2.8. Two piezoelectric thin film actuation methods.....	2-24
2.9. SMA tactile stimulator example	2-26
2.10. Steps in SMA actuator fabrication.....	2-27
2.11. Bimorph cantilever beam fabrication process.....	2-31
2.12. Microvalve cross section.....	2-35

2.13. Process steps in microvalve fabrication.....	2-36
2.14. Electromagnetic MEM device	2-39
3.1. Bimorph cantilever beam.....	3-2
3.2. Deflection of a supported beam.....	3-3
3.3. Forces and moments on a cross section of a bimorph beam	3-4
3.4. Multi-morph system with six layers	3-9
3.5. Energy balance of a heated cantilever beam.....	3-11
3.6. Electrostatic cantilever beam.....	3-14
3.7. Possible layers in a CMOS process available through MOSIS.....	3-16
3.8. Typical CMOS cantilever beam design	3-18
3.9. Resistor variations in cantilever beams	3-21
3.10. Structural support variations in cantilever beams	3-22
3.11. Typical heating CMOS element.....	3-23
3.12. Layers and thicknesses in the MUMPS process	3-24
3.13. Typical cantilever beam using electrostatic attraction forces	3-25
3.14. Side view of a typical cantilever beam using electrostatic repelling forces	3-26
3.15. Typical comb driven arching beam	3-27
3.16. Typical flexure beam.....	3-28
3.17. Typical heating element.....	3-28
4.1. Optical photograph of Traychip 1 after MOSIS fabrication and before etching .	4-2
4.2. SEM micrograph of poorly etched oxide due to fabrication defects	4-3
4.3. SEM micrograph of poorly defined OPEN layer after release on Traychip 1	4-4
4.4. Optical photograph of MUMPS 4 chip after fabrication and before etching	4-5
4.5. Optical photograph of Traychip 2 after MOSIS fabrication and before etching .	4-6
4.6. SEM micrograph of poor quality OPEN layer cut on unreleased Traychip 2	4-7
4.7. EDP etching apparatus for CMOS chips.....	4-9
4.8. Optical photograph of the partially released etch gauge	4-10

4.9. SEM micrograph of the etch gauge with broken oxide beams showing the partially etched silicon beneath.....	4-11
4.10. SEM micrograph of a portion of Traychip 1 after EDP etching.....	4-12
4.11. SEM micrograph of stress induced curling of cantilever beams on Traychip 1	4-12
4.12. SEM micrograph of a released heating device from Traychip 1 showing the etched pit.....	4-13
4.13. SEM micrograph of a released electrostatic attraction beam from MUMPS 4 chip	4-15
4.14. SEM micrograph of a released electrostatic repelling beam from MUMPS 4 chip	4-16
4.15. SEM micrograph of a released flexing actuator from MUMPS 4 chip	4-16
4.16. SEM micrograph of a released arching actuator based on comb drive from MUMPS 4 chip.....	4-17
4.17. SEM micrograph of a released heating element from Traychip 1.....	4-19
4.18. Experimental and theoretical deflections for beam U-5, 1,2,3,5,6,7,8 layer combination.....	4-23
4.19. Experimental and theoretical deflections for beam U-6, 1,3,4,5,6,7,8 layer combination.....	4-24
4.20. Experimental and theoretical deflections for beam U-7, 1,2,3,5,6,7 layer combination.....	4-25
4.21. Experimental and theoretical deflections for beam U-11, 1,2,3,5,7,9 layer combination.....	4-26
4.22. Experimental and theoretical deflections for oxide beam U-12.....	4-27
4.23. Best fit results of experimental deflections for five bimorph beam combinations	4-28

4.24. Experimental and theoretical deflections for five bimorph beam combinations	4-29
4.25. Best fit average electrical resistance of the beams versus input power.....	4-30
4.26. Force tester for MEM actuators	4-34
4.27. Experimental data and best fit line for beam deflection vs load of beam U-1 (1,3,4,5,6,7 layer combination) using the force tester	4-36
4.28. Laser interferometer experimental setup	4-37
4.29. Sample measurement of beam U-7 (1,2,3,5,6,7 layer combination) layer combination, showing input sine wave and output interferometer data.....	4-39
4.30. Comparison of best fit curves for beam U-7 (1,2,3,5,6,7 layer combination) using both optical microscope and the laser interferometer.....	4-40
4.31. Square wave input to beam U-7 (1,2,3,5,6,7 layer combination) and the laser interferometer output.....	4-42
4.32. 2 volt, 1.55 mW peak power, 50 Hz, square wave input to beam U-7 (1,2,3,5,6,7 layer combination) measuring 0.997 m	4-43
4.33. 2 volt, 1.55 mW peak power, 40 Hz, square wave input to beam U-7 (1,2,3,5,6,7 layer combination) measuring 1 m.....	4-44
4.34. 2 volt, 1.55 mW peak power, 30 Hz, square wave input to beam U-7 (1,2,3,5,6,7 layer combination) measuring 1 m.....	4-45
4.35. 2 volt, 1.55 mW peak power, 20 Hz, square wave input to beam U-7 (1,2,3,5,6,7 layer combination) measuring 1 m.....	4-46
4.36. 2 volt, 1.55 mW peak power, 10 Hz, square wave input to beam U-7 (1,2,3,5,6,7 layer combination) measuring 1 m.....	4-47
4.37. 4 volt, 5.7 mW peak power, 11 Hz, triangle wave input to beam U-7 (1,2,3,5,6,7 layer combination) measuring 4.3 m	4-50
4.38. Deflection versus frequency for a triangle wave input to beam U-7, ox/P1/ox/M1/ox layer combination	4-51

4.39. Deflection versus peak power for triangle wave input to beam U-7 (1,2,3,5,6,7 layer combination) at 20 Hz	4-52
4.40. Deflection versus peak power for sine wave input to beam U-7 (1,2,3,5,6,7 layer combination) at 20 Hz	4-53
4.41. Deflection versus peak power for square wave input to beam U-7 (1,2,3,5,6,7 layer combination) at 20 Hz	4-54
4.42. Deflection comparison of the three waveforms used as input to beam U-7 (1,2,3,5,6,7 layer combination) at 20 Hz	4-55
4.43. Contour plot of beam U-7 (1,2,3,5,6,7 layer combination) with a 20 Hz, triangle wave at 1.55 mW peak power	4-56
4.44. Contour plot of beam U-7 (1,2,3,5,6,7 layer combination) with a 20 Hz, triangle wave at 3.5 mW peak power	4-57
4.45. Contour plot of beam U-7 (1,2,3,5,6,7 layer combination) with a 20 Hz, triangle wave at 5.7 mW peak power	4-58
4.46. Contour plot of beam U-7 (1,2,3,5,6,7 layer combination) with a 20 Hz, triangle wave at 8.6 mW peak power	4-59
4.47. Contour plot of beam U-7 (1,2,3,5,6,7 layer combination) with a 20 Hz, triangle wave at 11.8 mW peak power	4-60
4.48. Contour plots of beam U-7 (1,2,3,5,6,7 layer combination) with a 20 Hz, triangle wave from 1 to 6 peak volts	4-61
4.49. Experimental and theoretical beam deflection versus input electrical power for beam S-1 (1,3,4,5,6,7 layer combination) with a 20 Hz, triangle wave input	4-63
4.50. Experimental and theoretical beam deflection versus electrical input power for beam S-2 (1,2,3,5,7,8 layer combination) with a 20 Hz, triangle wave input	4-64
4.51. Experimental and theoretical beam deflection versus electrical input power for beam S-3 (1,3,4,5,7,8 layer combination) with a 20 Hz, triangle wave input	4-65

4.52. Experimental and theoretical beam deflection versus electrical input power for beam I-4 (1,3,5,6,7,8 layer combination) with a 20 Hz, triangle wave input.....	4-66
4.53. Experimental and theoretical beam deflection versus electrical input power for beam S-5 (1,2,3,5,6,7,8 layer combination) with a 20 Hz, triangle wave input	4-67
4.54. Experimental and theoretical beam deflection versus electrical input power for beam S-6 (1,3,4,5,6,7,8 layer combination) with a 20 Hz, triangle wave input	4-68
4.55. Experimental and theoretical beam deflection versus electrical input power for beam U-7 (1,2,3,5,6,7 layer combination) with a 20 Hz, triangle wave input	4-69
4.56. Experimental and theoretical beam deflection versus electrical input power for beam U-8 (1,3,5,7,8 layer combination) with a 20 Hz, triangle wave input	4-70
4.57. Experimental and theoretical beam deflection versus electrical input power for beam S-9 (1,3,5,6,7 layer combination) with a 20 Hz, triangle wave input.....	4-71
4.58. Experimental and theoretical beam deflection versus electrical input power for beam S-12 (1,3,5,7,9 layer combination) with a 20 Hz, triangle wave input.....	4-72
4.59. Best fit curves of beam deflection versus electrical input power for beams constructed of different material combinations with a 20 Hz, triangle wave input ...	4-73

List of Tables

Table	Page
1.1. Mechanical Properties of Selected Materials.....	1-3
2.1. Cutaneous Tactile Receptor Systems.....	2-14
2.2. SMA Comparison with Other Actuation Techniques	2-29
3.1. Coefficient of Thermal Expansion and Young's Modulus for Some Microelectronic Materials	3-6
3.2. Figure of Merit for Different Material Combinations	3-7
3.3. CMOS Fabrication Layers Available Through MOSIS	3-17
3.4. Different Layer Combinations Used in CMOS Designs.....	3-19
4.1. Experimental Estimation of the Constant C	4-21
4.2. Heating and Cooling Times for a Range of Frequencies on Beam U-7	4-48
5.1. Summary of Results of CMOS Bimorph Testing	5-3

Abstract

Silicon based microelectromechanical (MEM) devices using both surface and bulk micromachining have been realized to provide tactile stimulation. MEM actuators have not previously been used as tactile stimulators. The bulk MEM devices utilize the bimorph principle and are fabricated in a complementary metal oxide semiconductor (CMOS) process through MOS implementation system (MOSIS). The surface MEM devices utilize the electrostatic principle and are fabricated in the multi-user MEM process (MUMPS) through MCNC. Eleven major designs are presented and tested to determine if they are suitable to provide tactile stimulation.

The bimorph and electrostatic designs were tested using a probe station, a laser interferometer, and a force tester. Measurements were taken on the deflections, cutoff frequencies, and loaded operation of the devices.

The bimorph designs fabricated in the CMOS process showed the most potential. The test results indicate that the cantilever beam designs deflect over 30 μm . They operate at frequencies below 130 Hz. The devices operate under a load of approximately 5 mg. An endurance test was performed by actuating a device over 2.5 million times.

Silicon Based Microactuators for Telerobotic Tactile Stimulation

1. INTRODUCTION

1.1. Background.

In order to effectively control any system, accurate feedback from the system is required. This feedback can be transferred in any number of ways; information might be audio, visual, numerical, electrical, etc. For a remotely controlled robotic (telerobotic) system transporting hazardous materials (radioactive material or explosives), this feedback is critical. The human operator must have real-time, precise data from the remote robot being controlled. In the ideal case the human operator would have the same or better perceptions than if he was actually present at the robot location. At a minimum, video, audio, and touch perceptions are needed for precise control. Video and audio feedback are easily realized with current technology and are drastically improving with the advent of Virtual Reality. However, precise control of what the remote robot is grasping or touching is not currently feasible.

The Human Sensory Feedback and Telepresence branch of the USAF Armstrong Laboratory, Wright-Patterson AFB, OH is working to improve the remote robot control process. One aspect of control under study is tactile stimulation. Tactile stimulation is a way of providing information by stimulating the skin. The goal is to provide accurate tactile stimulation to allow a human operator to know when the robot is in contact with an object, how much pressure is being applied, what the texture of the object is, and if the object is slipping. This information would be passed to the operator by stimulating the human finger.

The human finger tactile stimulator will not only benefit the Air Force, but also society. If remote robots can be controlled with greater precision, danger to human life could be reduced. Any situation that involves working with hazardous materials would be performed by a robot. With a better system of tactile stimulation, the control of a telerobotic system would be greatly enhanced.

1.2. Justification.

Precision manipulation of remote complex objects has been a goal since the 1960's [1]. Initial work was concerned with force reflection and not precision finger stimulation. More recently, tactile feedback from telerobotic systems to the operators finger has been shown to increase the pass/fail rate of complex tasks by 17-40% [2]. This study also indicated that when an object is obscured from vision, fragile, or needs accurate positioning, tactile stimulation improves efficiency in manipulating it.

Current research into tactile stimulation involves large or "macro" scale stimulators. These devices have shortcomings that limit their effectiveness as a tactile stimulator. However, silicon based microelectromechanical (MEM) tactile stimulators have the potential to stimulate the human finger and overcome the problems inherent in "macro" stimulators.

There are several reasons why silicon based MEM tactile stimulators have the potential to perform better than current tactile stimulation techniques. First, silicon is inexpensive compared to most "macro" actuation materials. Second, silicon has very good mechanical properties [3]. Table 1.1 shows that silicon is nearly as strong as steel and that it compares favorably with other materials. Third, silicon has been studied for over 30 years and integrated circuit (IC) processing techniques are mature. The infrastructure for semiconductor processing is already in place and easily adaptable to MEM devices. Fourth, silicon based micro structures have the ability to be monolithically integrated [4]. These same silicon based MEM devices can be integrated with complex electronic

circuitry to amplify and process the data. Fifth, silicon MEM actuators can be implemented in large two dimensional arrays for greater resolution. Sixth, micro scale devices are inherently smaller, lighter, and faster than their macro counterparts.

Table 1.1. Mechanical Properties of Selected Materials [3].

Material	Yield Strength (10^{-10} dyne/cm ²)	Knoop Hardness (kg/mm ²)	Young's Modulus (10^{12} dyne/cm ²)	Density (g/cm ³)
Diamond*	53	7000	10.35	3.5
SiC*	21	2480	7.0	3.2
TiC*	20	2470	4.97	4.9
Al ₂ O ₃ *	15.4	2100	5.3	4.0
Si ₃ N ₄ *	14	3486	3.85	3.1
Iron*	12.6	400	1.96	7.8
SiO ₂ (fibers)	8.4	820	0.73	2.5
Si*	7.0	850	1.9	2.3
Steel (max str)	4.2	1500	2.1	7.9
W	4.0	485	4.1	19.3
Stainless Steel	2.1	660	2.0	7.9
Mo	2.1	275	3.43	10.3
Al	0.17	130	0.7	2.7
* Single Crystal				

An additional contribution of this thesis is the overall increase of knowledge about MEM devices. Microelectromechanical systems (MEMS) is a very new field and this is the first thesis dealing with MEM structures at the Air Force Institute of Technology (AFIT). Yet this field has potentially limitless applications; some current uses include micromotors, micropumps, microvalves, accelerometers, and deformable mirrors.

1.3. Problem Statement.

The need for precise control of telerobotic systems is evident. Tactile stimulation is needed to improve feedback to the remote human operator. Current technology does not acceptably meet all the goals of a tactile stimulator, as will be shown in Chapter 2. A better method of tactile stimulation is needed.

Specific objectives for a tactile stimulator include the following. First, the device should fit into a glove worn by the human operator. This requirement would insure that the stimulation system does not interfere with the other robot control systems. Second, the tactile stimulator should have higher resolution than the current "macro" scale stimulator [5]. This would imply a multiple element array of actuators (devices that stimulate the finger to transmit information) with greater than 5x6 elements over an area 1.2 cm wide by 1.5 cm long. Third, the device should be safe with no excessively high voltages, currents, or temperatures that could harm the operator or the area being stimulated. Forth, the device should be compatible with standard complementary metal oxide semiconductor (CMOS) circuitry. This means the device would not require special equipment for operation and could be activated with 5 volt signals. Fifth, the actuators should operate from DC to 400 Hz with a rapid onset at lower frequencies.

Since current tactile stimulators fail to meet one or more of the above criteria, a new tactile stimulator should be developed. Devices need to be designed, modeled, fabricated, and tested with the above criteria as a goal.

1.4. Approach.

The objective of this thesis is to investigate silicon (Si) based MEM tactile stimulators. This research involves (1) investigating the structural and mechanical properties of Si based MEM devices fabricated through the two processes available to AFIT; (2) designing a variety of tactile stimulators utilizing both of these processes; and (3) fabricating, testing, and evaluating the tactile stimulator designs.

1.4.1. Silicon Micromachining. The two fabrication processes available to AFIT are surface micromachining and bulk micromachining. Both processes involve wet chemical etching of silicon and thin film materials, thereby taking advantage of typical IC fabrication techniques. These processes allow MEM devices to be formed by anisotropically etching silicon with bulk micromachining or selectively etching certain materials with surface micromachining. The end product from both processes is some form of released three dimensional structure. By controlling which layers are removed and how much undercutting is done, MEM structures can be formed.

1.4.1.1. Bulk Micromachining. The first process, bulk micromachining, was discovered in the 1950s. Certain chemicals like potassium hydroxide (KOH) and ethylene diamine pyrocatechol (EDP) were found to etch silicon faster along the (100) and (110) crystal planes than the (111) crystal plane [6]. EDP has an etch rate ratio of 35:1 for the (100) plane relative to the (111) plane, and KOH has a rate of 400:1 for the same planes. The primary crystal planes of silicon are shown in Figure 1.1.

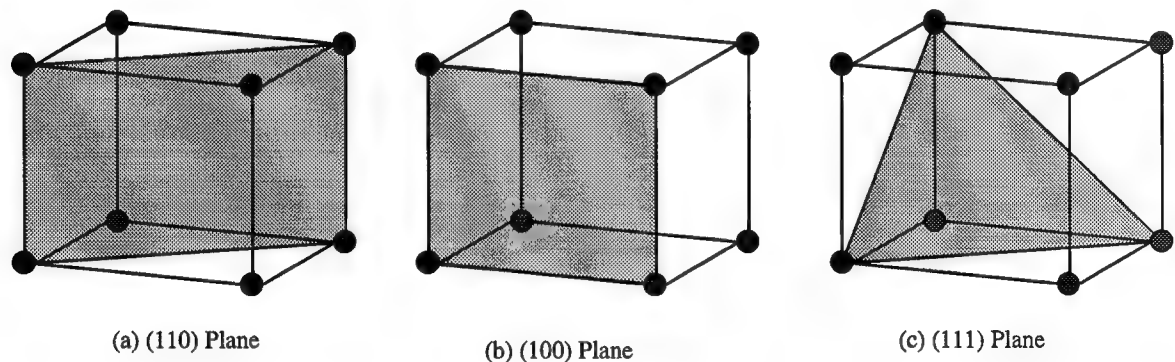


Figure 1.1. Cubic lattice structure showing primary crystal planes [7].

The orientation dependent etch rates are believed to be a function of the different atomic densities in one plane relative to another. Figure 1.2 shows the effect that anisotropic etchants have on different orientations of silicon. Figure 1.2a shows the wafer before EDP or KOH is added, but after the mask has been applied; Figure 1.2b indicates the effect of the anisotropic etchant on a (100) oriented silicon wafer, and Figure 1.2c shows the effect on a (110) oriented silicon wafer. Figure 1.2 indicates that the wafer orientation is critical in bulk micromachining and shows how the different etch rates affect the different crystal planes. The (111) plane is at an angle of 54.74° with the (100) plane [6], so the exact shape of the etched cavity can be determined.

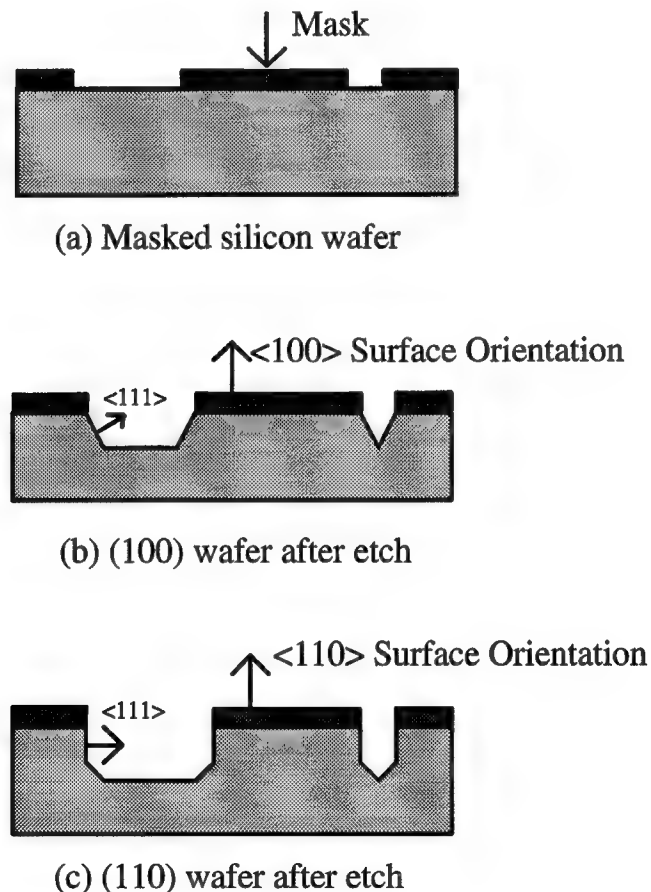


Figure 1.2. Anisotropic etch of (100) and (110) oriented silicon [6].

Nearly all commercial silicon processes use (100) oriented silicon wafers, but other orientations can be used. Also, the masks are usually aligned along the (110) plane in industry. These factors indicate that commercial processing can be adopted for bulk micromachining.

As an example of bulk micromachining, Figure 1.3 shows how a masking material can be used to form a cantilever beam. Bulk micromachining works by etching the silicon underneath a mask, called undercutting. Masking materials are generally silicon dioxide or silicon nitride. Both mask materials have slower etch rates in KOH or EDP than silicon (approximately 0.2-1.4 nm/min masked versus 0.75-1 $\mu\text{m}/\text{min}$ unmasked). In addition to using masking materials, heavy boron doping (greater than $5 \times 10^{19} \text{ cm}^{-3}$) of the silicon may be used as an etch stop. This is because boron doped silicon etches 20 to 50 times slower than undoped silicon [6]. Figure 1.3a shows the mask used to make a cantilever beam. Figure 1.3b indicates that after the etch, the mask is free from the silicon underneath it and the beam is released.

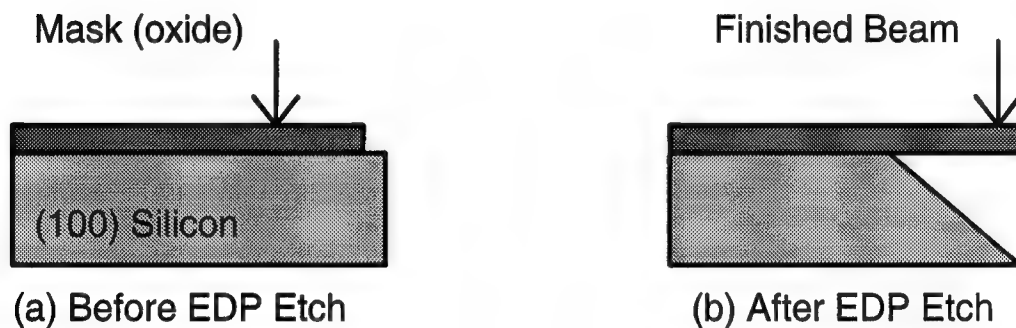


Figure 1.3. Example of released bulk micromachined cantilever beam on silicon [7].

1.4.1.2. Surface Micromachining. The second process, surface micromachining, is also used to form MEM structures. It was first demonstrated in the

1960's on metal films [8]. It is performed by selectively etching sacrificial layers of thin films on a base wafer. This releases the structural material making movable devices possible. The sacrificial layer is usually phosphosilicate glass (PSG). This phosphorus doped silicon dioxide is etched much faster by hydrofluoric acid (HF) than polysilicon or the silicon wafer. Therefore, polysilicon is typically used as the structural material in these processes.

An example of the surface micromachining process is shown in Figure 1.4. The initial step, shown in Figure 1.4a, is to lay down a sacrificial layer. Figure 1.4b shows the result of a HF etch on a masked sacrificial layer (after mask removal). The next step, shown in Figure 1.4c, is to deposit the structural material. Polysilicon is used as the structural material since it is etched much slower in the HF etchant. The final step is a maskless HF etch to remove the remaining sacrificial material. Figure 1.4d shows the cantilever beam after this final HF etch.

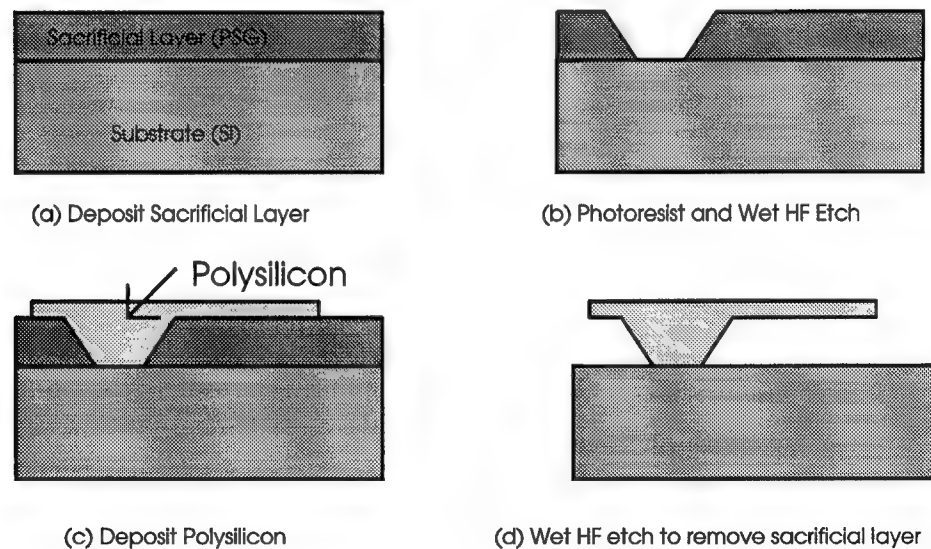


Figure 1.4. Surface micromachining of cantilever beam.

IC processing methods allow both surface and bulk micromachining with a tremendous amount of variety. There are many different materials that can be deposited and grown on a base wafer. These materials can be varied according to amount, shape, and doping concentrations. Nonetheless, there are limitations. All of the materials are thin films, with small thicknesses (usually less than a few μm). This means that the aspect ratio (height to width ratio) is much lower than in typical mechanical structures. Also the more exotic processes are expensive and not always readily available.

1.4.2. Commercial Fabrication Facilities. Since AFIT does not have the facilities to perform chemical vapor deposition (CVD), plasma etching, or ion implantation, commercial fabrication facilities will be used in this thesis. The benefits of using commercial processing facilities are high quality processes, rapid turn around time, and low cost. The main drawback to this method is that the designer has no real control over thicknesses, materials used, or process steps. The processes that are available for MEMS design are the MOS implementation service's (MOSIS) CMOS process and MCNC's MUMPS process [9]-[10].

1.4.2.1. CMOS Process. The CMOS process utilizes a two micron process available through MOSIS vendors. This process has two metal and two polysilicon layers. Only minor changes need to be made to the CIF file (Caltech Intermediate File, this file describes the geometries of each layer) to allow MEMS to be built using this well established technology base. At this time, Orbit (a MOSIS vendor) is the only vendor that recognizes the altered MEMS layers, therefore particular run dates must be chosen carefully. The Magic (IC layout tool using manhattan geometry) technology file must be modified to allow OPEN layers and PSTOP layers to be painted [9].

The OPEN layer represents bare silicon. In a normal CMOS process oxide layers are deposited between the polysilicon layers, the wafer surface, and the metal layers to provide isolation. When connections are desired, the oxide is masked and a hole is etched to make a via. Similarly when an OPEN box is painted in a MEM design, every oxide layer has this box removed from it. The box becomes an opening in the oxide going down to the bare silicon. The open layer allows either surface, or bulk micromachining, but is better suited for bulk.

A PSTOP box simply informs the fabrication facility to boron dope the silicon wherever this layer is painted. As discussed above heavily boron doped silicon is etched much slower than undoped silicon. This makes an effective etch stop. After OPEN and PSTOP layers are added to MOSIS's CMOS process, all that remains is an anisotropic etch. Bulk micromachining through MOSIS has been demonstrated for a number of applications [11]-[15] and can be used in tactile stimulator design. Figure 1.5 shows the basic idea behind the OPEN and PSTOP layers and how a cantilever beam may be formed using bulk micromachining.

Bulk micromachining is highly orientation dependent. Fortunately this is not a problem with commercial fabrication since nearly all MOSIS sites use (100) oriented silicon wafers with the y axis of the mask parallel to the (110) flat. The chips require relatively simple post processing (including anisotropic etching) to complete the fabrication, and therefore local post processing such as sputtering, deposition, and diffusion is an option. The aluminum and silicon dioxide standard CMOS layers are used as the structural materials. The polysilicon layers in the CMOS process can be used as a heating resistor or as structural material since they are enclosed in oxide and are not etched by the EDP or KOH.

One of the drawbacks of this process is that the designer does not have any control over the thicknesses of the layers used. The thicknesses are determined by the vendor and are based on Very Large Scale Integration (VLSI) needs, not MEMS needs. Also there is

no flexibility in the processing steps or the order they are performed in. Another pitfall is that not all MOSIS fabrication sites support the OPEN and PSTOP layers and a correct fabrication facility must be used.

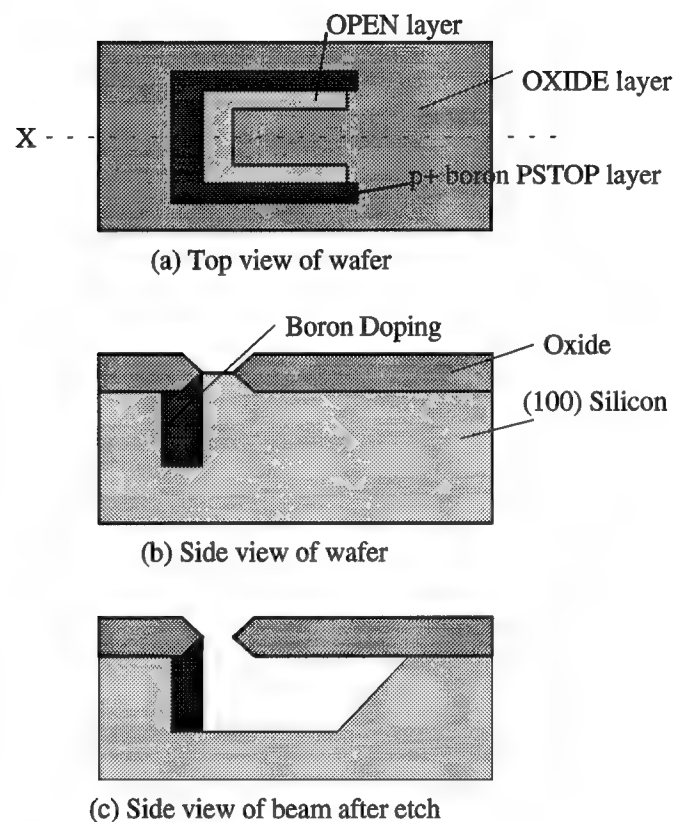


Figure 1.5. OPEN and PSTOP layers in a bulk micromachining MOSIS's CMOS process used in fabricating a cantilever beam.

1.4.2.2. MUMPS Process. The second process available to AFIT is the MUMPS process. This process is tailored specifically to MEMS design. It is provided by MCNC Electronic Technology Division in North Carolina through an advanced research projects agency (ARPA) grant. It is a surface micromachining process with three layers of polysilicon, one metal layer, one silicon nitride layer, and two layers of sacrificial PSG.

The thickness of each layer varies, but all are less than 2 microns. Figure 1.6 shows the different layers involved. MUMPS devices can also be designed with Magic. The technology file is modified so that the CIF file gives the correct layer names.

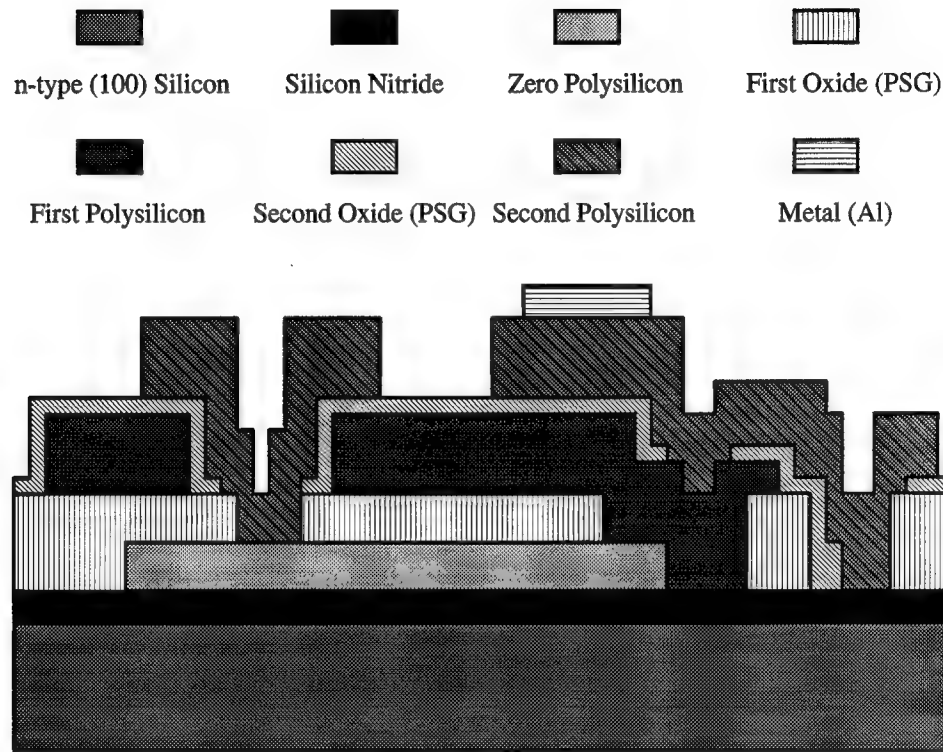


Figure 1.6. MUMPS layers [10].

Since this is a surface micromachining process, the two PSG layers will be used as the sacrificial material. The first and second polysilicon layers become the structural material. The zero polysilicon layer is used only as a ground plane when needed and is not releasable. The silicon nitride layer is not a maskable layer and is used as an insulator. In the CMOS process oxide insulates all layers, but since in the MUMPS process the oxide is sacrificially removed from the fabricated chip, the silicon nitride is needed to keep the polysilicon layers from shorting through the silicon substrate. The metal layer is aluminum

and is used for wiring and for reflective surfaces. There is more flexibility in the MUMPS process than in a CMOS process since the MUMPS process has three polysilicon layers and one metal layer. The only post processing required is a HF etch to remove the sacrificial oxide layers.

An obvious problem is that since the oxide is removed there is no isolation material left. This prevents monolithic integration with electronic circuitry and care must be taken so that the actuating device does not short itself out. Also there are more than 50 design rules in this process and currently no design rule checker. This increases the complexity of the MUMPS design process.

1.4.3. Actuation Methods. Above is a brief discussion of bulk and surface micromachining and the limitations imposed by the available fabrication processes. With this knowledge one can narrow down the possible actuation methods that are achievable with these processes and that could provide tactile stimulation.

There are many actuation methods for MEM devices including piezoelectric, bimorph, shape memory alloy (SMA), magnetic, thermopneumatic, thermal, and electrostatic. Because of the inherent limitations, not all actuation methods are suited for tactile stimulation. Bimorph, electrostatic, and thermal are possible methods that can be used for tactile stimulation and are briefly explained below.

1.4.3.1. Bimorph. One form of MEM actuation which shows promise is bimetallic, also called bimorph [16]. The basic idea is a sandwich of two materials having different coefficients of thermal expansion. For MEMS the materials would be etched into a cantilever beam with a heating resistor as the driving element. Figure 1.7 shows the basic structure, and the theory behind this actuation is discussed in Chapter 3. When the beam is heated the different materials will expand at different rates causing the beam to curl. The larger the difference in coefficients of thermal expansion, the larger the amount

of curl. Bimorph beams have been demonstrated many times [16] - [19] and could be used as a tactile stimulator, since the deflection is normal to the plane of the substrate. The response time of this beam is dependent on how fast the element can dissipate heat.

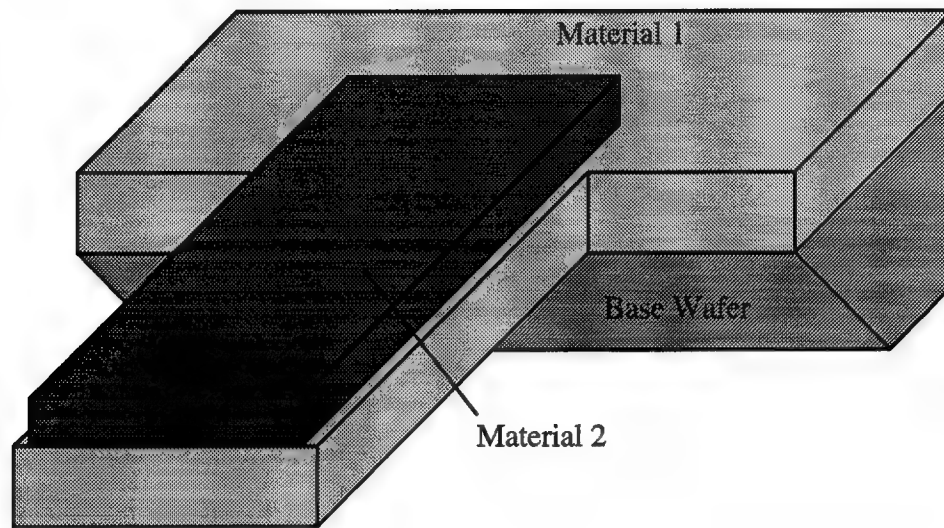
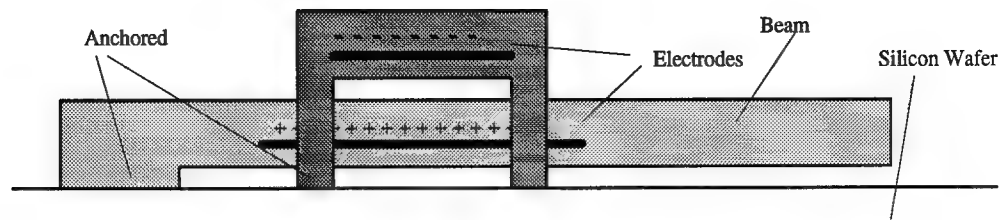


Figure 1.7. Bimorph cantilever beam.

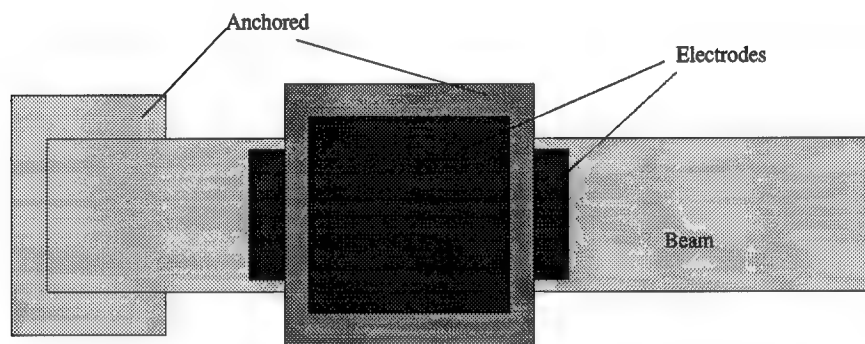
The CMOS process is well suited for fabrication of bimorph actuation devices. The beam material has to be oxide and a combination of aluminum and/or polysilicon. The other layer of polysilicon can be used as a heating resistor between the layers in the beam. This combination is not perfect since oxide must be used and will enclose individual material layers.

1.4.3.2. Electrostatic. The second type of actuation that could be used for a tactile stimulator is electrostatic. This actuation has been used for micropumps, microvalves, and deformable mirrors [20] - [22], and the theory of electrostatic actuation is discussed in Chapter 3. The basic idea behind the actuation force is the attraction or

repulsion between oppositely charged plates. A MEM actuator using electrostatic force, is shown in Figure 1.8.



(a) Side view of electrostatic attraction beam



(b) Top view of electrostatic attraction beam

Figure 1.8. Electrostatic cantilever beam on a silicon wafer.

MUMPS could be used to fabricate electrostatic actuators using the polysilicon layers as the electrodes and the structural material. One of the drawbacks to this process is that since there is no oxide for insulation, the beams will short if they touch. Also the lack of oxide makes wiring much more difficult. The CMOS process could be used for electrostatic actuation only if the silicon wafer is used as one of the electrodes and repels/attracts an electrode encased in oxide.

1.4.3.3. Thermal. The third method of tactile stimulation is not an actuator. If an actuator that stimulates the nerves on the finger with force can relay

information, then other forms of stimulating the nerves should work as well. A heating element designed to heat quickly to a certain temperature could rely information to the finger. Since heating elements made from MEMS do not have to heat the base wafer, they should have a fast response time. Also the amount of heat generated could be precisely controlled by limiting current. Silicon MEM heating elements have been realized many times [13]-[14] and have the potential to provide tactile stimulation.

1.4.4. Designs. The first type of actuation uses the bimorph process. Various cantilever beams are designed using the Magic layout tool. The technology file of Magic is edited to allow OPEN and PSTOP layers. These layers are reflected in the CIF plot that is sent to MOSIS for fabrication. A maskless EDP anisotropic etch is used to release the structures. The devices are then tested and evaluated.

The second set of designs is based on electrostatic actuation. Different beam designs are laid out in Magic. The Magic technology file is changed to support the MUMPS design rules. The MUMPS process is then used to fabricate the devices. The processed chips are etched in a diluted HF bath to remove the sacrificial layers and release the structures. The devices are then tested to determine if they are suitable for tactile stimulation.

The third form of stimulation is heating elements. These are designed in Magic and fabricated using both CMOS and MUMPS processes. They are released using the respective micromachining processes and tested.

The fabricated devices are tested and evaluated to determine how they meet the criteria given in the problem statement. A laser microscopic interferometer is used to measure the deflection of the released devices. A force gauge is built to determine how the cantilever actuators perform under a load. The heating elements are tested to determine what the operating currents are required to stimulate the finger and what

amount of resolution is possible using heat to stimulate. With this information conclusions are drawn to determine if a MEM tactile stimulator is possible.

1.4.5. Summary of Approach. To summarize the approach section, three different methods of tactile stimulation are investigated. All designs attempt to fulfill the criteria given in Problem Statement section 1.3. The designs are based on the micromachining techniques given in subsection 1.4.1 and fabricated through the facilities described in subsection 1.4.2. The designs include bimorph actuation, electrostatic actuation, and thermal stimulation. These approaches are used to determine if silicon based MEM devices are a viable solution to the tactile stimulation problem MEM devices have not been previously investigated as tactile stimulators.

1.5. Thesis Overview.

Chapter 2 of this thesis is the literature review. It covers the current research into tactile stimulators and current research into applicable MEM devices. Chapter 3 covers the theory and the designs. Chapter 4 describes the experimental procedure and results. Chapter 5 provides conclusions and recommendations for future research.

2. LITERATURE REVIEW

There are many different ways to provide tactile stimulation. Common large scale techniques use piezoelectric, electro-magnetic, shape memory alloy (SMA), electrostatic, pneumatic, and electrodes to provide stimulation. All of these fail, in one way or another, to acceptably meet the objectives for a tactile stimulator to be used in a telerobotic system. Because of their shortcomings, better ways of producing tactile stimulation should be researched. This chapter discusses the current techniques for tactile stimulation and possibilities for improving these techniques.

First of all, this chapter covers the history of tactile stimulation. Second, ways of providing tactile stimulation used today are discussed, along with the advantages and disadvantages of these methods. Third, current research into the human response to tactile stimulation is reviewed. Fourth and finally, the history and applications of silicon based MEM actuators, that could be used as tactile stimulators, are discussed.

2.1. History of Tactile Stimulation.

Tactile stimulation has been used as a way of imparting information for a long time. The Braille system has been an effective method of providing information to the blind for over 100 years. This simple system uses patterns of raised dots in a 2 x 3 matrix to represent the alphabet. By moving the finger across these patterns, a person can "read" with their fingertips. An experienced user can read at a rate of 125 words/minute [30]. This indicates that with proper training, tactile stimulation can be a very effective form of communication.

Another tactile communication form is Tadoma. With Tadoma, a deaf person uses one hand to feel the vibrations from the throat, and the other to feel the airflow from the lips of a speaker. When this tactile stimulation is combined with visual monitoring of the

speakers lips, greater than 80% keyword recognition of 3 syllables/second can be obtained. This is the highest speech communication rate for tactile only communications [30]. Although this system does not use mechanical stimulations, it does show that the finger is a good method of communicating information.

The Braille and Tadoma systems have led to the development of active mechanical stimulators. Although some of the more recent mechanical stimulators have been developed to improve communication with the blind, the majority of the mechanical tactile stimulators are developed with the goal of obtaining better control of telerobotic systems. Initially, the stimulators were designed to provide force feedback from the remote system, or to indicate the remote system had contacted an object [31]. More recently, research has been directed towards stimulating the finger to not only give information about contact and force, but also information on contour, edges, texture, and slippage [32]-[36]. These systems are described below.

2.2. Current Tactile Stimulation Methods.

Now that the history of tactile stimulation has been discussed, current methods will be examined. Current actuation mechanisms that are or can be used for tactile stimulation are reviewed in this section. The advantages and disadvantages of each actuation method are discussed. Although most of the actuation mechanisms found in the "macro" devices are used in MEM devices, not all of the forces employed are readily scalable. The major actuation methods in the "macro" world are not necessarily the chief methods in the MEMS world, so the scalability of these methods to the micro world will be discussed.

2.2.1. Piezoelectric. Piezoelectric materials have been used as actuators for many years. The actuation is caused when the crystalline structure of a material contracts or expands due to an applied electric field. The uses vary from quartz crystals in watches to

"macro" actuators which provide more than 2 cm of deflection. Some of these piezoelectric actuators require 300 or more volts for actuation [23].

2.2.1.1. Optacon. One successful commercial device is the Optacon (Optical to Tactile Converter by TeleSensory, Mountain View, CA), which was developed in the 1960's [32]. This system is a portable reading unit for the blind which transforms printed text or graphics to a tactile display. A representation of the device is shown in Figure 2.1. The Optacon uses an array of 6 columns (spaced 2.54 mm apart) by 24 rows (1.27 mm apart) to display information. The entire array is 12.7 x 29.2 mm².

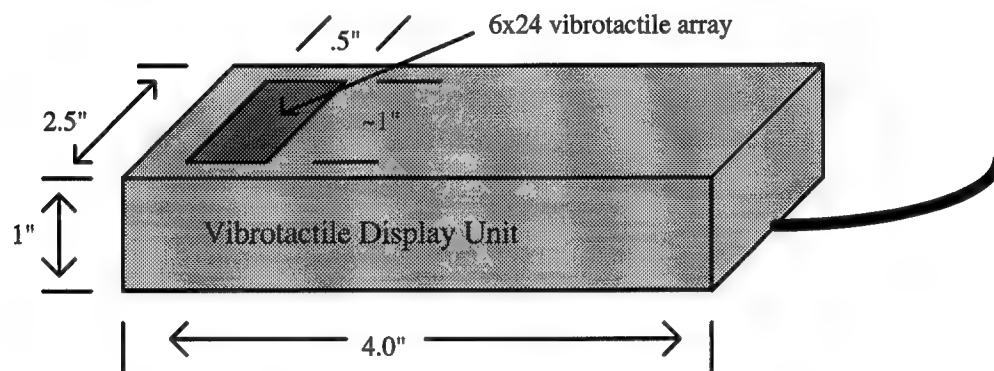


Figure 2.1. The vibrotactile display unit from an Optacon (TeleSensory, Mountain View, CA) [32].

The actuators in this device use lead zirconate titanate (PZT) as the piezoelectric material. The stimulators are piezoelectric bimorphs and are electrically actuated at 230 Hz. Each actuator vibrates producing a 100 μ m deflection. Although the exact voltage range was not given, the deflection can be varied by the user by adjusting the voltage applied to the PZT [32].

The device allows a trained blind person to read 30 words/minute, and studies show 90 words/minute are possible [30]. Other advantages are that it is easy to use, provides reliable, adjustable-amplitude stimulation, can provide information as fast as the user can disseminate it, and has a large array of stimulators for better resolution. Disadvantages are that the device requires a long training period, the frequency of the device is not adjustable causing lower resolution and limiting the range of information passed [5], the 144 actuators have a wide variation in the individual amplitudes [32], and the system is too bulky for a glove-sized tactile stimulator.

2.2.1.2. Other Piezoelectric Devices. Piezoelectric materials have been used as tactile stimulators in other studies. A 4 x 12 array of vibrators was developed using piezoelectric bimorphs [2]. This device operates on a 250 Hz square wave, and testing has shown that it increases the ability of a user to do complex tasks such as putting pegs in a hole and manipulating latches. As with the Optacon, this device is limited to one frequency. In another study, deflections of 2500 μm were obtainable at 300 volts using a piezoelectric bimorph [23]. But this system is too large and the voltages required limit its effectiveness as a tactile stimulator.

2.2.1.3. Advantages and Disadvantages. None of these piezoelectric devices are ideally suited to meet the requirements for a tactile stimulator. The deflections of 100 to 2500 μm are excellent and the resolution is generally high. However, the systems are bulky, they generally operate at set frequencies, and they need high voltages for actuation. These factors limit the effectiveness of piezoelectric materials for tactile stimulation.

2.2.2. Shape Memory Alloy.. Shape memory alloy (SMA) refers to materials that have the property of shape recovery when heated above a certain temperature [35].

This process is shown in Figure 2.2. The SMA material has an amorphous crystalline structure when it is initially formed [28]. It takes on a highly ordered Austenite crystalline structure when heated above a certain temperature (usually above 400°C).

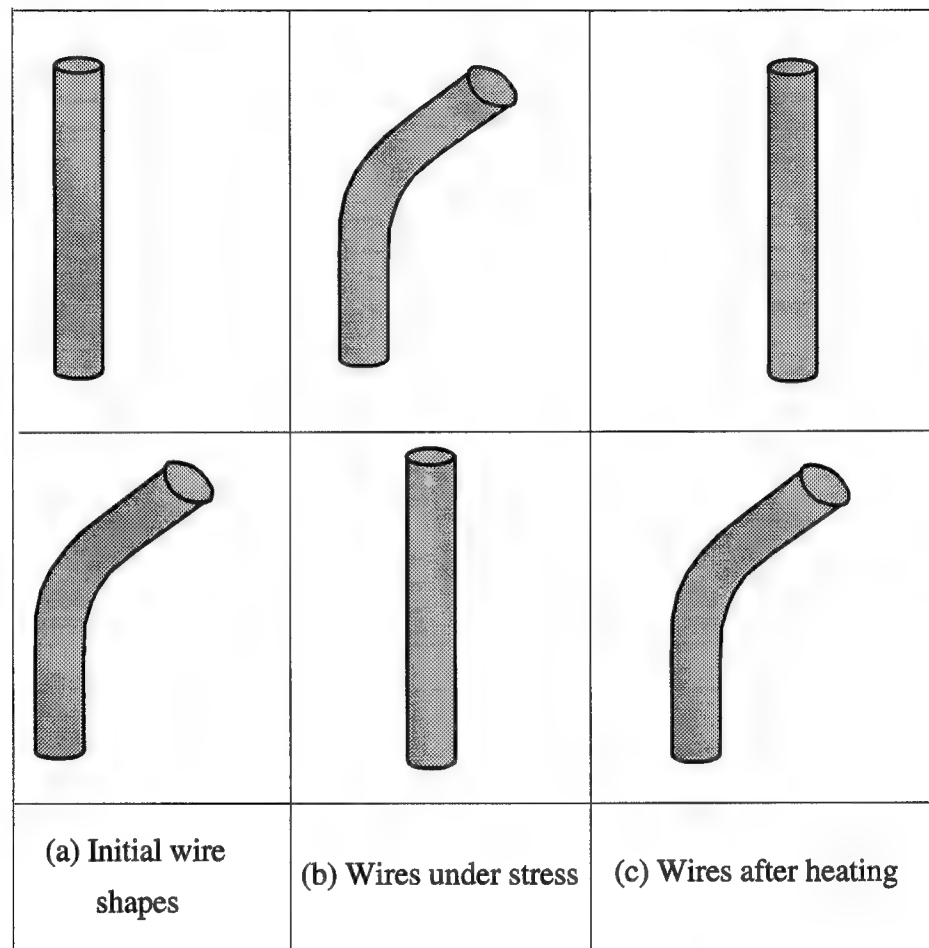


Figure 2.2. Modes of shape memory alloy [29].

This process is called training. This shape that the wire is originally formed in, shown in Figure 2.2(a), is remembered when the wire is deformed. When the material cools, it has a Martensite crystalline structure that can be easily deformed (Figure 2.2(b) shows the

wire after being deformed). The remarkable thing about this material is that when heated again, it returns to its original Austenite shape as in Figure 2.2(c). The temperature at which the material changes shape is process dependent and varies from -40 °C to 100 °C. The change in shape produces a combination of force and displacement. Heat is provided by simply running current through the SMA wire. This allows the actuator to be powered by very low voltages, although the current usually is in hundreds of milliamps.

2.2.2.1. Current SMA Design. The current SMA system used by Armstrong Laboratory is a 5 (columns) x 6 (rows) array of tactile stimulators [5]. The array covers an area of 1.2 cm x 1.5 cm with the pins spaced approximately 3 mm apart. The area of the pin tip is 0.129 mm². This device uses 15.24 mm long, 76 µm diameter titanium nickel (TiNi) SMA wire to move each of its beryllium copper (BeCu) spring cantilevers. The actuator is shown in Figure 2.3. The overall size of the system including the touch plate was not given, but it is approximately 2.5 cm x 5 cm. A 3% contraction in the SMA wire produces a deflection of 450 µm above the touch plate. The tips achieve 90% actuation in 0.1 seconds with a recovery time of approximately 1.6 seconds when driven with 0.24 A current through the SMA wire [24]. At this current, each stimulator uses 1.2 W of power. The stimulators are protected by a touch plate that prevents the finger from snapping off the SMA wire. When fully actuated, the elements exert approximately 0.2 N of force [34]. The entire system is under computer control, allowing each element to be actuated individually by simply running current through the SMA wires.

One benefit of this system is that it can be actuated with pulse width modulation to provide a large range of frequencies and keep a large deflection. This SMA device has excellent out of the plane deflections. Also, the device satisfies the requirement of being compatible with standard IC voltages since 5 volts provides actuation (although the high current is a disadvantage). This "macro" attempt to solve the problem is too bulky for a

glove and can not be implemented in a large array [5]. If all 30 elements were actuated, the devices would consume over 30 W of power which mandates large power supplies and bulky systems. Since the SMA wires are connected to the BeCu stimulators by hand, it is difficult to provide uniform tension, and thus uniform out of the plane deflection. The device is thermally operated and therefore can only be actuated as fast as the wire is cooled. Also, with 30 elements over a 1 cm x 1 cm area, the resolution of the device is hindered.

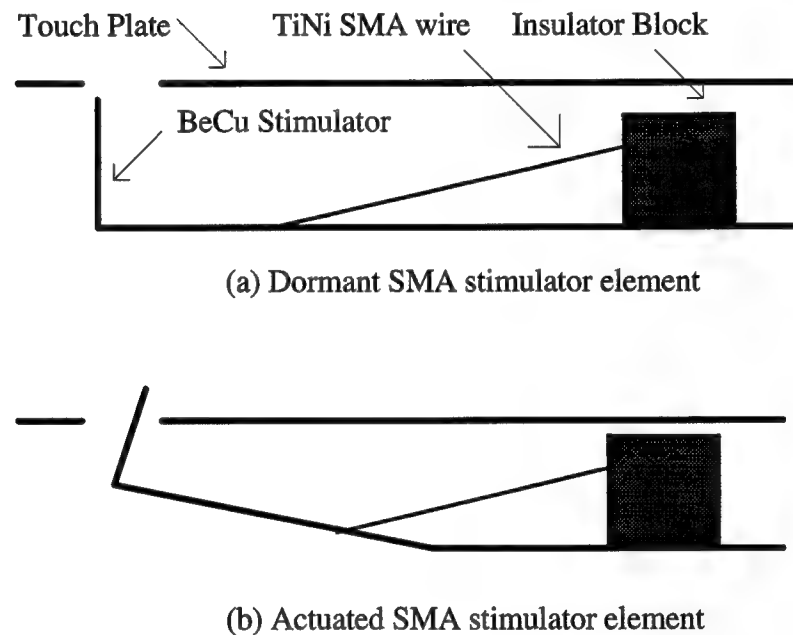


Figure 2.3. SMA tactile stimulator element, dormant and actuated [34].

2.2.2.2. Other SMA Devices. A nine element device has been developed with larger SMA wires [1]. This 3 x 3 array has elements spaced 2.2 mm apart. The elements produce a 3 mm unloaded deflection. The SMA wires are the same thickness (75 μm diameter wire), but are longer (30 mm vs 15 mm). The device uses a 3:1 lever

arm to produce much more force (1.2 N). This device has no touch plate and therefore the pins rest on the users fingertips. The overall dimensions are 67 x 26 x 31 mm. The large deflections obtained with this devices require 100s of milliamps and therefore large power consumption. The thermal problem is more pronounced in this system with maximum frequencies of 0.1 Hz. To reduce this, air cooling was implemented (forced air at 20 psi) which increased the performance to 10 Hz.

2.2.2.3. Advantages and Disadvantages. The advantages of SMA actuators include the following: small voltages produce a large deflection, both designs reported here produce enough deflection to be felt by operators, and the voltage is compatible with IC electronics. Also, TiNi SMA wire has shown high reliability and have been cycled over 20 million times [25]. However, macro-scale SMA actuators have several problems that limit their usefulness as tactile stimulators. They have slow actuation rates. This could be solved by providing some form of cooling to decrease the recovery time. Moving air or liquid cooling could be used. Another drawback is that the large size of these devices limits resolution. If SMA actuators could be produced with a planar process, the size and resolution problems might be solved. The large power required to activate these devices is also a drawback. Therefore, "macro" SMA actuators do not address all the problems of a tactile stimulator.

2.2.3. Air Jets. Another common way of providing tactile stimulation uses forced air to provide sensations. There have been many different examples of using air jets as tactile stimulators. The first is a study using a 12 x 12 array of mini air jets to stimulate alphabetical characters on the index finger [36]. A second attempt used air to actuate pneumatic pins. This 5x5 array operates at a maximum speed of 7 Hz [1]. More recently, a 3 x 3 array of air jets was employed to enable operators to recognize changing patterns [36]. The fourth device is a 24 element device which stimulates over the entire human

hand [2]. These jets of air pulse at 200 Hz while actuated and each burst lasts for 100 ms. The peak pulse pressure is 1.5 psi.

Very little data is available on the effectiveness of these devices. They all require bulky systems for providing the air, which can not be readily put in a glove. They are not actuated with electrical signals, but require complex valves and tubing for actuation. Therefore, these devices are not ideal for tactile stimulation.

2.2.4. Other Macro Actuation Methods. The last two methods currently used as tactile stimulators are electrotactile and electromagnetic. The electrotactile studies use electrical current to stimulate the skin through electrodes [36]. Studies have shown that the stimulus can provide information, without causing discomfort or pain. This method of stimulation has been tried on other parts of the body also. A 384 point electrotactile system was developed to stimulate the abdomen [30]. The principle limitation of a electrotactile stimulation system is the limited spatial resolution. Also, this system must have a neutral electrode to be used as a return path for the current. If it is not near the stimulated electrode, then undesired areas can be stimulated.

The final "macro" attempt to produce the tactile stimulator is electromagnetic. These actuators use solenoids and are usually static. One device has an array of 8 × 8 miniature solenoids over an area of 4 cm x 4 cm [1]. The actuators can be set at any of four deflections: 0 mm, 0.33 mm, 0.67 mm, and 1 mm. This device has several problems. It is bulky, with large mechanical parts. Each solenoid uses 0.5 W of power which prevents battery operation [30]. Also, the device has low spatial resolution.

2.2.5. Summary of Current Actuation Methods. In order to design a better tactile stimulator, it is important to understand all of the current actuation techniques and their limitations. Several of the current "macro" actuation techniques have been discussed

along with their advantages and disadvantages. These include piezoelectric, SMA, air jet, electrotactile, and electromagnetic techniques.

Of these, all are larger than an ideal tactile stimulator, the entire array of which should be able to fit into an operators glove. All of the actuators provide adequate stimulation, but none allow for variable frequencies of operation. The above devices do not meet all of the goals for a tactile stimulator.

2.3. Human Factors.

Now that the current macro actuation techniques have been examined, the human factors involved in designing a tactile stimulator are considered. The questions which warrant answers include the following. How much deflection is needed to perceive stimulation? How does altering the frequency of the stimulus affect perception? How does frequency affect deflection needed for perception? What is the spatial resolution of the finger? How and at what resolution does the finger perceive heat? How does the body perceive electrical current? These questions need to be addressed in order to design an effective tactile stimulator.

Although we use the sense of touch everyday, the mechanics of the finger are not completely understood. The signals the brain uses to classify vibration, shape, force, and slip are still being studied. By studying how this information is received by the nerves on the finger, a better tactile stimulator can be developed. This section discusses the current understanding of how the finger receives information. The known specifics on amount of force needed for stimulation and minimum resolution are covered. Also, how the perception of information changes when it is presented in different ways is discussed.

2.3.1. Cutaneous Sensory System. Before any system can be designed, basic requirements for the system must be considered. Since a tactile stimulator for the human finger is desired, the mechanical requirements of the human finger should be discussed.

The system that receives signals through the finger is called the cutaneous sensory system. Although the system has been studied since the 19th Century, a complete understanding of the workings of the cutaneous sensory system still remains a goal [39].

One reason the cutaneous sensory system is difficult to study is that there are four separate nerve endings that receive stimulation. There are a large number of each type of nerve endings in the hand, and some endings have a receptive field covering an entire digit [39]. It is impossible to stimulate only one nerve ending and very hard to determine which of the four is being stimulated.

The four endings can be divided into two categories: slow adapting (SA) and fast adapting (FA). SA means that the nerve response to a stimulus continues for more than a second, where FA nerve responses last only a fraction of a second [39]. These two nerve ending categories are further classified as Type I, small receptive areas with well defined boundaries, and Type II, large areas with poorly defined boundaries [1]. Not only do these systems all reside in the same area of skin, but also the roles of the systems overlap and one type of stimulus may affect all four or just a few of the endings [37]. Figure 2.4 shows the structure of the skin typically found on the fingers. The four endings are referred to as SA I, SA II, FA I, and FA II. Each of these have other names as described below.

SA I or slow adapting small field is the primary spatial system. The cells, originally given the name Merkel's Cells, can be seen in Figure 2.4. These nerve endings are responsible for roughness and shape perception of surfaces [30]. The endings show minimal response to vibrating stimuli and they exhibit surround suppression. This reduces their response to uniform stimuli and enhances detection of isolated stimuli like edges [37].

SA II or slow adapting large field nerve endings may not pass tactile information at all; they have large receptive fields and do not respond to stimulation when isolated [30]. These endings are labeled as free nerve endings in Figure 2.4 and are also called Ruffini

endings. SA II is the only ending sensitive to stretch and perpendicular indentions [39]. SA II endings provide information on net force [1] and are excited by strong mechanical displacements [39]. These endings may provide the force and position feedback needed for motor control of the hand [30].

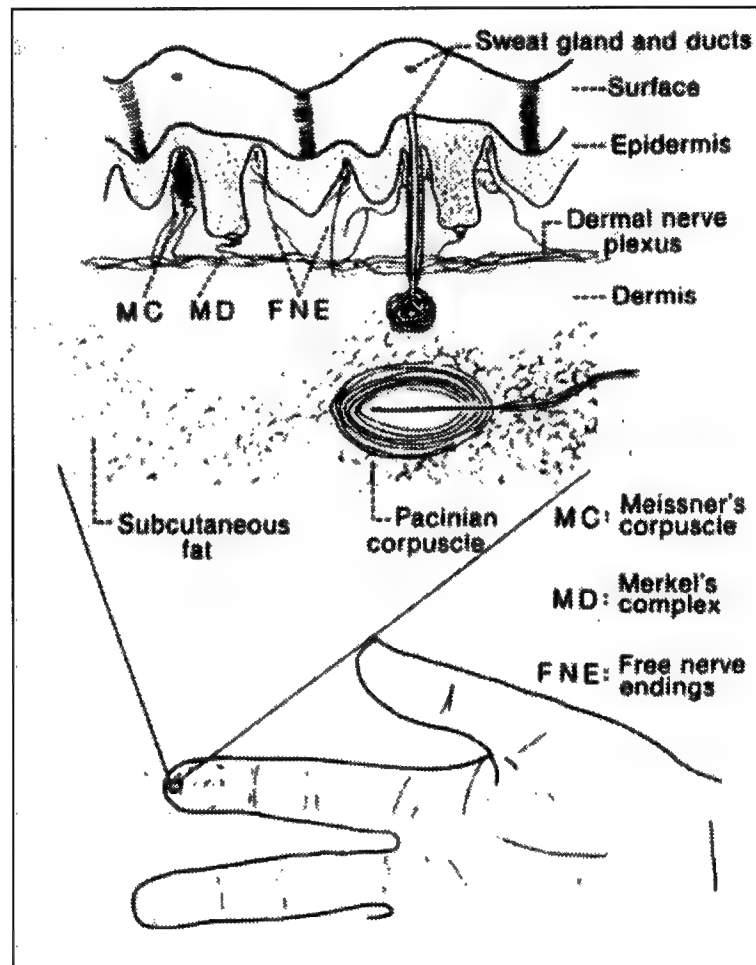


Figure 2.4. Cross section of skin showing the four receptors [39].

FA I endings are sensitive to vibrations. They are labeled as Meissner's corpuscle in Figure 2.4 and are usually $30\text{ }\mu\text{m} \times 80\text{ }\mu\text{m}$. They are not as sensitive as SA I in general, but they have a higher sensitivity to local vibration. FA I endings also provide form and

texture information when the surface variation is too small for the SA I system to detect [30], [37]. The Meissner corpuscle is usually 0.5 mm below the surface of the skin and ends in fluid filled corpuscles. This isolates the endings from low frequency, large deformations. They are very sensitive to micron level vibrations at intermediate frequencies (2-200 Hz) [37]. Additionally, these cells may provide information representing slip.

The final nerve ending is the FA II or Pacinian corpuscle shown in Figure 2.4. FA II nerve endings are found deep in the skin (2-3 mm) [1], are ovoid in shape and are 0.5 mm x 1.5 mm in size [39]. They are responsible for receiving high frequency stimulation [30]. The FA II ending is responsible for areas over 100 mm² (vibrating) where FA I ending covers a much smaller area than this (12.6 mm²) [30]. Pacinian corpuscles respond to changes in pressure, not to pressure itself [32]. The Optacon device discussed above stimulates the Pacinian corpuscles. FA II nerve endings record a pattern by preserving the temporal structure of the vibration [37]. Pacinian corpuscles also acts as a high pass filter to isolate large low frequency stimulation.

In general, it is difficult to compare the four types of nerve endings. There is no best ending to stimulate since they all respond to different types of stimulation. However, it is generally believed that for static experiments SA I is the best for spatial resolution. Studies have shown that SA I can discriminate gratings at 0.5 mm resolution, where FA I can only resolve 1.5 mm gratings [37]. Also, some studies indicate that static stimulation may be better than vibrotactile, or electrotactile. Letters are recognized with 50% accuracy with 4-6 mm letter height with static touch, while the Optacon requires letters of 12-20 mm in height to achieve the same accuracy rates. This is most likely because the 230 Hz Optacon device excites only FA I and FA II nerve endings, where static touch excites the SA I system [30]. Table 2.1 shows a summary of the information on the four nerve endings that make up the cutaneous sensory system.

Table 2.1. Cutaneous Tactile Receptor System [1], [30]

Probable Receptor	Class	Receptive Field (mm ²)	Frequency Range (Hz)	Perception Threshold of Skin (μm)	Sensations They Can Receive	Receptors per cm ²
Meissner's Corpuscle	FA I	12.6	2-200	4-500	touch, motion, flutter,tickle, tap, vibration	140
Pacinian Corpuscle	FA II	101	40-800	3-20	vibration, tickle	21
Merkel's Cells	SA I	11	DC - 100	7-600	edges, pressure	70
Ruffini Ending	SA II	59	DC - 15	40-1500	skin stretch	9

Figure 2.5 is an example of how the different nerve endings respond to stimulation. In this case the middle finger is scanned over raised Braille dots at a rate of 60 mm/second in the direction of the arrow. Each of the dots is 0.43 mm high and spaced every 2.3 mm. The finger exerted 0.6 N of force when scanning the dots. Figure 2.5 measures the concentration and location of the action potentials firing as the finger is stimulated. The figure shows that the principle receptor is the SA I endings. The FA I endings are not ruled out as interpreting the information since the Braille patterns are at least visually discernible. But SA II and FA II endings provide no coherent information in this example. From this example it can be inferred that SA II and FA II do not resolve spatial data at static rates [37].

The above information is the most probable match of each nerve ending with its specific purpose. There are discrepancies though; some studies show that fine 2 μm bumps activate only FA I, and other studies show that 0.1 μm bumps were detected only by the FA II [37]. These variations in the normal roles of the nerve endings indicate that

the understanding of the cutaneous sensory system is incomplete. This is especially true when it comes to electrical stimulation. It is known that electrical stimulation elicits responses from the cutaneous system, but which nerve endings are being stimulated is not known [39].

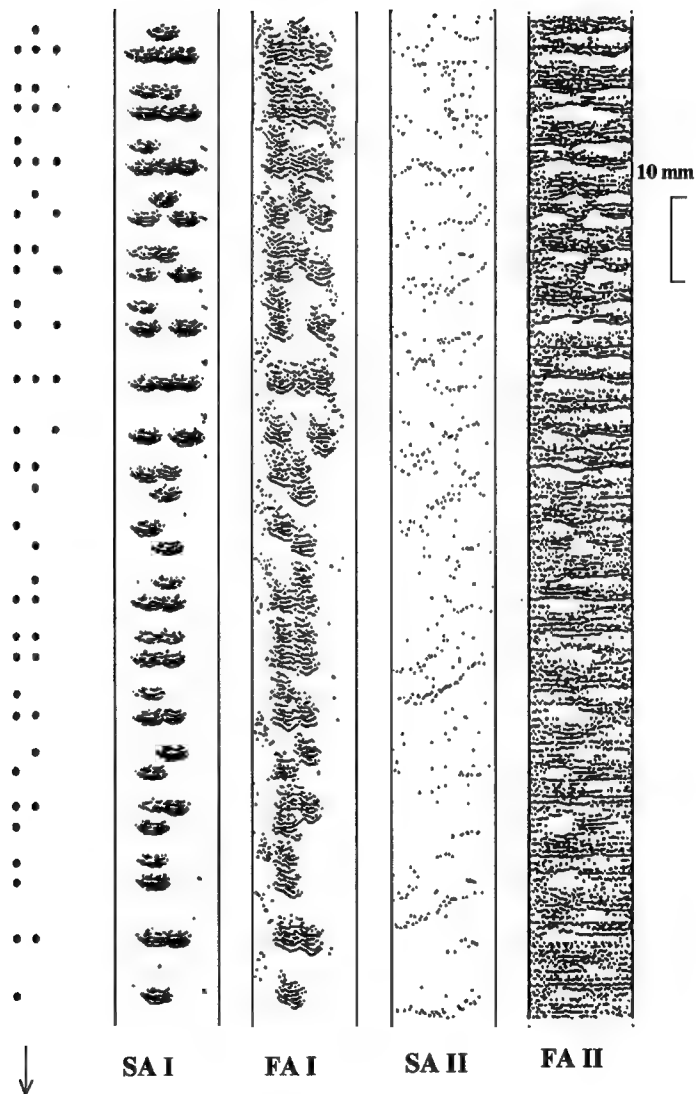


Figure 2.5. Action potentials of the four nerve endings scanned over Braille dots [37].

Although the understanding of the cutaneous sensory system is incomplete, it is still valuable in designing a tactile stimulator. After deciding what type of sensation should be mimicked, a tactile stimulator can be designed to stimulate a particular type of nerve ending. The actuator can be optimized for frequency, deflection, and force needed for that particular type of nerve ending.

2.3.2. Fingertip Specifications. More than an understanding of the biological mechanisms of the fingertip is necessary to properly design a tactile stimulator. The characteristics of the finger must be defined. This section details the known specifications of the human finger. Although some researchers prefer energy as a measure of stimuli intensity, all of the studies here report force and amplitude values.

This section is prefaced with the fact that mechanoreceptors respond in non-linear and time varying ways [1]. The measured sensitivities depend on stimulus size, shape, and duration [1], and also skin location, thickness, density, vascularity, electrical conductivity, and moduli of elasticity [39]. Since most of the studies here vary in several of the above categories, no concrete numbers are available. The general consensus will be reported.

The fingertip is the most tactually sensitive part of the body [32]. The tactile system has over 17,000 mechanoreceptors in the human hand [1] and can respond to stimuli as short as 10 ms [30].

The first measure of sensitivity of the finger is the two point discrimination threshold (TPDT). The TPDT defines the minimum distance that the body can discern two separate stimulations applied at separate points. If the two stimulations are less than the TPDT, then the stimuli will be perceived as only one stimulation. The first attempts to measure this quantity used machinist's calipers and found 4 mm to be the smallest TPDT [32]. More recently, precision stimulators have become available and the new TPDT is 2.5 to 3 mm for static deflections, and 2 mm for vibrotactile [30]. However, these values

are reported by various authors using different testing procedures and equipment, so they can not be taken as absolute numbers. Another factor is that the TPDT for static probing worsens due to fatigue or improves with training and familiarity with the testing procedure. Finally, some studies show that by delaying the second stimulation in a TPDT measurement by a small amount (not given in the source), results in a TPDT ten times smaller than the value of $2.5\text{ }\mu\text{m}$ given above.

The next important piece of information needed about the skin is the amount of force required to detect stimulation. This value is given in either pressure or force. The body varies in the amount of force needed to stimulate it. Using a horse hair (diameter was not provided in source), 355 mg at the toe are needed to perceive the stimulation, but only 5 mg are needed at the lips [39]. This source uses grams as a unit of force. Gravitational acceleration is assumed to be 9.8 m/s^2 and $F = m \cdot a$ can be used to obtain force in Newtons. The finger is generally believed to require 100 or more mg of force for stimulation. When modeling the finger, the skin can be modeled as a complex value [38]. The real part is a dampening component and the complex part has mass (positive reactance) and elastic (negative reactance) components. The measured stiffness of the finger is 80 to 150 N/meter [1]. This value is helpful, since it takes into account the spring action of the skin when stimulating. The human finger can sense force variations of as low as 0.5 N using a horse hair. However, if the force is spread out over an area, this can be reduced to 0.2 N/cm^2 [36].

As reported earlier, some studies have shown that FA II endings can detect very small displacements when vibrating. Figure 2.6 shows the measured frequency response for a 5 mm diameter probe indented 0.5 mm into the skin of a finger and vibrated from 20 to 700 Hz [39]. This data is collaborated in a study that varied the force, site, area of probe and presence of sound. The area of the probe was varied from 0.071 cm^2 to 0.785 cm^2 . The resonant frequency in all cases was found to be 330 Hz and a deflection of $0.28\text{ }\mu\text{m}$ [38].

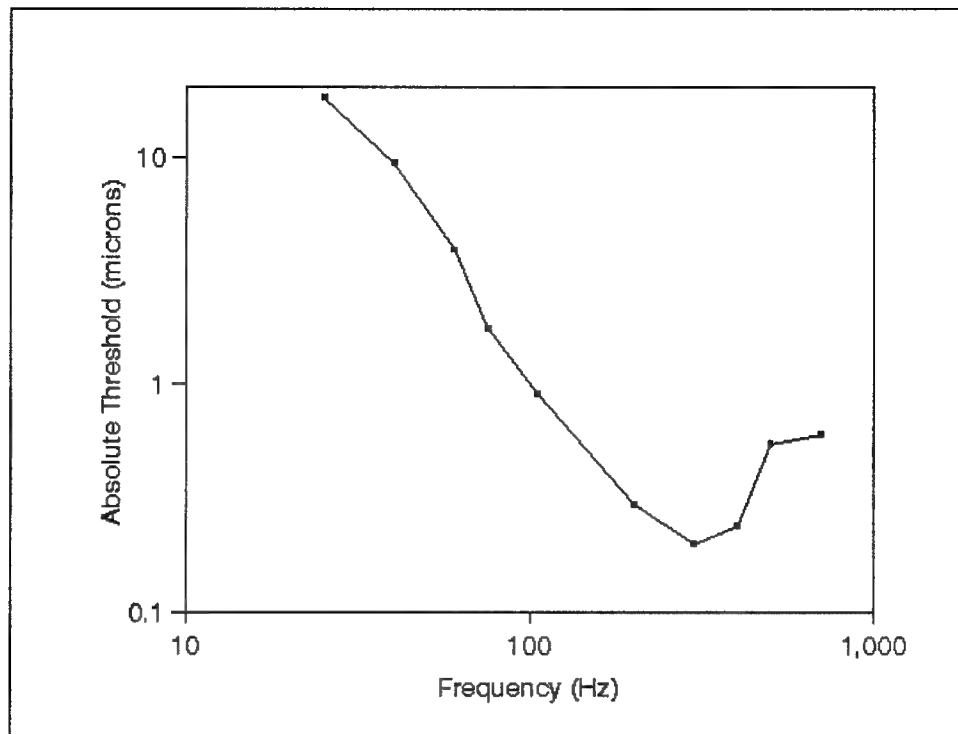


Figure 2.6. Displacement required to stimulate the finger given as a function of frequency [39].

The information above deals with mechanical stimulation and how the body responds, but electrical stimulation behaves differently. Little is known about how electrical stimulations are detected by the body, but it is believed that current flowing through sweat ducts passes the signal [30]. The sweat ducts are low resistance spots with a density of 3.7 ducts per mm^2 in the palm. The reported TPDT of the finger for electrotactile stimulation is 7 mm [30]. The electric current stimulates bundles of nerves and not individual receptors, so it is more difficult to obtain high resolution.

Another problem with electrotactile stimulation is that if large electrodes are used (sizes were not reported), one of the conductive sweat glands will short. This causes all

the current to flow through this one channel [30]. This spike in current can surpass the threshold of pain causing a prickly sensation at low levels, stinging at mid levels, and burning at high levels. The maximum voltage applied should be under 70 volts [30]. Electrical stimulation requires two electrodes and the placement of the second electrode defines the path of the current. This makes it difficult to control which nerve endings are stimulated.

In summary, the human finger is very capable of receiving information. It has a TPDT of 2 mm and needs approximately 100 g of force over less than 0.785 cm² for stimulation. Some of the receptors are frequency dependent and at resonance the minimum mechanical deflection is only 0.2 μ m. Electrical signals do not stimulate individual nerve endings. They have a TPDT of 7 mm. Care must be taken with electrical stimulation to prevent discomfort to the user. With the above information, a better tactile stimulator can be designed.

2.3.3. Information Presentation. A third important aspect of tactile stimulation to consider is how the information is presented. By changing the stimulus and the way it is presented, different results can be achieved. The highest goal of tactile stimulation is to perfectly mimic the sensation a human operator would have if he/she was actually performing the task, rather than controlling a remote robot. This includes differentiating between taps, contact, pressure, vibration, texture, and roughness. By varying the way the information is presented, some of these sensations can be replicated. Some common ways of varying the presentation include: changing the frequency of stimulation and changing the way a character is scanned. As with the above discussion, these processes are not completely understood.

There have been a number of studies to determine the best method of presenting symbolic information through tactile stimulation [32]-[33], [37]. Some studies have developed new codes as better ways of presenting information [32], but using the alphabet

is popular since it is a standard code and does not have a large learning curve. There are five main ways of presenting characters, with different results for each method. The character scan types are : static, scan, split scan, continuous sequential, and discontinuous sequential [33]. These are shown in Figure 2.7.

In static mode shown in Figure 2.7(a), all actuators used in the letter are stimulated at the same time and continue to be actuated for the duration of the presentation. Scan mode, shown in Figure 2.7(b) as five instances in time, passes the letter from right to left. In split-scan mode, Figure 2.7(c), the letter is exposed 2 columns at a time. Which two columns are exposed changes with each frame and moves from left to right. The continuous sequential mode shown in Figure 2.7(d) divides the letter into parts that are presented sequentially. And finally Figure 2.7(e), discontinuous sequential mode, is the same as continuous sequential, except only the current segment is actuated at one time.

One study of a large 20 x 20 array of vibrating actuators stimulating the back of the subject showed that the two scan modes produced better results in letter recognition [33]. Split scan mode achieved the best results for letter recognition, with scan mode as the second best of these modes. However, not all studies agree. A second study using the Optacon showed that static mode produced better performance than scan mode [32]. A third study confirms the first results, stating a 10 - 20 % improvement of scanned information over static [37]. Since the studies disagree, no concrete conclusion can be drawn about the presentation mode. The perception changes if the signal is vibrating or static, how much deflection is used, the frequency of signal, the area stimulated, and other factors.

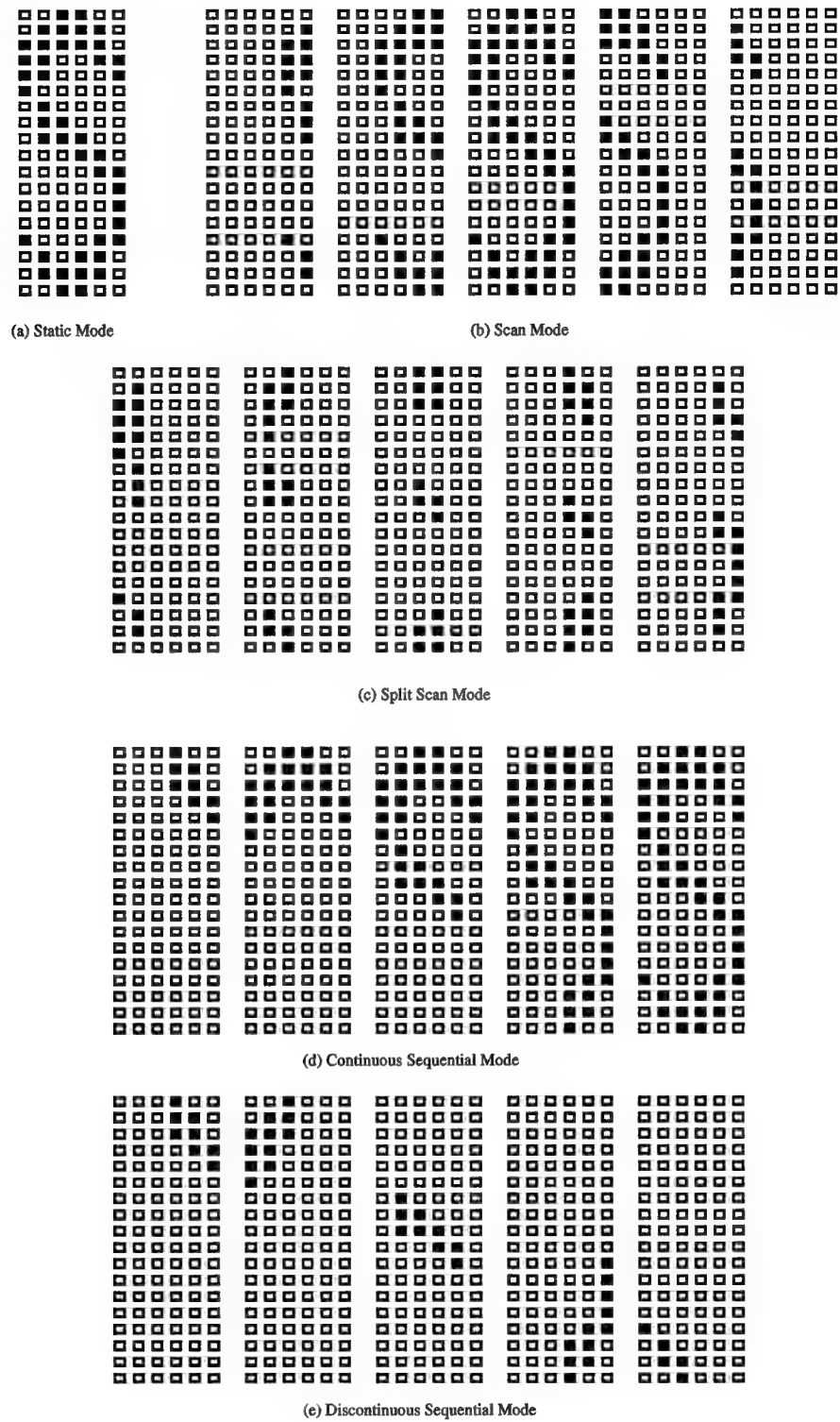


Figure 2.7. The letter "S" in five different modes of presentation [32].

Letter presentation is not the only method of relaying information. Many studies present shapes or patterns to pass information. Braille is an example of this type of code. According to one researcher, using a 2 x 2 array there are 11 patterns out of 20 that are highly discernible, 24 patterns for a 3 x 3 array, and 31 highly discernible patterns for a 5 x 5 array [32]. By using these optimum patterns, recognition of the correct pattern is greatly improved.

A final area of presentation is concerned more with presenting shapes and texture information, than information via a code. Texture discrimination and roughness all depend on motion. It does not matter if the finger is moved or if the surface is moved under a stationary finger [37]. Friction does not increase the perception of roughness, but contact force does. Also roughness increases linearly with the distance separating two stimulators (below 3 mm). This means that the further two points are spaced, the more rough the surface will seem. Finally, only SA I and FA I nerve endings respond to roughness patterning. It is possible that by using this information and the scanning modes in Figure 2.7, roughness and texture can be simulated.

2.4. Current Silicon MEM Actuators and Heaters.

The current "macro" actuators used for tactile stimulation have been listed above, along with their limitations for telerobotic applications. Also the human requirements for tactile stimulation have been given. With this information in mind, current MEM actuation techniques are now examined to determine which can be adapted to provide tactile stimulation. MEM actuation methods that are discussed include piezoelectric, SMA, electrostatic, bimorph, and electromagnetic mechanisms.

2.3.1. Piezoelectric. The piezoelectric materials are materials that change their shape with an applied electric field. Piezoelectric materials have been used for many years

in the "macro" world, but not until recently have thin film piezoelectric materials become possible.

There are three main piezoelectric thin films used in microactuators. They are zinc oxide (ZnO), the PZT family, and polyvinylidene fluoride. Of these, PZT has the largest actuation per field applied [3]. PZT does not sputter, so it must be spun on. By using multiple spin coats and an annealing process at 500 °C, thicknesses of 0.4 μm are obtainable [41]. Initially, zinc oxide was the main thin film piezoelectric material since it can be sputtered using a radio-frequency magnetron. But PZT has better dielectric and piezoelectric coefficients, providing more torque and strain.

Designs using piezoelectric films include valves, micromotors, pumps, positioning devices, and ultrasonic micromotors [3]. Common actuation methods with piezoelectric materials use either the disc method or the bimorph method. The disc method shown in Figures 2.8(a,b) causes the substrate membrane to deflect. This is typically used in micropumps where a volume under the substrate membrane is changed when the disc is actuated [20]. Figures 2.8(c,d) show the bimorph method. With this method, the tip of the beam is deflected.

One advantage of piezoelectric materials is that high mechanical forces can be produced with only a small amount of dissipated electrical power [40]. The actuation voltage required to actuate piezoelectric materials depends on the thickness of the material and its particular piezoelectric properties, but the voltages are generally less than what is required for electrostatic actuators. Another advantage is that higher stored energy densities are available at lower voltages than in most other micro actuation techniques [41].

The main disadvantage of this actuation method is that with current piezoelectric thin film deposition techniques, only small thicknesses (0.4 μm typical) are obtainable. This results in a very small actuation (0.1 μm typical) [41]. Typical macro piezoelectric materials are stacked layers that can produce large deflections (as much as 2500 μm), but

the thin film piezoelectric materials are difficult to stack. Another fabrication problem is that sputtering and spin coating produce polycrystalline material and since the piezoelectric phenomenon requires a uniform crystal orientation for optimum efficiency, microactuators fail to take full advantage of the piezoelectric property. Due to the small deflections inherent in the piezoelectric material, and the limitations of the fabrication process, piezoelectric actuators do not seem to fit the requirements for a tactile stimulator.

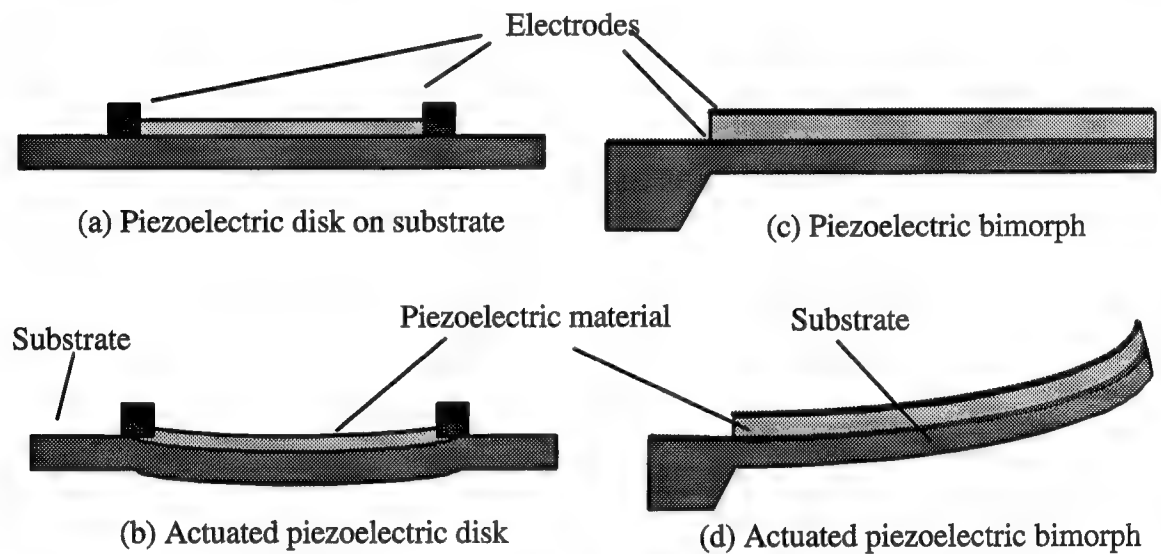


Figure 2.8. Two piezoelectric thin film actuation methods.

2.3.2. Shape Memory Alloy. As discussed above, SMA is used in large scale tactile stimulators. The obvious drawback is the large size of these devices and slow actuation rate. SMA tactile stimulators do not meet the desired performance goals. The usual activation times for a 156 μm diameter SMA wire are on the order of seconds [25]. Since SMA wires are heat driven, it takes 50 Joules of heat energy input to obtain one

Joule of mechanical energy output [26]. Also, the heat must be removed before the next cycle can start. So the cycle rate is limited to the achievable rate of heat transfer.

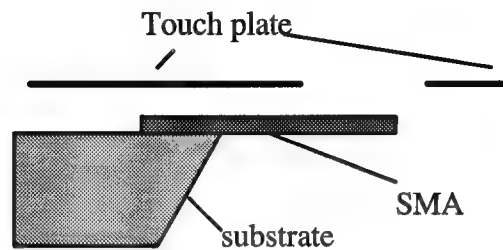
One possibility for improving on the speed and size of a SMA actuator is by using a thin film process, since heat transfer is very rapid in smaller devices (heat transfer does not scale linearly). This has been demonstrated with fair success [26]-[28]. The SMA metal used in these thin film processes is TiNi (Nitinol), which is sputter deposited with thicknesses up to 15 μm .

The TiNi thin film could be used as a tactile stimulator. It can be adapted to multiple element arrays for resolution. The smaller size also allows it to cool faster than large devices. Although it has not been demonstrated, monolithic integration should be possible since it is a planar process and compatible with other IC processing steps.

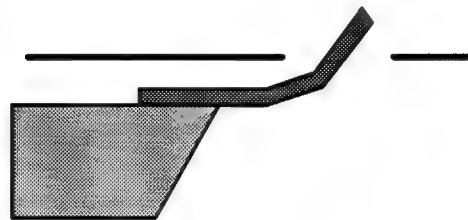
A possible example of a SMA tactile stimulator is shown in Figure 2.9. This device would have a touch plate similar to the macro SMA actuator currently in use. It would require a different method of heating since it does not form a circuit for current to flow through. Also it would have to be annealed in the "up" state, so that when heated it will curl up. The force of the finger on the touch plate would lower the beam when the beam was not being heated.

2.3.2.1. Fabrication. TiNi can be sputtered in argon atmosphere using a direct-current magnetron sputtering system [25]-[27]. The actuation temperature range (determined when the material is formed) is extremely sensitive to the alloy composition, therefore, sputtering, which produces very precise alloy compositions, is used. With three hours of sputtering, a typical thickness of 10 μm can be obtained [27], and thicknesses of up to 20 μm have been produced [26]. These films are in an early stage of development and are typically sputtered on glass, but they have been sputtered onto Si, GaAs, and other substrates [26]. This process has several limitations, but one major concern is oxygen contamination during sputtering. One percent of oxygen contamination lowers the

actuation temperature by 100 °C [26]. Only recently have researchers been able to produce SMA thin films that operate at slightly above ambient [26].



(a) Unactuated SMA beam



(b) Heated SMA strip in actuated position

Figure 2.9. SMA tactile stimulator example.

2.3.2.2. Fabrication Example. Figure 2.10 shows the steps involved in fabrication of a SMA spring [28]. The substrate used in these processes was glass. First, a 3 μm layer of polyimide was spun as the sacrificial layer. The TiNi film was then sputter deposited at a pressure of 0.05 mTorr and a current of 50 mA. The deposition was performed in argon, since oxygen contaminates the material during formation. These conditions produced a deposition rate of 0.5 μm per hour. This is shown in Figure 2.10(b). After 1 to 2 μm of TiNi were deposited, photoresist was applied (Figure 2.10(c)). After the resist was masked and patterned, the metal was then wet etched in a hydrofluoric and nitric acid solution (Figure 2.10(d)). Dry etching with a reactive ion etch

of $\text{SF}_4\text{-O}_2$ plasma at high pressures was used on the polyimide since typical polyimide wet etches destroy the SMA (Figure 2.10(e)). After annealing for 60 minutes at a temperature of 350°C , the SMA changed from amorphous film to an Austenite crystal structure having the SMA properties [28].

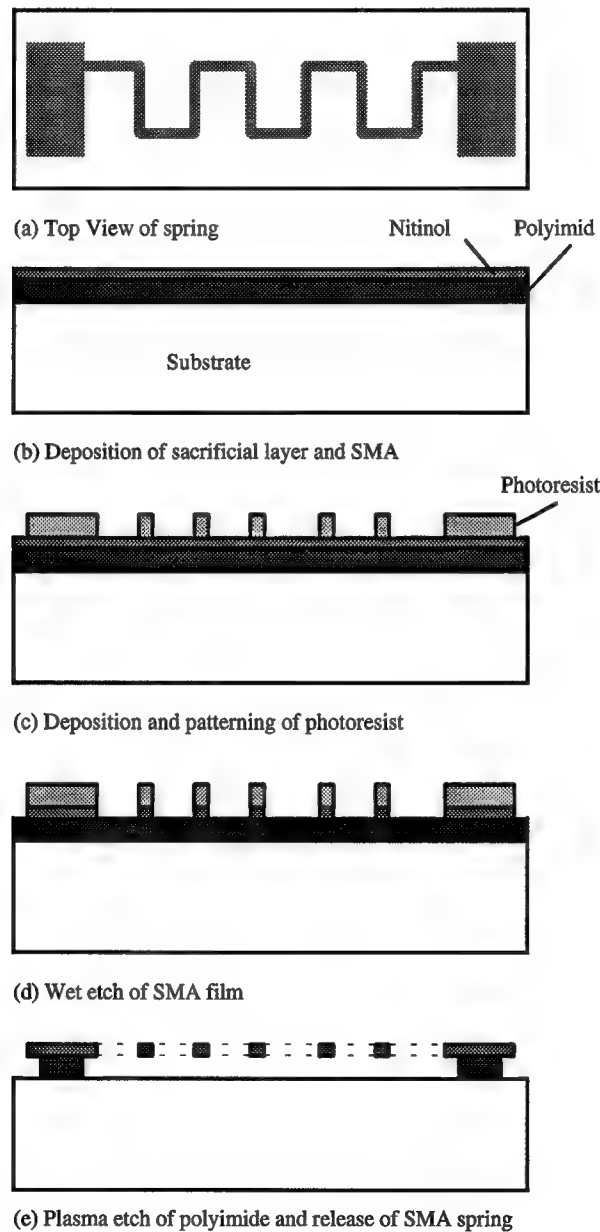


Figure 2.10. Steps in SMA actuator fabrication [28].

2.3.2.3. Typical Results. The 2000 μm long, 500 μm wide spring described in Figure 2.10 exhibited the memory property when resistive heating was applied. A 2 mA current was applied (40 volts) to cause actuation. The device operated up to 20 Hz without any loss of performance. Although, no force testing was reported for this structure, the device does indicate that the technology is compatible with MEM devices and has a much better response time than larger SMA devices [28].

The transition temperatures of an annealed SMA thin film are very dependent on the oxygen contamination. A second example of thin film SMA actuators was annealed at 480 °C and had a 80 °C hysteresis between Martensite and Austenite states [27]. This was caused by the internal stress of the film. One difficulty was that the Martensite state occurred at -54 °C and the Austenite state at 30°C. Although this film was only slightly above ambient, the overall SMA properties were in excellent agreement with bulk TiNi. This sample was etched into a beam 10 μm thick and could lift a 0.4 g load [27].

2.3.2.4. Advantages and Disadvantages. In the realm of MEM systems, SMA actuators have at least an order of magnitude more available energy than electric or magnetic devices [3]. Table 2.2 shows that SMA materials produce more work for the input energy and that they are compatible with the objectives proposed in this thesis research. Another advantage of SMA thin film actuators is that the required driving voltage is compatible with standard IC voltages. The heat energy required to cause shape recovery is produced by resistive heating [28]. The thin film SMA behavior is comparable to that of bulk SMA, which suggests that the same large work is obtainable. Finally, the thin film versions have a much better heat response compared to the "macro" wires. A

0.5 mm SMA wire cools and heats in seconds, but a 20 μm film can be operated at 20 Hz [26].

The main disadvantage and limitation is that SMA thin films are still very new and the process is not perfected. Very little information is available about what forces are obtainable with the thin film process. More work is necessary to stabilize the physical process parameters of thin film SMA's [40]. The immediate problems are that oxygen contamination lowers the operating temperature to near ambient. This requires the material to be cooled to achieve the Martensite state [26]. Also, the internal stress in the thin film during annealing causes the actuators to deform when released [28]. Finally, SMA actuators are not ideal for tactile stimulators since they require annealing in the Austenite state. This means that in order to get actuation out of the plane, the film must be deformed and then annealed.

Table 2.2. SMA Comparison with Other Actuation Techniques [26].

Principle	Maximum work energy density ($\text{J}\cdot\text{cm}^{-3}$)	Drive conditions
Electrostatic	0.4	$E = 300 \text{ V}\cdot\mu\text{m}^{-1}$
Piezoelectric (PVDF)	$4.8\cdot 10^{-4}$	$E = 30 \text{ V}\cdot\mu\text{m}^{-1}$
Shape Memory Alloy (TiNi)	10.4	$P = 1.4 \text{ W}\cdot\text{mm}^{-3}$

In conclusion, SMA thin films are not ideal for tactile stimulation needs. They are limited to approximately 20 Hz of frequency [26]. The fabrication process does not readily lend itself to actuation out of the plane. Present films need to be cooled much

below ambient to observe the SMA property and this would require bulky cooling systems.

2.3.3. Bimorph. As described in Chapter 1, bimorphs are a sandwich of materials with different coefficients of thermal expansion. When heated the two materials expand at different rates causing a curling action. Thin film piezoelectric and SMA materials are relatively recent actuation methods, and still require much development before they can be used as effective microactuators. Bimorphs, on the other hand, have been an effective form of microactuation for many years [16]. The process is very flexible, any two different materials can exhibit the bimorph property and large deflections (greater than 30 μm) are possible.

The bimorph property has been used for many years in temperature controlled electrical switches in thermostats. The basic design is two strips of metal that curl toward the material with the smaller coefficient of thermal expansion when there is a change in temperature [42]. There are many different micro-bimorph examples to date, using various materials [16]-[19], [42]-[43].

2.3.3.1. Fabrication. Any combination of materials with different coefficients of thermal expansion will exhibit the bimorph effect, therefore, there are no real material limitations for fabrication. Even different types of oxide sandwiched together can cause the bimorph effect [42]. In general materials with large differences in thermal expansion coefficients are desirable. Of the typical IC fabrication materials silicon dioxide - aluminum sandwiches exhibit the largest theoretical deflection [16].

Although the great flexibility in fabrication is inherent, fabrication facilities are not available to everyone. Recently several bimorph designs have been fabricated through commercial fabrication facilities like MOSIS [42], [18]. This solution insures

compatibility with ICs, but some design flexibility and process control is lost. The CMOS fabrication process is described extensively in Chapter 1.

A typical bimorph is described in the next section. It does not use the CMOS process, but contains all the essential elements of the bimorph design.

2.3.3.2. Fabrication Example. The example device is fabricated using silicon and gold as the sandwich materials [16]. A 20 kW polysilicon heating resistor (encased in Silicon Nitride) is deposited between the two layers. The beam is 500 μm long and 100 μm wide. The silicon layer is 4 μm thick and the gold layer is 1.8 to 2.5 μm thick. The fabrication process steps are shown in Figure 2.11.

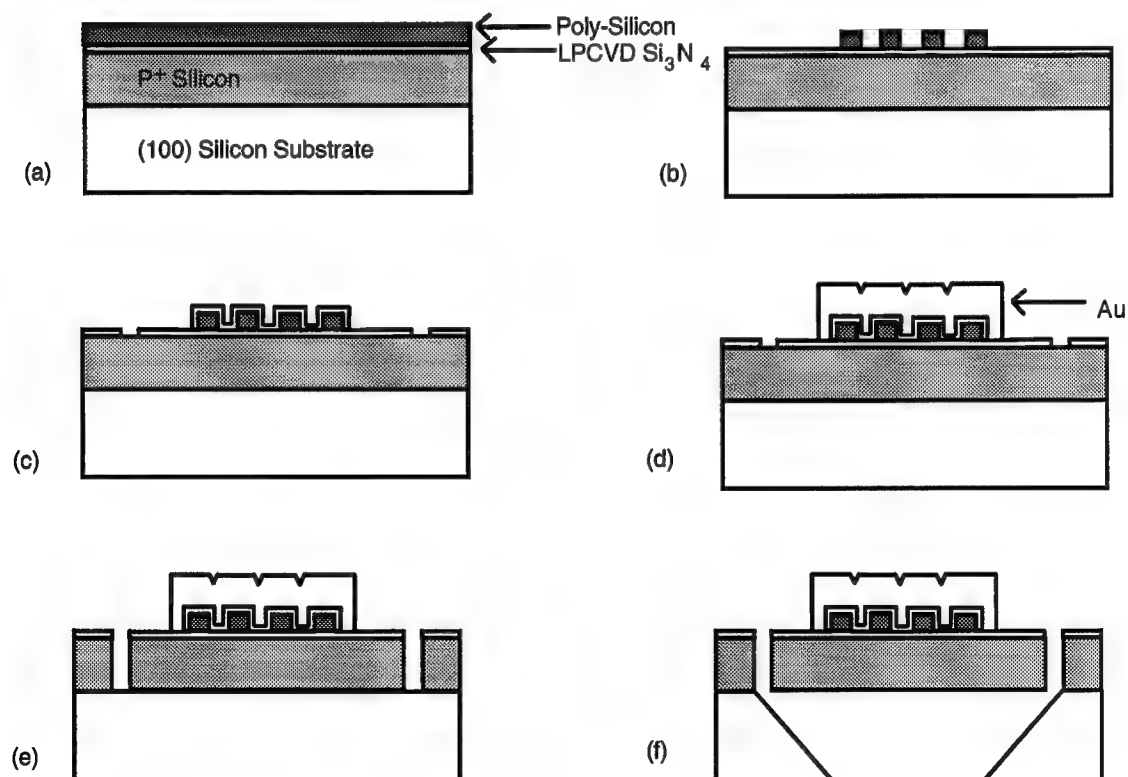


Figure 2.11. Bimorph cantilever beam fabrication process [16].

First, a highly doped boron layer is epitaxially deposited. Since boron doped silicon is an etch stop, the doped silicon will remain after anisotropic etching and becomes the bottom layer of the beam. A thin layer of silicon nitride is deposited using a LPCVD (low pressure chemical vapor deposition) process. This layer acts as an isolation layer for the heating resistor. The polysilicon layer is deposited to a thickness of 0.5 μm . This is shown in Figure 2.11(a). Second, the polysilicon is patterned and etched to make the long heating resistor (Figure 2.11(b)). This heating resistor typically reaches 300 °C. Third, a second passivation layer of silicon nitride is deposited and the etch holes are defined as shown in Figure 2.11(c). Fourth, the gold layer is electroplated to form the second layer of the bimorph cantilever. Fifth, isotropic etching is used on the boron doped silicon (Figure 2.11(e)). Sixth, the structure is released by anisotropically etching the silicon substrate as shown in Figure 2.11(f).

2.3.3.3. Typical Results. Using a 12 volt source, static deflections of greater than 90 μm were obtained with the example beam shown above. This deflection depends on the input electrical power which produces the heat. Full deflection was obtained at frequencies up to 10 Hz and motion is observed up to 35 Hz. The gold begins to melt above 300 mW applied power and this is the limiting factor [16].

Silicon and gold were chosen as the beam materials because they are easy to work with and thicker materials could be deposited. This design had two basic problems. The first was the low melting point of gold, and the second was that the beam has an upward pre-buckle. The internal stresses of the silicon nitride used for the passivation layers caused the beam to have an upward pre-buckle.

Deflections vary depending on the length of the beam and the coefficients of thermal expansion of the materials used. The thickness and width of the beam do not dramatically affect the performance of the beam. As a figure of merit, deflection to length

ratios can be used. The Si-Au beam reported above has a ratio of 0.3. Other sources report deflections from 1 μm for a resonant beam at 30 KHz (0.0003 ratio) [18] to 4 μm for an oxide - oxide sandwich operated up to 1 KHz (0.013 ratio) [42]. An example using thin film polymers with a higher ratio of thermal expansion coefficients has produced deflections of 900 μm with a deflection to length ratio of 0.18 [43].

The deflection of a beam is elastic until a certain temperature is reached and then the beam experiences plastic deformation. For the Si-Au example above this was due to the gold melting [16]. In the CMOS processes the plastic deformation occurs when the oxide is heated enough to anneal and generate permanent strain [42].

2.3.3.4. Advantages and Disadvantages. Bimorphs have the potential to fulfill the tactile stimulation design requirements. The beam can be powered with relatively low voltages. This keeps the device compatible with standard electronics and makes it possible to integrate the tactile stimulator with drive electronics. Also the low voltage devices are safer to the human operator. Another important property is that the mechanical force of the beam is independent of the actuator position, unlike electrostatic actuators that have less force as the distance between the electrodes increases. Bimorphs have a high mechanical rigidity and can be produced using standard processing steps. Since the choice of materials is flexible and the designs are simply layers with integrated resistors, commercial CMOS process like MOSIS can be utilized [18], [42]. An array of beams has been demonstrated with 512 bimorph actuators in a 1 x 1 cm^2 area [19]. Finally, the bimorph beams have very large deflections compared to other micro actuation techniques.

One disadvantage is that the bimorph actuation is due to a thermal process. This implies that heat transfer will be the limiting factor and will limit the actuation speed. Therefore, these devices are generally low frequency (typically under 100 Hz). The heat transfer can be improved by external cooling. In one study, actuation times were reduced

to 1 ms by using fluid cooling [17]. The common IC fabrication materials generally have high thermal conductivity. This high thermal conductivity increases the thermal losses of the devices, thus requiring high currents for actuation. A final problem is that nearly all the released cantilevers exhibit pre-buckle. This internal stress can cause the beam to curl out of the plane as much as 1/2 of the length of the beam [19]. The curling is due to residual stress inherent in the thin film materials used in fabrication. It manifests itself when the beams are released by beam curling out of the substrate plane.

2.3.4. Electrostatic. The next important type of actuation is electrostatic.

Electrostatic forces are used in micromotors, valves, resonators, switches, micropumps, and torsional mirrors [3], [40], [44]-[47]. The electrostatic force is inversely proportional to the square of the separation of the electrodes. Therefore, in general it works only over small distances and requires high voltages. Although no out of the plane electrostatic devices have been reported thus far, the technique may be utilized for tactile stimulation.

Micromotors are the most common type of electrostatic devices. They generally have a rotor and stator as the opposing electrodes, and a pin as an axle. They have been demonstrated to operate at voltages between 30 - 100 volts and at speeds of 15,000 revolutions per minute [3]. The gap between the stator and the rotor is usually between 1 and 3 μm . The devices are generally limited by the power supply and not by any fundamental limit of electrostatic forces [46]. Also, friction and wear are significant concerns when designing micromotors.

Another electrostatic device is a comb actuator. Comb actuators consist of interdigitated fingers that resonate in the lateral plane. They are suspended above the plane and rely on large springs for support. Comb actuators have been fabricated that produce as much as 10 μm of deflection and have been operated at 10 KHz [3]. The typical operating voltages for these devices are 50-60 volts [45].

Beam devices make up a third type of electrostatic devices. They are by far the simplest of the devices. These devices consist of a beam that deflects downward due to attraction with an electrode embedded in the substrate. One example of an electrostatic beam uses an aluminum process which utilizes large sacrificial layers. A deflection of $1\text{ }\mu\text{m}$ is obtained at 10 volts. Since the beam is all aluminum, it has a small spring constant and is permanently deformed at 33 volts [48]. A microvalve design using electrostatic beam actuation is shown in Figure 2.12.

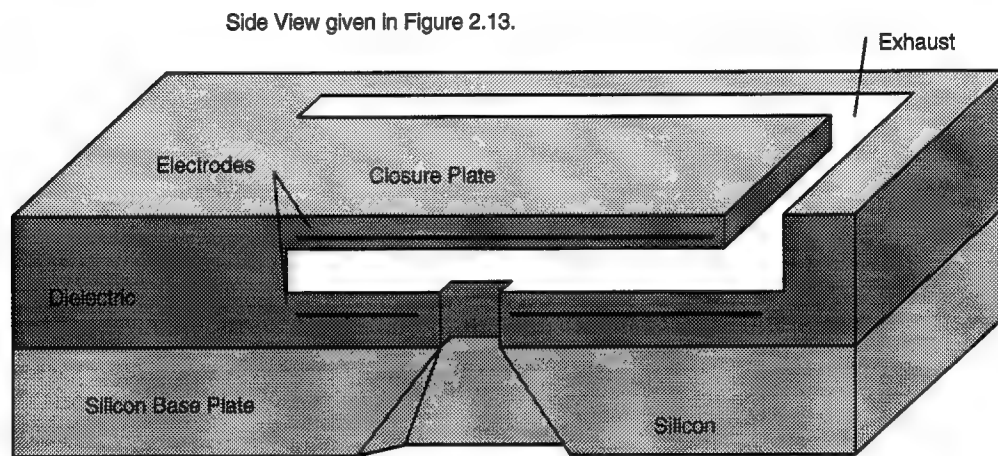


Figure 2.12. Microvalve cross section [21].

The microvalve in this design is a normally open valve with the gas flowing through the substrate and out the exhaust flap. This diagram shows how the embedded electrodes cause the beam to deflect downward closing the valve. For a tactile stimulator, this design would have to be changed to deflect the beam upwards.

2.3.4.1. Fabrication. A fabrication example of the micromachined valve is given below. The basic micromachining steps are shown in Figure 2.13. This device was fabricated as a 5×5 array of beams. Each beam measured $390 \times 350\text{ }\mu\text{m}$. The first

of the three steps in Figure 2.13 shows the silicon nitride deposited on both sides of the device. The base plate electrode was deposited, patterned, and etched on the front side of the wafer. A second layer of silicon nitride was then deposited, patterned and etched using plasma etching. It was patterned to leave via holes for the anisotropic etch at the end of the process that releases the beam and opens the orifice. The silicon nitride serves as an isolation material for the electrodes. The sacrificial layer (the actual thin film used as the sacrificial layer was not given) was deposited and patterned next.

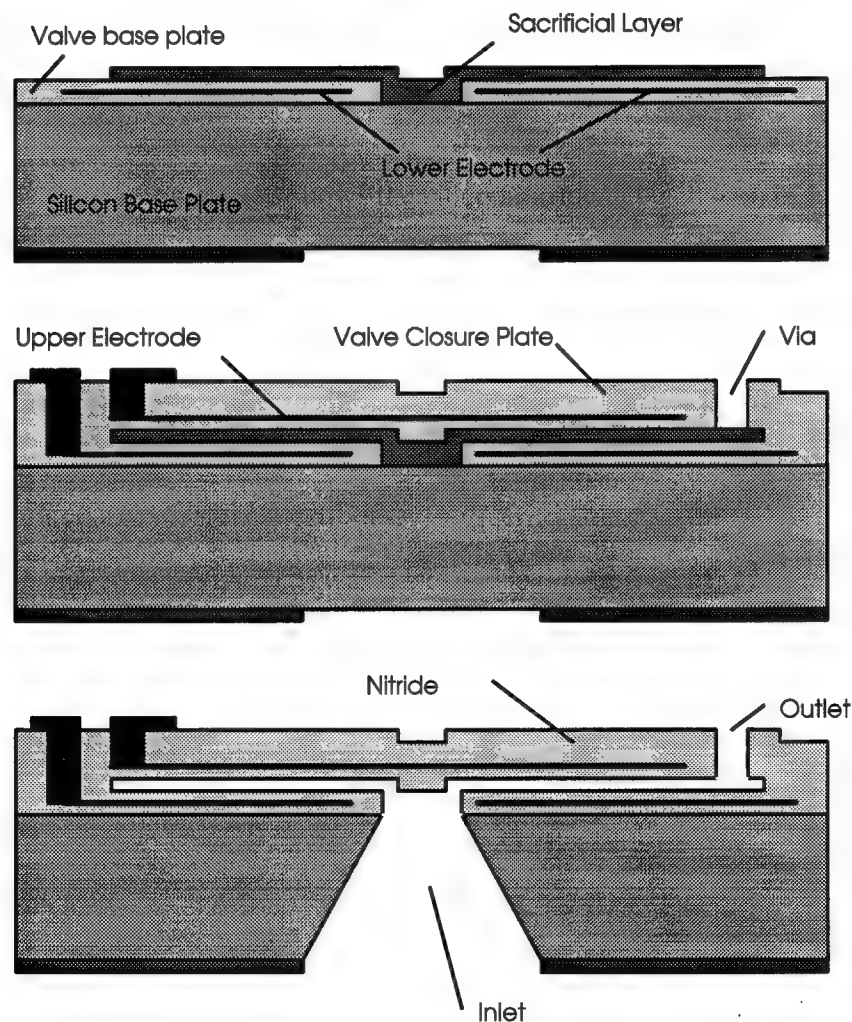


Figure 2.13. Process steps in microvalve fabrication [21].

The second step in Figure 2.13 shows that the second electrode was deposited. Similar to the first step, silicon nitride was used as the passivation layer and becomes the structural material for the beam. The total valve closure plate thickness was 1 μm . Via holes were then cut using plasma etching. Holes were cut to the sacrificial layer and to the two electrodes. The electrode contact metals were then deposited.

The next step was to anisotropically etch the valve with KOH to open the orifice. After anisotropically etching, the sacrificial layer was removed using selective etching.

In general it is important to have a small separation between the driving electrodes since the force is stronger over small distances [47]. Another important point about fabrication is that if the electrodes are not insulated, a landing pad that does not have applied voltages, should be used.

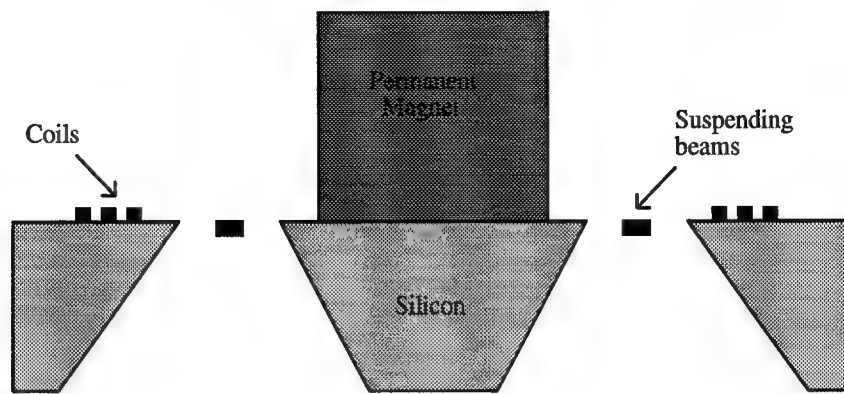
2.3.4.2. Typical Results. The valve was actuated at 30 volts, with gas pressures up to 110 mmHg (1 mmHg = 133.32 N/m²). Once closed the valve remained closed under pressures of 740 mmHg. The leaking does not damage the device and it can be reused. The beam can also be operated with pulse width modulation. The amount of gas flow is controlled by the frequency and the width of the pulse.

2.3.4.3. Advantages and Disadvantages. Some of the advantages of electrostatic actuation are given below. First, electrostatic forces scale much better than electromagnetic, since the forces are not coupled to volumes, but to surfaces. The MEM electrostatic devices generally consume little power and they have very high switching speeds [40]. Electrostatic MEM devices generally have long life cycles; with some motors being operated more than 10^{10} cycles [47]. Another important benefit is that electric field breakdown in air is two orders of magnitude higher with micro gaps than macro gaps. This allows for more stored energy [3].

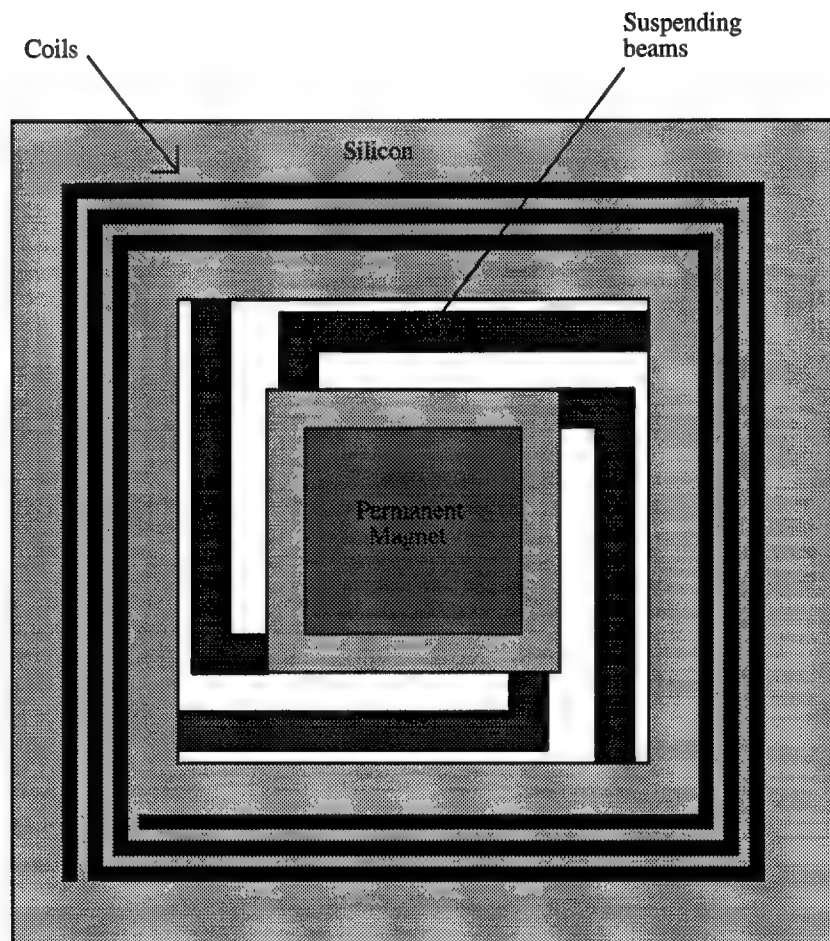
A disadvantage is that dust can be a severe problem, causing shorts (unless insulated) or mechanical problems since the gaps are very small. Another problem with the electrostatic beams that deflect down is that they tend to bend until a threshold point is reached. After this threshold point they become unstable and the tip suddenly touches the bottom of the well [47]. This is because the force increases as the tip gets closer to the bottom of the pit. Electrostatic actuation generally requires high electric fields and high voltages [26]. Also, some processes do not have insulating layers and shorting of the two electrodes after the threshold point is reached is a problem. A landing electrode can be used if insulation is not available. Although the actuation force itself is not ideally suited for tactile stimulation, since the force decreases with the increasing amount of separation between the electrodes, it does have the possibility to provide tactile stimulation.

2.3.5. Electromagnetic. Although electromagnetic devices power the macro world as solenoids and actuators, they are not well suited for micro actuation and tactile stimulation. The magnetic forces do not scale well to the micro domain [44]. Magnetic forces are dependent on the volume of the magnet, therefore thin film soft magnets can not produce large forces. Electromagnetic forces occur due to either a moving coil carrying current, or a moving magnet [49]. Electromagnetic microactuators require the flow of current through metal windings, and therefore tend to be large and consume more power than other microactuation techniques [3]. Due to this large current, the moving coil is not feasible. A thin film spring weak enough to provide motion could not carry the current necessary for electromagnetic actuation [49].

2.3.5.1. Fabrication. There have been several MEM devices that operate due to the electromagnetic principles [49]-[50]. An example of an electromagnetic MEM device is shown in Figure 2.14. In this device an integrated planar coil is used to excite a permanent magnet that is attached to the substrate by springs.



(a) Side View



(b) Top View

Figure 2.14. Electromagnetic MEM device [40].

The permanent magnet cube had sides of 1 mm and was glued to the substrate. The spring and magnet base were formed by bulk micromachining using an etch stop. Gold was electroplated in 30 μm by 26 μm lines to produce the coils. The spring thickness was 8.5 μm with a length of 2800 μm and 400 μm width [49].

2.3.5.2. Results. The electromagnetic actuator shown above moves out of the plane. The devices were driven with 300 mA which resulted in a dissipated power of 1.3 W. The magnet moved 80 μm in the vertical direction, but due to the large weight of the magnet, the springs were initially deflected down 30 μm . The device operated at frequencies up to 1 KHz, although movement was reduced to only 1 μm [49].

2.3.5.3. Advantages and Disadvantages. The main advantage of electromagnetic devices is the large deflections. Electromagnetic forces can operate over large distances and are not restrained by small gaps as in electrostatic devices.

Electromagnetic actuators have several disadvantages. They require very high currents. Since permanent magnets must be attached to the substrate, no monolithic integration is currently possible. This also causes a size problem, since there is a limit to how small the permanent magnet may be cut. In addition, the planar coils reduce the flexibility of the design.

2.4. Conclusions.

This chapter describes the advantages and disadvantages of conventional actuation methods. Tactile stimulation requirements are discussed. MEM devices that have the potential to provide tactile stimulation are discussed.

The current methods of tactile stimulation are not adequate, therefore, some other form of actuation must be found. The requirements for human tactile stimulation are

discussed. It is shown that MEM devices have the potential to provide mechanical stimulation. The promising MEM devices given above are based on bimorph and electrostatic actuation techniques. These forces should be studied to determine if they are adaptable to tactile stimulation.

3. THEORY AND DESIGN

This chapter develops the theory for MEM cantilever beams. The theory is limited to MEM actuators driven with bimorph and electrostatic forces only. Chapter 2 indicates that these two actuation forces may produce tactile stimulators. After both of these forces are discussed, design considerations and experimental devices are described.

3.1. Bimorph Actuation.

Bimorph beams have been investigated since the 1920's [51]. The theory behind bimorph actuation forces has been developed by several researchers, but none of the derivations agree [16]-[17], [51]-[53]. This situation is further complicated by the fact that the devices presented in this thesis are all of multi-morph design. Since the CMOS fabrication process uses oxide to isolate each layer, all beams are encased in oxide. Any beam designed with this process will have a minimum of three layers. Very little development of multi-morph systems has been presented so far. Bimorph actuation principles are presented below. After the bimorph, a multi-morph theory is developed.

3.1.1. Bimorph Theory. The basic design of a bimorph thermal actuator is given in Figure 3.1. It is simply a sandwich of two materials with different coefficients of thermal expansion. Some method of applying heat to the system is required, and it is usually done with an embedded heating resistor (not shown in the figure). In developing the bimorph theory, the thickness of the heating resistor is neglected since it is usually thin compared to the two primary layers. Figure 3.1 shows some of the standard convention to be used in this chapter.

Different material layers are denoted by subscripts with 1 being the first layer and 2 being the second layer. The beam width is b , thickness is t , and length is l . The material

constants E and α are the Young's modulus and the thermal coefficient of expansion, respectively.

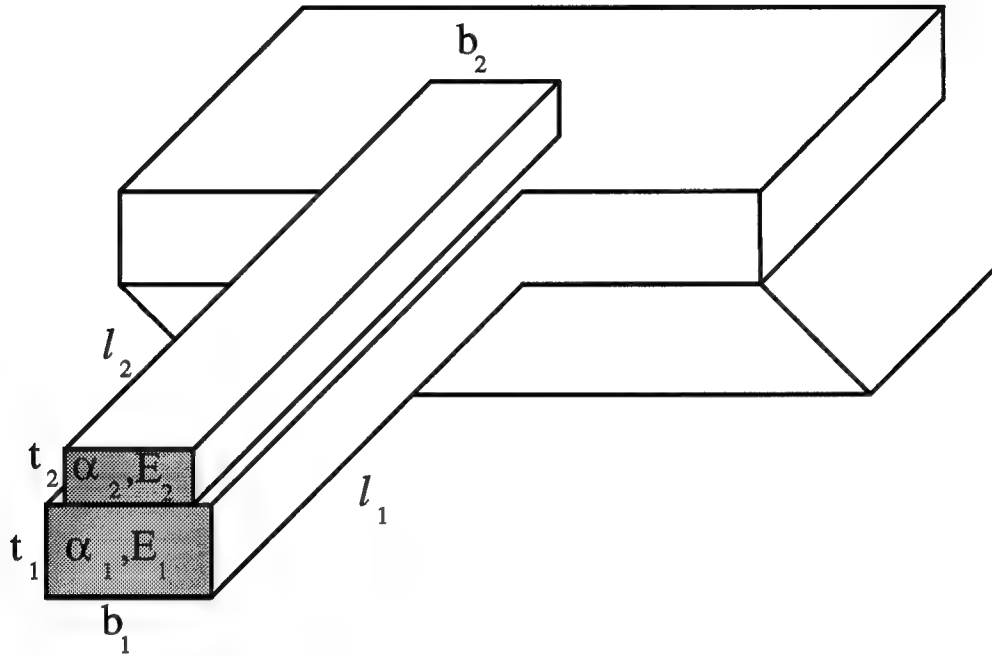


Figure 3.1. Bimorph cantilever beam [16].

The deflection of the beam is derived by analyzing the curl caused by the thermal expansion of the two materials. Due to the nature of the force, beams of equal length will produce the most force, hence the lengths of the two beams are assumed equal.

Figure 3.2 shows the basic geometry of the beam during deflection. If we assume that the beam will curl with a constant radius of curvature, r , then the deflection, d , can be derived simply from r and the length of the beam l . The arc length l of the beam yields the angle θ by

$$\theta = \frac{l}{r} \quad (1)$$

where θ is in radians. The length x from Figure 3.2 can be determined by simple geometry as

$$x = 2r \cdot \sin \frac{l}{2r} \quad (2)$$

The angle ϕ is obtained similarly as $\phi = \theta/2$. Once the values of ϕ and x are known, the deflection d is obtainable.

$$d = 2r \cdot \left(\sin \frac{l}{2r} \right)^2 \quad (3)$$

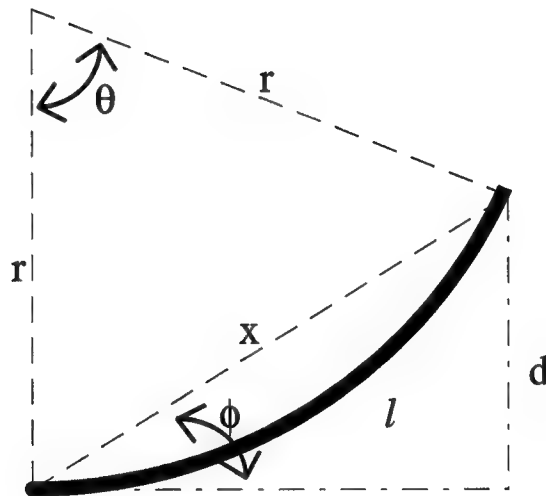


Figure 3.2. Deflection of a supported beam.

In most of the cases, the radius of curvature is much larger than the length of the beam, $l \ll 2r$. This allows Eq. (3) to be simplified to

$$d = \frac{l^2}{2r} \quad (4)$$

The deflection d is now dependent on r and l only. Since l is a design parameter, r is the only undetermined parameter remaining. To determine the radius of curvature, r , the beam is described with the basic layers shown in Figure 3.3. The symbol F denotes the axial tensile force acting on the beam and M is the bending moment of the segment. Force F includes all the applied stress internal to the beam, and since there are no external forces the forces over any cross section of the beam must be in equilibrium [52].

$$F = F_1 = F_2 \quad (5)$$

$$\frac{F(t_1 + t_2)}{2} = M_1 + M_2 \quad (6)$$

The flexural rigidity of the beam is denoted by EI , where E is the Young's modulus and I is the inertia of the beam [54]. The bending moment and the flexural rigidity are related through the radius of curvature

$$M_i = \frac{E_i I_i}{r} \quad (7)$$

In Eq. (7) and in the following discussion, subscript i will indicate either layer 1 or layer 2.

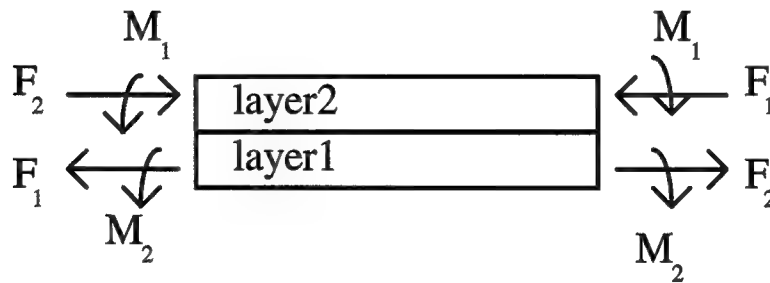


Figure 3.3. Forces and moments on a cross section of a bimorph beam [52].

By using (7), Eq. (6) becomes:

$$\frac{F(t_1 + t_2)}{2} = \frac{E_1 I_1 + E_2 I_2}{r} \quad (8)$$

A second equation is needed since Eq. (8) has two unknowns (F and r). This equation comes from considering the normal strain at the interface which must be the same for the two layers. The expansion of the metal layer interface in Figure 3.3 in the horizontal direction must be equal, resulting in Eq. (9), where ΔT is the change in temperature above ambient [51]. The change in temperature assumes that the temperature is evenly distributed over the entire length of the beam.

$$\alpha_1 \Delta T + \frac{F}{E_1 t_1 b_1} + \frac{t_1}{2r} = \alpha_2 \Delta T - \frac{F}{E_2 t_2 b_2} - \frac{t_2}{2r} \quad (9)$$

By inserting F from Eq. (8) into (9) the following can be obtained.

$$\frac{t_1 + t_2}{2r} = (\alpha_2 - \alpha_1) \Delta T - 2 \left(\frac{E_1 I_1 + E_2 I_2}{r(t_1 + t_2)} \right) \left(\frac{1}{E_1 I_1 b_1} + \frac{1}{E_2 I_2 b_2} \right) \quad (10)$$

From beam theory the inertia I in equation (10) can be described as [52]

$$I_i = \frac{b_i t_i^3}{12} \quad (11)$$

Now by inserting (11) into (10) and solving for r , the following is obtained [51]-[53]:

$$r = \frac{(E_1 b_1 t_1^2 + E_2 b_2 t_2^2)^2 + 4 E_1 b_1 t_1 E_2 b_2 t_2 (t_1^2 + t_1 t_2 + t_2^2)}{6 E_1 b_1 t_1 E_2 b_2 t_2 \Delta T (\alpha_2 - \alpha_1) (t_1 + t_2)} \quad (12)$$

For the beams designed in this thesis, the width was held constant ($b_1 = b_2$). This allows some simplification:

$$r = \frac{(E_1 t_1^2 + E_2 t_2^2)^2 + 4E_1 t_1 E_2 t_2 (t_1^2 + t_1 t_2 + t_2^2)}{6E_1 t_1 E_2 t_2 \Delta T \Delta \alpha (t_1 + t_2)} \quad (13)$$

where $\Delta\alpha=(\alpha_2-\alpha_1)$. By using Eqs. (13) and (4) the deflection of the beam tip is obtained. The resulting deflection depends on temperature, material constants, and design parameters (length and thickness). From these equations it can be inferred that the deflection perpendicular to the initial cantilever plane will increase with larger l , ΔT and $\Delta\alpha$. Less obvious is the fact that larger deflections are obtained with smaller t and that the Young's modulus does not greatly change the deflection. If $\alpha_2 > \alpha_1$ then the beam will deflect into the plane of the supporting substrate. If the opposite is true, then the beam will deflect out of the plane of the supporting substrate. Therefore, a positive value for r will reflect a toward the substrate motion, where negative r will lead to an away from the substrate motion. Table 3.1 lists the α and E values for some of the materials used in integrated circuit (IC) fabrication.

Table 3.1. Coefficient of Thermal Expansion and Young's Modulus for Some Microelectronic Materials [16].

Material	Young' Modulus (10^{11}N/m^2)	Coefficient of Thermal Expansion ($10^{-6}/\text{K}$)
Aluminum	0.69	23
Gold	0.8	14.3
Lead	0.16	28.7
Silicon Dioxide	0.74	0.4
n Polysilicon	--	2.33
Monocrystalline Silicon	1.62	2.6

Table 3.2 gives a figure of merit for common planar material combinations. The figure of merit is based on Eq. (13). The equation is modified with the thicknesses held constant and all parameters except E and $\Delta\alpha$ were ignored. The modified equation is given as:

$$\beta = \frac{E_1 + E_2 + 12 E_1 E_2}{12 E_1 E_2 \Delta\alpha} \quad (14)$$

where β is the figure of merit. This table shows that a combination of silicon dioxide and aluminum (some of the most common IC fabrication materials) has excellent bimorph properties.

Table 3.2. Figure of Merit for Different Material Combinations [16].

Material	Figure of Merit
Si - Au	9.67
SiO ₂ - Au	11.88
Si - Al	16.59
SiO ₂ - Al	19.48
Si - Pb	14.09
SiO ₂ - Pb	20.16
SiO ₂ - Polysilicon	1.165

Although the width of the cantilever beam does not affect the deflection in the reduced equation, it must be taken into account along with thickness to insure the beam has mechanical strength. When the beam heats it is better to have a smaller surface area so

that it will heat faster, but during cooling it is better to have more surface area to dissipate the heat. These factors all affect the operation of the bimorph beams.

3.1.2. Multi-morph Theory. Although bimorph systems are simpler to analyze, they are difficult to achieve. All of the bimorph systems described recently, [16]-[19], [42], [52], have not been true bimorphs. These systems require a heating resistor along the beam which must be encased in an insulator. These extra layers are assumed to have negligible affect on the devices, since the two important layers are much thicker. But, the CMOS process leaves little flexibility in design. All layers used in this process must be encased in silicon dioxide. The oxide thickness is comparable to other layers and must be considered in calculations. This means that the low α material is above and below the high α material (see Table 3.1). Since the designs presented in this thesis are fabricated using the CMOS process, the multi-morph theory needs to be discussed.

Figure 3.4 shows a basic multi-morph beam. The thicknesses are exaggerated in this drawing to stress the difference of the materials. Once again subscript i designates the layers (in this case layers 1 through 6).

The theory behind a piezoelectric multi-morph system is described in [53]. This analysis can be adapted for thermally actuated devices. Following the axis given in Figure 3.4, the radius of curvature is [53]

$$r = \frac{\langle EI \rangle}{\left\langle \frac{zfA}{S_{yy}^E} \right\rangle} \quad (15)$$

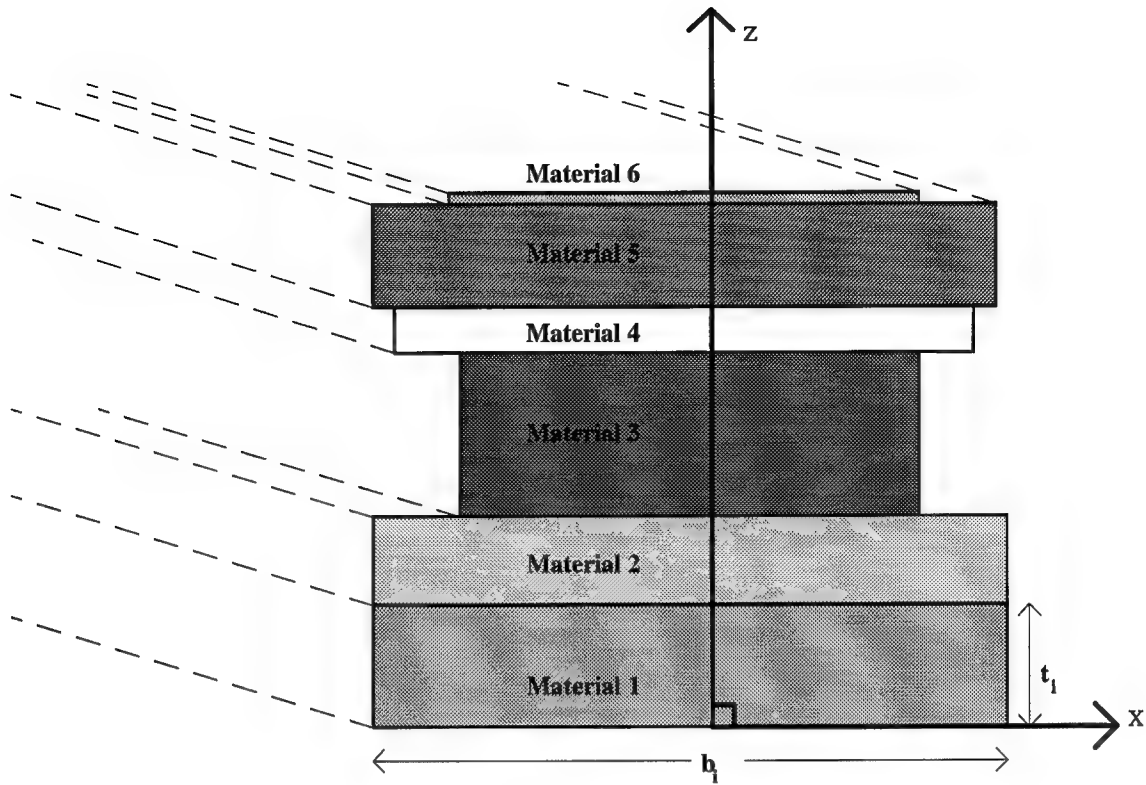


Figure 3.4. Multi-morph system with six layers [53].

The flexural rigidity $\langle EI \rangle$ can be defined as:

$$\langle EI \rangle = \frac{\sum_{i=1}^n \left((c_i t_i)^2 + \sum_{k=1}^{i-1} c_i c_k (t_i^2 + t_k^2 + 3(\gamma_i + \gamma_k)^2) \right)}{12 \sum_{i=1}^n c_i} \quad (16)$$

The denominator of (15) is given by

$$\left\langle \frac{zfA}{S_{yy}^E} \right\rangle = \frac{1}{2} \cdot \sum_{i=1}^n \sum_{k=1}^i c_i (\gamma_i + \gamma_k) (f_k - f_i) \quad (17)$$

where S_{yy}^E is the elastic compliance and $1/S_{yy}^E$ is the elastic stiffness or Young's modulus E [55]. Also, c is defined as:

$$c_i = t_i b_i E_i \quad (18)$$

As given in the bimorph theory, t and b , represent thickness and width of the individual layers. The symbol, γ , is defined as:

$$\gamma_i = (t_{i+1} + \dots + t_n) - (t_1 + \dots + t_{i-1}) \quad (19)$$

The temperature expansion force, f_i , is.

$$f_i = \Delta T \alpha_i \quad (20)$$

The value of ΔT given in equation (20) is assumed to be constant over the entire beam and throughout all the layers. The symbol α once again represents the coefficient of thermal expansion. When (16) and (17) are combined into (15) the radius of curvature is given by [53]:

$$r = \frac{\sum_{i=1}^n ((c_i t_i)^2 + \sum_{k=1}^{i-1} c_i c_k (t_i^2 + t_k^2 + 3(\gamma_i - \gamma_k)^2))}{6 \sum_{i=1}^n \sum_{k=1}^i c_i c_k (\gamma_i - \gamma_k) (f_k - f_i)} \quad (21)$$

Once (21) has been solved the deflection is determined by (4). Equation (21) can be further simplified if the widths of all the layers are assumed to be equal:

$$r = \frac{\sum_{i=1}^n ((E_i t_i^2)^2 + \sum_{k=1}^{i-1} E_i E_k t_i t_k (t_i^2 + t_k^2 + 3(\gamma_i - \gamma_k)^2))}{6 \sum_{i=1}^n \sum_{k=1}^i E_i E_k t_i t_k \Delta T (\gamma_i - \gamma_k) (\alpha_k - \alpha_i)} \quad (22)$$

Although [53] is the only source that derives a multi-morph radius of curvature equation, Eq. (21) reduces to Eq. (12) if only two layers are used and Eq. (12) has been derived several times [51]-[52].

3.1.3. Heat Transfer. Since the deflection of a multi-morph system is based solely on a change in temperature, heat transfer must be considered. The temperature capacity of the beam is determined by energy loss to the surroundings. Heat loss occurs through three paths: heat transfer to the air, heat transfer to the substrate through the support, and radiation loss. Of these three, nearly all of the heat loss occurs into the surrounding air. The other losses can be neglected [16], [17].

The speed of operation is governed by how fast the beam can heat and cool. Therefore, more surface area is desired to allow easier transfer of heat to the surroundings. Figure 3.5 indicates the heat loss for a beam. In the figure T_a is the temperature of the ambient air and T_b is the temperature of the beam. The symbol ΔT in the above derivations is then given by $T_b - T_a$. The symbol, P_{el} , is the electrical input power. The internal energy of the cantilever is denoted by U . Also, Q_a , Q_s , and Q_r are the heat loss to the air, substrate, and radiation, respectively. Of these Q_s can be neglected since the surface area through which heat can pass to the substrate is more than two orders of magnitude smaller than the air exposed beam area. Q_r , which is much smaller than Q_a , is also ignored when analyzing the heat loss.

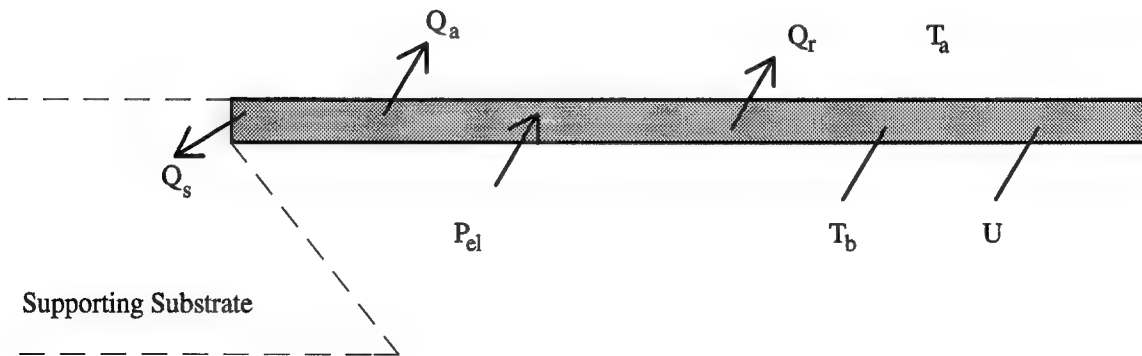


Figure 3.5. Energy balance of a heated cantilever beam [17].

The equilibrium heat equation is given by [17]:

$$cm \frac{d\Delta T}{dt} + \delta A \Delta T = P_{el} \quad (23)$$

where cm is the average of the mass of the different layers times the specific heat of those layers, A is the surface area of the beam where the heat transfer takes place, and δ is the average heat transfer coefficient [17]. From (23) a relationship can be inferred between the input electrical power, P_{el} , and the change in temperature ΔT .

$$\Delta T = P_{el} C \quad (24)$$

where under steady state conditions, C is a constant based on material properties and geometry of the beam [13], [15]-[17], [56]. C is difficult to determine analytically and is usually determined experimentally. By using (24) both (13) and (22) can be rewritten:

$$r = \frac{(E_1 t_1^2 + E_2 t_2^2)^2 + 4E_1 t_1 E_2 t_2 (t_1^2 + t_1 t_2 + t_2^2)}{6CE_1 t_1 E_2 t_2 P_{el} \Delta \alpha (t_1 + t_2)} \quad (25)$$

for a bimorph, and

$$r = \frac{\sum_{i=1}^n ((E_i t_i^2)^2 + \sum_{k=1}^{i-1} E_i E_k t_i t_k (t_i^2 + t_k^2 + 3(\gamma_i - \gamma_k)^2))}{6C \sum_{i=1}^n \sum_{k=1}^i E_i E_k t_i t_k P_{el} (\gamma_i - \gamma_k) (\alpha_k - \alpha_i)} \quad (26)$$

for a multi-morph beam.

3.1.4. Force. When the beam is actuating, a force is generated from the thermal expansion. This force is uniformly distributed along the entire beam length. If this force is counteracted at the tip of the beam with an equivalent force, F_{eq} , the beam will not move [52]. This force is given by

$$F_{eq} = \frac{3EI d}{l^3} \quad (27)$$

Here EI is from Eq. (16) and is the average flexural rigidity of the composite cantilever beam, and d is given by Eq. (4).

3.2. Electrostatic Actuation.

The electrostatic actuation can be modeled as a parallel plate capacitor. Figure 3.6 shows a simple cantilever beam. The fringing electric fields may be important in these cantilever beams, but since they are difficult to calculate they are neglected. The analysis is still a good approximation even after neglecting these fields [47]. If the beam is treated as a perfect spring then the force balance can be modeled with Eq. (28) [57].

$$K(g_0 - g) = \frac{\epsilon V^2 l b}{2g^2} \quad (28)$$

As shown in Figure 3.6, g_0 is the initial gap, V is the applied voltage, and l is the length of the beam. The symbol K is a lumped mechanical spring constant for the beam material, ϵ is the permittivity of air, b is the width of the beam, and g is the gap between the beam and the ground plane. Solving for deflection d yields:

$$d = (g_0 - g) = \frac{\epsilon V^2 l b}{2g^2 K} \quad (29)$$

The deflection is an elastic process until the gap becomes sufficiently small and the beam becomes unstable. At this pull-in voltage, V_{pi} , the beam undergoes a spontaneous deflection to the lower electrode. The instability occurs when the beam gap, g , approaches $2g_0/3$ [57]. By rearranging (28) we have

$$V_{pi} = \sqrt{\frac{8Kg_o^3}{27\epsilon l b}} \quad (30)$$

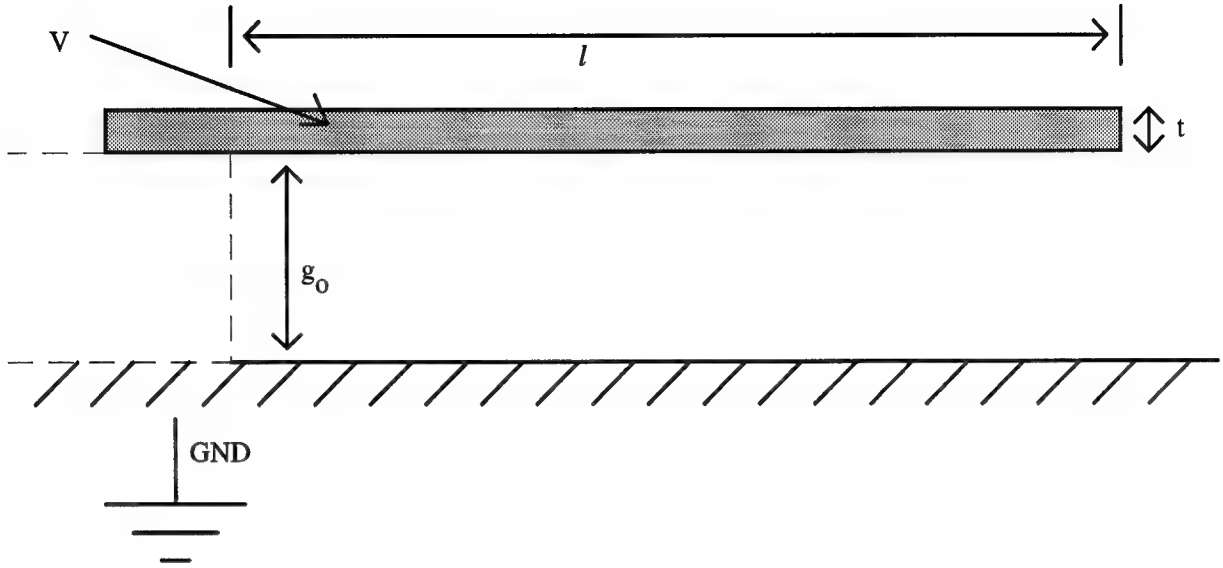


Figure 3.6. Electrostatic cantilever beam.

The force between the beam and the lower electrode (which behaves as plates of a capacitor) can be obtained from (28)

$$F = \frac{\epsilon V^2 l b}{2 g^2} \quad (31)$$

The resonant frequency of the beam may be determined from simple beam theory.

The dynamic response f is given by [58]:

$$f = \frac{3.52}{2\pi l^2} \left(\frac{EI}{\rho b t} \right)^{\frac{1}{2}} \quad (32)$$

Here ρ is defined as the density of the beam. By using Eq. (11), Eq. (32) may be simplified as

$$f = 0.16 \frac{t}{l^2} \left(\frac{E}{\rho} \right)^{\frac{1}{2}} \quad (33)$$

3.3. Design.

In designing tactile stimulators, both the CMOS and MUMPS processes were utilized. Both processes have several limitations which are discussed below. The CMOS process was used as a bimorph process, but did not prove useful for electrostatic actuation. It is ideally suited as a bimorph process since the multiple layers provide a heating resistor and the change in thermal expansion coefficients. Electrostatic actuation is only effective over small gaps as shown in the theory above. Bulk micromachining, which creates large gaps between the released structures and the ground plane, is used in the CMOS process. On the other hand, the MUMPS process is not useful for thermal actuation perpendicular to the plane of the chip, since the process does not allow bimorph sandwich structures. Electrostatic actuation is possible since surface micromachining leaves much smaller gaps than bulk micromachining. Therefore the CMOS designs rely on the multi-morph theory described above and the MUMPS designs rely only on the electrostatic actuation theory.

3.3.1. CMOS Designs. Chapter 1 describes the basic theory behind bulk micromachining and describes the CMOS process. The CMOS process is well suited for bulk micromachining since the fabrication allows cuts to be made through the oxide leaving bare silicon for the bulk etching. The CMOS process for MEMS that is available through MOSIS is a two metal, two polysilicon process. Each layer is encased in oxide which protects it from the etchant during release. The available layers are shown in Figure 3.7.

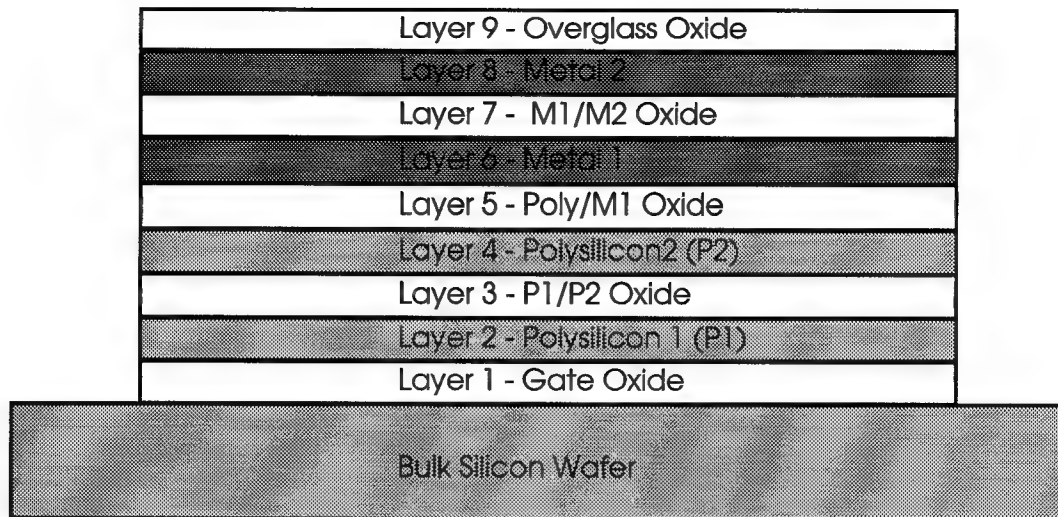


Figure 3.7. Possible layers in a CMOS process available through MOSIS.

Some of the layers shown in Figure 3.7 may be masked to prevent their fabrication. All polysilicon layers must be encased in oxide to protect them from the etchant during micromachining. Table 3.3 lists the available layers, their thicknesses, and if they are maskable.

In developing a CMOS cantilever beam with bimorph actuation principles, heat must be applied in some way. The easiest way to apply heat is to use one of the polysilicon layers as a heating resistor. Either polysilicon layer may be utilized since they are both the same thickness. The oxide encasing the polysilicon resistor prevents it from shorting out with the metal layers. The sheet resistance of the polysilicon is 21 Ohms/Square for P1 and 28 Ohms/Square for P2. Since the resistance of the metal lines is more than four orders of magnitude lower than the polysilicon, then the heat generated due to the metal lines can be neglected.

Table 3.3. CMOS Fabrication Layers Available Through MOSIS [59].

Layer	Thickness (μm)	Maskable
1. Gate Oxide	0.6	No
2. Polysilicon 1 (P1)	0.4	Yes
3. P1/P2 Oxide	0.075	No
4. Polysilicon 2 (P2)	0.4	Yes
5. Poly/M1 Oxide	0.85	No
6. Metal 1 (aluminum)	0.6	Yes
7. M1/M2 Oxide	0.65	Yes
8. Metal 2 (aluminum)	1.15	Yes
9. Overglass Oxide	1.0	Yes

The top view of a basic cantilever beam using bimorph actuation is shown in Figure 3.8. The bare silicon allows the EDP to underetch the beam and release it. The resistor can be either polysilicon 1 or polysilicon 2. Both are connected to metal 1 as the wiring layer. The Pstop layer is boron doped silicon which acts as an etch stop and prevents surrounding structures from being underetched. The beam material can be any combination of the layers given in Table 3.3.

There were several unknown factors at the time of designing the cantilever beams. The designs attempt to experimentally determine this information by using several sets of tests. The tests are to determine the best combination of CMOS layers for bimorph actuation, the optimum size for an actuator, the best heating resistor design, the proper beam support width, if a surrounding wall will protect the structures from contact with the finger, and how micromachined heaters may perform as tactile stimulators. These tests are

described below. Two separate CMOS chips (Traychip 1 and Traychip 2) were designed and fabricated. They both had variations of the test designs.

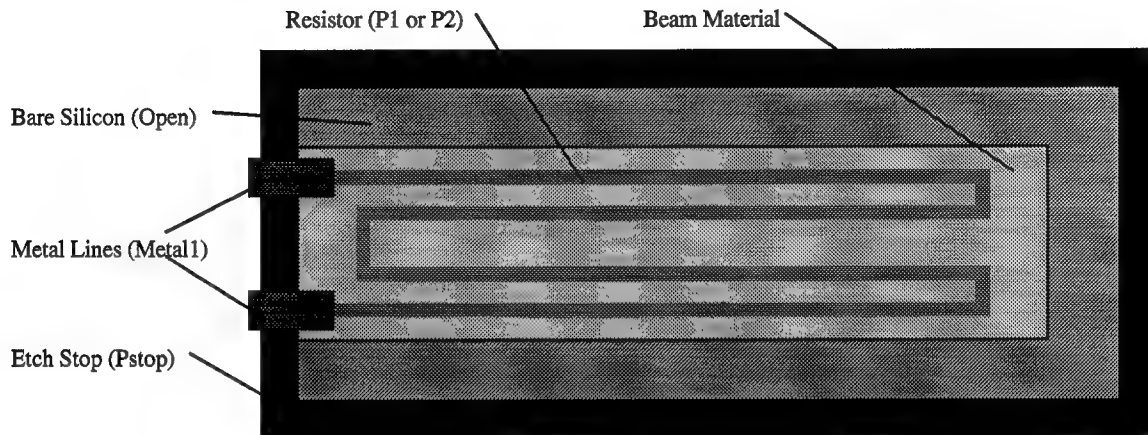


Figure 3.8. Typical CMOS cantilever beam design.

3.3.1.1. Layer Test. In order to determine which combination of layers produces the maximum deflection, sixteen different combinations of the layers in Table 3.3 were used as the beam material. In this set of designs, the lengths, widths, and resistor values of the beams were held constant. This insures that the beam deflection is completely dependent on the combination of the layers forming the beam.

Table 3.4 lists the combinations of layers used for the layer test for the two chips. The table also lists the theoretical deflection value based on a change in temperature, defined in Kelvin, K . This deflection is obtained from Equations (4) and (22). As described above, negative values indicate deflection out of the substrate plane and positive deflections indicate movement towards the substrate. Length is held constant at $300\text{ }\mu\text{m}$ for all the beams. The values for Young's modulus and coefficient of thermal expansion

for each layer are given in Table 3.1. Without control of the layer thicknesses in the CMOS process available through MOSIS, these are the only deflections possible.

Table 3.4. Different Layer Combinations Used in CMOS Designs.

Beam Number	CHIP 1 Layers	Deflection ($\mu\text{m}/\Delta\text{K}$)	CHIP 2 Layers	Deflection ($\mu\text{m}/\Delta\text{K}$)
1	1,3,4,5,6,7	0.1316	1,3,5,7,9	0
2	1,2,3,5,7,8	0.323	1,2,3,5,7,9	-0.0157
3	1,3,4,5,7,8	0.327	1,3,5,7,8	0.4102
4	1,3,5,6,7,8	0.303	1,2,3,5,6,7,9	0.010
5	1,2,3,5,6,7,8	0.267	1,2,3,5,7,8,9	0.094
6	1,3,4,5,6,7,8	0.269	1,3,5,6,8	0.465
7	1,2,3,5,6,7	0.129	1,2,3,5,6,8	0.402
8	1,3,5,7,8	0.4102	1,2,3,5,6,7,8	0.267
9	1,3,5,6,7	0.1426	1,3,4,5,6,7,8	0.269
10	1,3,4,5,7,9	-0.0147		
11	1,2,3,5,7,9	-0.0157		
12	1,3,5,7,9	0		

3.3.1.2. Size Test. The second major design question involved what size to make the cantilever beam. Both CMOS test chips contain beams of various lengths. The theory developed earlier indicates that the width of the beam does not influence deflection if it is held constant for all layers in the beam and that the deflection is

proportional to the square of the length of the beam. The experimental test of this theory involved designing many arrays of beams containing the same layers and widths, but of different lengths. The lengths were varied in increments of 50 μm from 180 μm to 430 μm . A few designs contained variations of beams with different widths and constant lengths. All of the beam designs for this test are similar to the example beam given in Figure 3.8, except that the lengths, widths, or layers were varied in different arrays to determine which size is optimum for a tactile stimulator.

3.3.1.3. Resistor Test. The bimorph theory developed earlier assumes a uniform distribution of heat along the entire cantilever beam and throughout all the layers. The resistor embedded in the beam shown in Figure 3.8 is used to provide this uniform distribution. The third test was to determine how the deflection is affected by changing the distribution of heat. This was done by changing the location of the heating resistors and their shapes. A sample of the designs in this test is shown in Figure 3.9. The understanding of heat distribution is complicated by the fact that the resistor value changes as the temperature increases in the beam. In Figure 3.9, the white indicates the beam material and the embedded resistors are simply drawn on the beams. One series of beams shown in Figure 3.9 puts a smaller resistor at the tip, middle, and base of the beam. A second series uses several different combinations of resistor densities to test heat uniformity as density increases. The third series of beams makes large changes in the resistor values to determine how current flow affects the resistor.

3.3.1.4. Support Test. Another important factor is the stiffness of the beam material. If the material is stiff, what is the optimum beam support needed for a tactile stimulator that makes the beam strong and allows for high deflections. To determine this information, several beams were designed. A sample is shown in Figure 3.10.

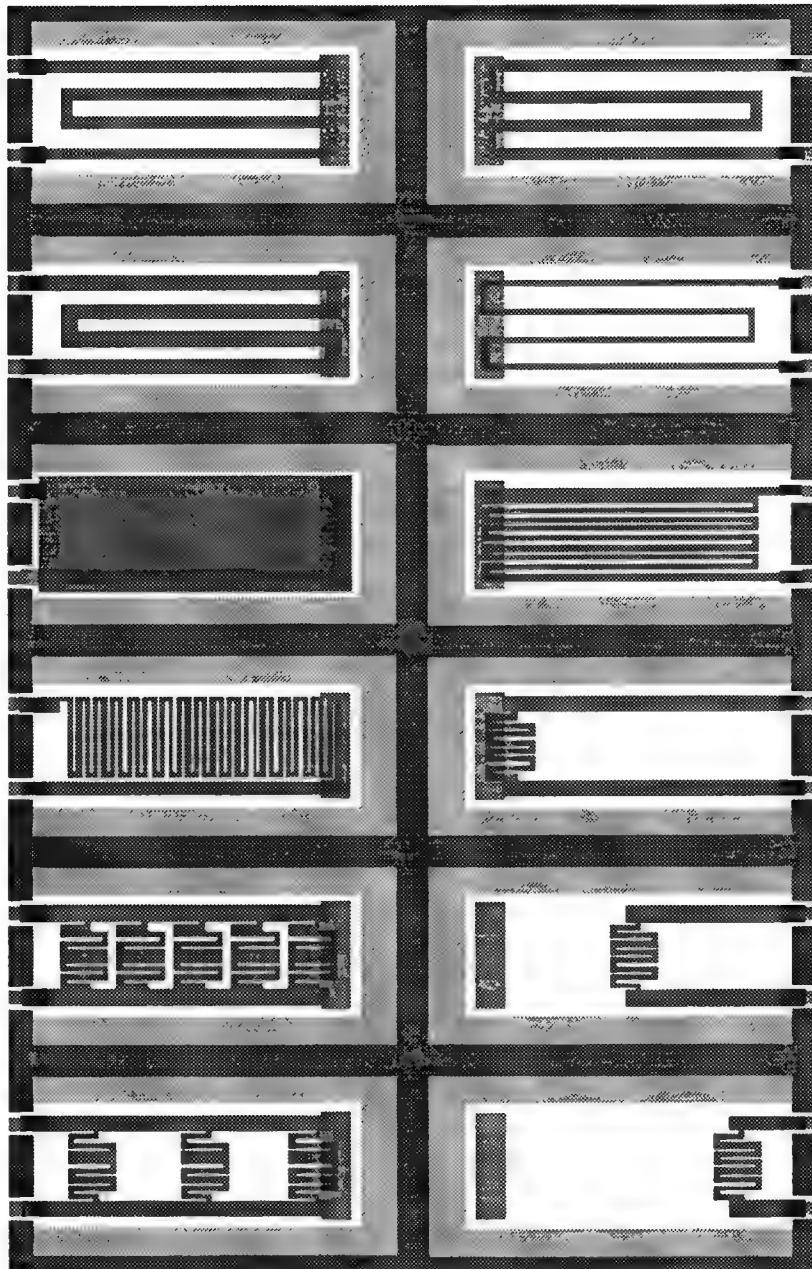


Figure 3.9. Resistor variations in cantilever beams.

This figure shows that the structural support of the beams was decreased by removing some of the material near the base. Different lengths and widths of the support "legs" were varied for the experiment.

3.3.1.5. Wall Test. One problem with using the CMOS cantilever beams as tactile stimulators may be the shear forces from the applied finger. In order to lessen this, a test set of beams was designed surrounded by walls built of all the possible layers. The finger should rest on this wall, and do less damage to the beam. This design uses the basic beam shown in Figure 3.8 and simply surrounds it with both polysilicon and metal layers.

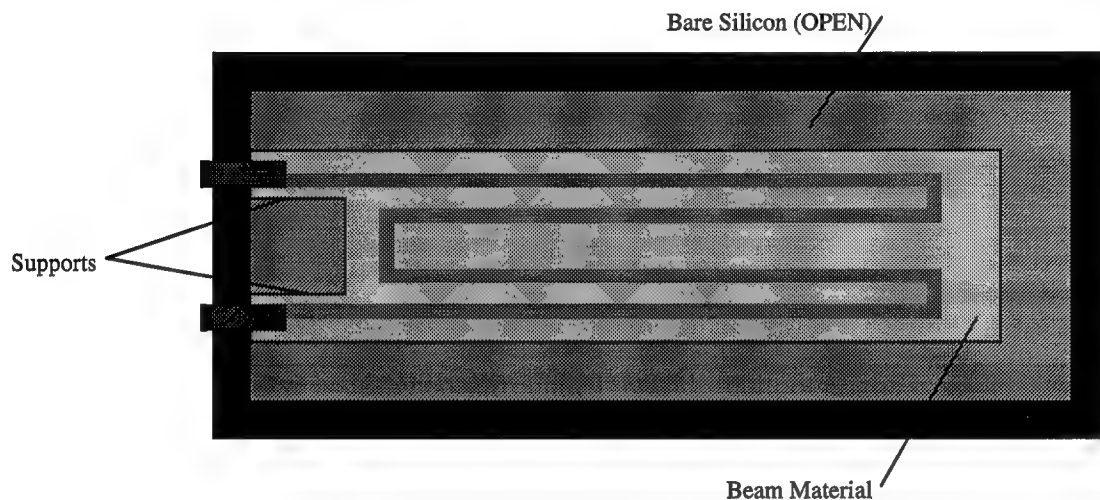


Figure 3.10. Structural support variations in cantilever beams.

3.3.1.6. Heater Test. The final test for the CMOS chips was to determine if finger stimulation could be achieved thermally. Many arrays of thermal elements were designed to heat the finger. A typical heating device is shown in Figure 3.11. The oxide makes up the structural material and the open areas mark the pits to be etched to undercut the heating element. These heating elements should help determine the heat resolution of the finger and the temperature required for stimulation.

3.3.2. MUMPS Designs. The MUMPS process and surface micromachining are discussed in detail in Chapter 1. The process is a three polysilicon, one metal process with two sacrificial layers of oxide. Bimorph beams are not nearly as feasible in this process, so all the designs use electrostatic forces.

The layers available in the MUMPS process are shown in Figure 3.12. The figure also gives the thicknesses of the individual layers. All of the layers in this process can be selectively masked, unlike in the CMOS process.

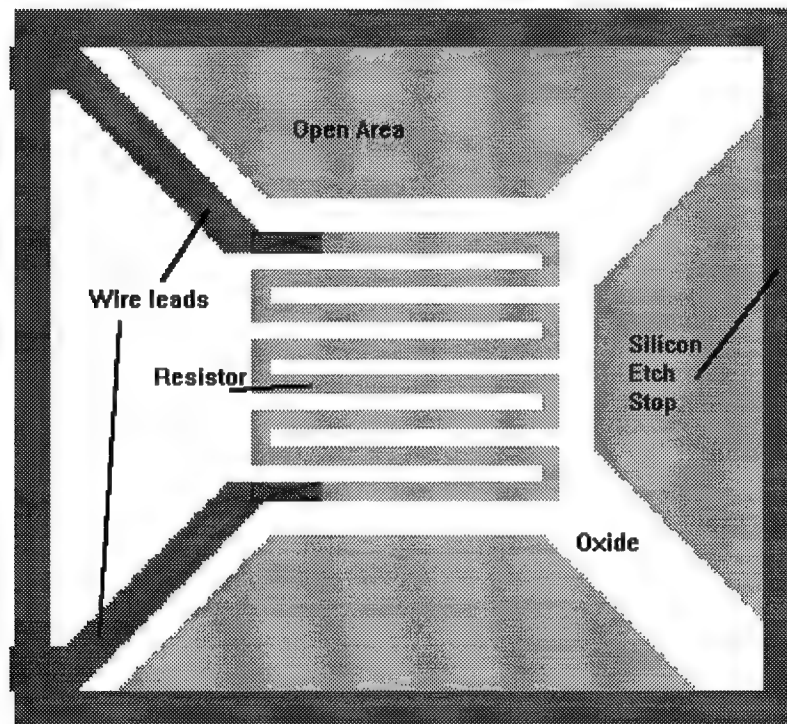


Figure 3.11. Typical heating CMOS element.

There were many different electrostatic actuators developed based on this process and they are shown below. The designs include attractive and repelling cantilever beams, arching devices, and flexure beams.

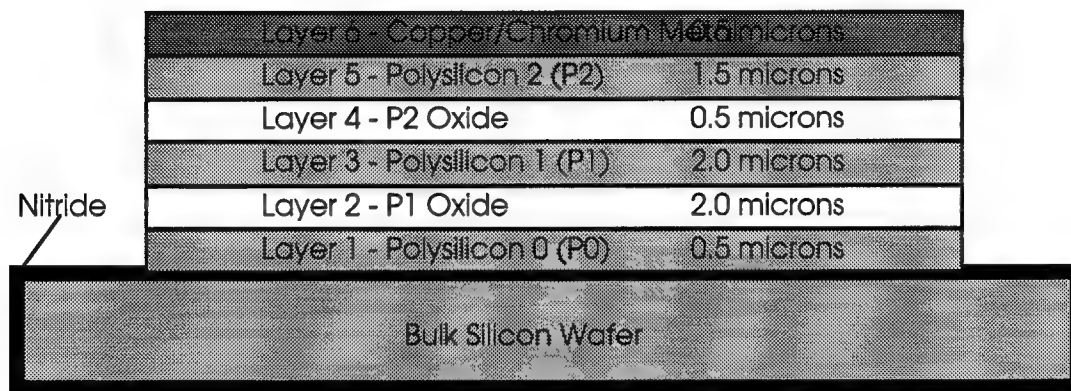
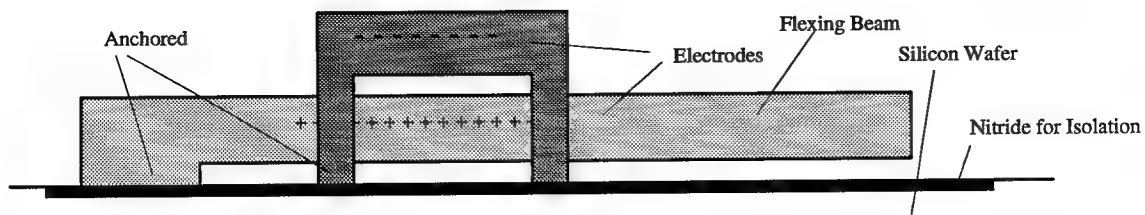
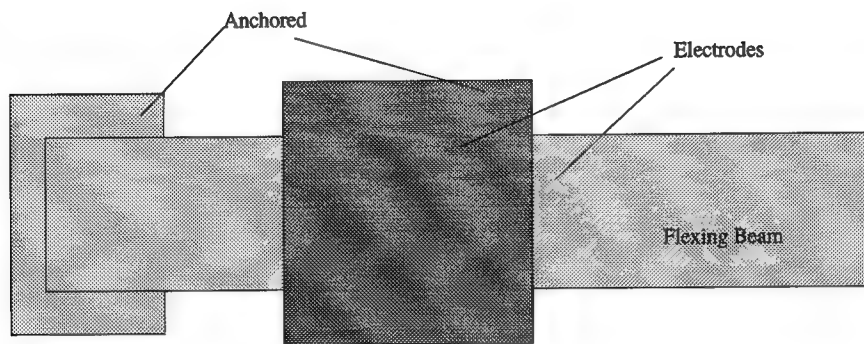


Figure 3.12. Layers and thicknesses in the MUMPS process.

3.3.2.1. Electrostatic Attraction Test. The first major test is to characterize the cantilever beams that use electrostatic attraction. The basic cantilever beam is shown in Figure 3.13. Many variations of this example were designed. The designs examine different lengths of the cantilever beam, different amounts of structural support, and different amounts of surface area for the upper electrodes since the amount of attraction is dependent on the surface area and the voltage applied. Since no current should flow, the polysilicon structures may serve as the electrodes.



(a) Side view of electrostatic attraction beam



(b) Top view of electrostatic attraction beam

Figure 3.13. Typical cantilever beam using electrostatic attraction forces.

3.3.2.2. Electrostatic Repelling Test. The second MUMPS test is to determine if a cantilever beam can be operated using electrostatic repulsion forces. In theory, if like charges are near each other they will repel. In order to design a cantilever beam that operates on this principle, the similar charges must be relative to a local reference potential. A sample design using this principle is shown in Figure 3.14. Since there is a common reference potential at the substrate, the similarly charged electrodes will repel and the flexing beam will curl up. The amount of force decreases with the square of the distance between the electrodes, so very little movement is possible with this design. Also, since the MUMPS process completely encases the substrate wafer in nitride, it is very difficult to obtain a good substrate contact for the reference voltage.

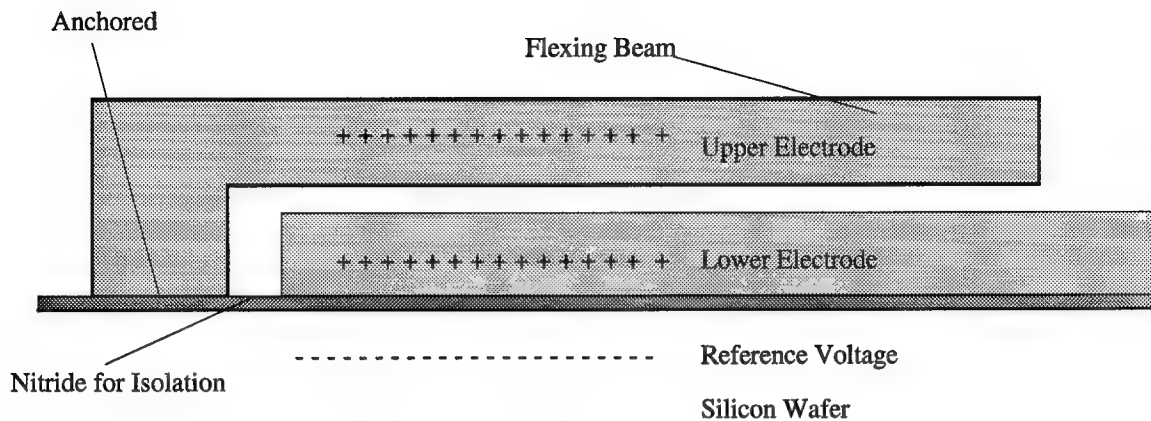


Figure 3.14. Side view of a typical cantilever beam using electrostatic repelling forces.

3.3.2.3. Comb Arch Test. Since the amount of force is dependent on the surface area available to the two electrodes, a comb design like that shown in Figure 3.15 will produce large forces. This design relies on the comb to produce the force. The motion of the free comb will be to the right and this will cause the thin polysilicon 2 arm to arch upward. The middle of this arm deflects vertically causing the actuating plate to contact with the finger. The anchored comb is charged through the positive contact shown in Figure 3.15 and the negative contact charges the moving polysilicon comb. The polysilicon arch acts as a spring to counteract the electrostatic force on the comb. This should prevent the two contacts from touching and shorting out the device. Different widths of polysilicon 2 arms were designed to determine the flexibility of the material. Also, some steps were designed into the polysilicon 2 arm to pre-bow it upward and insure movement out of the plane of the substrate.

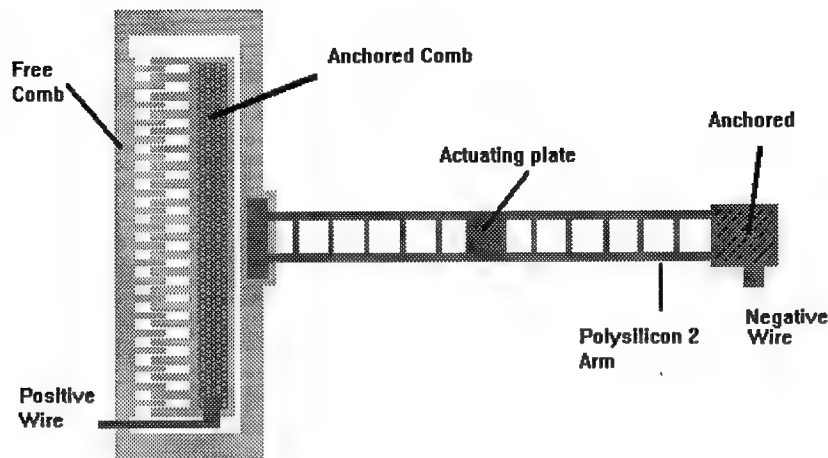


Figure 3.15. Typical comb driven arching beam.

3.3.2.4. Flexure Test. The next test involves a flexing beam. A sample beam is given in Figure 3.16. The light colored polysilicon is released and is only connected to the support posts through the flexure arms. The beam is actuated by applying voltage to the two attached electrodes. This causes the two actuating plates on the left side of the beam to attract and lift the actuating tip on the right. A landing electrode was designed into the system to prevent the two actuating plates from shorting out. Many different variations of flexing arms were designed to determine which arm requires the least voltage for actuation and which arm provides the most strength.

3.3.2.5. Heater Test. The final test involves designing many different heating elements. This test is very similar in objectives to the CMOS heater test. The black marks in Figure 3.17 indicate where the gray polysilicon is connected to the substrate. By elevating the polysilicon and lessening the heat path to the substrate, the element should heat faster than if it was resting on the substrate.

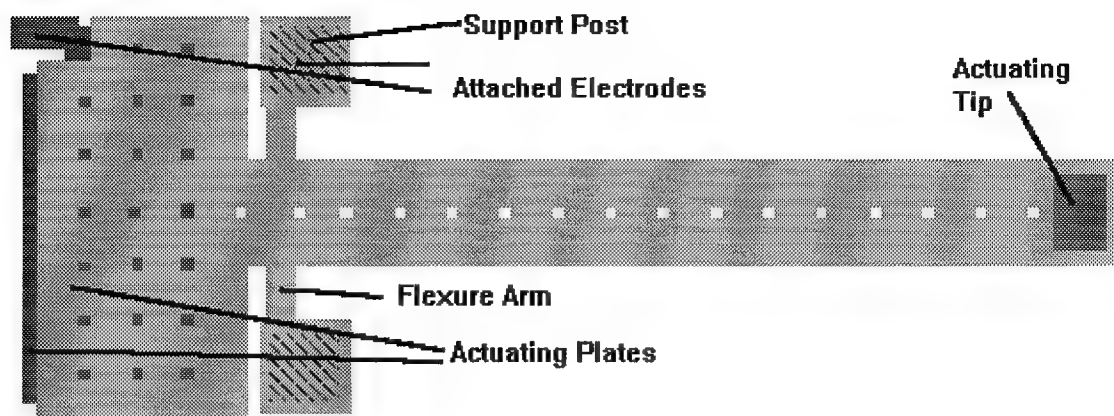


Figure 3.16. Typical flexure beam.

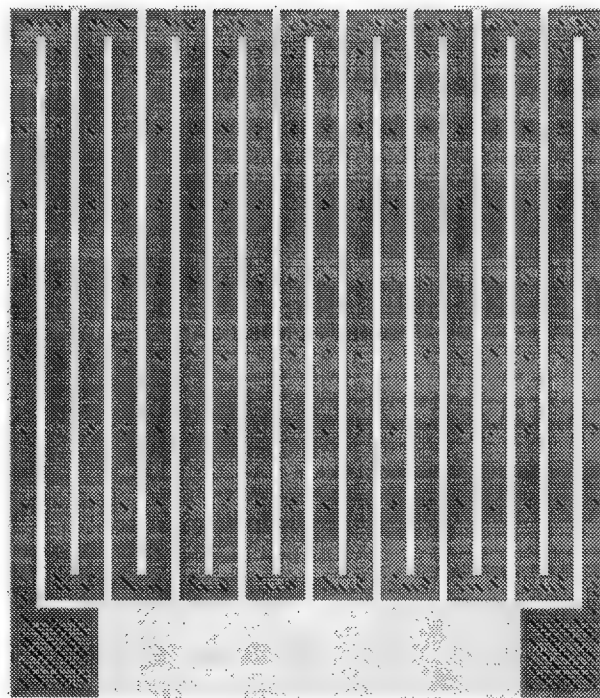


Figure 3.17. Typical heating element.

3.4 Conclusions.

This chapter reviewed the theory behind multi-morph systems and electrostatic actuation. The thermal properties of the MEM devices was discussed. Finally the MUMPS and CMOS designs were reviewed.

4. EXPERIMENTAL PROCEDURE AND ANALYSIS OF RESULTS

This chapter reviews the experimental procedures used in testing the MEM designs presented in Chapter 3. This includes fabrication, etching, bonding, deflection measurements, and force testing. Deflection measurements were taken with the micromanipulator station and the Air Force Institute of Technology (AFIT) laser interferometer probe. Force measurements were obtained with a force applying device designed at AFIT. The data from these tests are analyzed and presented in this chapter.

4.1. Fabrication.

All three chips (Traychip 1, Traychip 2, MUMPS 4) were designed using the MAGIC layout tool. Two separate technology files were created, which allowed both CMOS and MUMPS structures to be designed. The major changes to the technology files were to add the appropriate layer names and remove the design rule checking. The results of each of the designs are presented below.

4.1.1. Traychip 1 Fabrication. The first CMOS chip was designated Traychip 1. It was designed using MAGIC with the MEMS technology file. The designs in the seven test sets on this chip are described in Chapter 3. There are over 200 separate devices on each copy of Traychip 1. The CIF file describing the chip was submitted to MOSIS for fabrication on 27 April 1994. The chip is shown in Figure 4.1.

4.1.2. Traychip 1 Fabrication Results. The completed chip was returned in early July. Twenty-eight copies of the chip were returned. The quality of the MOSIS fabrication was generally good, but there were a few problems with some of the designs on the chip. The majority of the devices were fabricated as described in the CIF file, but

the wall test described in Chapter 3 was not releasable. The fabrication problem resulted in the poor etching of the OPEN layers described in the CIF file. Some glass remained along the edges of the beams hampering the etch process.

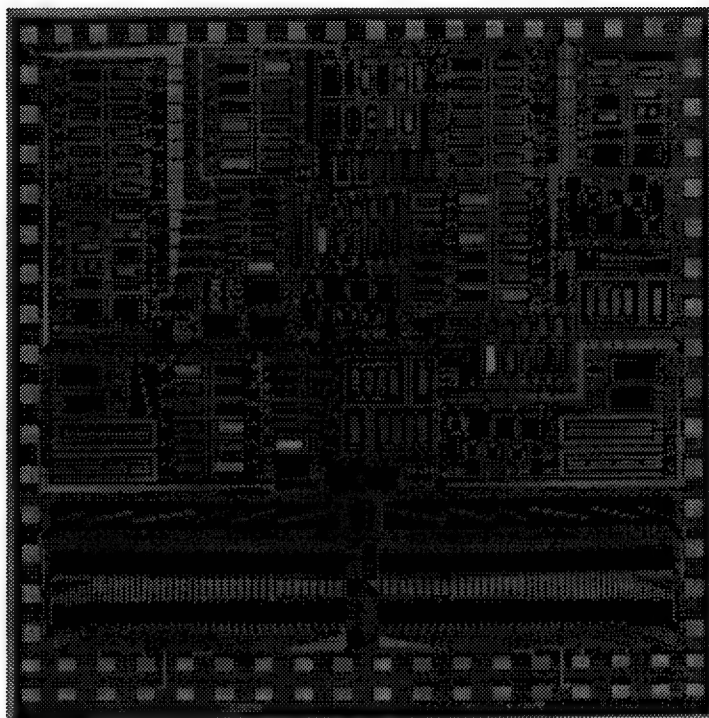


Figure 4.1. Optical photograph of Traychip 1 after MOSIS fabrication and before etching.

Since the beam will not release without bare silicon on its three sides, the wall test structures were not releasable. The undesired glass along the edges did have some pin holes which allowed some of the etchant to get through, but not enough to free the beam from the silicon substrate. Figure 4.2 is a scanning electron microscope (SEM) close up of the poorly etched glass along the side of one of these beams. The black squares in

Figure 4.2 are caused by pin holes in the oxide. As described in Chapter 1 the etchant works faster along lower index crystal planes and the pin holes produce square shaped pits of etched silicon. The light gray in the figure is the silicon substrate with oxide covering it. If the fabrication had gone well, the entire length of the figure would be free of oxide allowing the etchant to remove all the silicon along the edge of the beam and beneath it.

Although only the wall test beams were not releasable, all of the chip had poorly fabricated OPEN layers. This causes small amounts of oxide to remain along the wall of the etch pit and on the structures. Figure 4.3 shows a MEM device that has small amounts of oxide along its perimeter and at the edges of the etch pit.



Figure 4.2. SEM micrograph of poorly etched oxide due to fabrication defects.

Another problem with Traychip 1 was the result of faulty design. In order to reduce the number of bond pads and allow more MEM devices to be connected to the bond pads at the edge of the chip, wiring lines were reused. The problem with this method is that electrically the MEM devices consist of simple resistors. This caused all of the devices to be connected. The result is that when voltage is applied, the device, that electrically heats fastest will actuate. Since each of the devices was designed with local

probe pads, the problem could be fixed by isolating each of the test structures. This was done by cutting the wiring lines with the ultrasonic cutter on a micromanipulator station. By doing this, only one out of every four devices could be actually bonded, but all of the devices could be probed locally.



Figure 4.3. SEM micrograph of poorly defined OPEN layer after release on Traychip 1.

4.1.3. MUMPS 4 Fabrication. The second chip, designated MUMPS 4, was also designed using MAGIC. The MUMPS rules described in Chapter 1 were used in design and the chip was submitted to MCNC for fabrication on 1 May 1994. The devices on this chip were variations of five basic designs described in Chapter 3. There are more than 325 variations of the five basic designs for a total of over 500 devices per chip.

Figure 4.4 shows the entire chip after fabrication, but before etching.

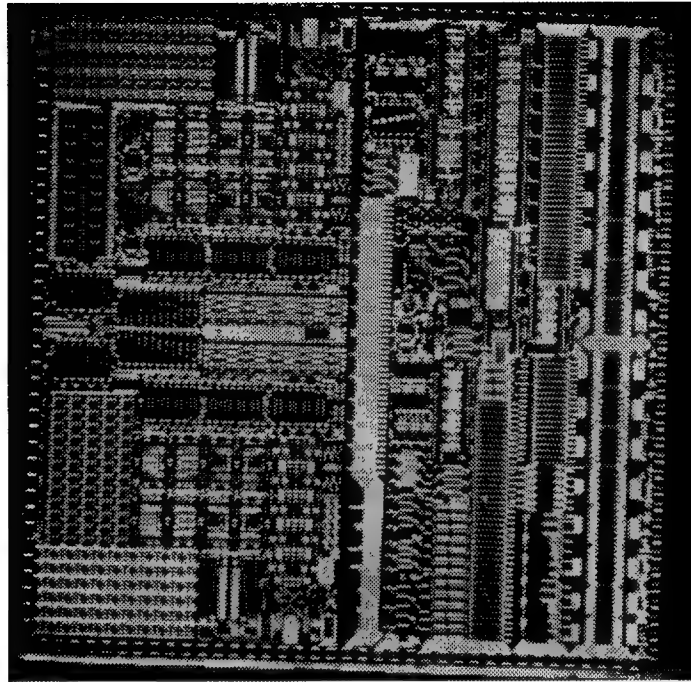


Figure 4.4. Optical photograph of MUMPS 4 chip after fabrication and before etching.

4.1.4. MUMPS 4 Fabrication Results. The chips were returned in mid July 1994. The fabrication results matched the designs, and over 45 copies of the chip were returned. The only fabrication problem was the poor choice of metals used in the metal layer. The previous MUMPS processes used aluminum for the metal, but the HF used to release the devices damaged the aluminum. In this fabrication run, a copper/chromium combination was used for the metal layer. It holds up during the HF etch, but tends to corrode over time due to humidity. If the pads are bonded soon after etching the connection will be good, but the metal used as mirrors on the devices and metal lines connecting the devices will start corroding after more than a week.

4.1.5. Traychip 2 Fabrication. The third chip, designated Traychip 2, was also a CMOS design. It contained over 330 different devices. The wiring problem of the Traychip 1 design was corrected on the Traychip 2 design. The CIF file was submitted to MOSIS on 27 July 1994. The chip is shown in Figure 4.5.

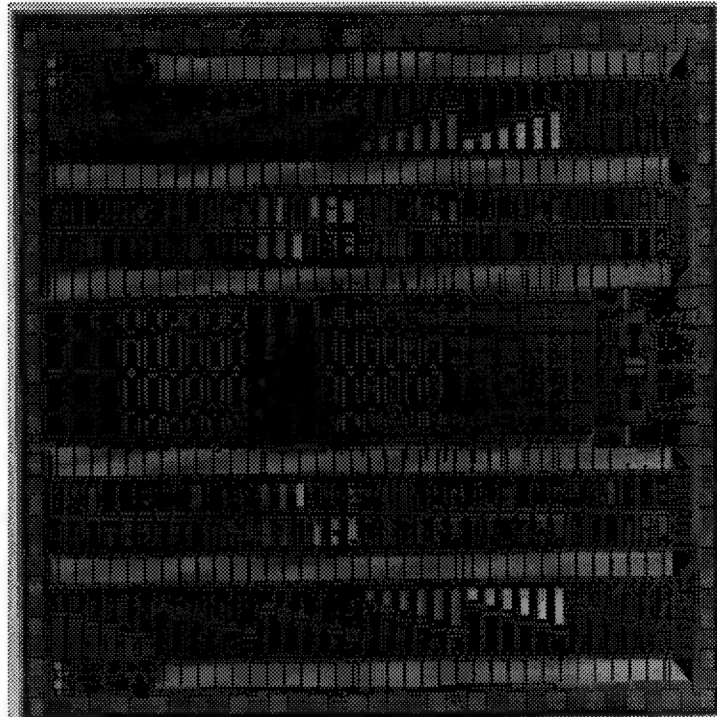


Figure 4.5. Optical photograph of Traychip 2 after MOSIS fabrication and before etching.

4.1.4. Traychip 2 Fabrication Results. Traychip 2 was returned on 1 Oct 1994. The fabrication was a failure. None of the OPEN layers were fabricated correctly and the sides of all the beams had glass covering the silicon. Figure 4-6 shows the extent of the problem. The light gray at the end of each beam is the bare silicon. The darker area along the sides of the beams is the oxide.

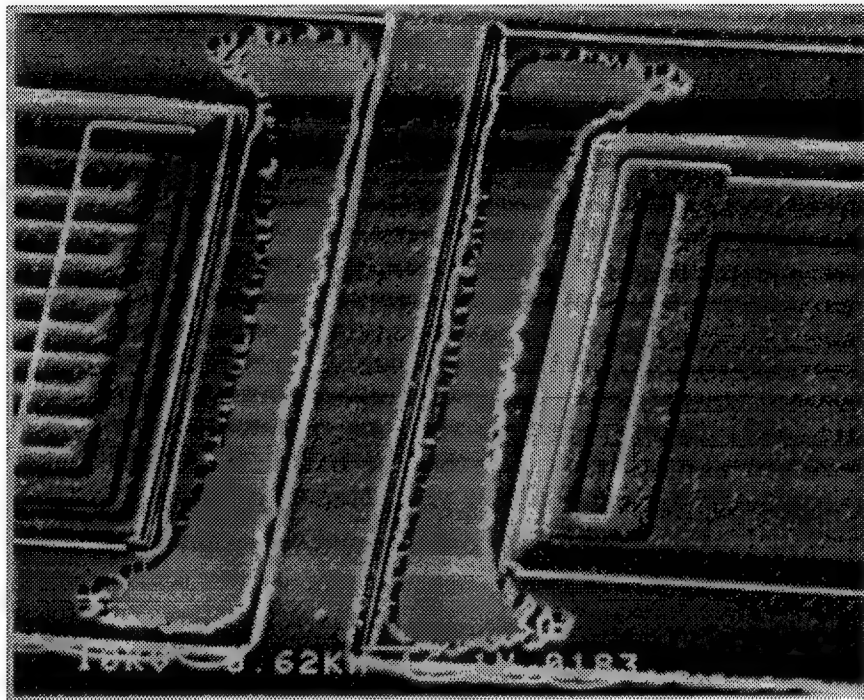


Figure 4.6. SEM micrograph of poor quality OPEN layer cut on unreleased Traychip 2.

Since the devices could not be released, none of the devices on Traychip 2 could be tested. Attempts were made to remove the unwanted oxide with HF, but the structural oxide on the beams was removed before the undesired oxide over the OPEN areas. The thickness of this undesired oxide was approximately $1.3\text{ }\mu\text{m}$ which is nearly as thick as the desired layers of oxide. The MOSIS service has been notified and they are attempting to determine the cause of the poor fabrication and a solution so that future runs are more successful

4.2. Etching Procedure.

The CMOS and MUMPS etching procedures were developed and tested at AFIT before this work. At least one test chip from both processes has been released and the

equipment and chemicals needed have not changed. Nevertheless, the tactile stimulator designs are much larger than the previous test designs. Thus, the etch times for both processes had to be obtained experimentally. The procedures are explained below.

4.2.1. CMOS Etch Procedure. As discussed in Chapter 1, ethylene diamine pyrocatechol (EDP) is an anisotropic etchant used for bulk micromachining. It is made by Transene co. and is 60% ethylene diamine 10% pyrocatechol and 30% DI water. The EDP is used at 100 °C and requires some fluid agitation to react properly. The EDP evaporates quickly under these conditions, so to limit waste and to contain the hazardous vapors the etch is done in an enclosed container. To achieve these conditions the etching apparatus shown in Figure 4.7 was devised.

The hot plate keeps the water bath and the EDP at 100 °C. The hot plate also provides the agitation through a magnetic stir bar in the bottom of the large beaker. The stirring bar is separated from the wafer holder by a second, smaller beaker. The small beaker has holes drilled in the bottom to allow the EDP to circulate. The thermometer helps monitor the accuracy of the temperature in the EDP. Finally, the wafer holder is a small plastic container with small holes in the top and bottom. The holes allow EDP circulation, but are not large enough for the chips to fall out.

The entire chemical procedure for releasing a typical CMOS chip is presented next.

1. Dip the chip in a 10:1 Deionized (DI) water:HF bath for 10 seconds.
2. Rinse chip in DI for 60 seconds.
3. Etch chip at 100 °C in EDP for approximately 135 minutes.
4. Rinse chip in DI for 60 seconds.
5. Rinse chip in methanol for 60 seconds.
6. With chip in a pool of methanol, heat in oven for 5 minutes at 100 °C.

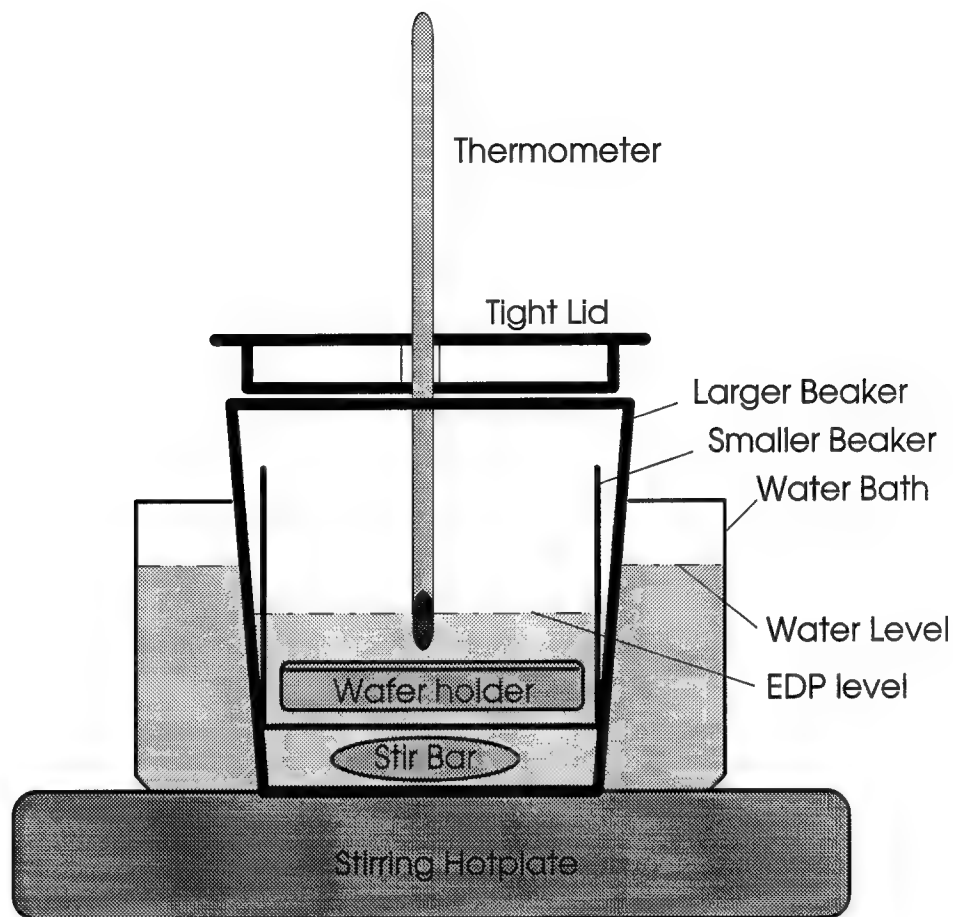


Figure 4.7. EDP etching apparatus for CMOS chips.

The initial dip in diluted HF removes any native oxide that may have formed over the open areas after fabrication. Given time, native oxide will form over any exposed silicon surface. The HF effectively removes this without damaging the structural oxide of the chip.

The etch time in the EDP depends on the size of the devices being released. For 300 μm long beams, this was approximately 135 minutes. An etch gauge was designed and put on the chip to determine the etch rate. It consists of an array of oxide beams (no

metal or poly) with varying lengths from the smallest releasable device to the largest. Since oxide is transparent and smooth silicon reflects light well; the beam will reflect before etching. During the etching process silicon will be removed and no light will reflect. This is shown in Figure 4.8. The white triangle in Figure 4.8 is unetched silicon under the light gray oxide beam. The black is the etched pit. The silicon under the oxide beam is shown in Figure 4.9 which is an SEM of the same chips with the oxide beams broken. Precise control of the etch rate can be obtained by using these etch gauges.

The methanol rinse is used to prevent the MEM structures from sticking to the substrate. This occurs when water is left on the chips. The methanol removes any DI water and then evaporates quickly in the oven.

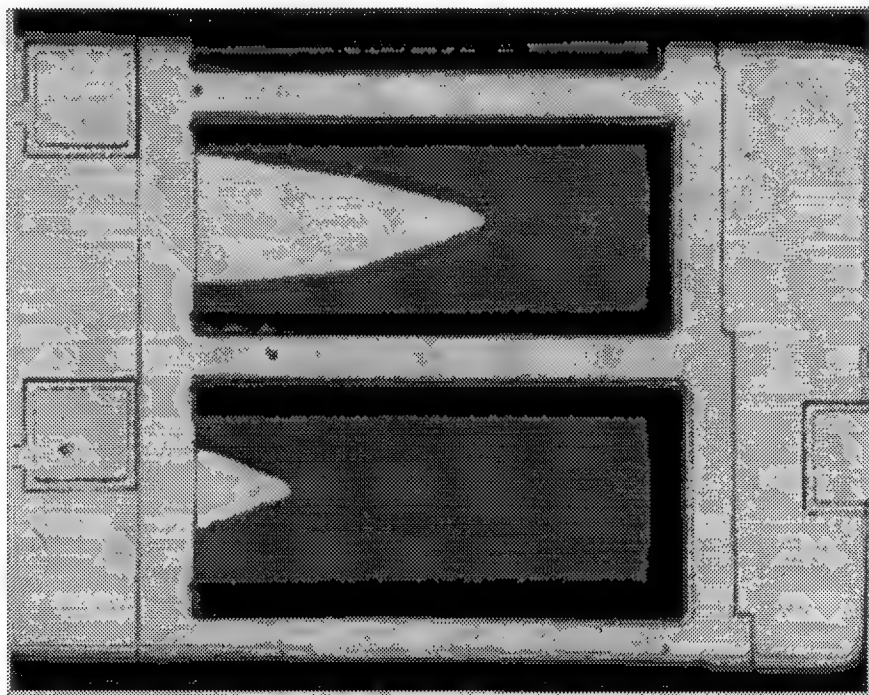


Figure 4.8. Optical photograph of the partially released etch gauge.

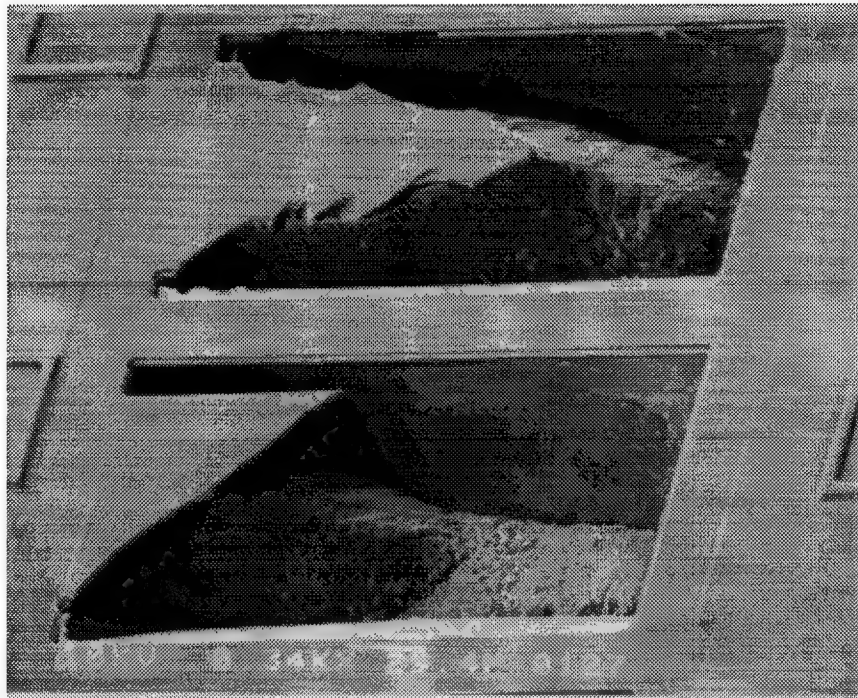


Figure 4.9. SEM micrograph of the etch gauge with broken oxide beams showing the partially etched silicon beneath.

4.2.2. CMOS Etch Results. The procedure given above works very well. Only a small amount of EDP is consumed, the chips are protected during release, and the etch rate can be monitored efficiently. All of the devices released well. A large portion of the released chip, Traychip 1, is shown in Figure 4.10.

Bimorph beams consistently experience some curling due to internal stress [16]-[17]. The internal stress is noticeable when the silicon substrate beneath the devices is removed and the beam is released. The amount of cantilever beam curling exhibited on Traychip 1 depends on the beam materials used and varies from nearly flat to over $50\text{ }\mu\text{m}$ out of the substrate plane for a $300\text{ }\mu\text{m}$ long beam. This curling can be seen in Figure 4.11.

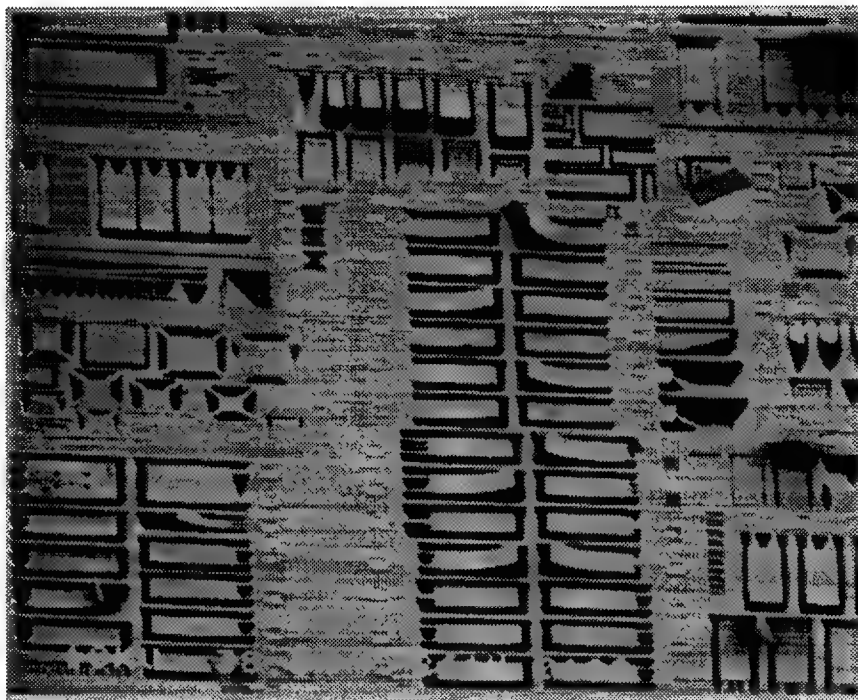


Figure 4.10. SEM micrograph of a portion of Traychip 1 after EDP etching.

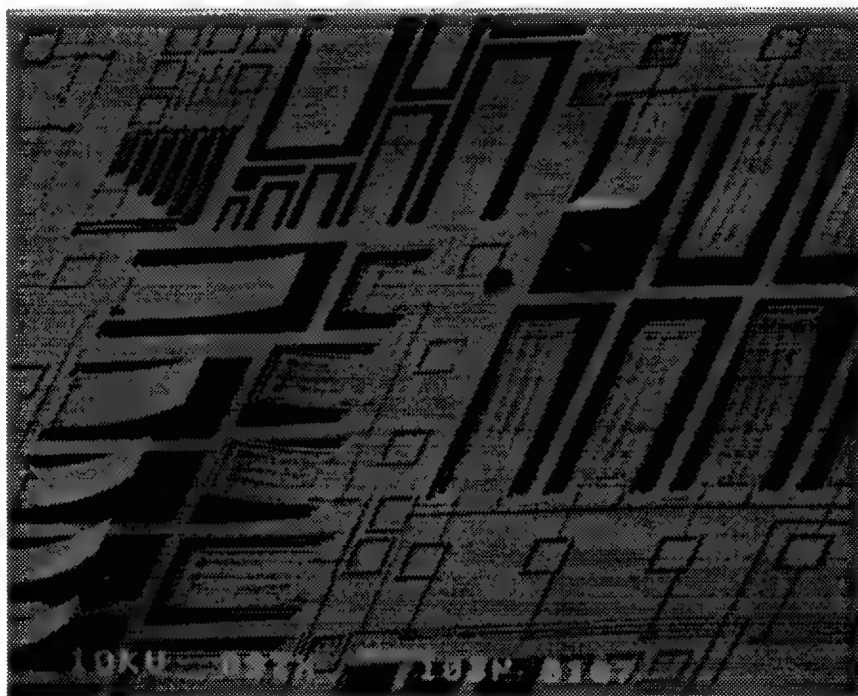


Figure 4.11. SEM micrograph of stress induced curling of cantilever beams on Traychip 1.

The EDP causes an inverted pyramid to be etched out of the silicon substrate as explained in Chapter 1. This can be seen in Figure 4.12, which shows one of the heating elements described in Chapter 3. The walls of the etched pit can be seen on the right of the micrograph. The embedded resistor is clearly evident in the middle of the X structure.

None of the devices from Traychip 2 released due to the fabrication problem described above. Overetching was attempted on these chips, but with poor success. The bond pads at the edge of the chip were destroyed because the EDP etched the silicon from the sides of the wafer.

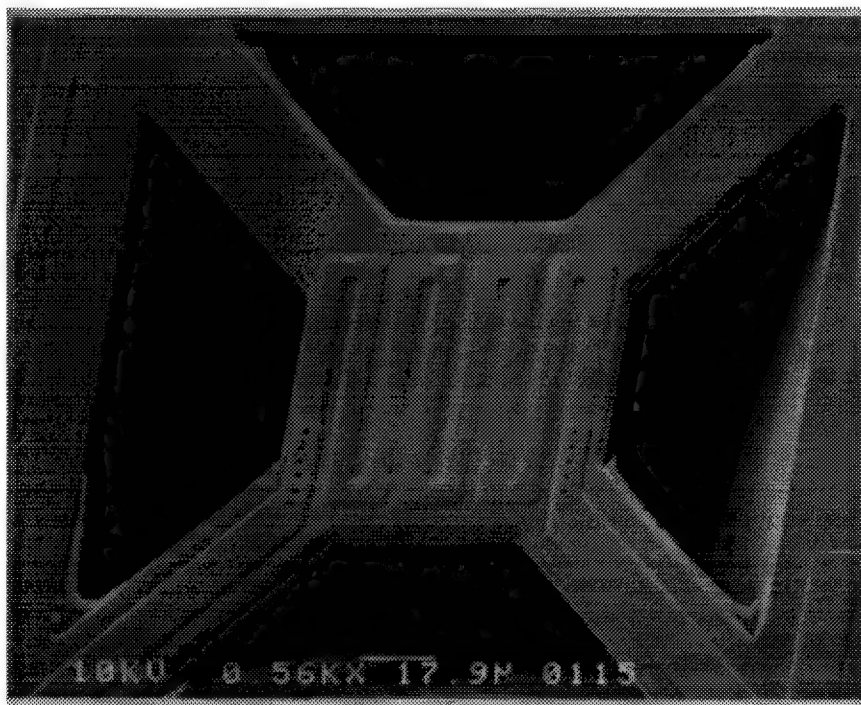


Figure 4.12. SEM micrograph of a released heating device from Traychip 1 showing the etched pit.

4.2.3. MUMPS Etch Procedure. Chapter 1 describes the theory behind surface micromachining. Since the sacrificial layer is oxide, HF is used to remove it completely. The procedure is given below.

1. Dip chip in acetone for 60 seconds.
2. Rinse chip in DI water for 60 seconds.
3. Dip chip in strait 49% HF for 90 seconds.
4. Rinse chip in DI water for 120 seconds.
5. Bath chip in methanol for 120 seconds.
6. With chip in a pool of methanol, heat in oven at 100 °C for 5 minutes.

The acetone removes the final photoresist layer remaining after fabrication. The HF acid removes all the sacrificial oxide in 90 seconds. Heat is not required for this etch process, but care must be taken to insure only plastic containers and equipment are used with the HF. Since HF attacks glass, any glass container would be destroyed.

4.2.4. MUMPS Etch Results. The etch procedure works very well with all sizes of MEM devices, therefore no etch gauge is needed. Since there were several annealing stages in the fabrication process, there is no stress-induced curling of the devices. The separation between substrate and the released devices is small. The mumps devices are very susceptible to sticking to the substrate if not dried properly, therefore, steps 5 and 6 of the etch procedure are very important.

Sample devices are shown in Figures 4.13 through 4.16. All of these devices are described in Chapter 3. Figure 4.13 shows an electrostatic attraction beam. Figure 4.14 is the electrostatic repelling beam. Figure 4.15 is the flexing beam and Figure 4.16 is the arching beam.

4.3. Bonding Procedure.

Initial testing was performed on the micromanipulator station by probing the individual device bonding pads with an input signal. This procedure is time consuming and error prone. The probe tips contact the bond pads by pressing into the metal and dragging along, thereby digging a groove in the metal. To check for a good contact on the bimorph beam probe pads a simple resistance check can be done. Low resistance (~50 Ohms) indicates a good contact. The MUMPS chips are electrostatic and do not have current paths between the pads, therefore, it is difficult to tell when a good connection is made. Once the connection is made, care must be taken to prevent the chip and probes from moving. If either of the two move, contact will be broken.

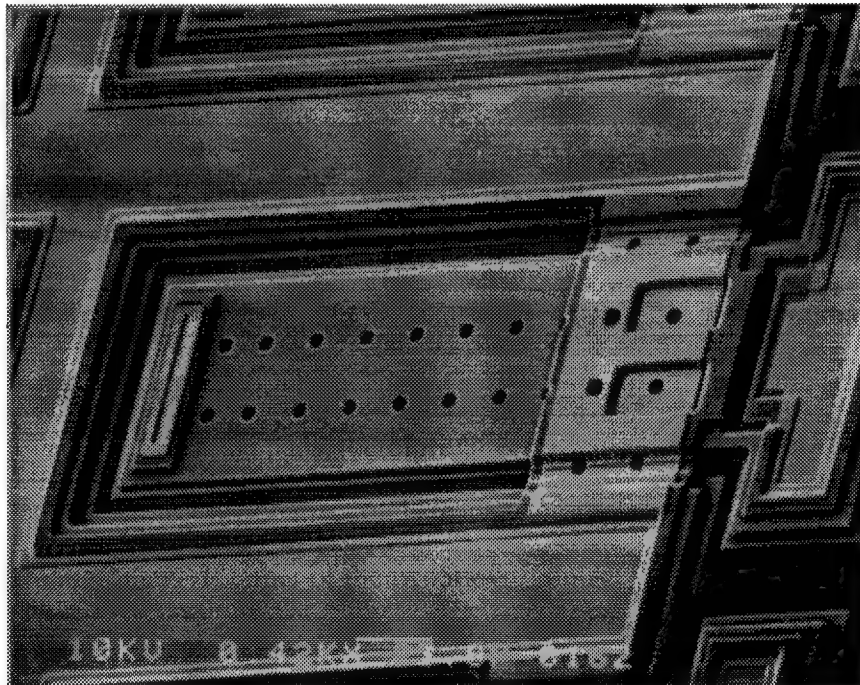


Figure 4.13. SEM micrograph of a released electrostatic attraction beam from MUMPS 4 chip.

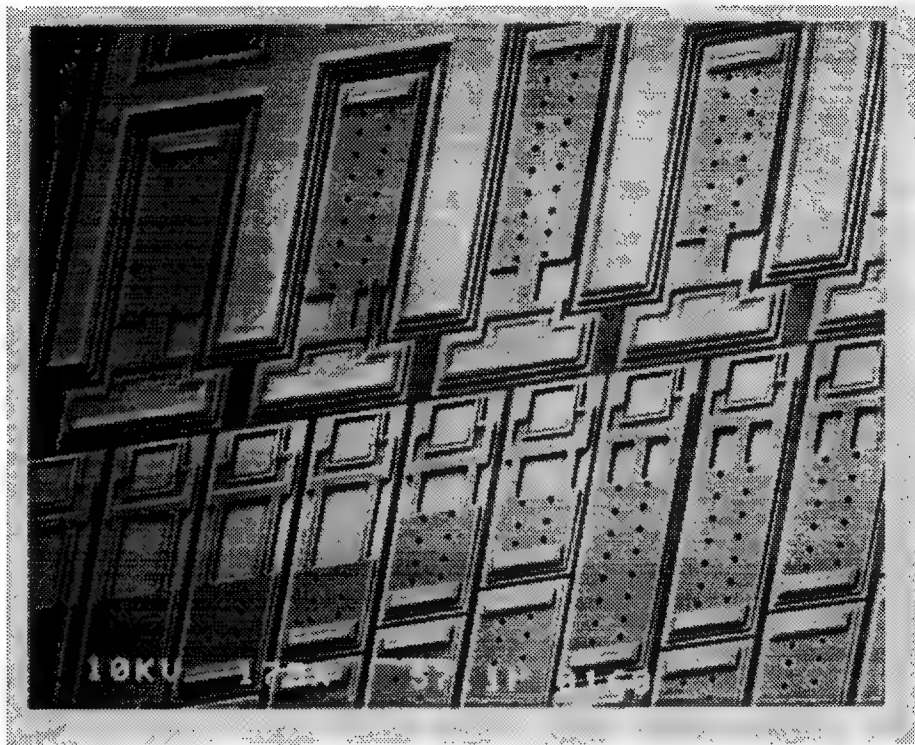


Figure 4.14. SEM micrograph of a released electrostatic repelling beam from MUMPS 4 chip.

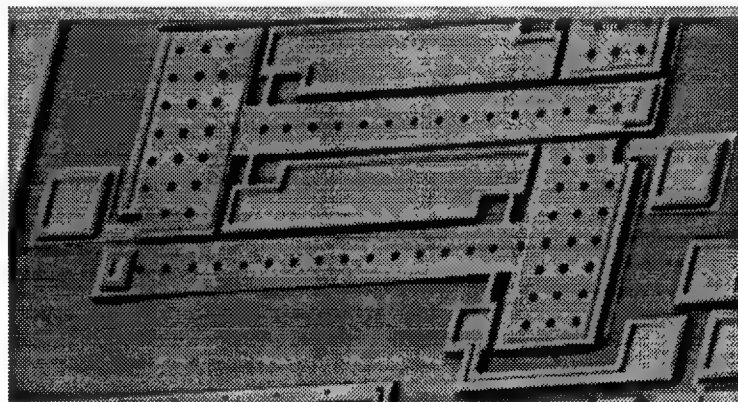


Figure 4.15. SEM micrograph of a released flexing actuator from MUMPS 4 chip.

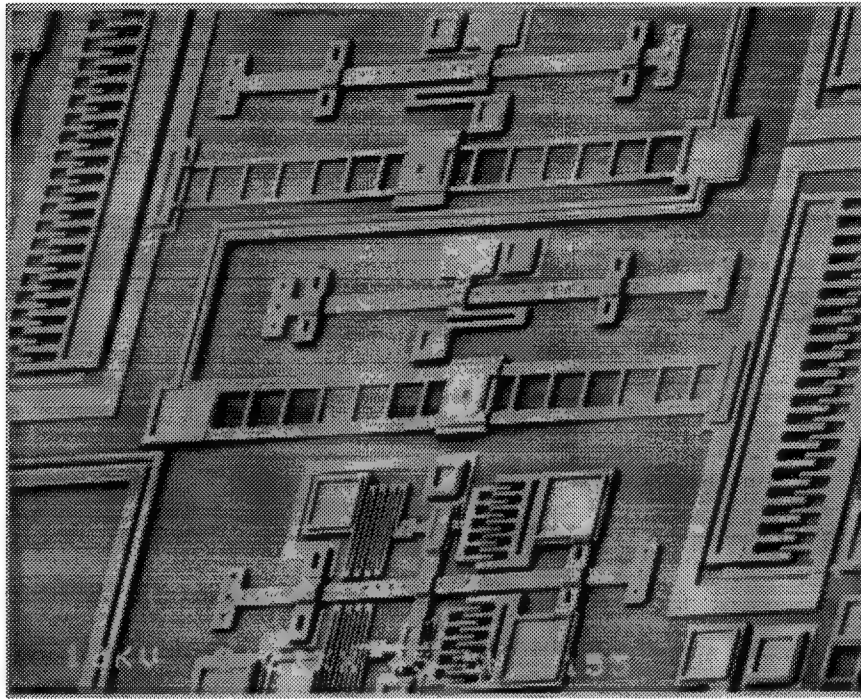


Figure 4.16. SEM micrograph of a released arching actuator based on comb drive from MUMPS 4 chip.

In order to solve this problem, both MOSIS and MCNC fabricated chips were bonded using a ball bonder. The chip was epoxied to a 64 pin package and the pads on the perimeter of the chip were bonded with a gold wire. Once packaged the devices can be tested easily with a protoboard. This greatly simplified the testing procedure.

4.4. Probe Station.

The Analytical Probe Station, Model 6200, The Micromanipulator Co., Inc., was utilized for the initial observations and testing. This station is capable of probing the devices and measuring vertical displacement. The test equipment consisted of a function

generator, electrometer, high voltage supply, oscilloscope, and digital multimeters. With this system the devices can be optically observed while being stimulated.

4.4.1. CMOS Tests and Observations. All of the tests described in Chapter 3 were initially performed. After the initial information has been gathered, the devices were thoroughly characterized with the test equipment.

4.4.1.1. Wall Test. The goal of the wall test was to build the highest possible wall around the devices in order to prevent device damage when contacting the finger as a tactile stimulator. The wall test structure did not release from the silicon as described in Section 4.2. If the beams in this set of test structures had released, the curling due to internal stress would have caused the tips to bend upward at least 20 μm . Since the surrounding wall in this test is composed of unetched CMOS layers (only 3 or 4 μm high), it would be completely useless as a guard around the beam. One solution to this problem would be to add an annealing phase, like the one in the MUMPS process, to prevent the stress induced curling. Another way to prevent damage to the beams would be to micromachine a second chip that would provide guard walls high enough to compensate for the beam curling and bond it to the original chip. This would allow the finger to move freely and exert any force without crushing the MEM beams.

4.4.1.2. Heater Test. The designs in the heater test set utilized a variety of structural supports and shapes. The goal was to produce a sturdy suspended heater. The heater would be able to withstand contact with a finger, and it should heat and cool quickly. By using suspended structures the substrate is isolated from the heating elements. Thus, the suspended devices will heat quicker than the heating elements directly on the substrate. A sample device is shown in Figure 4.17. Current was applied to some of these devices and the heating could be observed visibly. As the current was increased the

devices began to glow with a bright white color. The device temperature was not measured, but the devices certainly responded quickly and could easily reach a temperature that burns out the device. Of the twelve different heating designs, only 7 of them were completely releasable. No empirical measurements were taken of the structural strength of the devices, but they are definitely stronger than the bimorph beams due to the two extra supports.

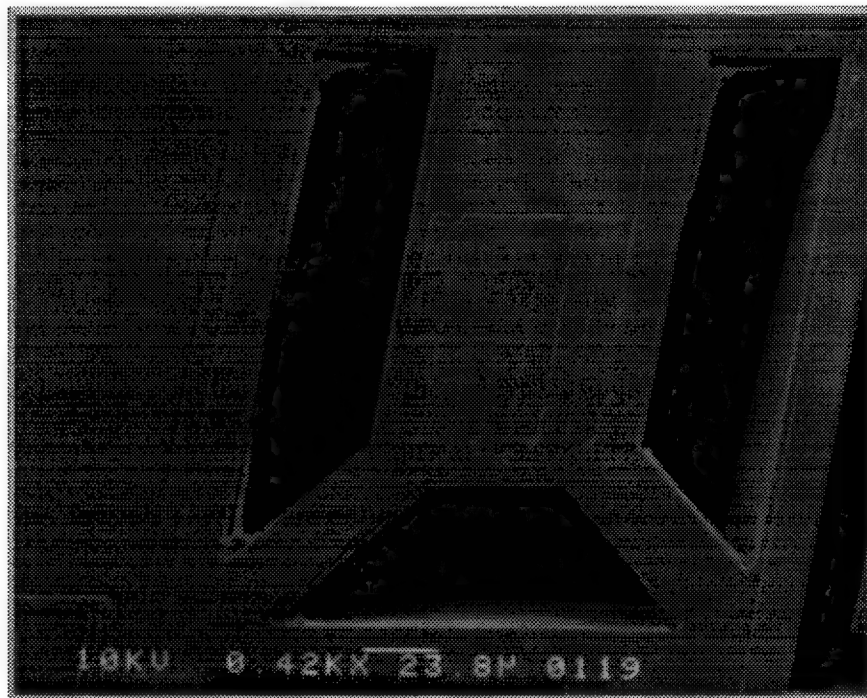


Figure 4.17. SEM micrograph of a released heating element from Traychip 1.

4.4.1.3. Support Test. This test seeks to determine how flexible the beam material is and if less support at the base will increase the flexibility. There were fourteen variations of the structural support of the typical bimorph beam. The result of this experiment was that any gains in deflection were offset by a loss of structural integrity of

the beam. The bimorph beams with the maximum support moved with much more flexibility than originally suspected and therefore, the increase in deflection is not as important as the loss of structural support and weakening of the beam.

The devices in this test consistently broke easier than the beams with the maximum support. Because of these observations, the structural weakening was determined to be both unnecessary and detrimental.

4.4.1.4. Layer Test. The next major test using the micromanipulator station was to compare the deflections of the beams constructed from different layer combinations. The different layer combinations are described in Chapter 3 and are listed in Table 3.4. The beam numbers given in Table 3.4, along with letters to designate which copy on the chip is being tested, were used to label the beams in this experiment. The letters A through Y represent the 25 major test groups. For example, beam U-5 is from test group U which is on the lower left portion of the chip and layer combination 5 given in Table 3.4. This test was performed by actuating each of the beams over a range of input electrical power and measuring the deflection. A square wave was used as the input. The square wave insures that the beam will heat and cool completely between cycles and makes optical measurement easier since movement occurs only after a change in voltage level. The optical measurement of deflection is obtained by focusing the microscope on the tip of the beam when it is at rest and when it is actuated. The movement of the microscope lens can be measured and is the exact deflection of the beam. The estimated error for this measurement technique is approximately $\pm 2 \mu\text{m}$. Five different layer combinations were compared using this method. The majority of the beams deflected downwards toward the substrate. Since the common direction of movement is toward the substrate, the positive z axis in Figure 3.4 is taken toward the substrate. For each of the set of data points a best fit line was estimated using a least squares method.

The measured results were compared to the theoretical deflections obtained from equations (4) and (26). The deflection generated by these equations is based on a change in temperature which is linearly dependent on the change in input power as given by equation (24). The value C , in equation (24), is determined empirically by averaging the experimental data from 8 of the 12 different layer combinations. For each beam, the slope of the experimental line was divided by the theoretical slope to determine C . Table 4.1 indicates the values of C for each different beam combination and the average C which is 4.56 K/mW.

Table 4.1. Experimental Estimation of the Constant C .

Beam	Experimental value of C (K/mW)
S-2	4.03
S-3	4.16
S-5	4.16
U-5	5.00
S-6	4.44
U-6	5.25
S-7	6.91
U-7	5.17
U-8	3.06
S-9	2.33
U-11	5.67
Average	4.56

Figures 4.18 through 4.22 show the experimental and theoretical curves for these beams. Figure 4.23 combines all the experimental data for the beams to indicate the best beam performance. Figure 4.24 shows the beam deflections measured using the optical technique along with the theoretical calculations.

The theoretical measurements agree very well with the experimental data. The trends of each layer combination are distinct and are consistent with the theory as shown in Figure 4.24. Figures 4.18 and 4.19 indicate that beams U-5 and U-6 have nearly the same amount of deflection. This agrees with theory since the only difference in the construction of the two beams is that beam U-6 uses P2 instead of P1. The layer combinations for Figure 4.20, beam U-7, do not include the M2 layer, therefore, it will not deflect as much as beams U-5 and U-6. Figures 4.21 and 4.22 (beams U-11 and U-12) are similar in that they do not have any metal and therefore have very small deflections. Figure 4.23 indicates that beams U-5 and U-6 produce the most deflection.

The optical measurement method is inappropriate for obtaining frequency information. The accuracy of this method depends on the beam being stable in the actuated or initial position so that the tip can be focused on. This method is not effective at high frequencies (greater than 40 Hz) where the beam is continuously moving and the tip position cannot be marked.

4.4.1.5. Resistor Test. The resistors in the bimorph beams are simply polysilicon wires. Since the polysilicon has a much higher resistance than the metal lines, it acts as a heater. One complication is that the resistance value of the polysilicon changes as the temperature of the material changes. The resistance returns to its original value when cooled. Figure 4.25 is a plot of the resistance change versus input electrical power. This plot is an average of the resistances changes from six different beams. The beams used in this test are the standard 300 μm x 150 μm beams used in the layer test.

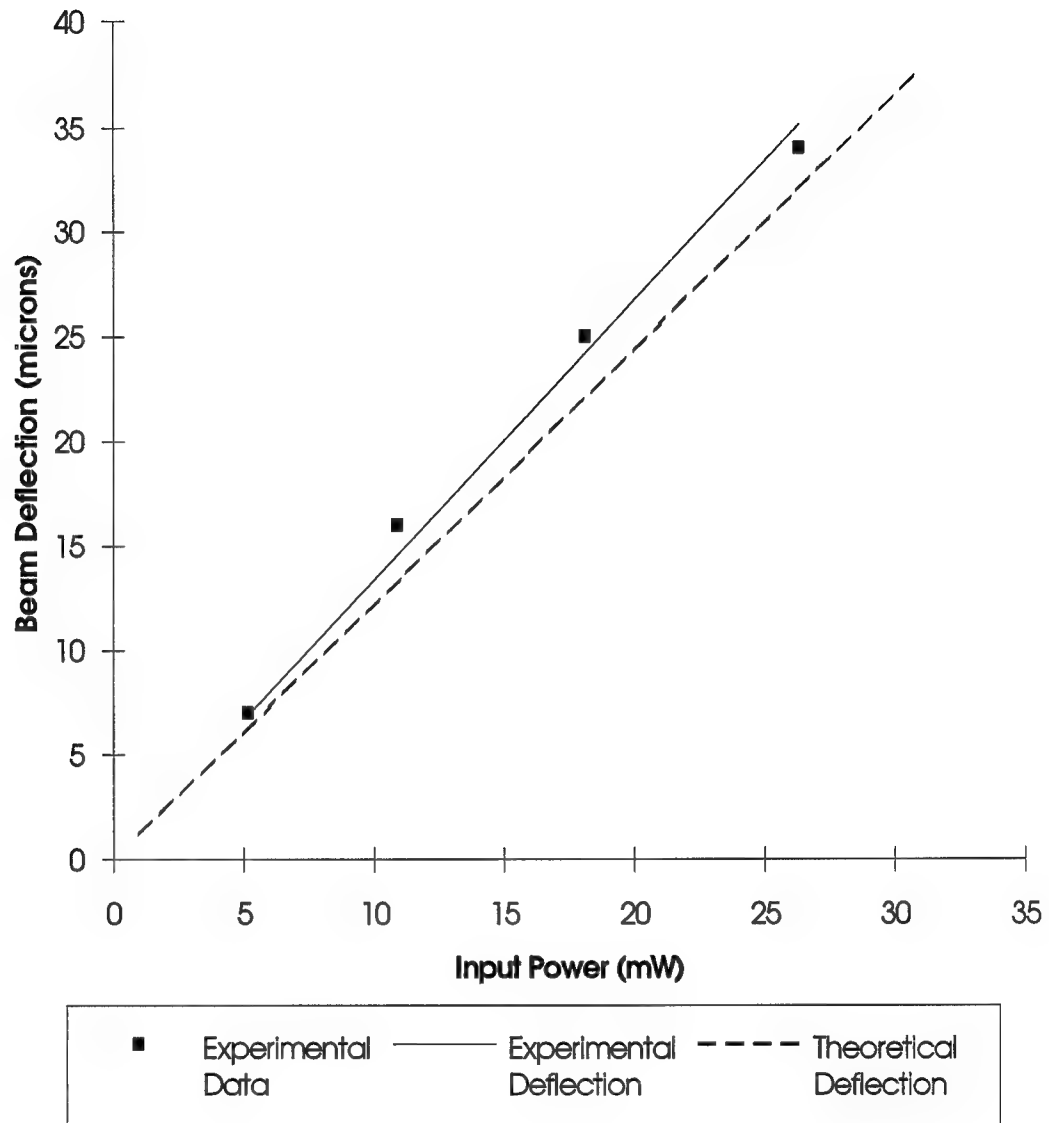


Figure 4.18. Experimental and theoretical deflections for beam U-5, 1,2,3,5,6,7,8 layer combination.

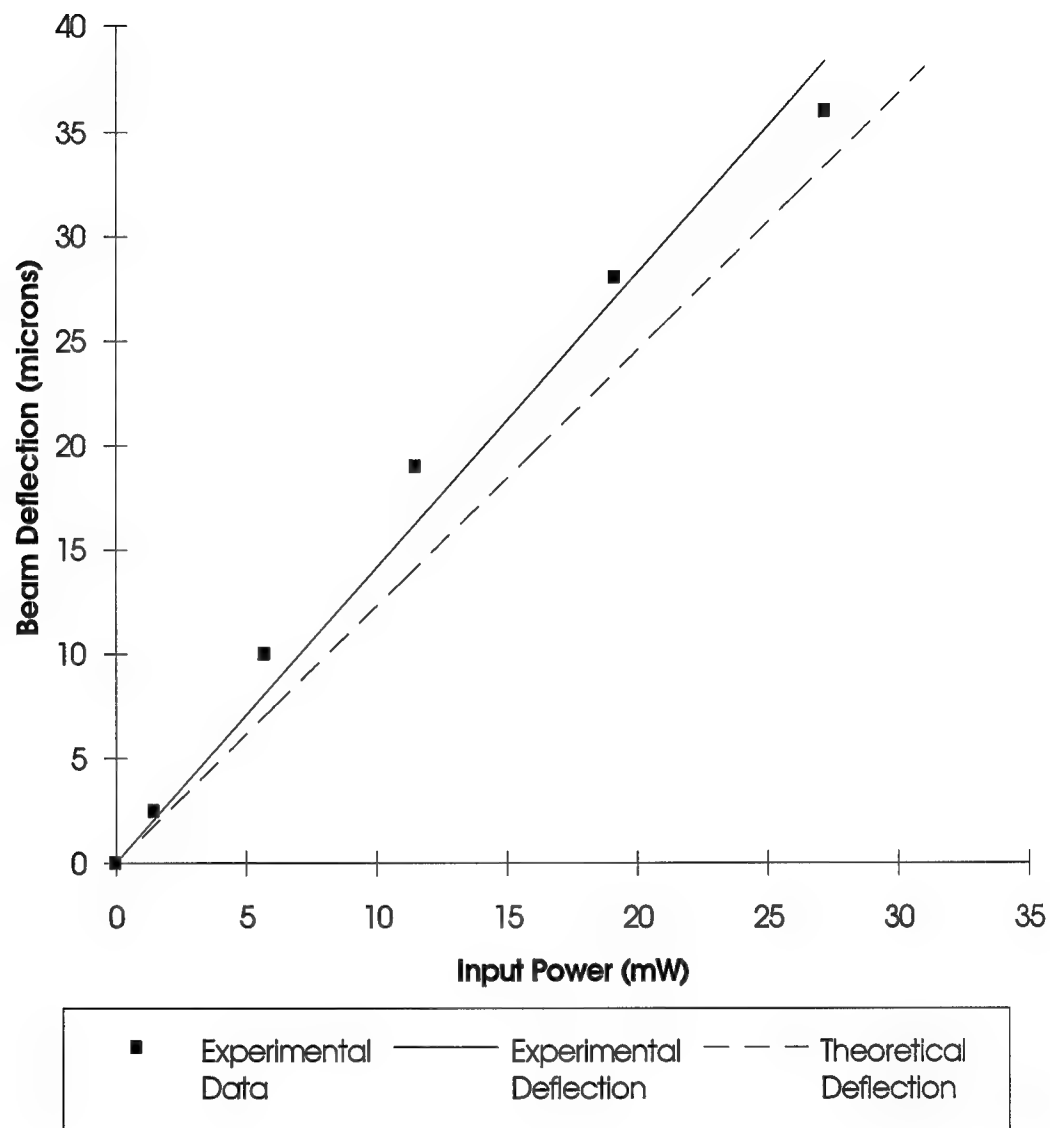


Figure 4.19. Experimental and theoretical deflections for beam U-6, 1,3,4,5,6,7,8 layer combination.

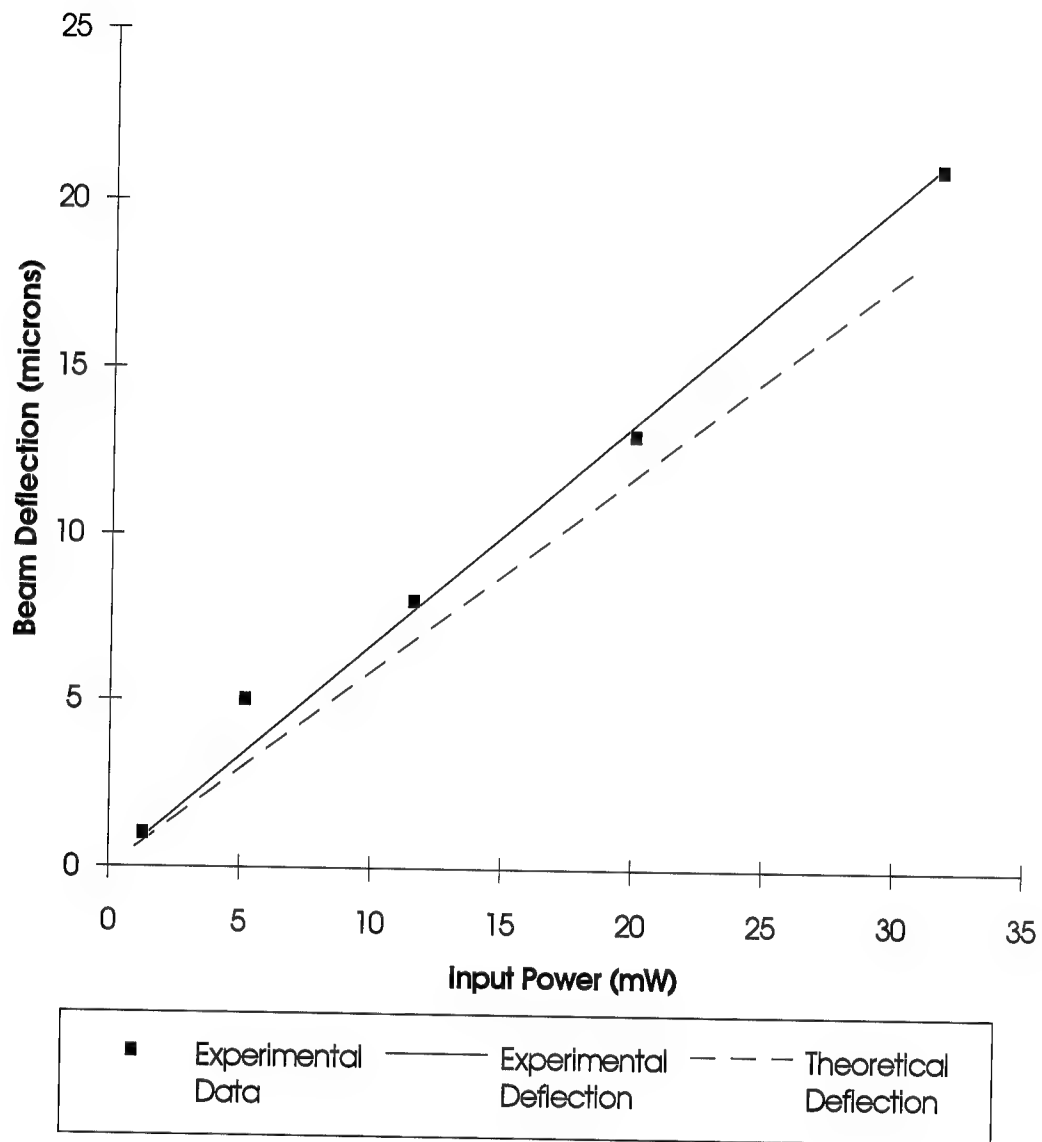


Figure 4.20. Experimental and theoretical deflections for beam U-7, 1,2,3,5,6,7 layer combination.

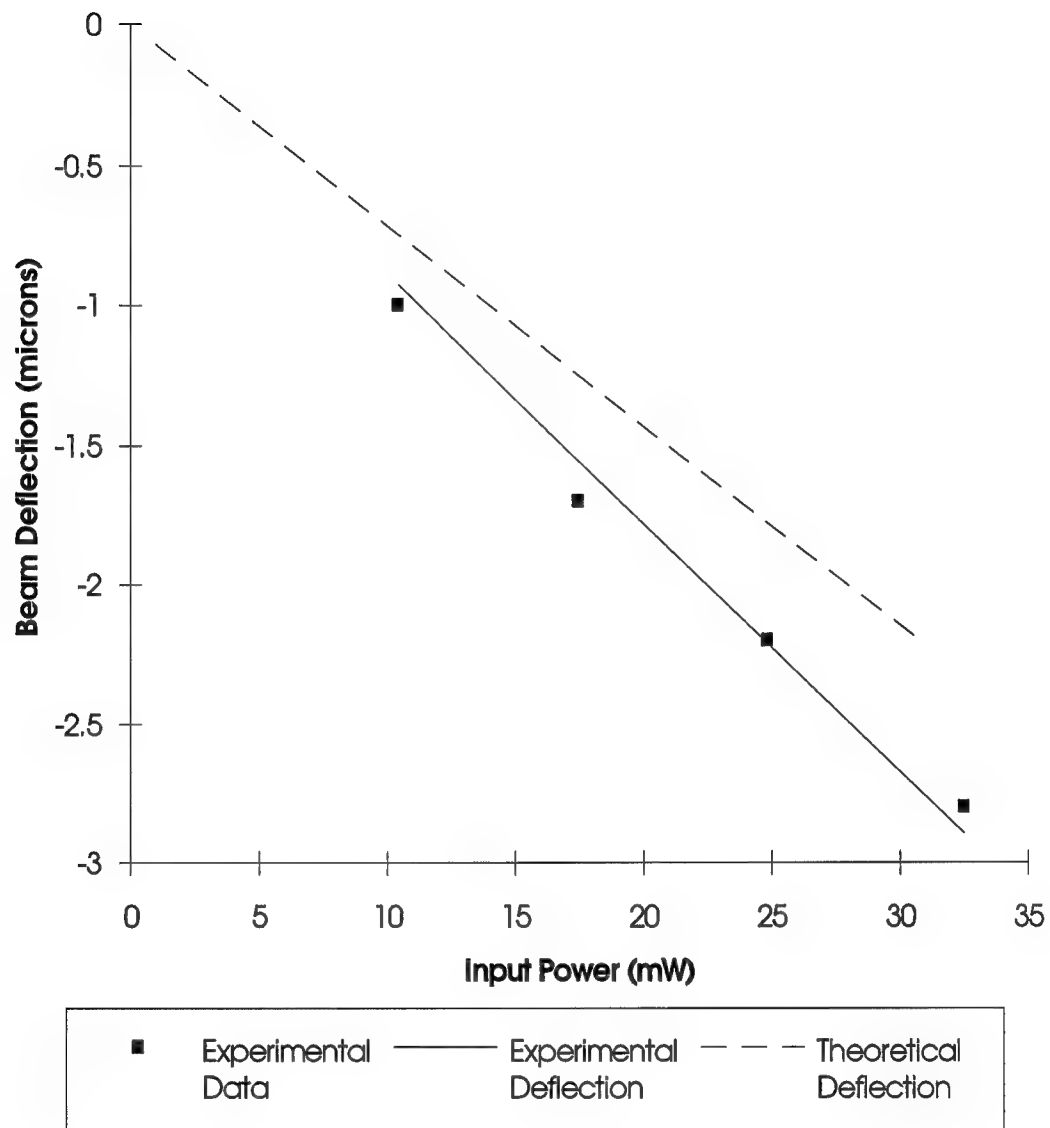


Figure 4.21. Experimental and theoretical deflections for beam U-11, 1,2,3,5,7,9 layer combination.

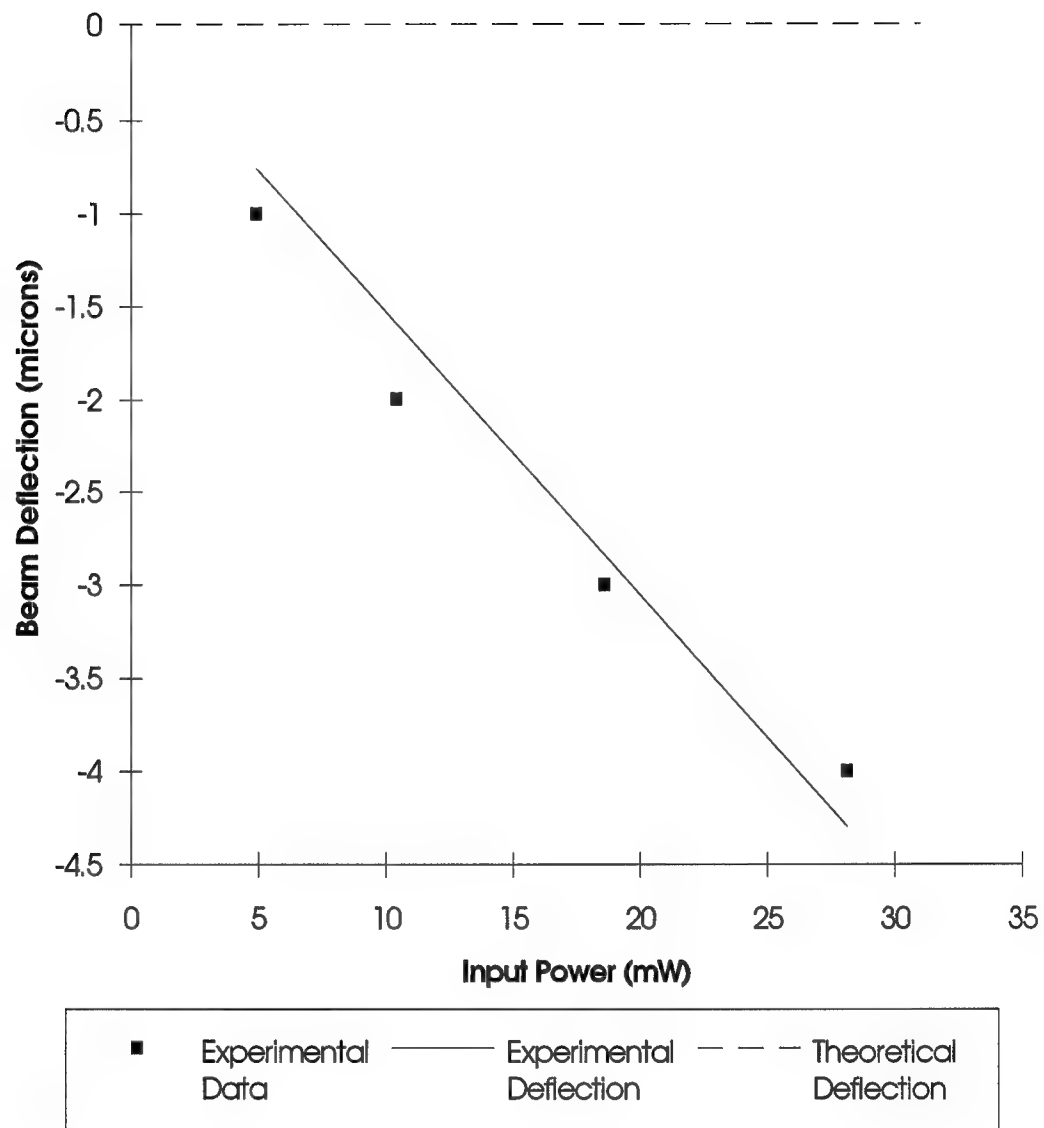


Figure 4.22. Experimental and theoretical deflections for oxide beam U-12.

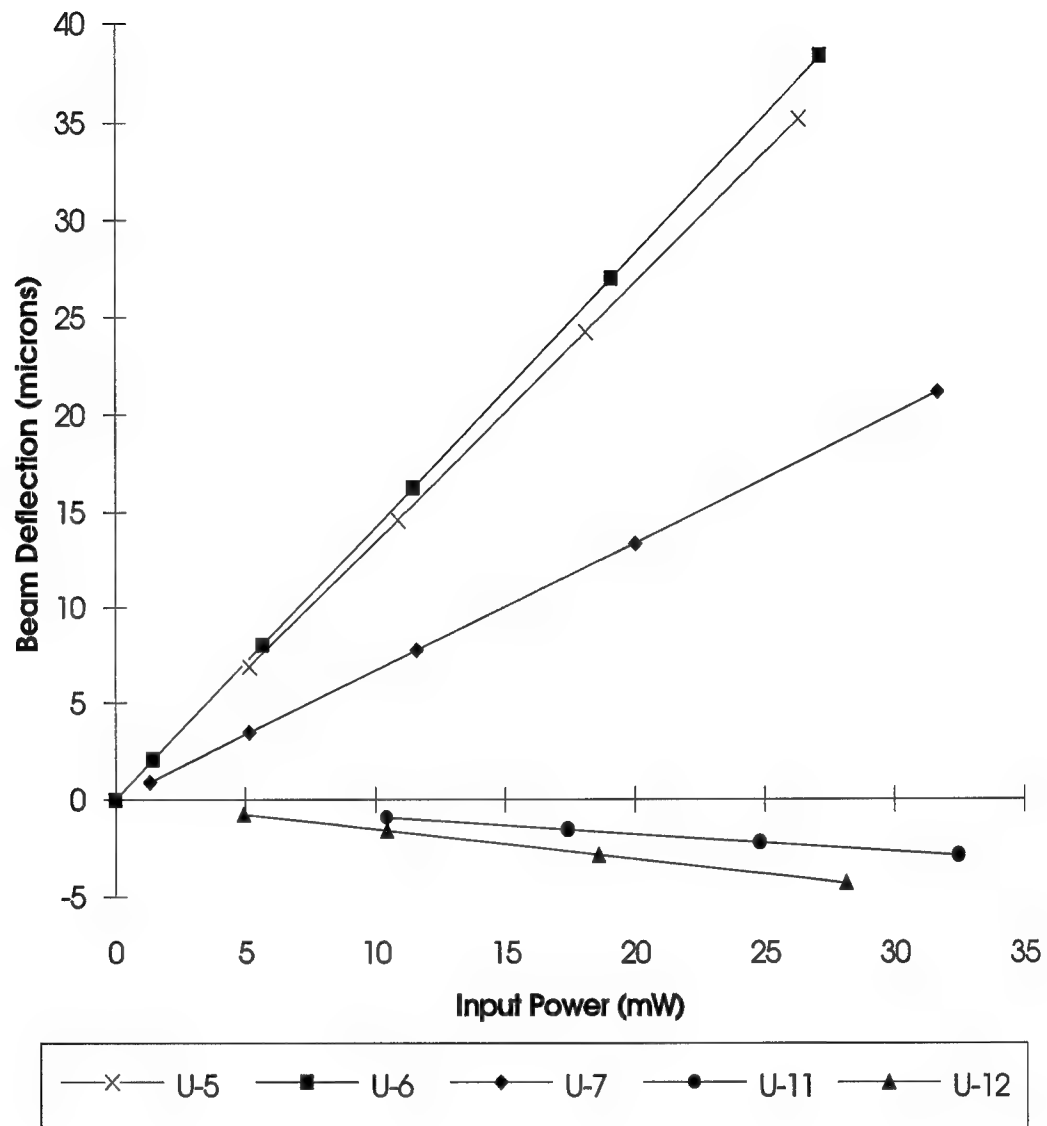


Figure 4.23. Best fit results of experimental deflections for five bimorph beam combinations.

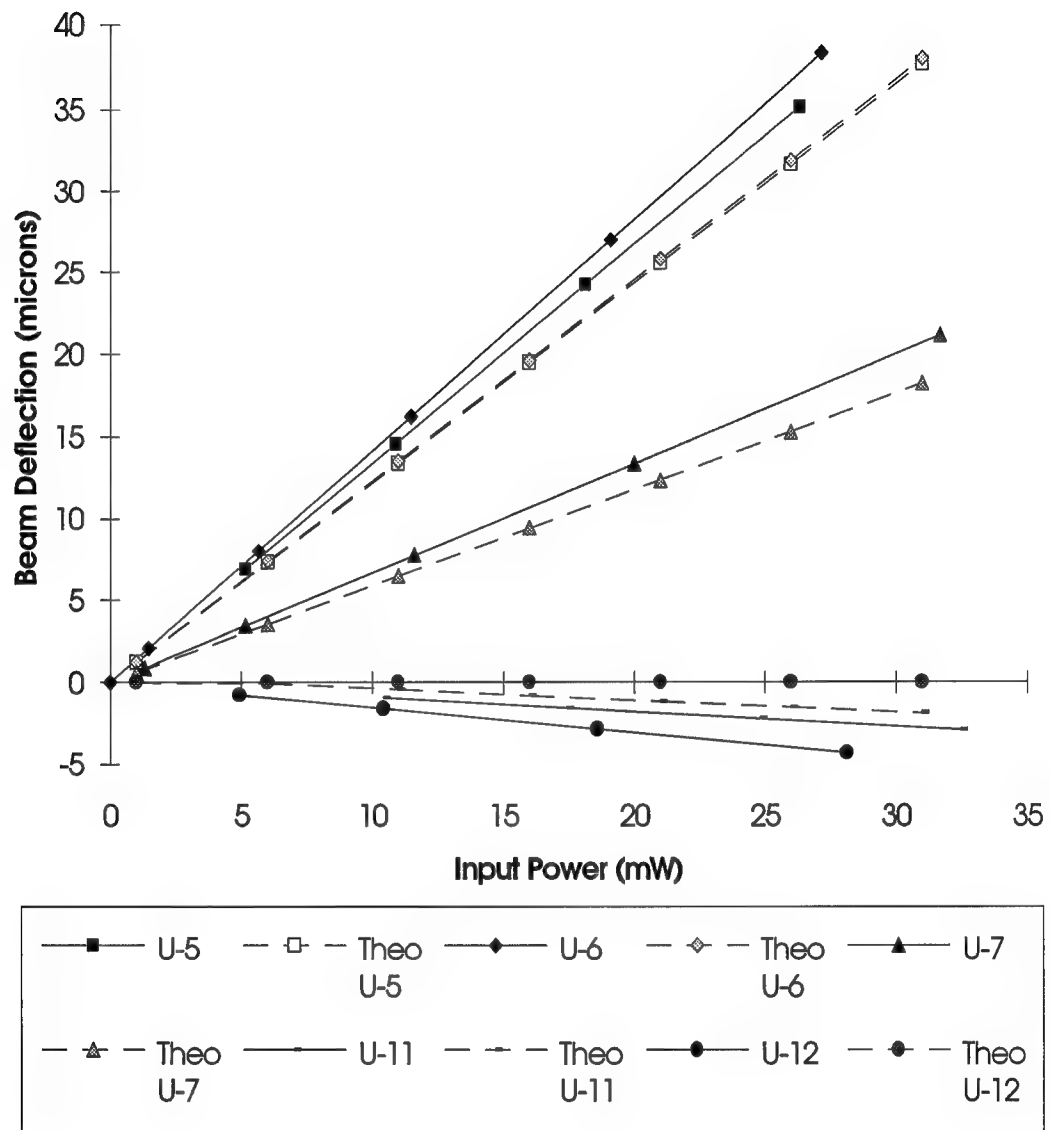


Figure 4.24. Experimental and theoretical deflections for five bimorph beam combinations.

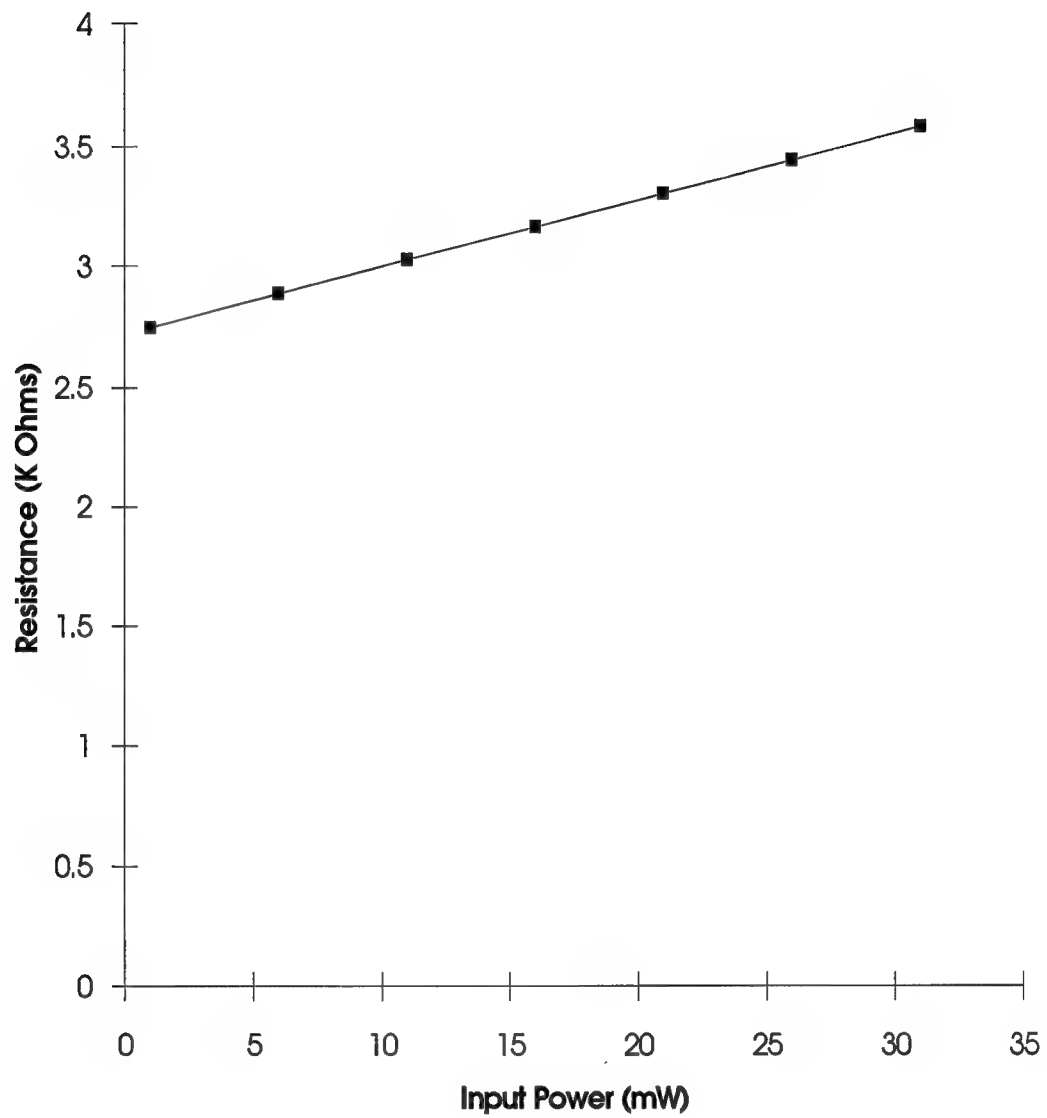


Figure 4.25. Best fit average electrical resistance of the beams versus input power.

The resistor test described in Chapter 3 was not completed due to insufficient time. General observation indicates that the beams heat quickly, therefore, the assumption that the beam has a uniform distribution of heat is true below the cutoff frequency of operation. The resistor placement will have a much more pronounced impact on deflection when beams are operated above cutoff frequencies.

4.4.1.6. Displacement Test. As noted above, most bimorph beams deflected downward. This agrees with the bimorph theory. The beams experience linear, elastic displacement below a certain input power. Above this input power, the beam operation moves from elastic deformation to plastic deformation. When operated above this power, the oxide on the beams melted allowing the resistors to short. The maximum input power varied depending on the layer combination in the beam, but 40 mW was a good operating limit. Below this power level, the beams continued to operate in the elastic range and produced consistent results.

4.4.1.7. Endurance Test. The bimorph beams exhibit a large amount of deflection. A typical 300 μm long beam can deflect more than 35 μm with elastic strain. This amounts to a deflection of over six degrees. How does the flexing affect the life of the beam? To answer this question an endurance test was performed on a beam X-3, which is similar to beam 4 from Table 3-4, but with a small resistor value. A 10 Hz, 4 volt square wave was applied producing a 28 μm deflection. The beam was actuated over 2.5 million times. The deflection did not change over the duration of this test. The test was halted after three days of continuous operation in order to use the test equipment for other experiments. This indicates that the beams weaken very little over time and that the deformation is an elastic process.

4.4.2. MUMPS Tests and Observations. The MUMPS 4 chip was not fully tested due to time constraints, problems with the test setup, and the poor performance of the devices as tactile stimulators. There were several problems with the setup for testing the MUMPS 4 devices. First of all, it is difficult to insure proper probing contacts with the electrostatic probe pads as described in Section 4.3 above. A simple conductivity test was all that was required in the CMOS devices, but with the electrostatic devices there was no way of determining if the probe is making a good contact with the pad. Second, the copper/chromium metal layer corroded easily. This made both wire bonding and probing difficult. Third, the range of motion of the electrostatic devices is much less than of the bimorph beams. This makes optical observation very difficult unless the devices are moving parallel to the chip surface. Since tactile stimulating devices must actuate out of the substrate plane, it is difficult to detect and measure the small movement with a microscope. The results of the limited testing are given below.

4.4.2.1. Electrostatic Attraction Beam. There are several problems with the design that is given in Figure 3.13. The MUMPS process does not provide insulating layers, therefore, if the beams are actuated above a critical voltage the two polysilicon layers (the electrodes) will contact. Due to the high voltages required for actuation this will cause irreversible damage to the devices. Another problem is that the maximum movement is limited by the stationary upper electrode. The gap between the P2 upper electrode and the P1 flexing beam electrode is $0.5\text{ }\mu\text{m}$. The longest electrostatic beam on the MUMPS 4 chip is $330\text{ }\mu\text{m}$ with the upper electrode extending $85\text{ }\mu\text{m}$ along this length. Simple geometry provides the maximum deflection out of the substrate plane as $1.94\text{ }\mu\text{m}$ using these dimensions.

These beam were tested with an electrometer to limit current flow between the two electrodes in case they touch. No motion could be detected with a microscope below 120 volts which was the maximum voltage of the source. Due to the apparent low

potential as a tactile stimulator and the design limitations, these devices were not exhaustively tested.

4.4.2.2. Electrostatic Repelling Beam. This design described in Chapter 3, requires a substrate contact to operate. The MUMPS process encases the entire substrate in silicon nitride without a substrate contact and does not provide a nitride cut. The designs were still attempted with the hope of making a substrate contact with the oxide cut layers. The design rules were violated by stacking three oxide cuts, with the hope of etching through the nitride and making a substrate contact. During testing two of these pseudo-substrate contacts were probed and there was no connection. Also, since the electrostatic force decreases with the square of the separation distance, there is little chance that this devices could have performed as a tactile stimulator. Large deflections out of the substrate plane would not be possible. Due to the lack of a good substrate contact and the low chance of success as a tactile stimulator, these devices were not thoroughly tested.

4.4.2.3. Flexure Test. This device shown in Figure 3.16 had the highest chance of success of all the MUMPS designs. Theoretically it is capable of large deflections and has a landing pad to prevent shorts. Unfortunately, this device is also the weakest of all the designs. The entire flexing beam is supported by two thin strips (flexure arms) that are required to twist allowing the beam to move.

4.4.2.4. Arching Test and Heater Test. Neither of these devices were tested fully due to lack of time. The arching device shown in Figure 3.15 also requires a substrate contact to prevent the comb from being attracted to the substrate. Also, this device is not very sturdy and would have problems as a tactile stimulator.

4.5. Force Testing.

The information on deflection of the bimorph beams presented above indicates that they can provide adequate deflection for stimulating the finger. These deflection measurements do not take into account loaded actuation. Since the finger acts as a load to the MEM stimulator, force characterization of the beams is essential. In order to measure deflection of the actuators under a load, the force tester shown in Figure 4.26 was developed.

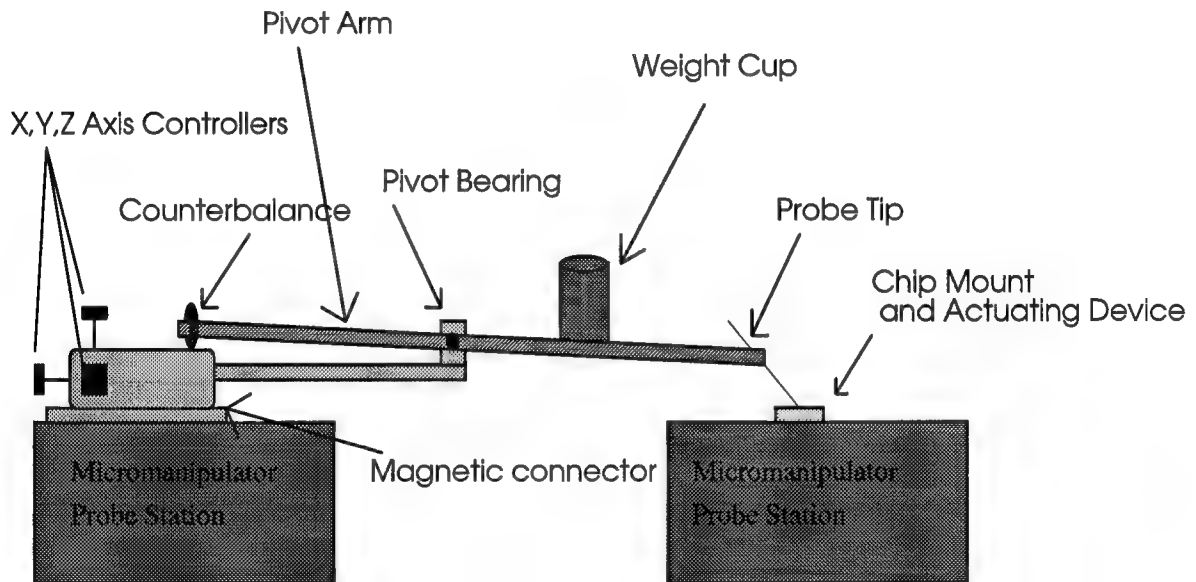


Figure 4.26. Force tester for MEM actuators.

The force tester operates based on a balance system. The pivot arm shown in the figure is connected at the pivot bearing. An adjustable counterbalance at one end balances the pivot arm. The opposite end of the pivot arm has a probe tip with an end diameter of approximately 5 μm . A weight is placed in the weight cup and the probe tip is placed on

the actuating device. This allows a known force to be applied to the beam. Thus, changes in beam deflection can then be measured over a range of weights. The base of the force tester is connected to the micromanipulator station with a magnet. There are X, Y, and Z axis controllers on the tester base which precisely position the tip. The weights used for the tester are calibrated by simply putting the probe tip on a weight scale (the scale has a resolution of 1 mg). An arbitrary amount of weight is added and the force at the tip is observed using weight. Using this system, precise forces can be applied. The deflection of the beam is measured optically while the probe tip is applied. The force tester was determined to have a ± 2 mg error due to the bearing quality.

Several MEM beams were tested to determine how different loads would affect their deflection. The typical beams, 300 μm long by 150 μm wide with a 2.6 K Ω polysilicon heating resistor and different layer combinations, continue to deflect with loads of 10-15 mg. Deflection was reduced to zero in all cases at weights above 15 mg. A typical result is shown in Figure 4.27. As can be seen from this figure, the deflection decreases linearly as the load is increased. The beam in Figure 4.27 was operated with a 6 volt, 0.1 Hz square wave input with the probe tip of the force tester placed at the end of the beam.

A second endurance test was performed using this beam. A 6 volt 0.33 Hz square wave was applied to beam U-1 for over 75 hours. A 5 mg load was placed at the end of the beam using the force tester. There was no noticeable change in the amount of deflection after 90,000 actuations. This indicates that the beams continues to operate in the elastic range even under heavy use.

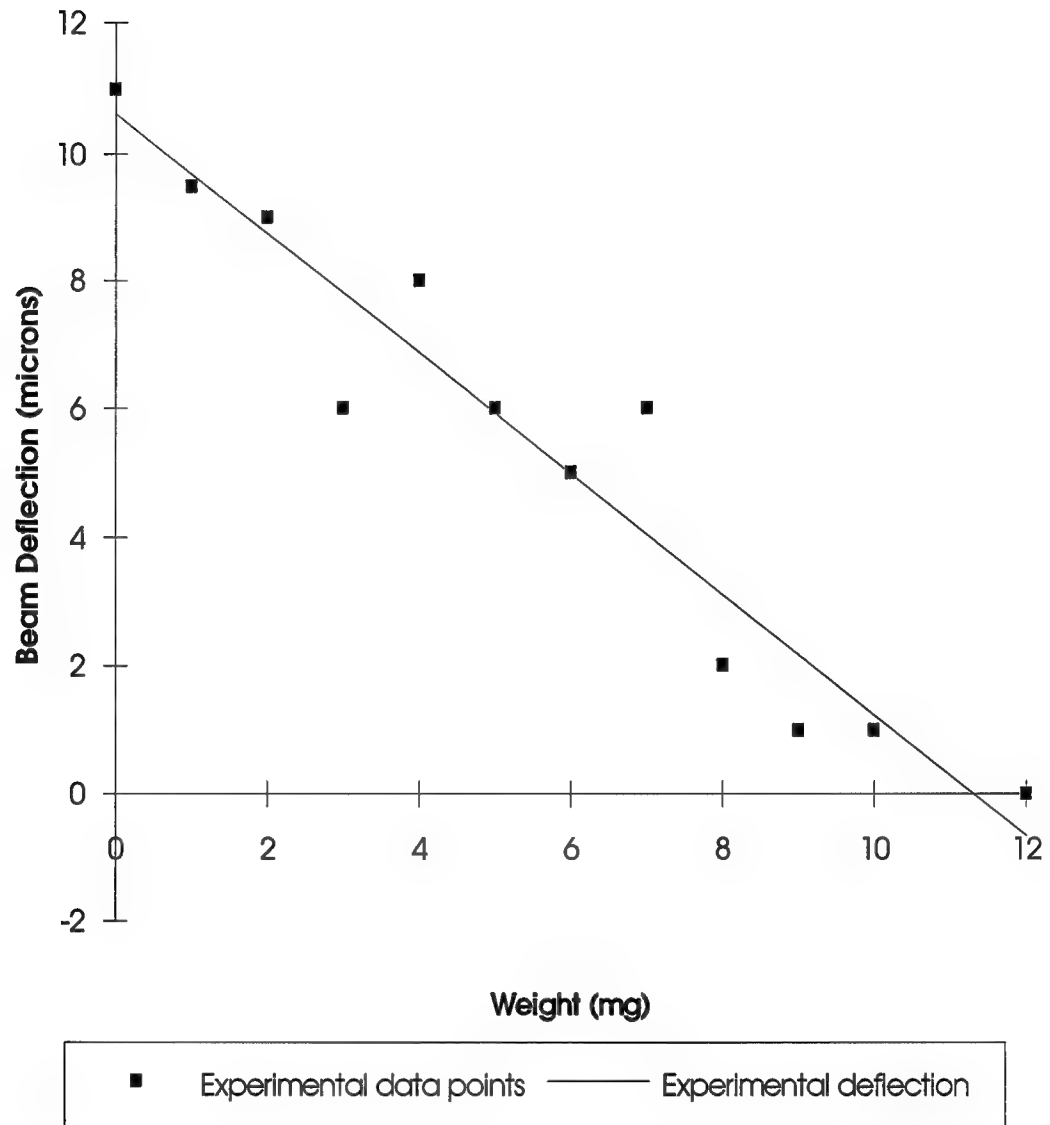


Figure 4.27. Experimental data and best fit line of beam deflection vs load for beam U-1 (1,3,4,5,6,7 layer combination) using the force tester.

4.6. Laser Interferometer Testing.

In order to obtain more accurate deflection measurements, the laser interferometer setup shown in Figure 4.28 was used.

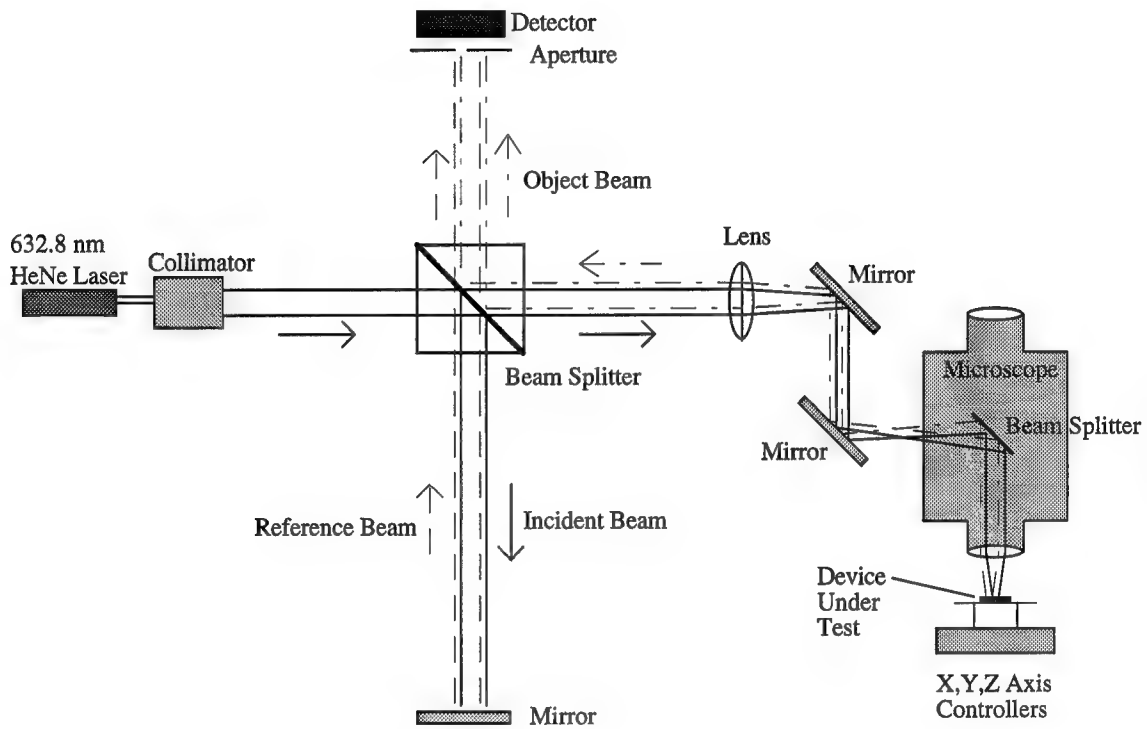


Figure 4.28. Laser interferometer experimental setup [60].

A 2 mW, 632.8 nm helium-neon laser is used as the light source. The collimator filters and focuses the light. The incident beam is split into two equal beams by the cube beam splitter. The reference beam is bounced off a mirror and travels to the optical detector. The object beam passes through a lens and two mirrors before entering the x32 microscope objective and being focused onto the MEM device being tested. The object beam then reflects from the MEM devices and returns to the optical detector by the same path. The object beam's path length changes as the MEM device is actuated. This change

in path length causes interference patterns to occur at the detector aperture. A 2π phase change in the interference pattern indicates a $0.316\text{ }\mu\text{m}$ deflection of the MEM device being tested. For a detailed description of the construction and operation of the laser interferometer see reference [60].

4.6.1. Sample Interferometer Data. Figure 4.29 shows the input signal and the interferometer output for a sample device. The bimorph beam used in this experiment was operated at 3.5 mW peak power, 3 volt peak to peak sine wave at approximately 20 Hz. The laser spot was focused on the bimorph beam tip. The formed laser spot was approximately $2\text{ }\mu\text{m}$ in diameter. As the input voltage changes between 0 volts and 3 volts, the interferometer detects 7.58 lambda or 15.16π of optical phase change. This corresponds to a $2.4\text{ }\mu\text{m}$ deflection of the tip of the bimorph beam. When the input power approaches zero, there is very little movement in the beam and the optical phase does not change. This is seen in Figure 4.29 as a long peak. The detector output during the rise in input power is mirrored by the output during the fall in input power. The slight rise in detector output phase at the peak of the input power appears because the total phase change (7.58 lambda) is not a multiple of $1/2$. The negative output values are due to the inverting amplifier used to boost the detectors signal.

4.6.2. Interferometer Comparison to Optical Microscope Measurements. A sample of the optical microscope measurement was compared to the interferometer measurement for the same bimorph beam, U-7 which is $300\text{ }\mu\text{m}$ long and $150\text{ }\mu\text{m}$ wide. The results are given in Figure 4.30. The two measurement methods indicate similar results. Since the optical microscope has an approximate estimated error of $\pm 2\text{ }\mu\text{m}$, both methods appear to agree well.

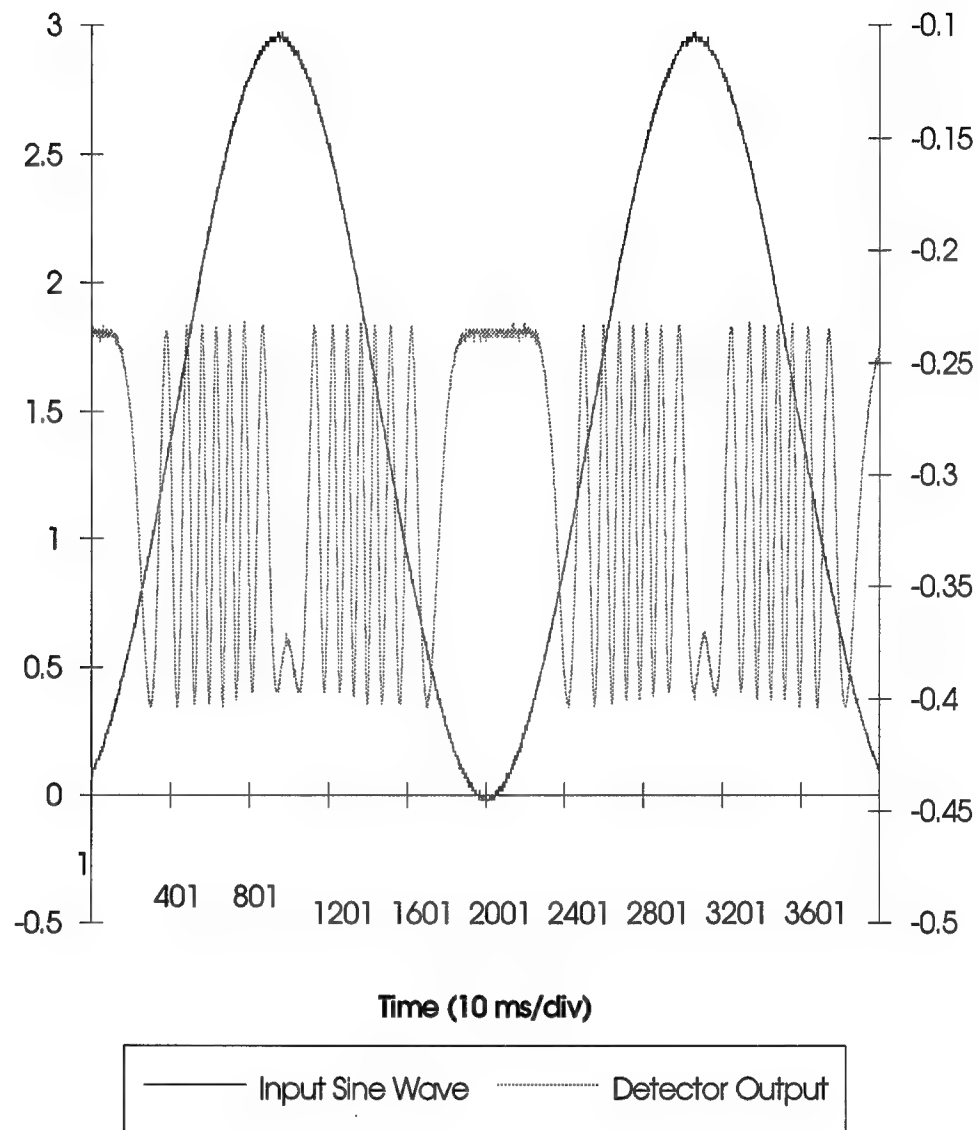


Figure 4.29. Sample measurement of beam U-7 (1,2,3,5,6,7 layer combination) showing input sine wave and output interferometer data.

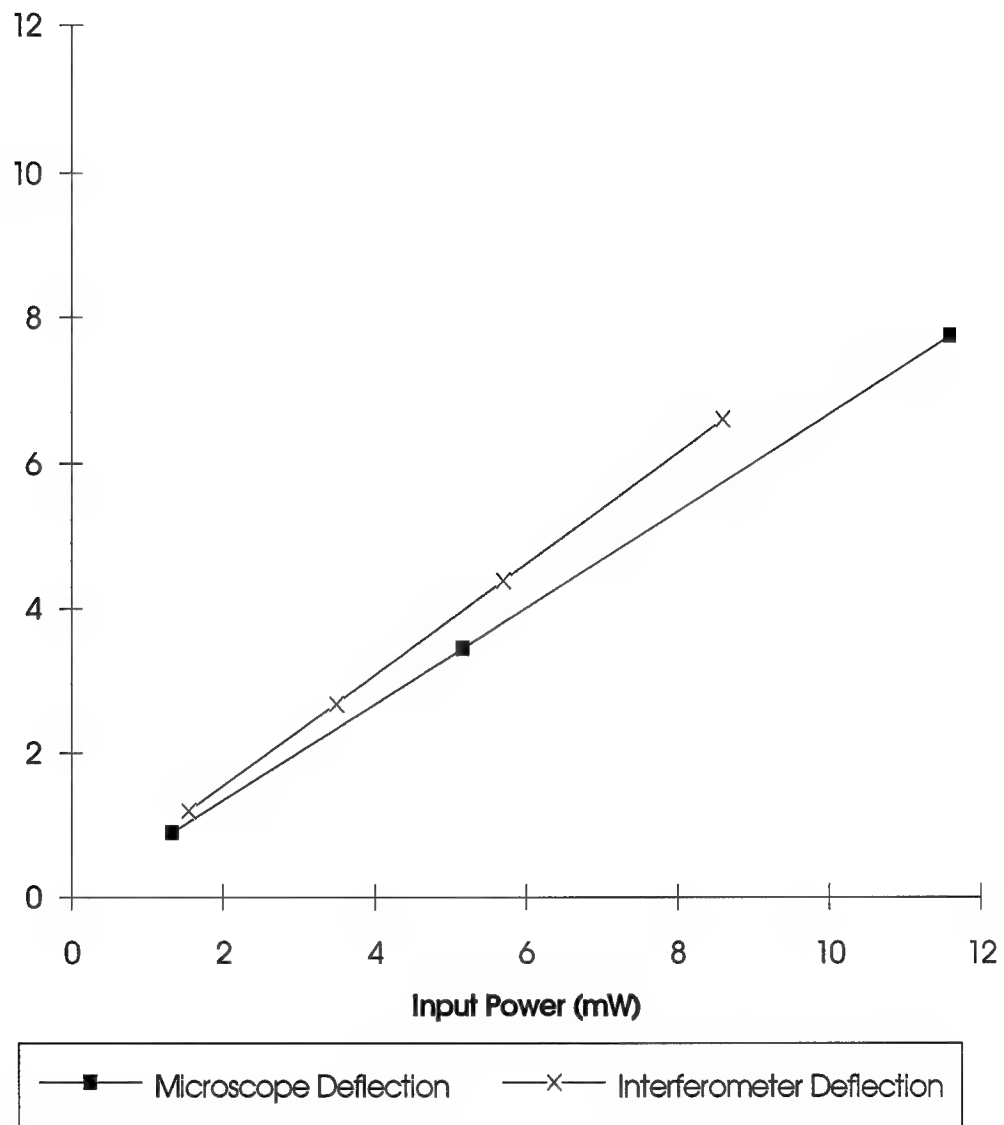


Figure 4.30. Comparison of best fit curves for beam U-7 (1,2,3,5,6,7 layer combination) using both optical microscope and the laser interferometer.

4.6.3. Heating and Cooling Measurements. The first test performed was to determine the time required to heat and cool a bimorph beam. Once again beam U-7 was used as the test beam. A 2 volt, 1.55 mW peak power, square wave at various frequencies was used to actuate the beam.

4.6.3.1. Typical Heating and Cooling Measurement. Figure 4.31 indicates a typical measurement for the U-7 beam. As can be seen in this figure, the movement caused by heating or cooling of the beam, occurs immediately after the voltage changes. The frequency of the input signal is 11 Hz. After the beam has reached a steady state temperature, the beam stops moving and the interference pattern does not change. The example beam shown in Figure 4.31 completes the entire 1.11 μm deflection in both the heating and cooling phases. The required time was calculated from the change in input voltage (the start of motion) and when the beam has moved 95% of its full swing (1.0545 μm). For this particular example the beam heat in 3.3 ms and cools in 3.35 ms. By assuming a period based on the slower of the two times, the minimum operating period of 6.7 ms is obtained. From this a maximum operating frequency of 149.25 Hz is obtained. This value will of course change with different power settings.

4.6.3.2. Average Heating and Cooling Time. The frequency of the input square wave was varied from 10 to 50 Hz to insure that the heating and cooling rates are not frequency dependent. The interferometer data is given in Figures 4.32 through 4.36. The poor quality of Figures 4.33 through 4.36 is due to a noisy amplifier. The noise was intermittent, but tended to increase with time. This information indicates that the deflection does not change over this range of frequencies. Therefore, the beam completely cools and heats during each cycle.

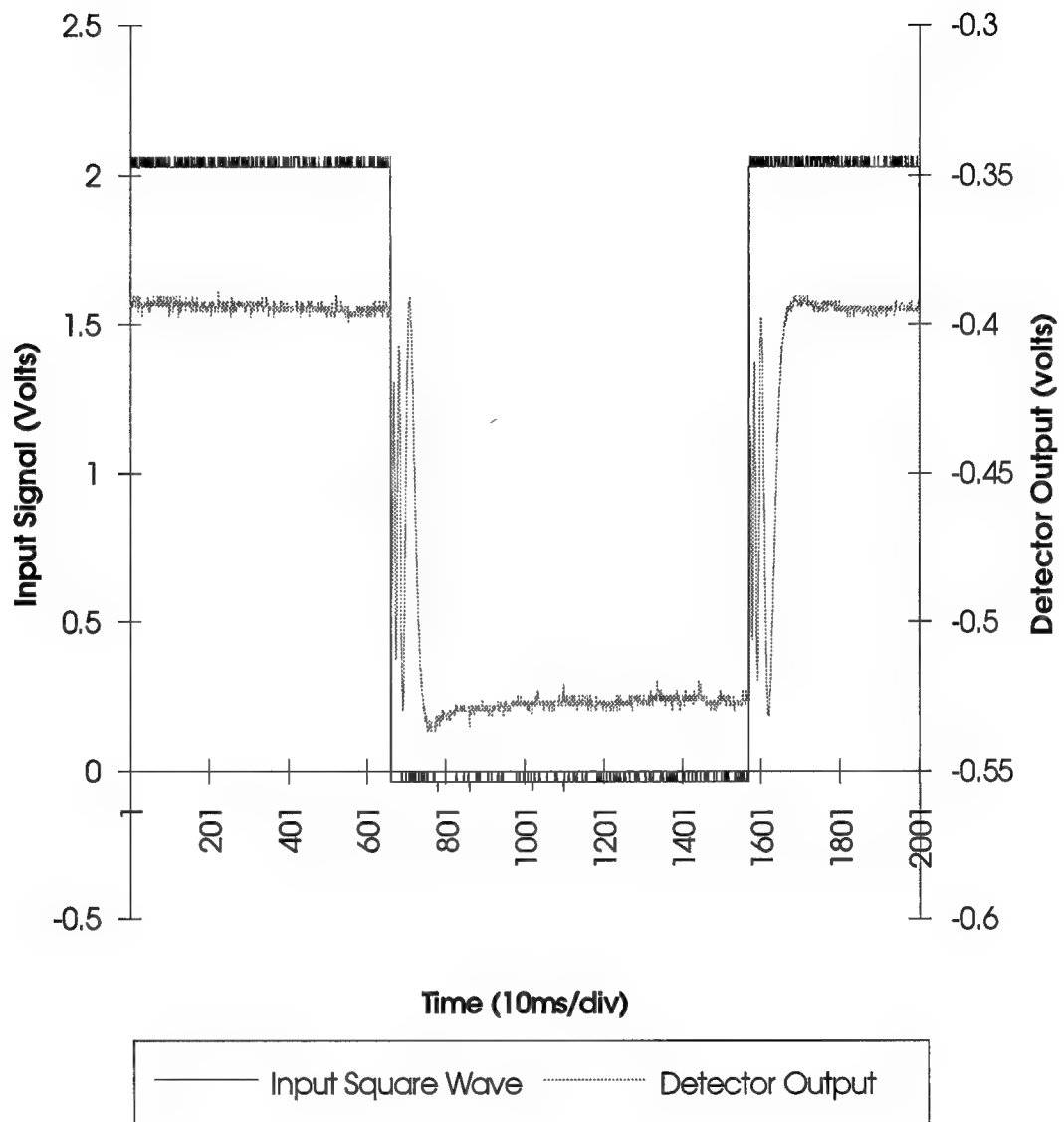


Figure 4.31. Square wave input to beam U-7 (1,2,3,5,6,7 layer combination) and the laser interferometer output.

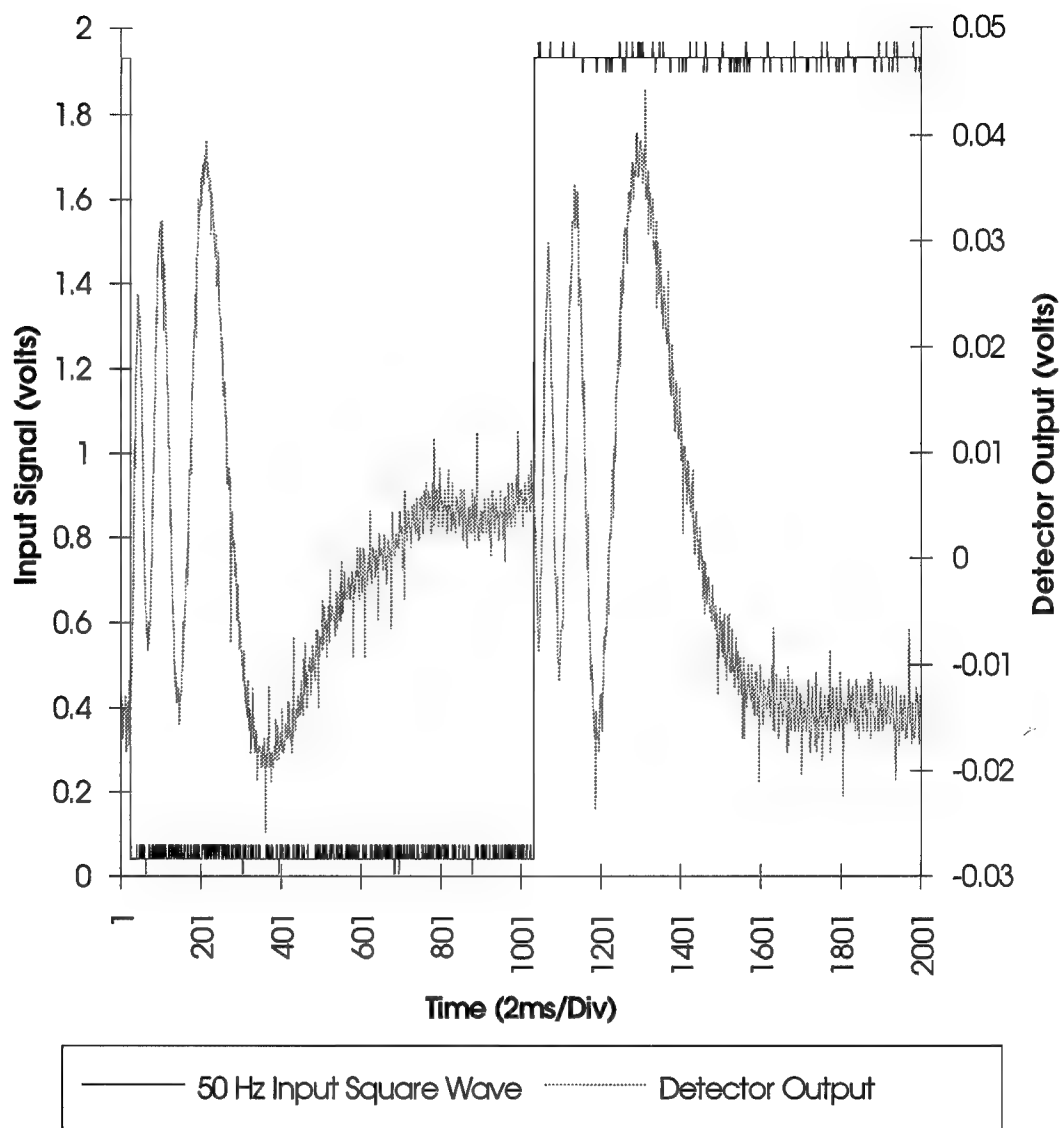


Figure 4.32. 2 volt, 1.55 mW peak power, 50 Hz, square wave input to beam U-7
(1,2,3,5,6,7 layer combination) measuring 0.997 μm .

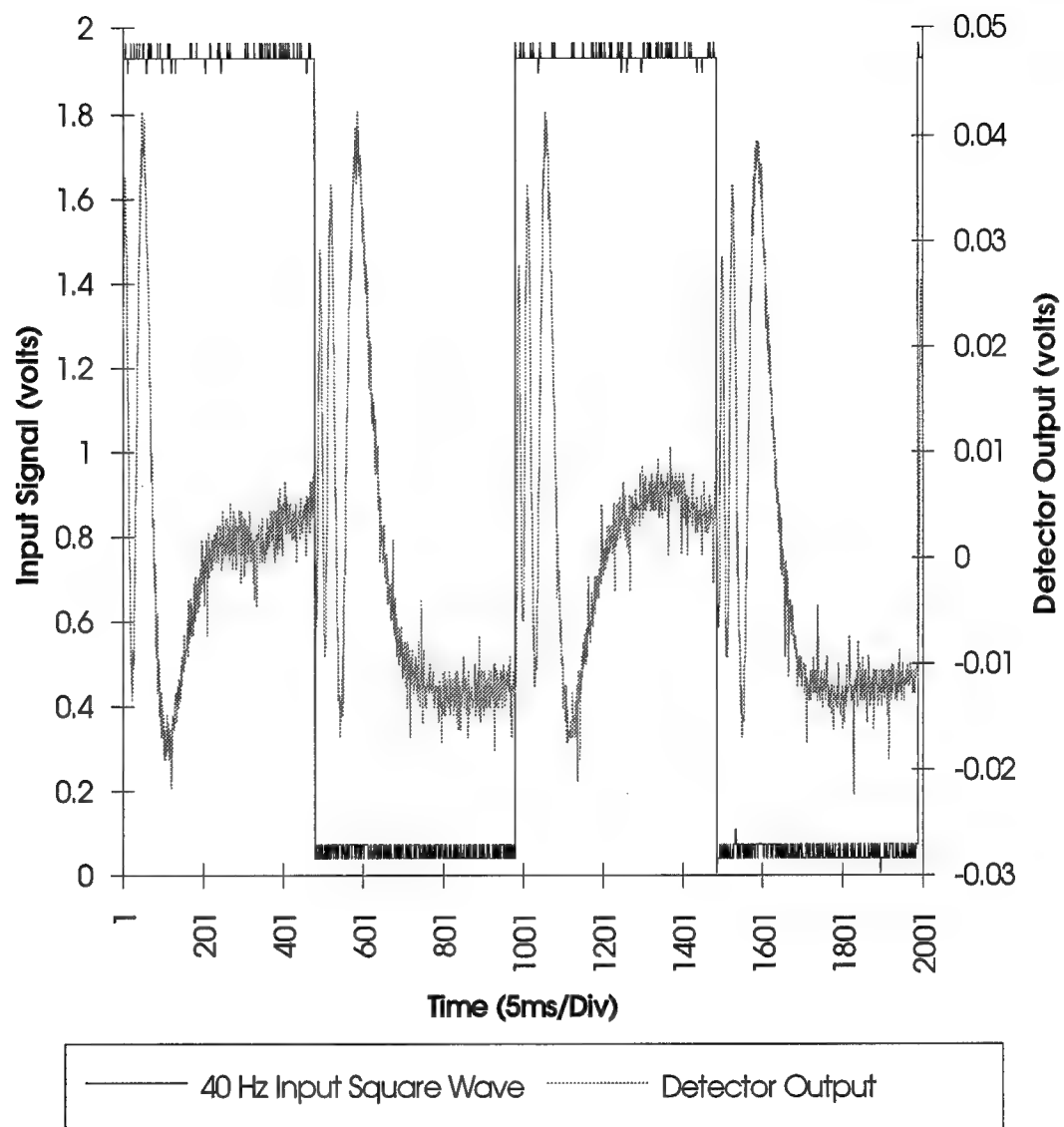


Figure 4.33. 2 volt, 1.55 mW peak power, 40 Hz, square wave input to beam U-7
(1,2,3,5,6,7 layer combination) measuring 1 μm .

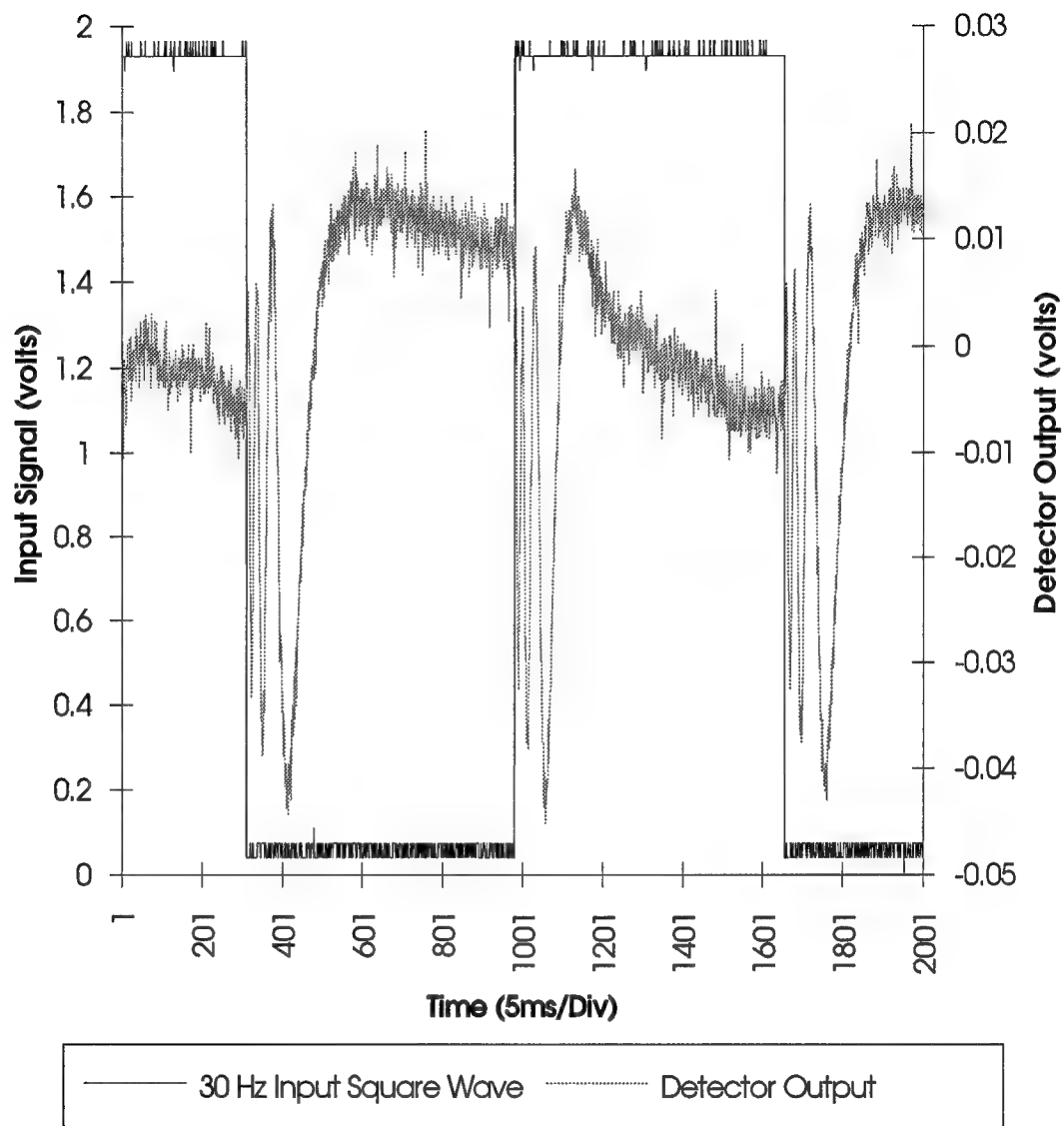


Figure 4.34. 2 volt, 1.55 mW peak power, 30 Hz, square wave input to beam U-7
(1,2,3,5,6,7 layer combination) measuring 1 μm .

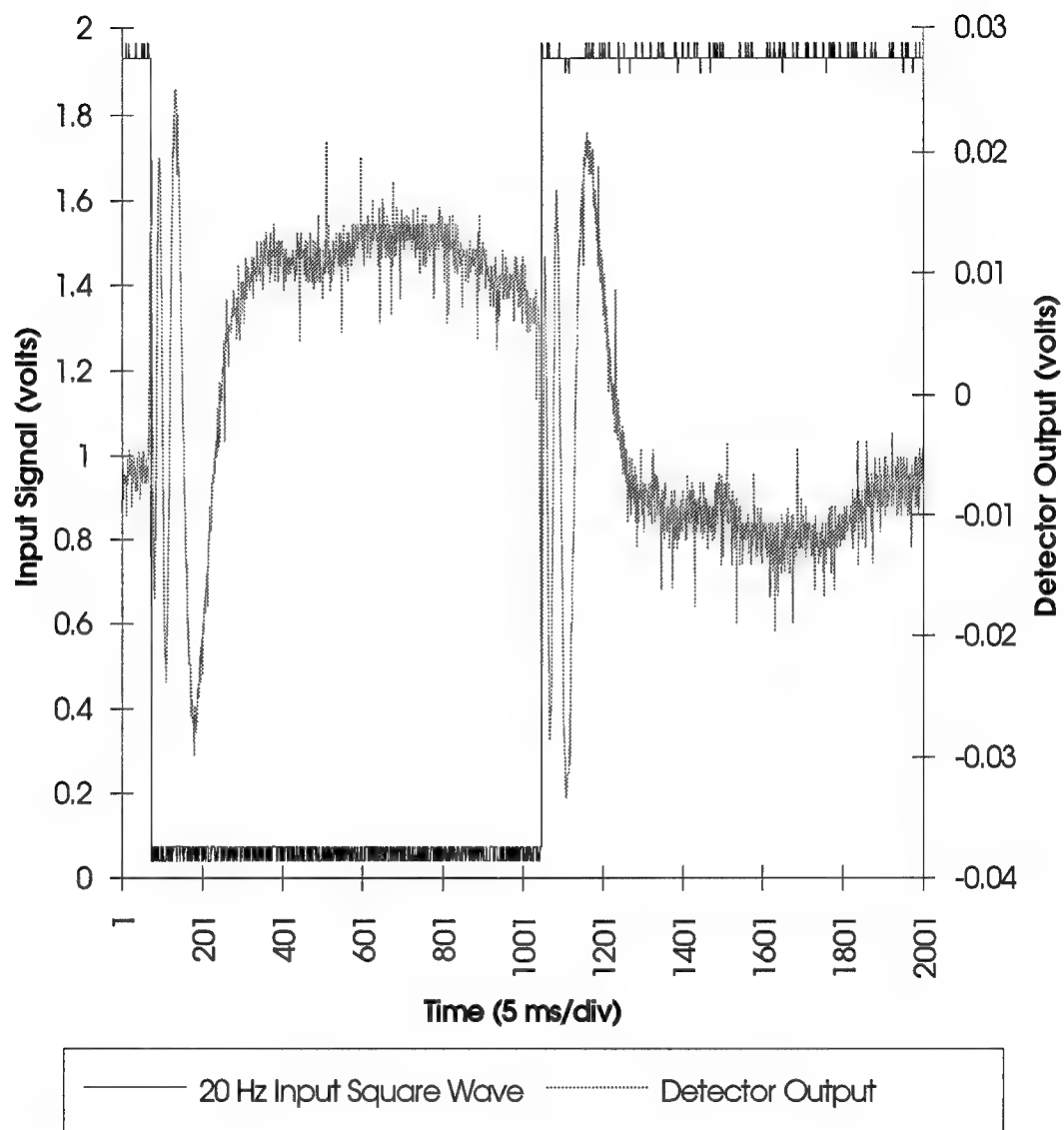


Figure 4.35. 2 volt, 1.55 mW peak power, 20 Hz, square wave input to beam U-7
(1,2,3,5,6,7 layer combination) measuring 1 μm .

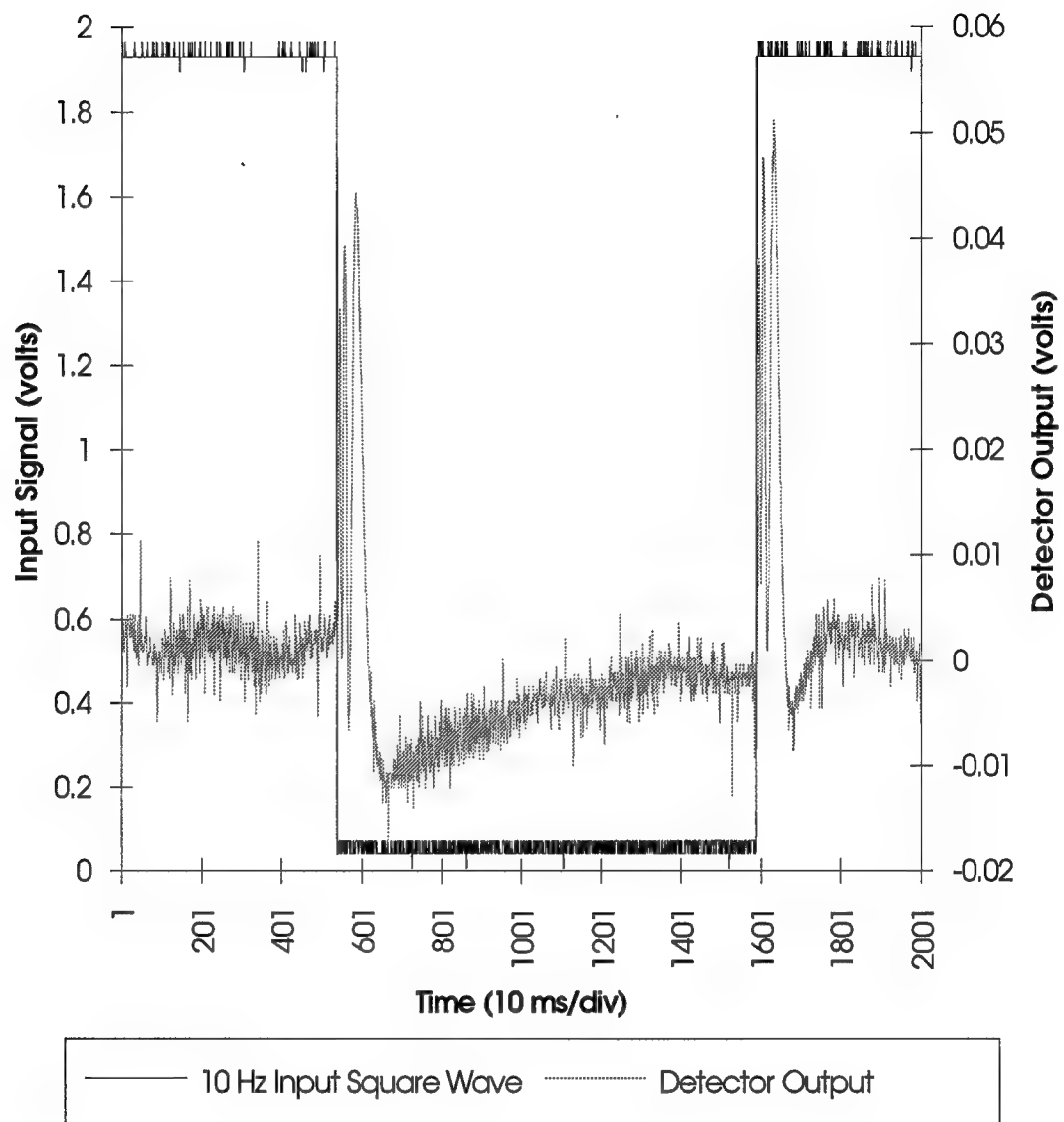


Figure 4.36. 2 volt, 1.55 mW peak power, 10 Hz, square wave input to beam U-7 (1,2,3,5,6,7 layer combination) measuring 1 μm .

The data also indicates that the heating and cooling times do not change significantly over the range of frequencies. From this we can determine the average heating and cooling times and the cutoff frequency at this power setting. The heating and cooling times for each of the data plots shown in Figures 4.32 through 4.36 are given in Table 4.2. Based on the average heating rate, a cutoff frequency of 130 Hz is obtained. Below this frequency the beam will completely heat and cool. Above this frequency, the beam will not have enough time to heat or cool and will not exhibit a complete deflection.

Table 4.2. Heating and Cooling Times for a Range of Frequencies on Beam U-7.

Frequency (Hz)	Heating time (ms)	Cooling time (ms)
60	--	3.58
50	4.17	3.93
40	3.825	4.165
40	4.0	--
30	3.775	3.925
30	--	3.75
20	4.075	3.875
11	3.3	3.35
10	3.65	3.9
Average	3.829	3.810

4.6.3.3. Beam Deflection for Triangle Wave Input. The frequency test described above was repeated using a triangle wave. A sample triangle wave input and interferometer output are shown in Figure 4.37. Similar data was taken for the range of

frequencies from 1 Hz to 60 Hz. The results are shown in Figure 4.38. This information indicates that as the frequency increases the beam does not have time to completely cool when using this form of input signal. This is due to the beam having a hotter average temperature as the frequency increases.

4.6.4. Comparison of Input Signals. In order to determine which input signal provides the most beam deflection, a square wave, a triangle wave, and a sine wave were used as inputs to the same beam. The peak voltage and frequency were held constant over the course of the test. The three wave produced the data given in Figures 4.39 through 4.41. The comparison of the three waves is shown in Figure 4.42. It is obvious from this information that at low frequencies there is no change in beam deflection caused by the wave form of the input signal.

4.6.5. Contour Plot During Actuation. The next test was to determine the contour of a typical beam as it deflects. Beam U-7 was used as the test beam. Deflection measurements were taken along the middle of the beam from its tip to near the base. The beam is 300 μm long from the base to the tip and it is pre-buckled up a total of 30 μm . The deflection measured is into the substrate. Figures 4.43 through 4.47 show the contour of the beam for varying voltages from 2 volts to 6 volts. Figure 4.48 is a combination of all these plots. Visual inspection appears to confirm the theoretical assumption that the beams deflect with constant radius of curvature.

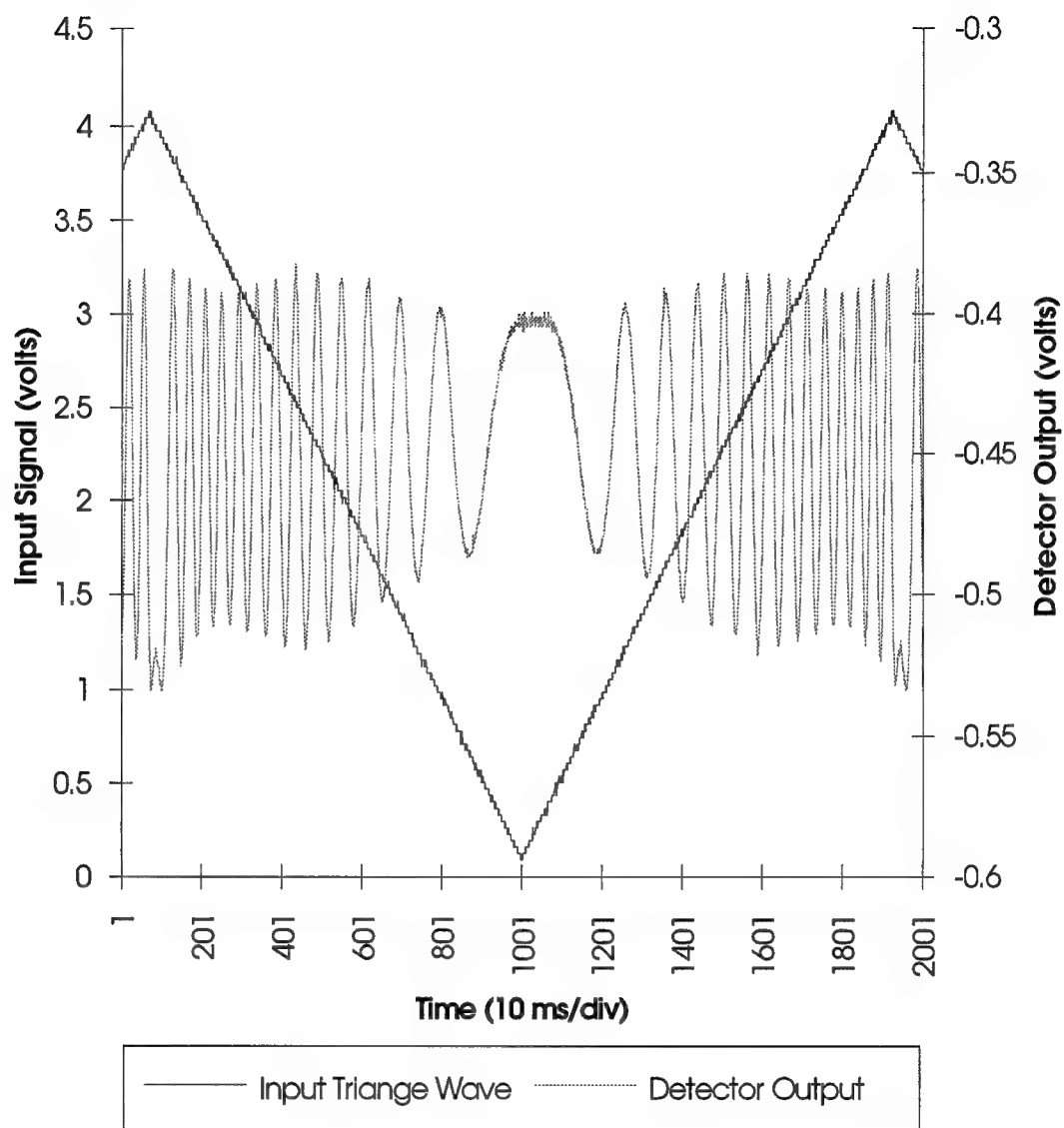


Figure 4.37. 4 volt, 5.7 mW peak power, 11 Hz, triangle wave input to beam U-7
(1,2,3,5,6,7 layer combination) measuring 4.3 μm .

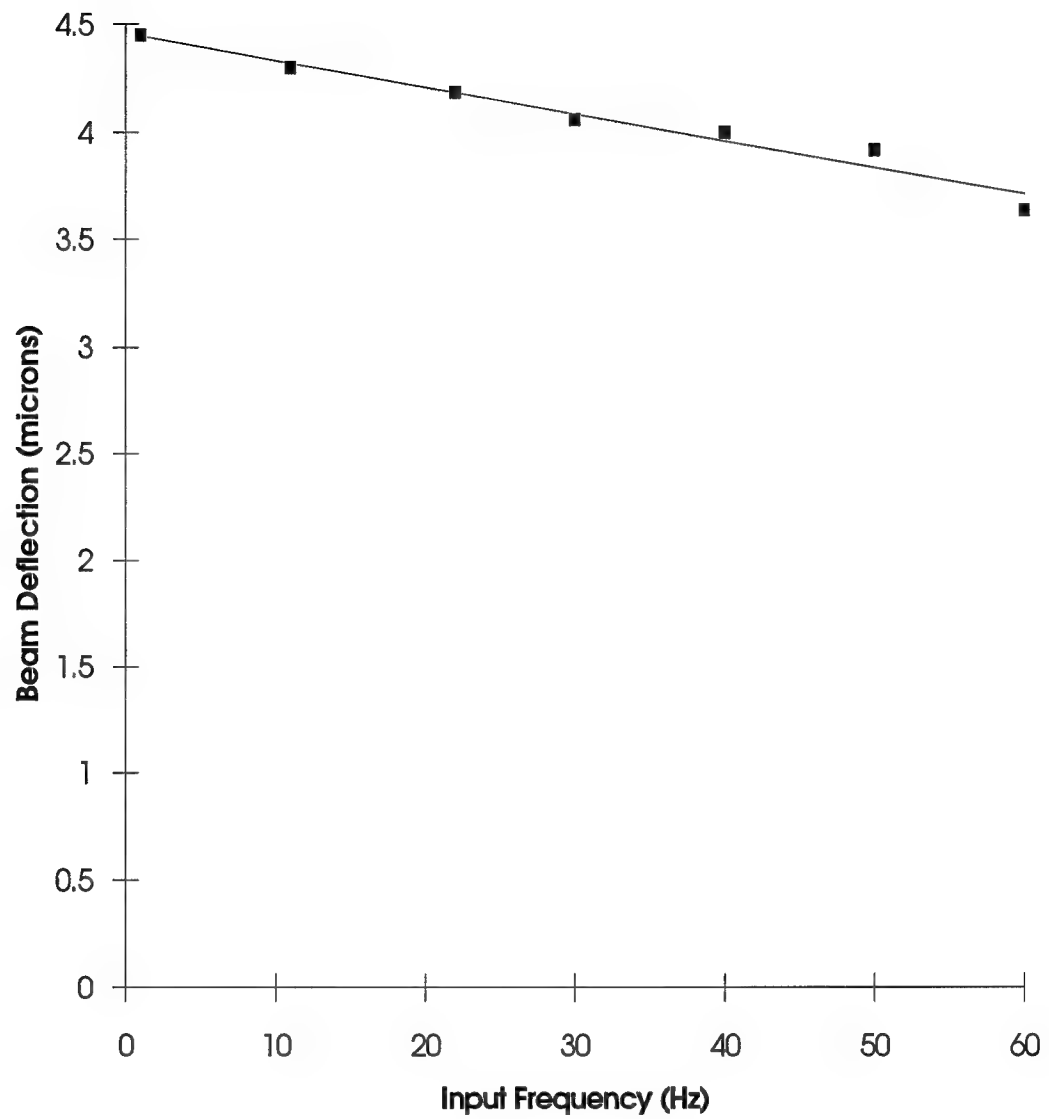


Figure 4.38. Deflection versus frequency for a triangle wave input to beam U-7
(1,2,3,5,6,7 layer combination).

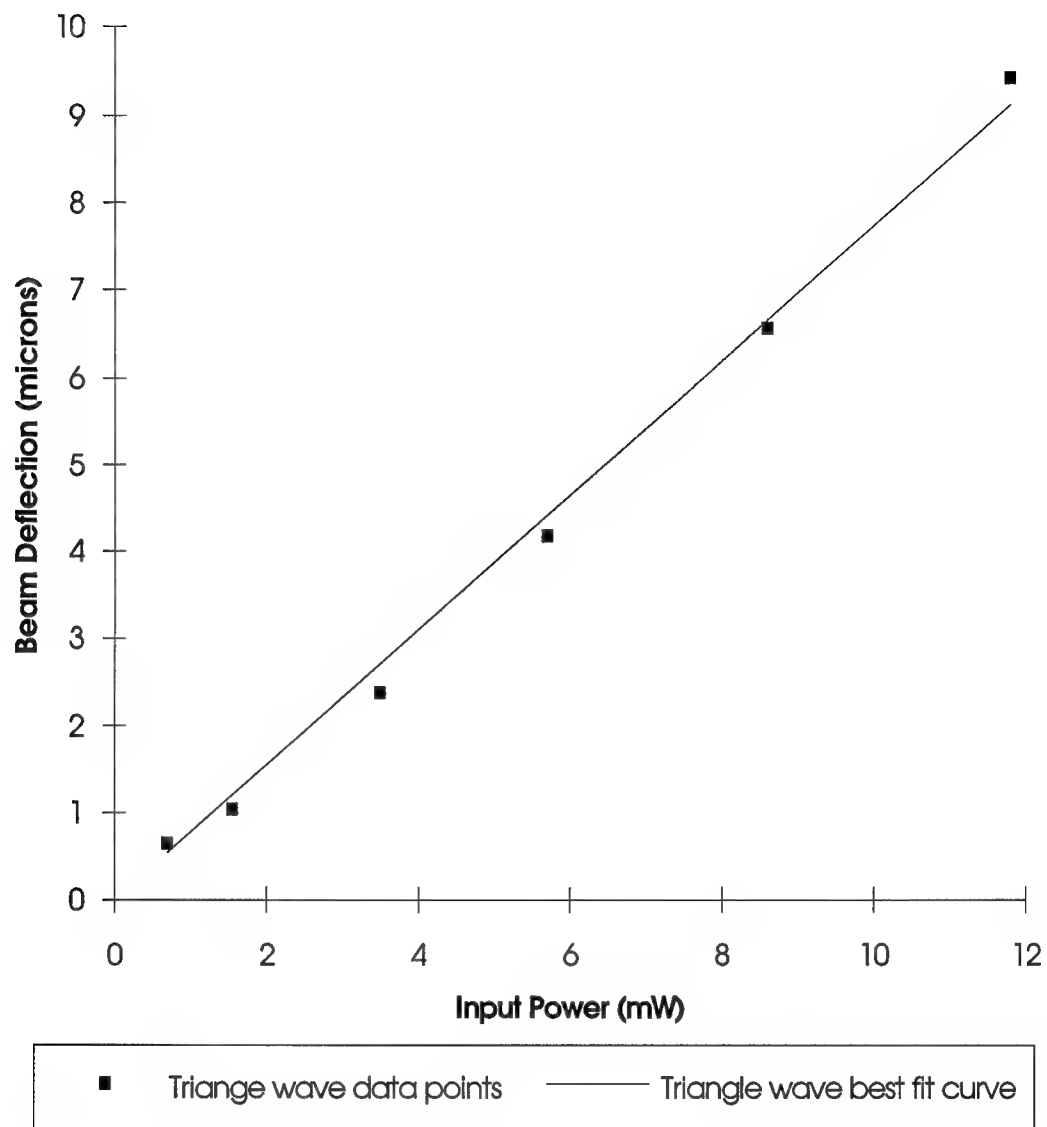


Figure 4.39. Deflection versus peak power for triangle wave input to beam U-7
(1,2,3,5,6,7 layer combination) at 20 Hz.

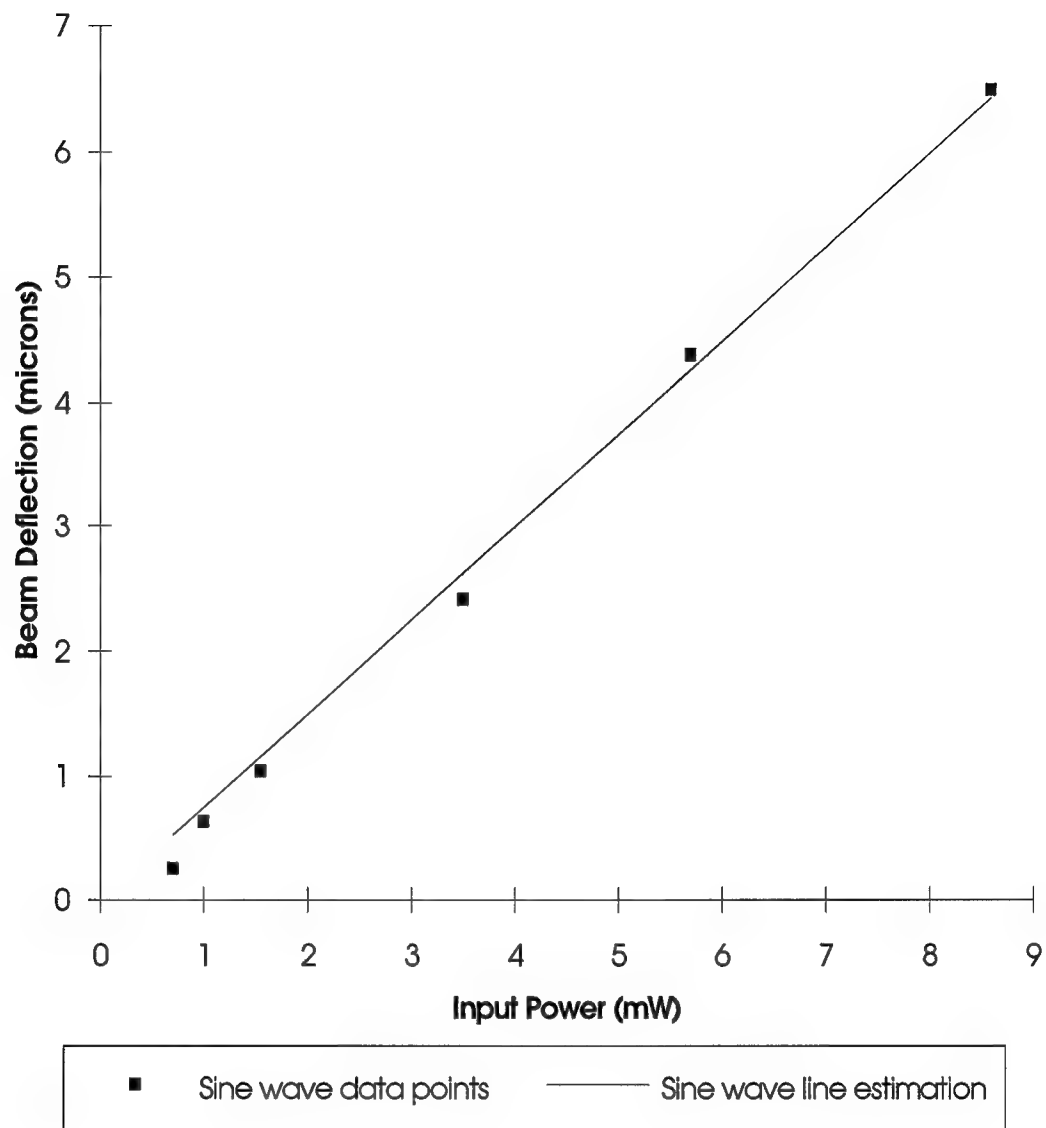


Figure 4.40. Deflection versus peak power for sine wave input to beam U-7 (1,2,3,5,6,7 layer combination) at 20 Hz.

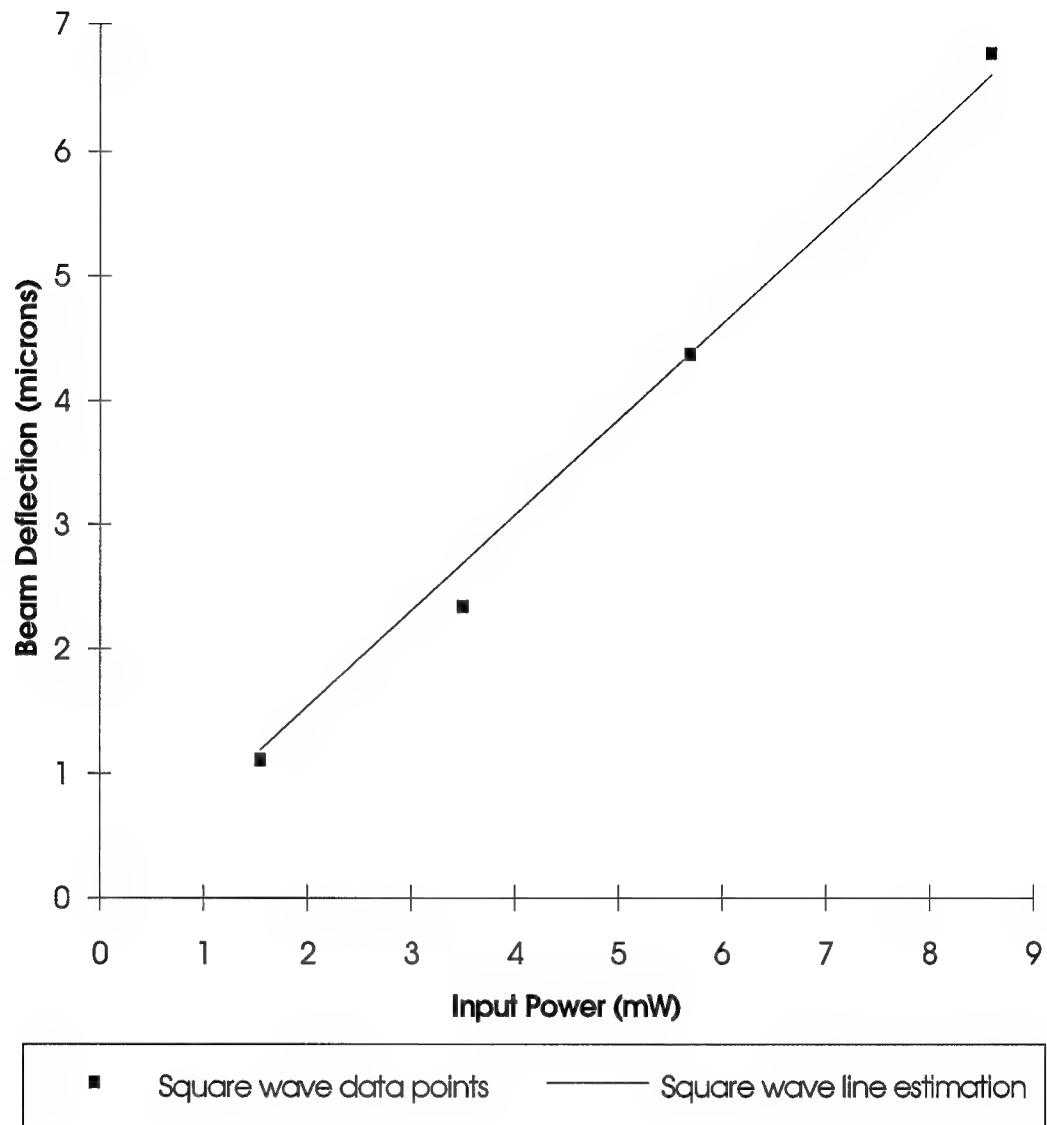


Figure 4.41. Deflection versus peak power for square wave input to beam U-7
(1,2,3,5,6,7 layer combination) at 20 Hz.

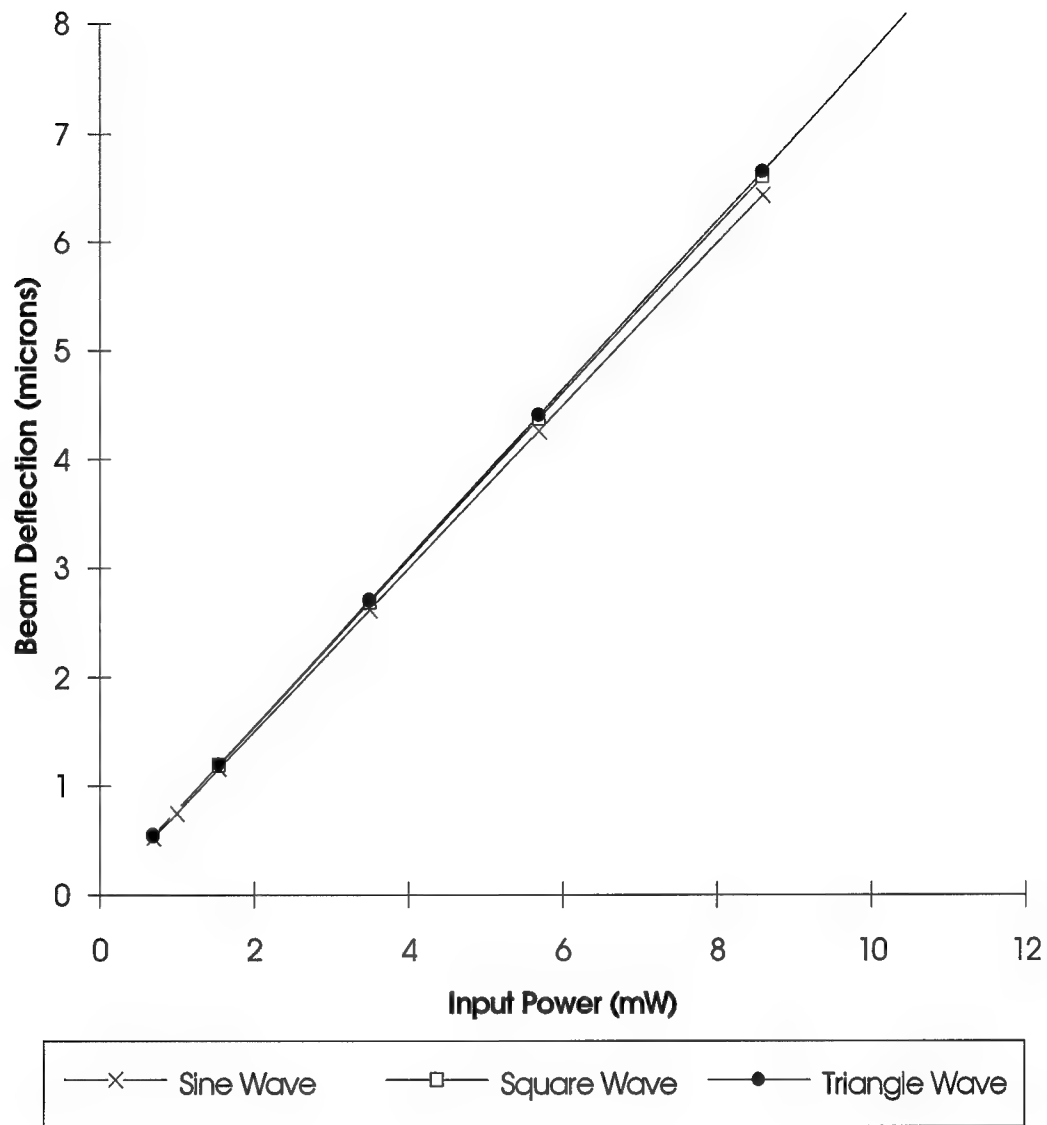


Figure 4.42. Deflection comparison of the three waveforms used as input to beam U-7 (1,2,3,5,6,7 layer combination) at 20 Hz.

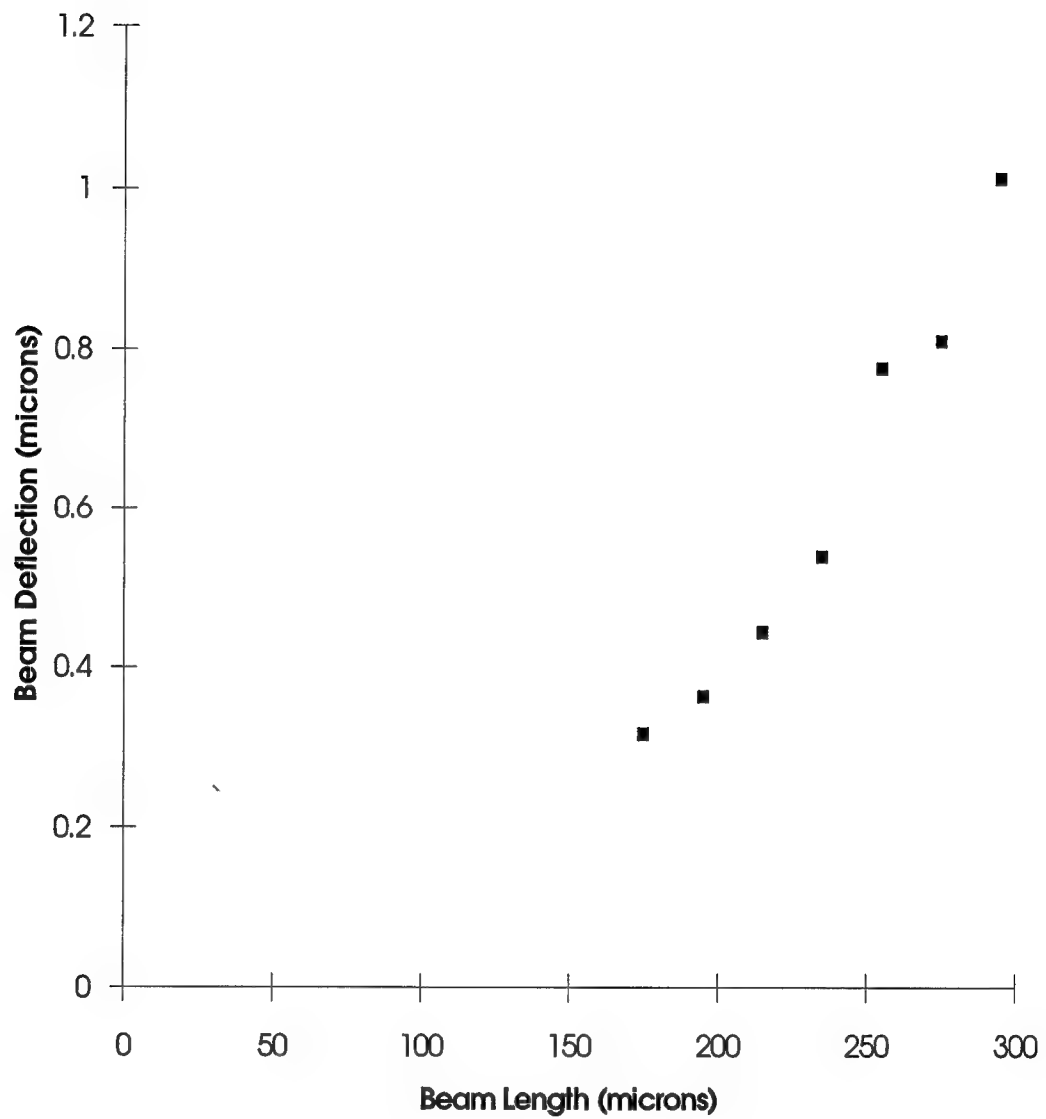


Figure 4.43. Contour plot of beam U-7 (1,2,3,5,6,7 layer combination) with a 20 Hz, triangle wave at 1.55 mW peak power.

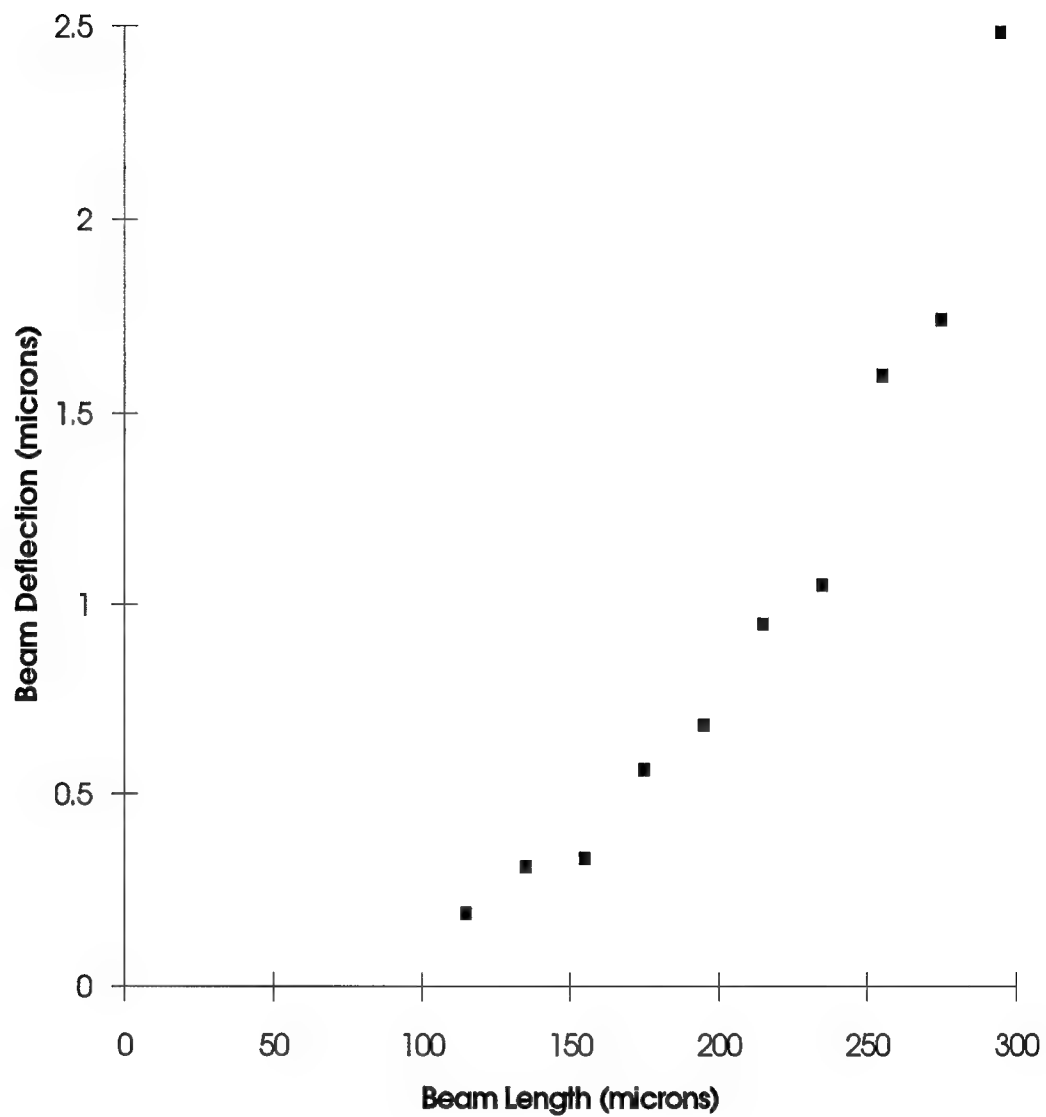


Figure 4.44. Contour plot of beam U-7 (1,2,3,5,6,7 layer combination) with a 20 Hz, triangle wave at 3.5 mW peak power.

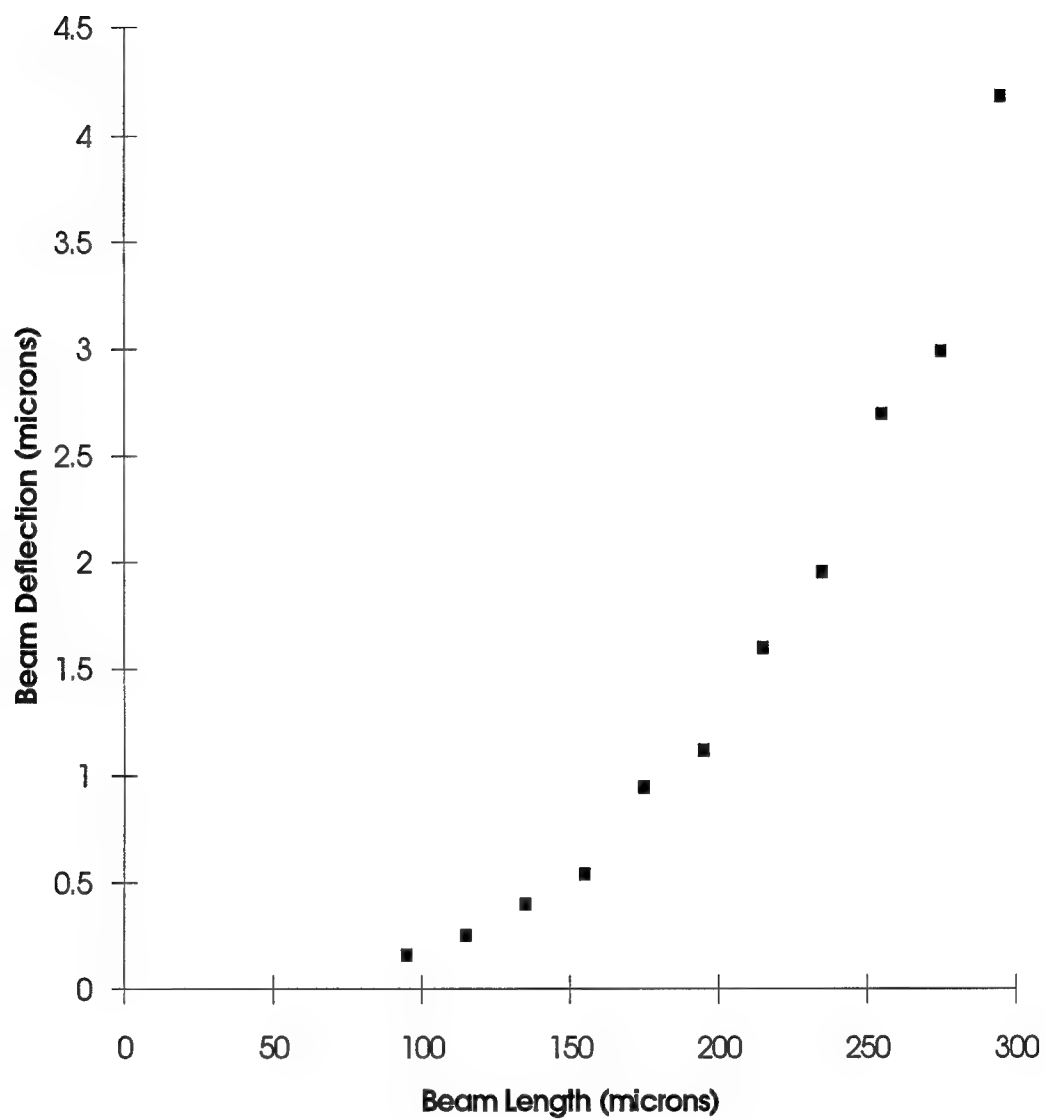


Figure 4.45. Contour plot of beam U-7 (1,2,3,5,6,7 layer combination) with a 20 Hz, triangle wave at 5.7 mW peak power.

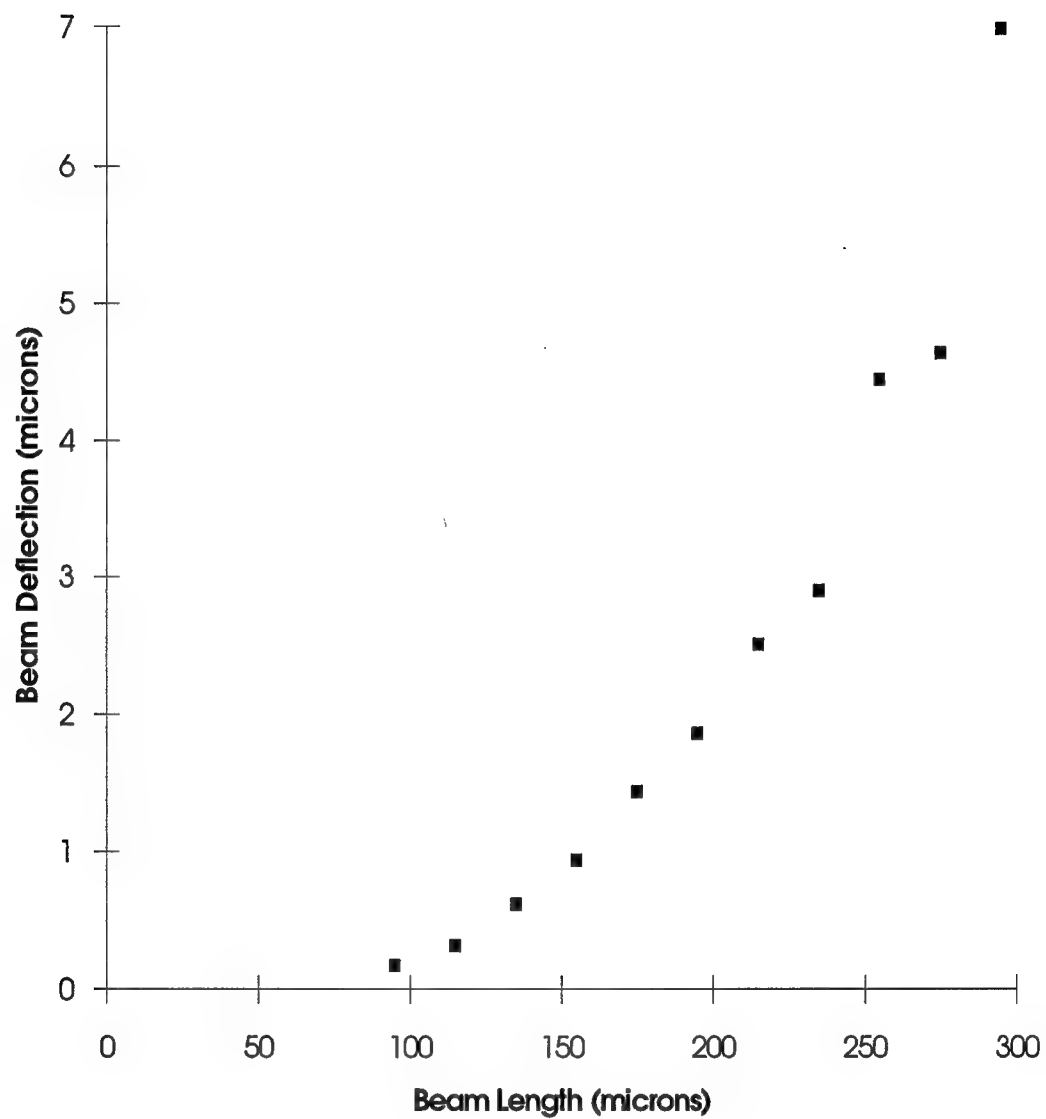


Figure 4.46. Contour plot of beam U-7 (1,2,3,5,6,7 layer combination) with a 20 Hz, triangle wave at 8.6 mW peak power.

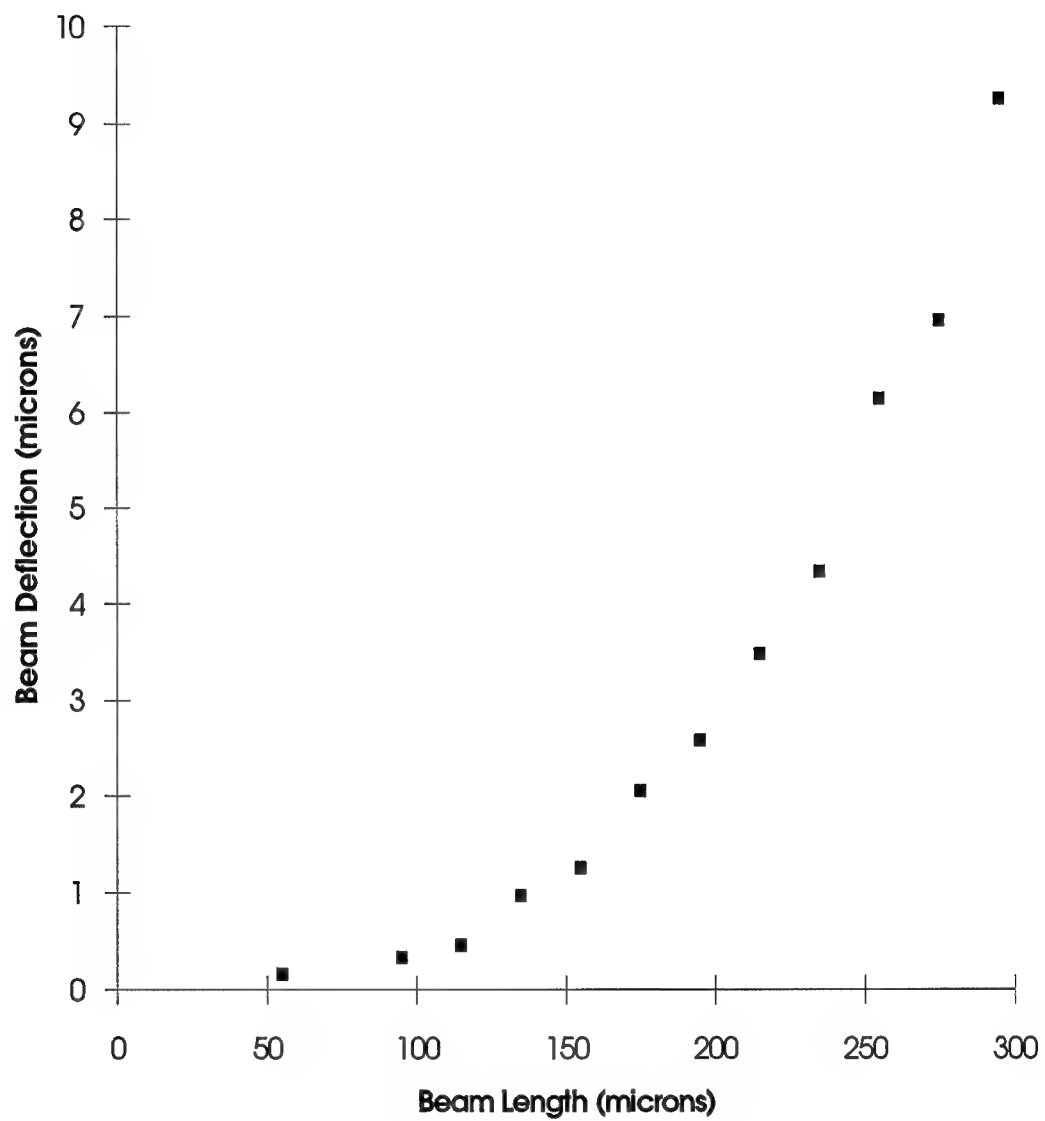


Figure 4.47. Contour plot of beam U-7 (1,2,3,5,6,7 layer combination) with a 20 Hz, triangle wave at 11.8 mW peak power.

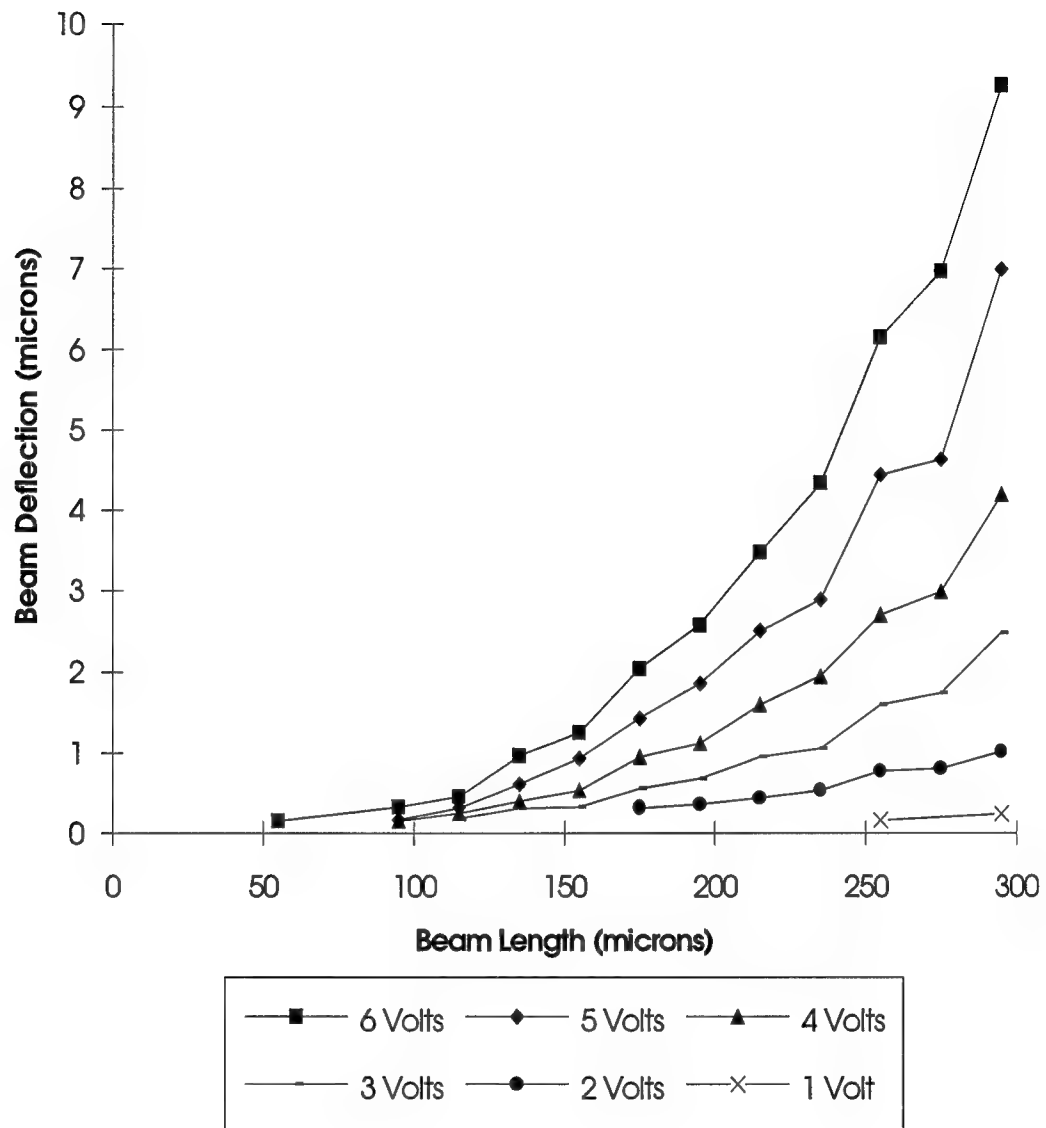


Figure 4.48. Contour plots of beam U-7 (1,2,3,5,6,7 layer combination) with a 20 Hz, triangle wave from 1 to 6 peak volts.

4.6.6. Layer Test Using Interferometer. The layer test described in Section 4.4.1.4. was repeated using the laser interferometer instead of the optical microscope measurements. More beams were tested and the results are given below. Figures 4.49 through 4.58 give the deflection versus input electrical power for 11 of the 12 combinations of beams listed in Table 3.4 along with the theoretical predicted measurement. Figure 4.59 compiles all these results into one chart. The data collected measures fairly well with the theoretical information. One possible source of error is that only 3 data points were taken for each beam at low power settings. This reduces the accuracy of the estimated experimental deflection.

4.7. Finger Test.

The cantilever beams were tested on a finger. A Kapton film, 25.4 μm thick, was used to protect the devices from dirt and oil on the test finger. Stimulation was not detected over the full range of operating powers and frequencies. The Kapton film limits the deflection of the cantilever beams and likely caused the failure of this test. The cantilever beams held up well under testing. The beams withstood 15 rigorous tests before breaking.

The CMOS heating elements were tested using the Kapton film and a finger. The heating elements glowed white hot before the finger was applied and had a response time of less than 0.1 seconds. This temperature was not enough to melt the Kapton film. The heater required a power of 0.7 W to stimulate the finger. When the finger was applied, the response time was over 1 second. This delay in response is due to either the slow response of the nerve endings in the finger or to the finger acting as a heat sink and slowing the heating time of the element. There was a definite localized point sensation rather than a large area sensation. This indicates that heating elements could be used as a tactile stimulator. The heat resolution test was not performed due to lack of time.

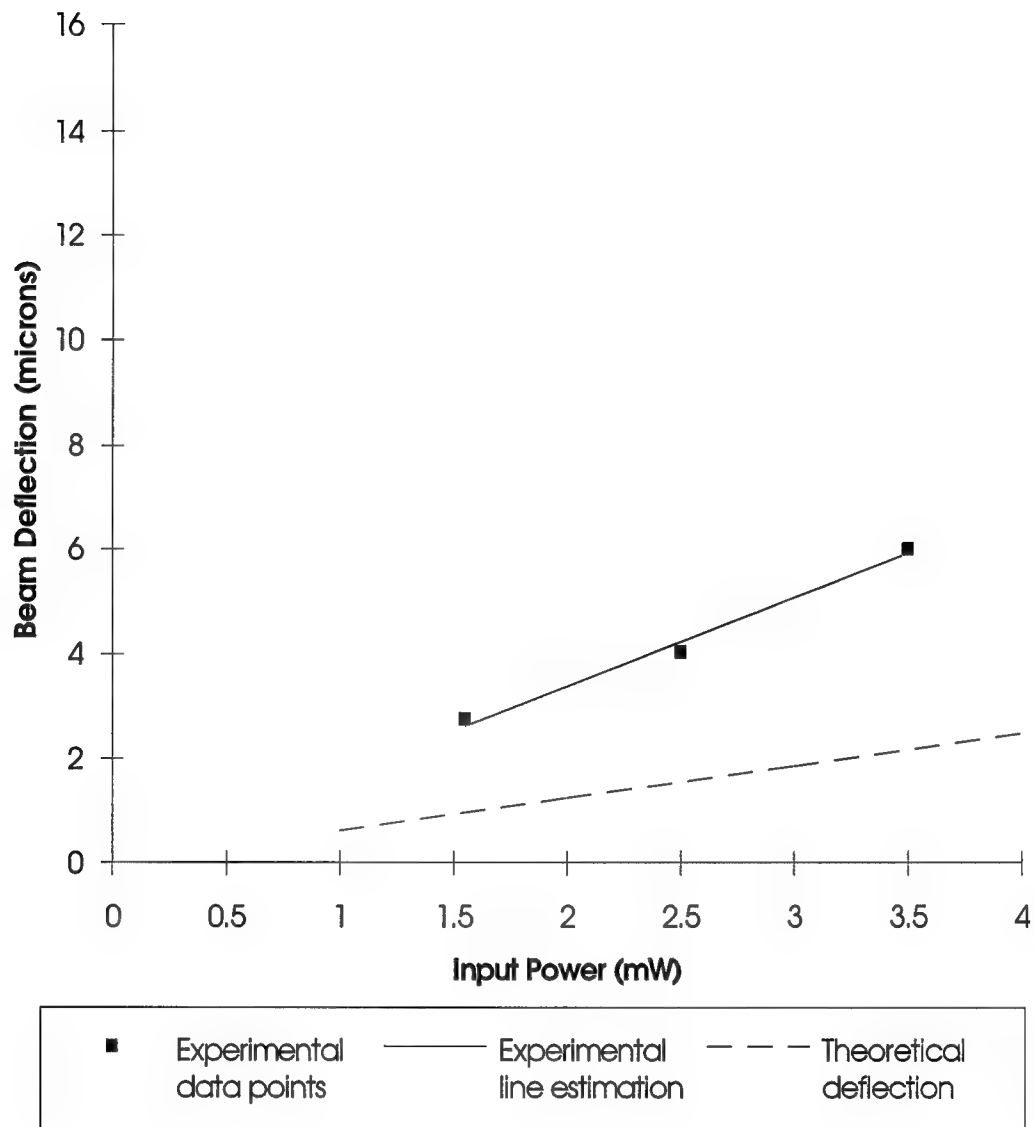


Figure 4.49. Experimental and theoretical beam deflection versus input electrical power for beam S-1 (1,3,4,5,6,7 layer combination) with a 20 Hz, triangle wave input.

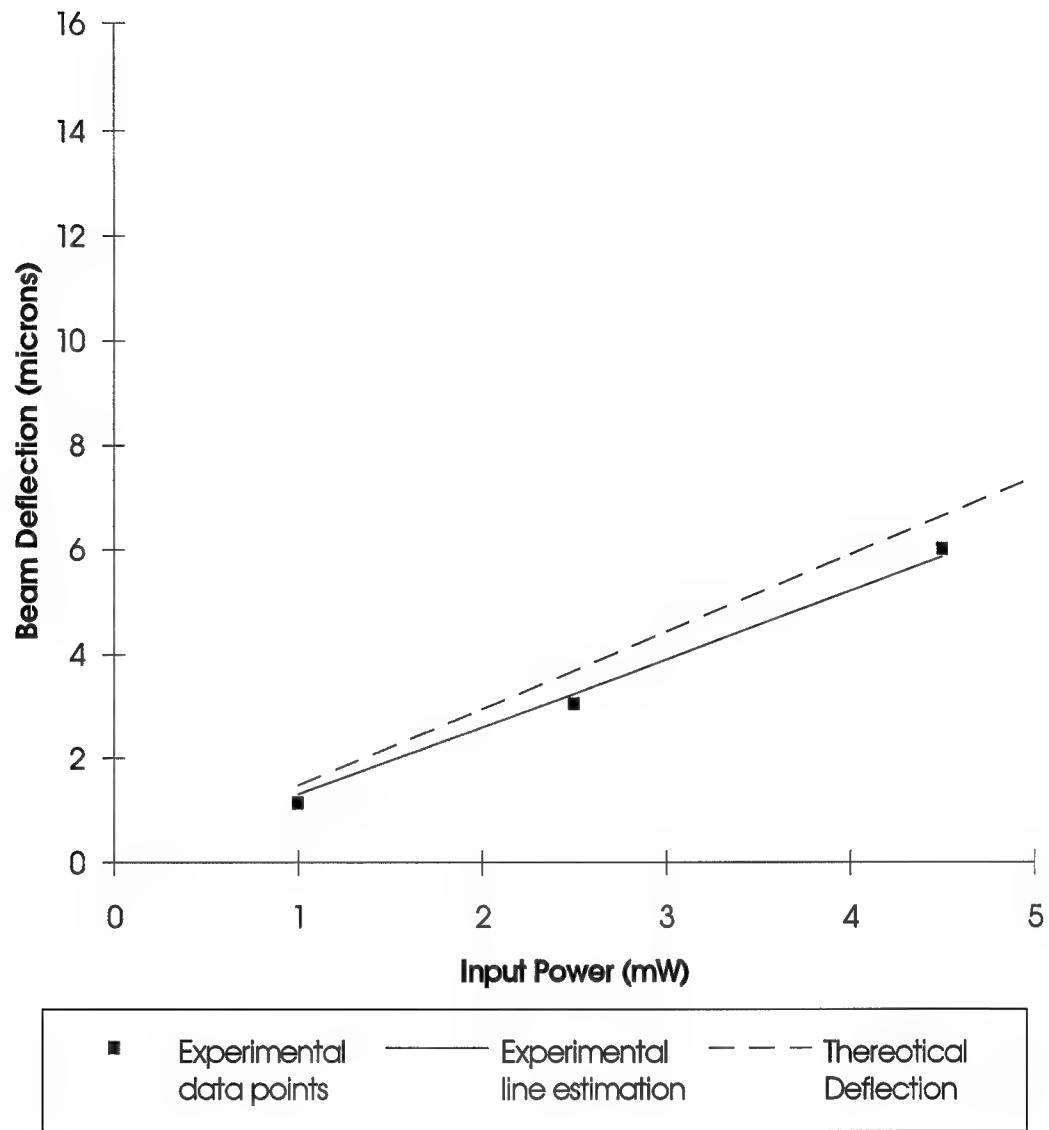


Figure 4.50. Experimental and theoretical beam deflection versus electrical input power for beam S-2 (1,2,3,5,7,8 layer combination) with a 20 Hz, triangle wave input.

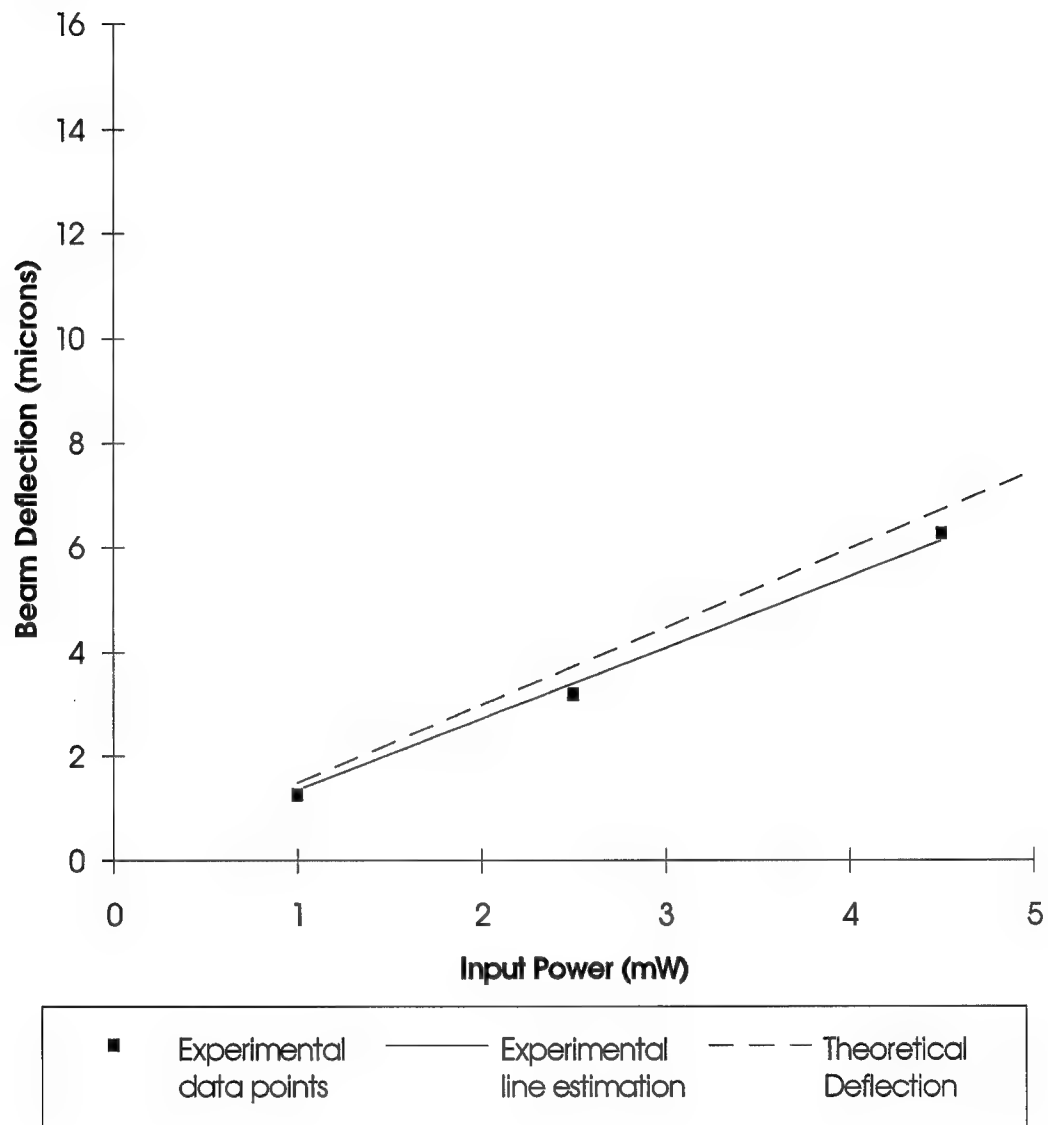


Figure 4.51. Experimental and theoretical beam deflection versus electrical input power for beam S-3 (1,3,4,5,7,8 layer combination) with a 20 Hz, triangle wave input.

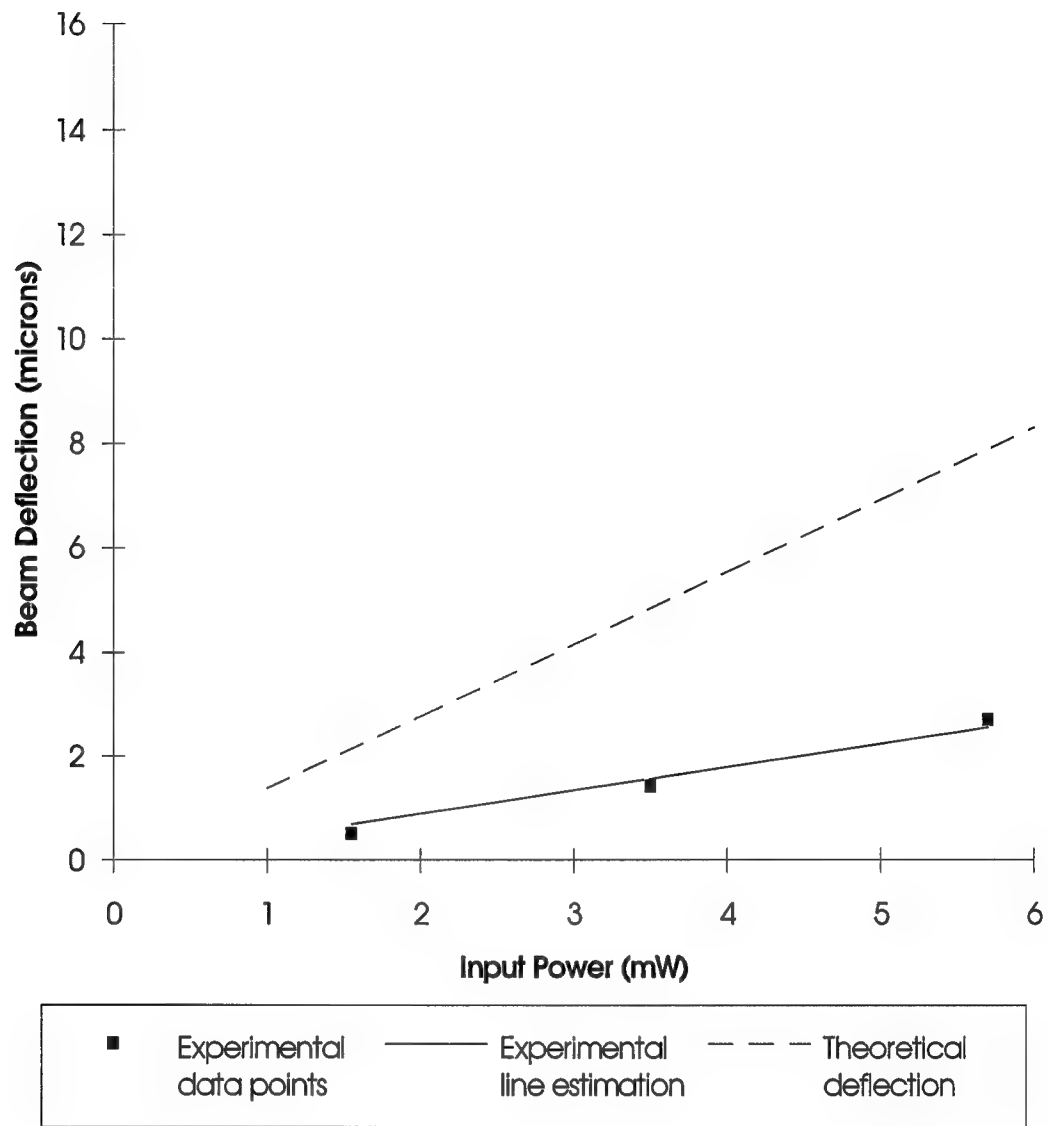


Figure 4.52. Experimental and theoretical beam deflection versus electrical input power for beam I-4 (1,3,5,6,7,8 layer combination) with a 20 Hz, triangle wave input.

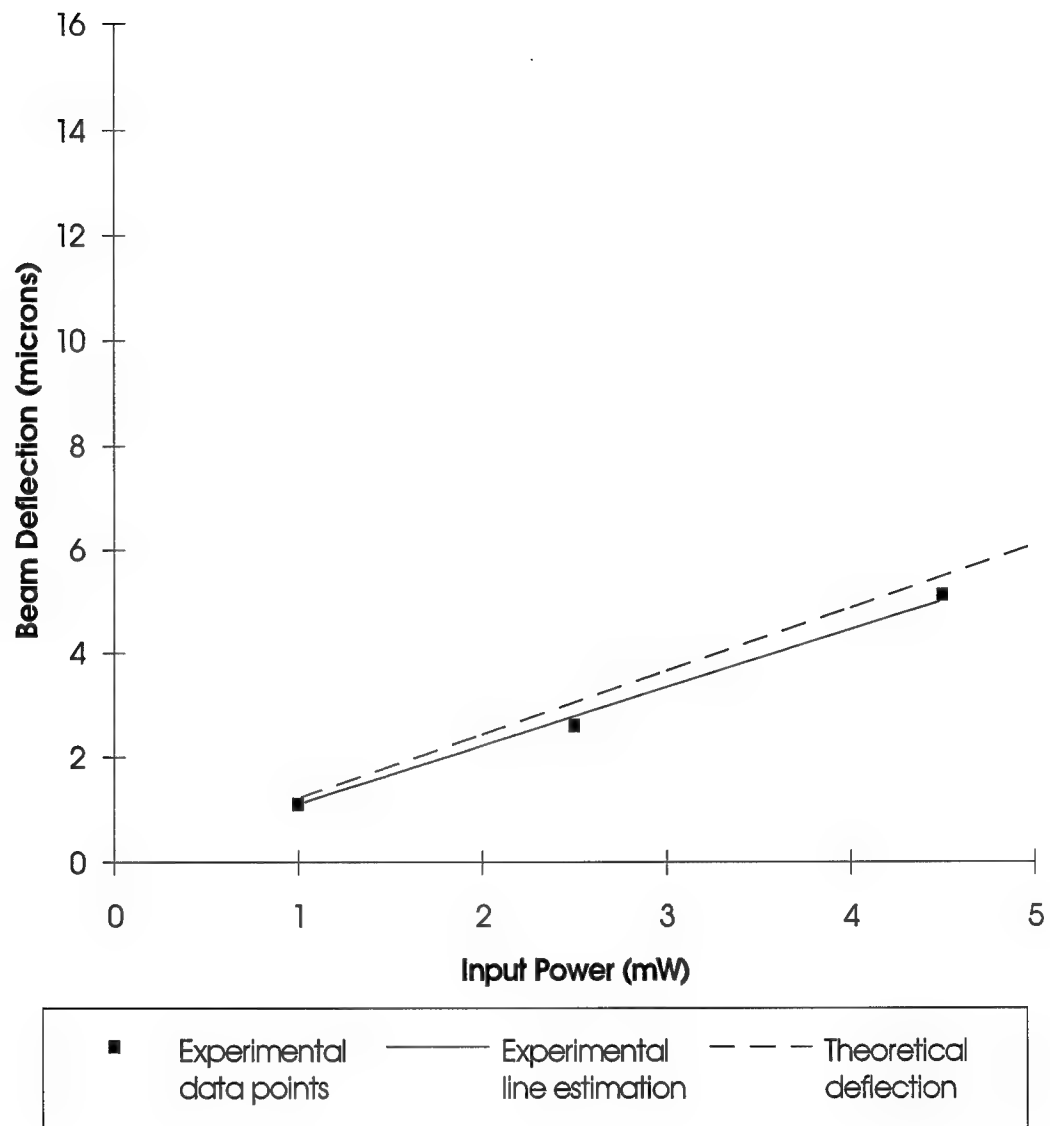


Figure 4.53. Experimental and theoretical beam deflection versus electrical input power for beam S-5 (1,2,3,5,6,7,8 layer combination) with a 20 Hz, triangle wave input.

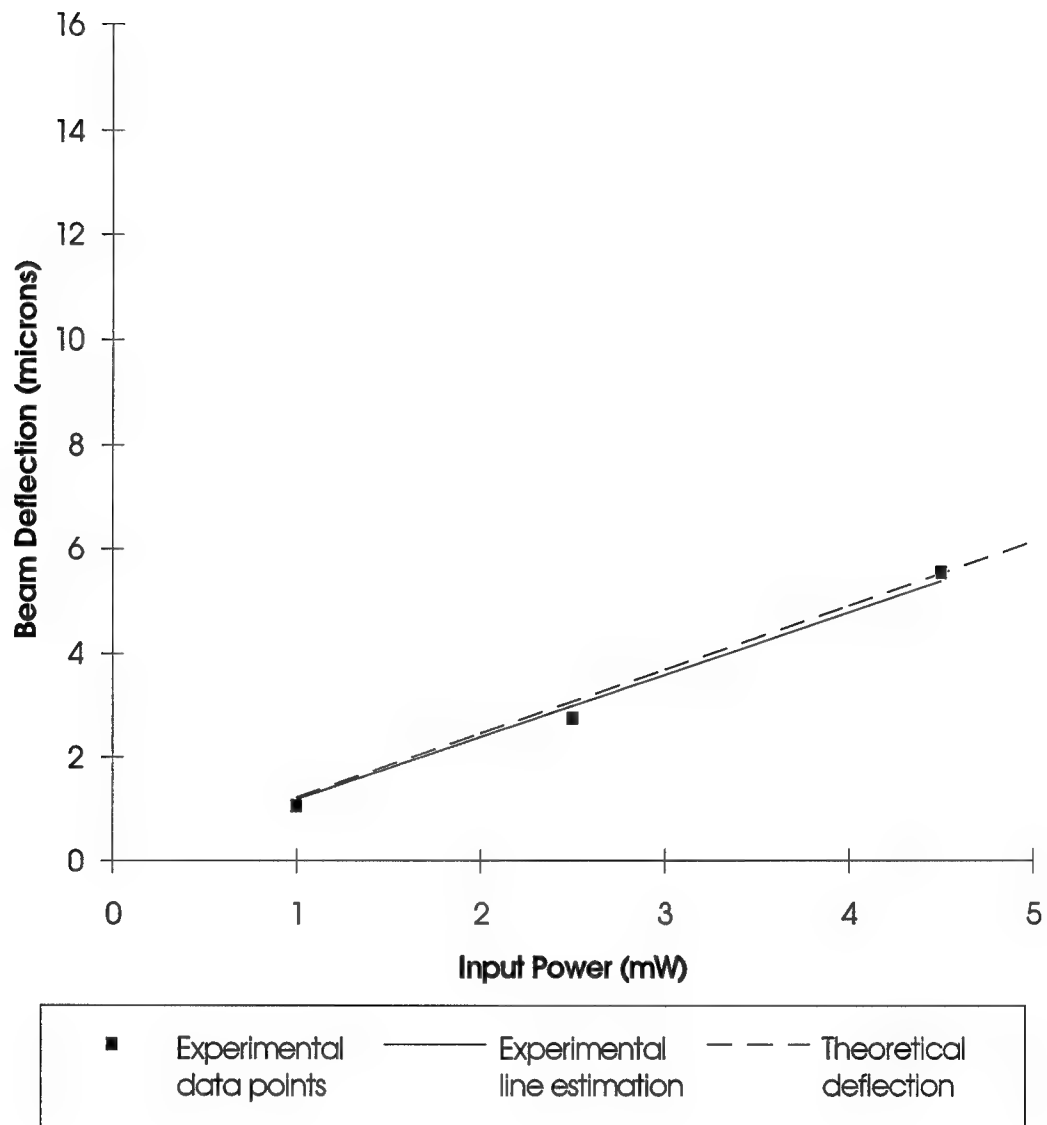


Figure 4.54. Experimental and theoretical beam deflection versus electrical input power for beam S-6 (1,3,4,5,6,7,8 layer combination) with a 20 Hz, triangle wave input.

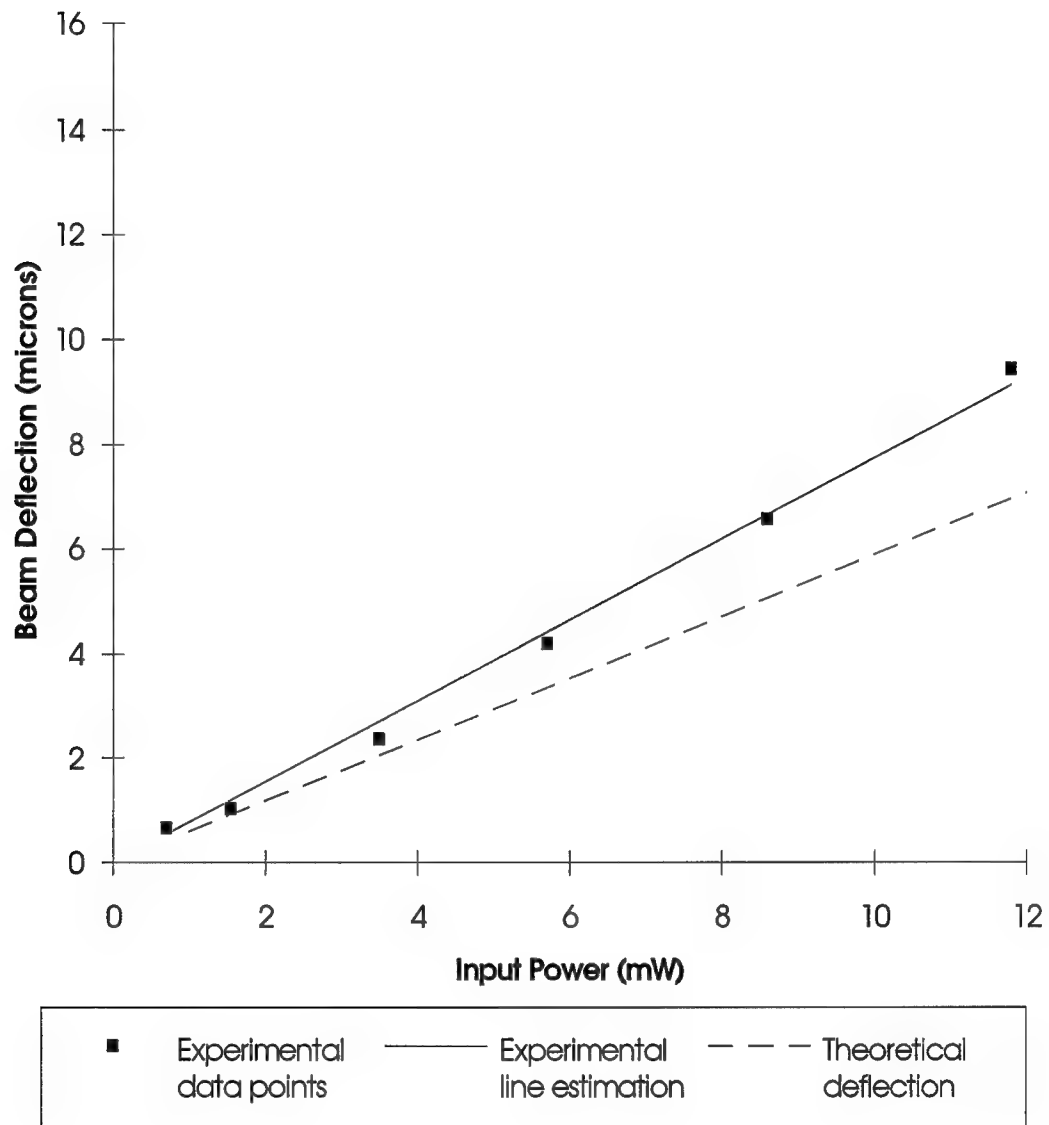


Figure 4.55. Experimental and theoretical beam deflection versus electrical input power for beam U-7 (1,2,3,5,6,7 layer combination) with a 20 Hz, triangle wave input.

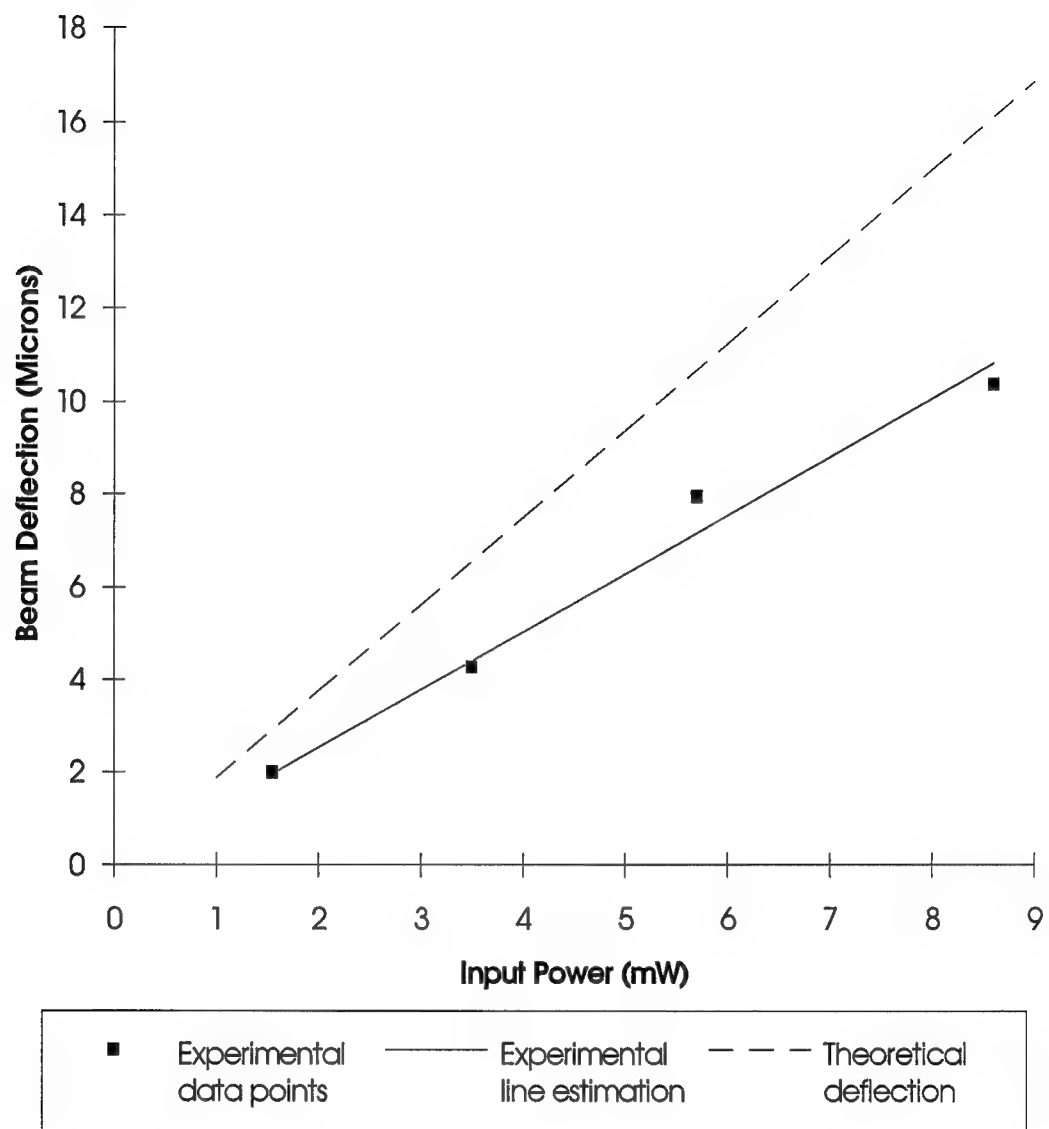


Figure 4.56. Experimental and theoretical beam deflection versus electrical input power for beam U-8 (1,3,5,7,8 layer combination) with a 20 Hz, triangle wave input.

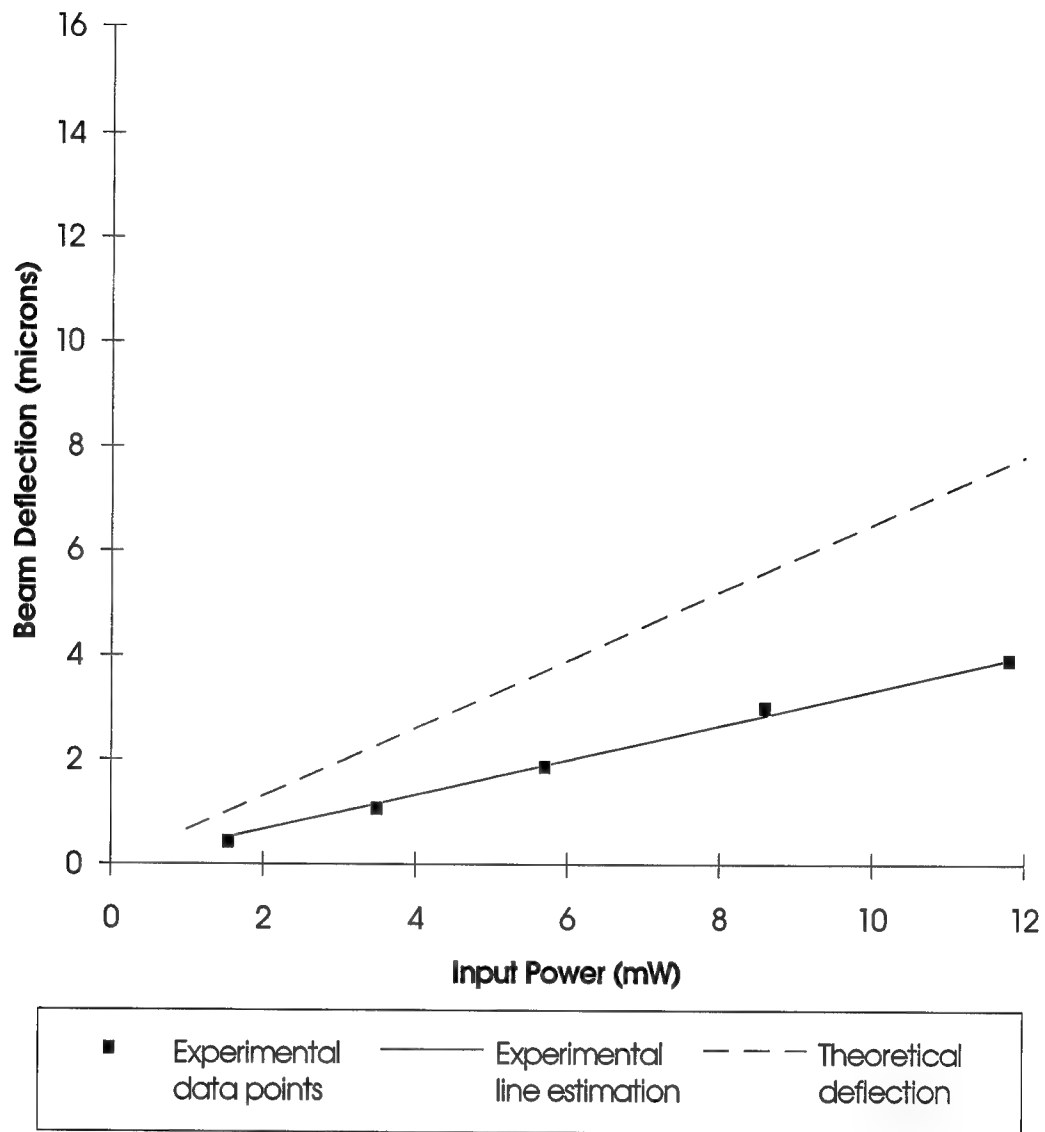


Figure 4.57. Experimental and theoretical beam deflection versus electrical input power for beam S-9 (1,3,5,6,7 layer combination) with a 20 Hz, triangle wave input.

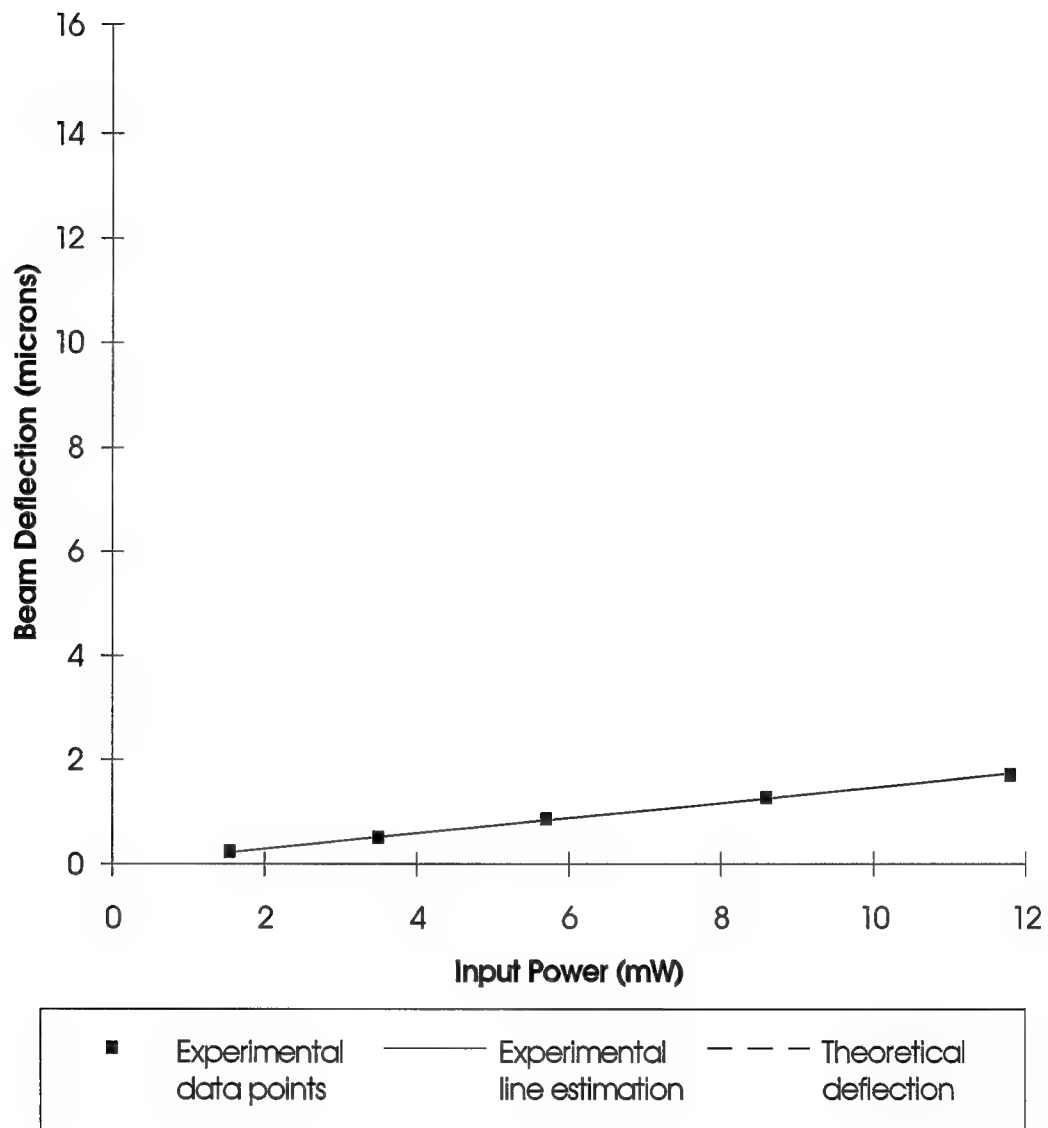


Figure 4.58. Experimental and theoretical beam deflection versus electrical input power for beam S-12 (1,3,5,7,9 layer combination) with a 20 Hz, triangle wave input.

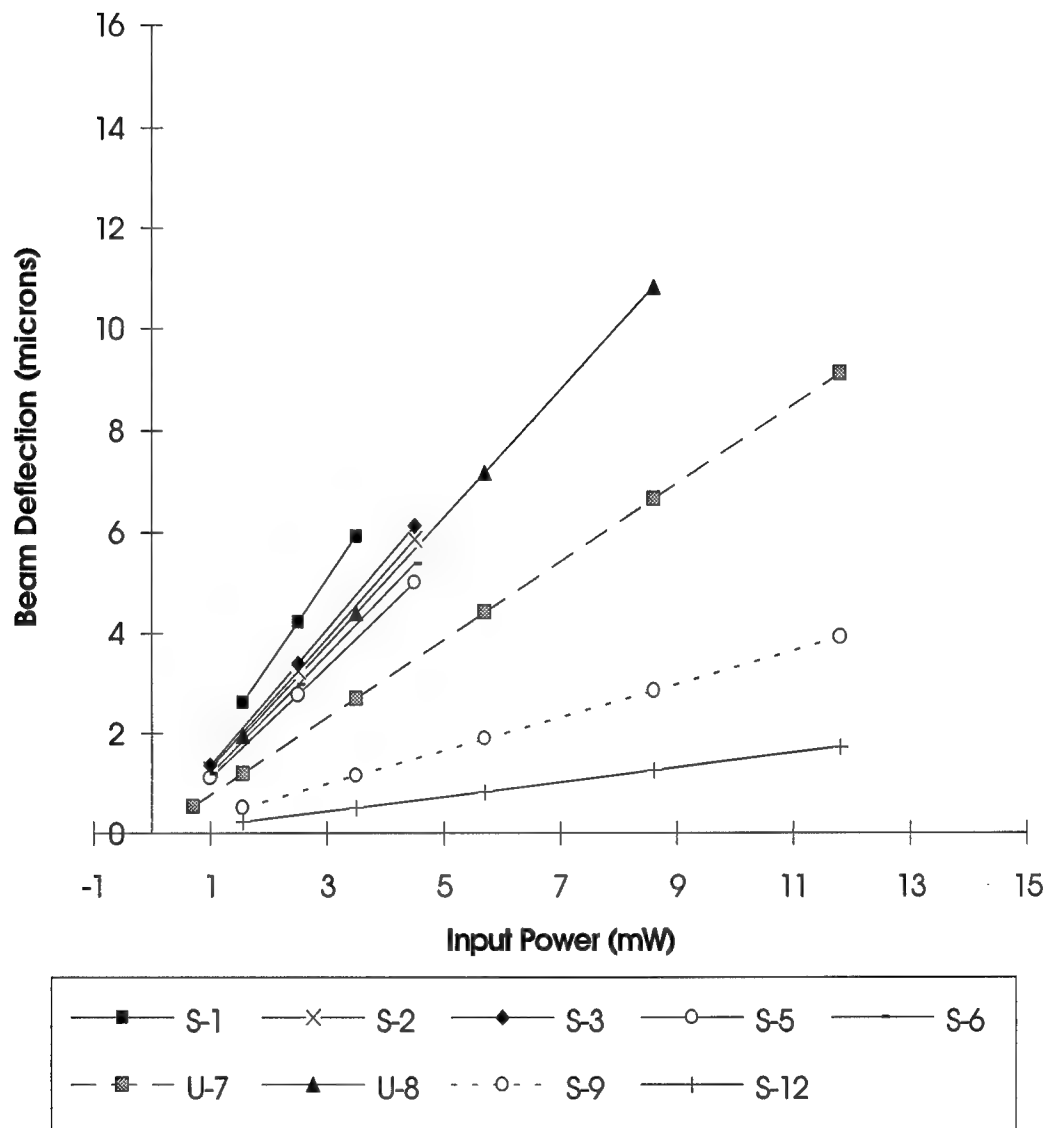


Figure 4.59. Best fit curves of beam deflection versus electrical input power for beams constructed of different material combinations with a 20 Hz, triangle wave input.

4.8. Summary of Experimental Results.

The results of testing of the designs described in Chapter 3 were presented in this chapter. The designs were fabricated, etched, and tested using a variety of methods. A summary of the results is given below.

There were some problems in fabrication of the CMOS chips. The entire second chip, Traychip 2, was not releasable and therefore not testable. MOSIS is aware of the problem and is attempting to solve it. The only problem with the fabrication of the MUMPS chip was the corrosion of the metal layer. The etching was accomplished without any major problems. The etching times were determined by using etch gauges.

The MUMPS chip was tested using the optical microscope. The devices required voltages of over 70 volts. The deflections from these devices were below 3 μm . The devices had the potential to operate at very high frequencies.

Most of the designs on Traychip 1 were tested using the optical microscope, the force tester, and the laser interferometer. The bimorph beams (300 μm long by 150 μm wide) performed extremely well. Beams deflections of up to 50 μm were obtained with under 50 mW of power. The beams perform under loads of up to 15 mg. They had an operating frequency of as high as 140 Hz at low input power (1.55 mW). Also, the beams showed no sign of wear after 2.5 million actuations. In conclusion, the bimorph beams from Traychip 1 had the performance characteristics needed for a tactile stimulator.

5. CONCLUSIONS AND RECOMMENDATIONS

This chapter summarizes the work accomplished in this thesis. The key results are summarized for the devices that were tested. Recommendations and suggestions are offered for further studies in this area.

5.1. Conclusions.

The purpose of this research was to investigate the feasibility of using microelectromechanical devices as tactile stimulators. MEM devices have not previously been investigated as tactile stimulators. The tactile stimulator would be used to convey information to the human finger. A good tactile stimulator would have several important characteristics.

5.1.1. Requirements for a Tactile Stimulator.

1. The stimulator should be small and lightweight. It should be small enough to fit into a glove of the human operator. It should be lightweight and portable enough to go into any environment.

2. The tactile simulator should operate at low voltage and power levels. It should be compatible with standard TTL voltages to insure compatibility with other systems.

3. It should provide high resolution information. The stimulators should have a minimum spacing of 0.5 mm on the finger since this is the resolution of the nerve endings. This would mean a 20x20 array for a 1 cm² area on the fingertip.

4. It should provide both static and dynamic operation. The device should operate up to 400 Hz which is the detection limit of the nerves on the finger.

5. The device should be safe for a human operator. It should not have high voltages, currents or temperatures.

6. The device should be robust and have a long operating lifetime.

Current tactile stimulators do not adequately meet all of the above criteria. As a possible better solution, MEM devices were designed, fabricated, and tested to determine if they could operate as a tactile stimulator and meet the above criteria.

5.1.2. MEM Designs. Two major designs were examined and tested. The MUMPS process was used for electrostatic designs, and the CMOS process was used for bimorph beams. MEM devices met several of the tactile stimulation criteria presented above. MEM devices are inherently small; the average size of the devices is $300\text{ }\mu\text{m} \times 200\text{ }\mu\text{m}$. The devices are easily integrated on a silicon chip that is less than 1 cm^2 . A final advantage to the MEM devices is that they are highly reproducible and inexpensive.

5.1.2.1. MUMPS Designs. The electrostatic devices from the MUMPS process that were tested had several drawbacks that limit their performance to act as tactile stimulators. The first drawback is the failure to meet criteria 2 and 5 above. Voltages of above 70 volts were required for actuation. These voltages are not only incompatible with other circuitry, but they could be potentially harmful to an operator who must come in contact with the device. The MUMPS devices in this thesis are limited to less than $3\text{ }\mu\text{m}$ of deflection which makes detection by the operator difficult. The more robust designs were the electrostatic cantilever designs and they had severe limitations, as described in Chapter 4. Due to these factors, the MUMPS electrostatic designs would not make effective tactile stimulators.

5.1.2.2. CMOS Designs. The bimorph beams designed with the CMOS process had much more potential to provide tactile stimulation. They do not have most of the problems that plague the MUMPS designs. Table 5.1 gives a summary of the results of the bimorph testing.

Table 5.1. Summary of Results of CMOS Bimorph Testing.

Property	Result
Typical deflection	25 μm
Typical operating voltage	6 volts
Typical operating current	2 mA
Typical operating frequency (3 mW peak power)	< 130 Hz
Typical mass load at tip	5 mg
Typical size	350 μm x 200 μm

The bimorph beams provide adequate deflection and force needed to stimulate the finger. They operate on TTL voltages and have relatively low power consumption. They are small enough to be put in an array of devices. They are the most structurally robust of all the MEM devices that were tested. The bimorph beams appear to have the capability to provide tactile stimulation.

5.1.2.3. Bimorph Problems. There are several limitations to the bimorph designs. Since the bimorph beams are thermally actuated, the operating speed is limited to the heating and cooling rate of the device. Performance of the designed beams (300 μm x 150 μm) began to deteriorate at 130 Hz. The load operation (5 mg typical) is at the lowest end of the human perception range. Also there are several problems that may

occur when the device is in contact with the human finger. The first is that the temperature of the beam when actuated is more than 100 °C. This could burn the operator if enough heat is transferred. Second, the performance of the device will change since some of the heat is transferred to the finger. A third problem with contacting the finger is the dirt and oils that would be transferred to the devices. These oils could possibly change the performance of the devices. Finally, without some form of protection it is very likely that the finger would physically damage some of the beams due to normal operation.

5.2. Recommendations.

There are several recommendations for future research into tactile stimulators using MEM devices.

1. Correct the problems with the MOSIS CMOS process. Without some changes any further designs may not fabricate correctly. Since the design phase is very time consuming, this problem should not be repeated.

2. Develop a protection for the MEM devices. If a wall could be built at the level of the tips of the beams, the finger would not be able to damage the MEM structures. This could be done by bonding a second chip to the first, or possibly by using a backside etch to allow the devices to stimulate the finger as it rests on the bottom of the chip.

3. Develop some protection from the oils and dirt on the finger. A coating should be developed to isolate the devices from the environment without limiting the performance of the devices.

4. Characterize the human finger better. With a more complete model of how the finger responds to stimulation, devices could be designed much more effectively.

5. Investigate in house fabrication and other fabrication sites. With a better fabrication control of the process, the stress induced curling of the MEM beams could be

reduced. Also, thicker metal layers could be deposited to produce more beam deflection and force.

The ideal beam would have multiple layers with each higher layer having a larger coefficient of thermal expansion. The resistor layer and isolation layers would be thin compared to the structural layers. Also the individual structural layers would be the same thicknesses. If only two structural layers are used, lead and oxide should be the materials since they have a large variation in thermal expansion coefficients.

6. Investigate other geometries of bimorph beams. A possible triangular beam with a wide base would have more support and could provide the same amount of deflection as a rectangular beam.

Appendix A: List of Common Acronyms

AFIT	=	Air Force Institute of Technology
BeCu	=	beryllium copper
CIF file	=	Caltech intermediate file
CMOS	=	complementary metal oxide semiconductor
DI	=	de-ionized
EDP	=	ethylene diamine pyrocatechol
HF	=	hydrofluoric acid
IC	=	integrated circuit
KOH	=	potasium hydroxide
MEM	=	microelectromechanical
MOSIS	=	MOS implementation system
MUMPS	=	multi-user MEM process
OPEN	=	bare silicon layer in CIF file
PC	=	pacinian corpuscle
PSG	=	phosphosilicate glass
PSTOP	=	doped silicon.
PZT	=	lead zirconate titanate
RA	=	rapid adapting
SEM	=	scanning electron microscope
Si	=	silicon
SMA	=	shape memory alloy
telerobotic	=	tactile sensor
TiNi	=	titanium nickel
TPDT	=	two point discrimination threshold
ZnO	=	zinc oxide

Bibliography

- [1] D. A. Kontarinis and R. D. Howe, "Tactile display of contact shape in dexterous telemanipulation," in *ASME Winter Annual Meeting-Session on Haptic Interfaces for Virtual Environment and Teleoperator Systems*, New Orleans, pp. 81-88, Nov. 1993.
- [2] J. C. Bliss, J. W. Hill, and B. M. Wilber, "Tactile perception studies related to teleoperator systems," NASA Technical Report CR-1775, Stanford Research Institute, Menlo Park CA, April 1971.
- [3] M. Mehregany, "Microelectromechanical systems," *IEEE Circuits and Devices*, pp. 14-22, July 1993.
- [4] C. Kim, A. P. Pissano, and R. S. Muller. "Silicon microgripper," *J. Micro-mechanical Sys.*, vol. 1, pp. 31-36, Mar. 1992.
- [5] A. D. Johnson, "Shape-memory alloy tactile feedback actuator," Technical Report AAMRL-TR-90-039, TiNi Alloy Company, 1144 65th Street, Oakland CA, Aug. 1990.
- [6] K. E. Petersen, "Silicon as a mechanical material," *Proc. IEEE*, vol. 70, pp. 420-457, May 1982.
- [7] J. Angell, S. C. Terry, and P. W. Barth, "Silicon micromechanical devices," *Scientific American*, vol. 248, pp. 44-57, Apr. 1983.
- [8] R. T. Howe, "Surface micromachining for microsensors and microactuators," *J. Vac. Sci. Technol. B*, vol. 6, pp. 1809-1813, Nov./Dec. 1988.
- [9] J. C. Marshall, M. Parameswaran, M. E. Zaghloul, and M. Gaitan, "High-level CAD melds micromachined devices with foundries," *IEEE Circuits and Devices*, vol. 8, pp. 10-17, Nov. 1992.
- [10] K. W. Markus and D. A. Koester, "Multi-User MEMS Process (MUMPS) introduction and design rules," MCNC Electronics Tech. Div., 3021 Cornwallis Road, Research Triangle Park, North Carolina, Mar. 1994.
- [11] J. S. Suehle, R. E. Cavicchi, M. Gaitan, and S. Semancik, "Tin oxide gas sensor fabricated using CMOS micro-hot plates and in-situ processing," *IEEE Electron Device Letters*, vol. 14, pp. 118-120, Mar. 1993.

- [12] J. Y. Chang, A. A. Abidi, and M. Gaitan, "Large suspended inductors on silicon and their use in a 2 micron CMOS RF amplifier," *IEEE Electron Device Letters*, vol. 14, pp. 246-248, May 1993.
- [13] M. Parameswaran, R. Chung, M. Gaitan, R. B. Johnson, and M. Syrzychi, "Commercial CMOS fabricated integrated dynamic thermal scene simulator," in *IEEE IEDM*, pp. 29.4.1-29.4.3, 1991.
- [14] M. Parameswaran, A. M. Robinson, D. L. Blackburn, M. Gaitan, and J. Geist, "Micromachined thermal radiation emitter from commercial CMOS process," *IEEE Electron Device Letters*, vol. 12, pp. 57-59, Feb. 1991.
- [15] M. Gaitan, M. Parameswaran, M. Zaghloul, J. Marshall, D. Novotny, and J. Suehle, "Design methodology for micromechanical systems at commercial CMOS foundries through MOSIS," in *Proceedings of the 35th Midwest Symposium on Circuits and Systems*, Washington, D.C., Aug. 1992.
- [16] W. Riethuller and W. Benecke, "Thermally excited silicon microactuators," *IEEE Transactions on Electronic Devices*, vol. 33, pp. 758-763, June 1988.
- [17] C. Doring, T. Grauer, J. Marek, M. S. Mettner, H. P. Trah, and M. Willmann, "Micromachined thermoelectrically driven cantilever structures for fluid jet deflection," in *Proceedings IEEE Workshop on Microelectromechanical Systems (MEMS)*, pp. 12-18, 1992.
- [18] O. Brand, H. Baltes, and U. Baldenweg, "Thermally excited silicon oxide beam and bridge resonators in CMOS technology," *IEEE Transactions on Electronic Devices*, vol. 40, pp. 1745-1753, Oct. 1993.
- [19] M. Ataka, A. Omodaka, N. Takeshima, and H. Fujita, "Fabrication and operation of polyimide bimorph actuators for a ciliary motion system," *J. Micromechanical Sys.*, vol. 2, pp. 146-150, Dec. 1993.
- [20] H. T. G. Van Lintel, F. C. M. Van De Pol, and S. Bouwstra, "A piezoelectric micropump based on micromachining of silicon," *Sensors and Actuators*, vol. 15, pp. 153-167, Oct. 1988.
- [21] T. Ohnstein, T. Fukiura, J. Ridley, and U. Bonne, "Micromachined silicon microvalve," in *Proceedings IEEE Workshop on Microelectromechanical Systems (MEMS)*, pp. 95-98, 1990.

- [22] U. Breng, T. Gessner, C. Kaufmann, R. Kiehnscherf, and J. Markert, "Electrostatic micromechanic actuators," *J. Micromechanical Microengineering*, vol. 2, pp. 256-261, Dec. 1992.
- [23] D. Brei and J. Blechschmidt, "Design and static modeling of a semicircular polymeric piezoelectric microactuator," *J. Micromechanical Sys.*, vol. 1, pp. 106-115, Sept. 1992.
- [24] C. J. Hasser, and J. M. Weisenberger, "Preliminary evaluation of a shape-memory alloy tactile feedback display," in *ASME Winter Annual Meeting*. New Orleans: ASME, pp. 73-80, 1993.
- [25] P. A. Neukomm, H. P. Bornhauser, T. Hochuli, R. Paravicini, and G. Schwarz, "Characteristics of thin wire shape metal alloy," *Sensors and Actuators*, A21-A23, pp. 247-252, Feb. 1990.
- [26] A. D. Johnson, "Vacuum-deposited TiNi shape memory film," *J. Micro-electromechanical Microengineering*, vol. 1, pp. 34-41, Nov. 1991.
- [27] J. D. Busch, A. D. Johnson, C. H. Lee, and D. A. Stevenson, "Shape memory properties in NiTi sputter deposited film," *J. Appl. Phys.*, vol. 68, pp. 6224-6228, Dec. 1990.
- [28] J. A. Walker, K. J. Gabriel, and M. Mehregany, "Thin-film processing of TiNi shape metal alloy," *Sensors and Actuators*, A21-A23, pp. 243-246, Feb. 1990.
- [29] L. M. Schetky, "Shape memory alloys," *Scientific American*, vol. 241, pp. 74-82, Nov. 1979.
- [30] K. Kaczmarek and P. Bach-y-Rita, "Tactile displays," in *Advanced Interface Design and Virtual Environments*, (W. Barfield and T. Furness, editors) Oxford University Press, 1993.
- [31] R. D. Howe, "A force-reflecting teleoperated hand system for the study of tactile sensing in precision manipulation," in *IEEE International Conf. on Robotics and Automation*, Nice, France, May 1992.
- [32] Z. Kuc, *A Bi-directional Vibrotactile Communication System*, PhD thesis, Stanford University, Stanford CA, Oct. 1989.
- [33] J. C. Craig, "Tactile letter recognition: Pattern duration and modes of pattern generation," *Perception and Psychophysics*, vol. 30(6), pp. 540-546, 1981.

- [34] C. J. Hasser, "Multi-element tactile feedback for teleoperation," in *SIG-Advanced Applications Teleoperation 1993 Conference*, pp. 1-6, New York, NY, Oct. 1993.
- [35] K. Ikuta, M. Tsukamoto, and S. Hirose, "Mathematical model and experimental verification of shape memory alloy for designing micro actuators", *Proceedings IEEE Workshop on Microelectromechanical Systems (MEMS)*, pp. 103-108, 1991.
- [36] K. B. Shimoga, "Perceptual feedback issues in dexterous telemanipulation," Technical Report RAL/KBS-2-92, Univ. of Toronto, Robotics and Automation Lab, 1992.
- [37] K. O. Johnson and S. S. Hsiao, "Neural mechanisms of tactual form and texture perception", *Annu. Rev. Neurosci.*, Vol. 15, pp. 227-250, 1992.
- [38] T. J. Moore and J. R. Mundie, "Measurement of specific mechanical impedance of the skin: effects of static force, site of stimulation, area of probe, and presence of a surround" *J. Acoustical Society of America*, pp. 577-584, Apr. 1972.
- [39] C. E. Sherrick and R. W. Cholewaik, "Cutaneous sensitivity" in *Handbook of perception and human performance* (K. R. Boff, Lloyd Kaufman, and J. P. Thomas, eds.), pp. 12-1 - 12-57, New York: John Wiley and Sons, 1986.
- [40] W. Benecke, "Silicon - microactuators: activation mechanism and scaling problems," in *IEEE Transducers*, pp. 46-50, 1991.
- [41] K. R. Udayakumar, S. F. Bart, A. M. Flynn, J. Chen, L. S. Tavrow, L. E. Cross, R. A. Brooks, and D. J. Ehrlich, "Ferroelectric thin film ultrasonic micromotors," in *Proceedings IEEE Workshop on Microelectromechanical Systems (MEMS)*, pp. 109-113, 1991.
- [42] M. Parameswaran, L. Ristic, K. Chau, A. M. Robinson, and W. Allegretto, "CMOS electrothermal microactuators," in *Proceedings IEEE Workshop on Microelectromechanical Systems (MEMS)*, pp. 128-131, 1990.
- [43] B. Rashidian and M. Allen, "Electrothermal microactuators based on dielectric loss heating," in *Proceedings IEEE Workshop on Microelectromechanical Systems (MEMS)*, pp. 24-29, 1993.
- [44] H. Fujita and K. Gabriel, "New opportunities for microactuators," in *IEEE Transducers*, pp. 14-20, 1991.

- [45] W. C. Tang, T. H. Nguyen, M. W. Judy, and R. T. Howe, "Electrostatic-comb drive of lateral polysilicon resonators," *Sensors and Actuators*, A21-A23, pp. 328-331, Feb. 1990.
- [46] M. Mehregany and T. Tai, "Surface micromachined mechanisms and micromotors," *J. Microelectromechanical Microengineering*, vol. 1 pp. 73-85, Apr. 1991.
- [47] K. E. Petersen, "Dynamic micromechanics on silicon: techniques and devices," *IEEE Transactions on Electronic Devices*, vol. ED-25, pp. 1241-1250, Oct. 1978.
- [48] C. W. Stormont, D. A. Borkholder, V. Westerlind, J. W. Suh, N. I. Maluf, and G. T. A. Kovacs, "Flexible, dry-released process for aluminum electrostatic actuators," *J. Micromechanical Sys.*, vol. 3, pp 90-96, Sep. 1994.
- [49] B. Wagner, W. Benecke, G. Engelmann, and J. Simon, "Microactuators with moving magnets for linear, torsional or multiaxial motion," *Sensors and Actuators*, A32, pp. 598-603, 1992.
- [50] K. Yanagisawa, A. Tago, T. Ohkubo, and H. Kuwano, "Magnetic micro-actuator," in *Proceedings IEEE Workshop on Microelectromechanical Systems (MEMS)*, pp. 120-124, 1991.
- [51] S. Timoshenko, "Analysis of bi-metal thermostats," *J. Optical Society of America*, vol. 11, pp. 233 - 255, 1925.
- [52] W. Chu, M. Mehregany, and R. L. Mullen, "Analysis of tip deflection and force of a bimetallic cantilever microactuator," *J. Microelectromechanical Microengineering*, vol. 3, pp. 4-7, Mar. 1993.
- [53] J. Soderkvist, "Similarities between piezoelectric, thermal, and other internal means of exciting vibrations," *J. Microelectromechanical Microengineering*, vol. 3, pp. 24-30, Mar. 1993.
- [54] S. P. Timoshenko and J. M. Gere, *Theory of elastic stability*, New York: McGraw-Hill, 1961.
- [55] J. F. Nye, *Physical properties of crystals: Their representation by tensors and matrices*, Oxford: Clarendon Press, 1957.
- [56] M. Gaitan, M. Parameswaran, R. B. Johnson, and R. Chung, "Commercial CMOS foundry thermal display for dynamic thermal scene simulation," in *Proc. SPIE*, Orlando Fl., Apr. 1993.

- [57] P. M. Osterberg, R. K. Gupta, J. R. Gilbert, and S. D. Senturia, "Quantitative models for the measurement of residual stress, poisson ratio and Young's modulus using electrostatic pull-in of beams and diaphragms," in *Solid-State Sensor and Actuator workshop*, pp. 184-188, Hilton Head, SC, June 1994.
- [58] J. Tiren, L. Tenerz, and B. Hok, "A batch-fabricated non-reverse valve with cantilever beam manufactured by micromachining of silicon," *Sensors and Actuators*, vol. 18, pp. 389-396, 1989.
- [59] MOSIS specification authors, "Orbit electrical parameters," The MOSIS Services, USC, CA, 1990.
- [60] T. A. Rhoadarmer, V. M. Bright, B. M. Welsh, S. C. Gustafson, and T. H. Lin, "Interferometric characterization of the flexure beam micromirror device," in *Proc. SPIE*, vol. 2291, pp. 13-23, Orlando FL, Jul. 1994.

Vita

Second Lieutenant Britton C. Read III was born on December 2, 1971, in Jackson, Mississippi. After graduating from Clinton High School in Clinton, Mississippi in 1989, he enrolled in Mississippi State University. In 1993, he graduated with a Bachelor of Science degree in Electrical Engineering and was commissioned as a Second Lieutenant through the ROTC program. Following graduation he moved to Wright-Patterson AFB, OH and entered the Graduate School of Engineering at the Air Force Institute of Technology, Wright-Patterson AFB, OH.

Permanent Address: 200 Gill Drive
Clinton, Mississippi 39056